



**HAL**  
open science

# Coupling geophysical and isotopic approaches to better simulate saltwater intrusion into coastal aquifers: a case study in the Crau aquifer

Bach Thao Nguyen

► **To cite this version:**

Bach Thao Nguyen. Coupling geophysical and isotopic approaches to better simulate saltwater intrusion into coastal aquifers: a case study in the Crau aquifer. Earth Sciences. Université d'Avignon, 2016. English. NNT: 2016AVIG0052 . tel-01398023

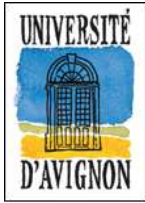
**HAL Id: tel-01398023**

**<https://theses.hal.science/tel-01398023>**

Submitted on 23 Nov 2016

**HAL** is a multi-disciplinary open access archive for the deposit and dissemination of scientific research documents, whether they are published or not. The documents may come from teaching and research institutions in France or abroad, or from public or private research centers.

L'archive ouverte pluridisciplinaire **HAL**, est destinée au dépôt et à la diffusion de documents scientifiques de niveau recherche, publiés ou non, émanant des établissements d'enseignement et de recherche français ou étrangers, des laboratoires publics ou privés.



**ACADEMIE D'AIX-MARSEILLE**  
**UNIVERSITE D'AVIGNON ET DES PAYS DE VAUCLUSE**  
**THÈSE**

pour obtenir le diplôme de DOCTORAT

Spécialité : **Hydrogéologie**

Ecole doctorale 536 « **Agrosociences et Sciences** » (A2S)

UMR 1114 EMMAH INRA-UAPV

Environnement Méditerranéen et Modélisation des Agro-Hydrosystèmes

**COUPLING GEOPHYSICAL AND ISOTOPIC APPROACHES  
TO BETTER SIMULATE SALTWATER INTRUSION  
INTO COASTAL AQUIFERS:  
A CASE STUDY IN THE CRAU AQUIFER**

Présentée par

**Bach Thao NGUYEN**

**Olivier BANTON Co-directeur de Thèse**

**Adriano MAYER Co-directeur de Thèse**

Directeur, Olivier Banton

Co-directeur, Adriano Mayer

Président, Vincent Valles

Rapporteur, Alain Dupuy

Rapporteur, Olivier Radakovitch



Laboratoire d'Hydrogéologie d'Avignon



Soutenue le 14 janvier 2016



*To my parents, my wife Thu Hang, my daughter Thao Nguyen  
and my brother Quang Toan  
Without their endless support, this could not have been possible.*



# Remerciements

Je tiens à remercier toutes les personnes qui ont contribué à ces travaux de thèse et qui ont soutenu mon séjour en France.

Je remercie mon directeur de thèse, Olivier Banton de m'avoir accueilli et m'avoir proposé ce sujet de recherche. Je remercie également mon co-directeur de thèse, Adriano Mayer pour son attention et ses motivations. Je leur suis également reconnaissant de leurs qualités pédagogiques et scientifiques, leurs nombreux conseils et l'encadrement qu'ils m'ont assuré tout au long de ces quatre années.

Je remercie Yves Travi, ex-directeur du laboratoire d'Hydrogéologie, de m'avoir accueilli au laboratoire et de m'avoir appelé : Chef. Merci aussi Mme. Liliana Di Pietro de m'avoir accueilli au sein de l'équipe EMMAH-INRA.

J'adresse mes remerciements chaleureux à ma « famille LHA » pour le soutien dont elle a fait preuve pour mes travaux durant ces 4 années passées au labo et aussi pour ses conseils, ses blagues et les bons moments passés ensemble au café. Merci Vincent, Jean Claude, Christophe, Aurélie, Marina, Anne-Laure et bien sûr Roland (M.Wikipédia) pour la tache de soleil. Je remercie Michel de m'avoir accompagné et aidé sur le terrain plusieurs jours et son épouse d'avoir accepté de dîner tard. Merci Milanka pour ses gâteaux, ses repas français, américains, asiatiques... et bien sûr vietnamiens.

Ce travail ayant nécessité de nombreuses journées de terrain, je remercie donc les propriétaires de m'avoir autorisé à venir faire des mesures régulières, merci à Reljic Christian et Petisi Vincent (GPMM), Marine Pascal (Vigueirat), Caroline Boesch et David Villesseche (SymCrau). Je tiens à remercier à l'équipe « Crau » du labo, Milanka, Anne-Laure et Marina de m'avoir accompagné et montré le terrain sur la Crau, les cailloux et aussi les moustiques pour les premières fois. Merci Albert Oliosio, Antoine Bailleux de l'INRA pour les données importantes de la zone de recherche. Merci Olivier, Kostas, Simon et aussi Jean-Christophe Comte pour tous leurs conseils et aides au terrain sur les géophysiques. Merci aussi à tous les stagiaires et collègues, Salah, Jairo, Ary, Marie, Zhora et les étudiants M1, M2 pour leurs aides sur le terrain avec les méthodes géophysiques et les campagnes piézométries.

Merci aux thésards du labo, Chloé et Floriant, aussi les ex-thésards, Salah, Laura, Aurore et Simon d'avoir partagé avec moi les bons moments au labo. Je n'oublie pas de remercier tous mes amis : Hong Hai, Thanh Tuan, Tram-Hieu, Huy-Trang, Tung-Ngoc, ... qui ont partagé avec moi notre culture vietnamienne et qui m'ont apporté de l'aide dans ma vie en France.

Je remercie mes collègues à la Faculté de Géologie et à l'Université des Mines et de la Géologie d'Hanoi ; et le gouvernement vietnamien de m'avoir donné l'opportunité d'étudier en France.

Enfin, je ne saurais oublier ma famille qui m'a toujours encouragé et soutenu. Ma reconnaissance va surtout à mes parents, mon épouse Thu Hang et ma fille Thao Nguyen pour tous leurs sacrifices, leur aide et leur encouragement. Et je ne peux pas oublier mon frère Quang Toan qui m'a aussi encouragé.

# Table of contents

<b>Remerciements .....</b>	<b>5</b>
<b>Table of contents .....</b>	<b>7</b>
<b>Chapter 1 INTRODUCTION.....</b>	<b>11</b>
<b>1.1 General context.....</b>	<b>13</b>
<b>1.2 Research objectives .....</b>	<b>14</b>
<b>1.3 Outline of thesis .....</b>	<b>15</b>
<b>Chapter 2 SALTWATER INTRUSION INTO THE COASTAL AQUIFER AND THE STUDY AREA .....</b>	<b>17</b>
<b>2.1 Hydrodynamics in coastal aquifers .....</b>	<b>19</b>
2.1.1 Dynamic balance of fresh water and salt water in a coastal aquifer .....	19
2.1.2 The pattern of fresh water flow in a coastal aquifer.....	20
<b>2.2 Effects of density in coastal groundwater .....</b>	<b>21</b>
2.2.1 Groundwater head of variable density .....	21
2.2.2 Variable-density flow .....	24
<b>2.3 The Crau aquifer and study area.....</b>	<b>28</b>
2.3.1 Introduction .....	28
2.3.2 Geological and hydrogeological setting.....	30
2.3.3 Topography .....	35
2.3.4 Climate .....	36
2.3.5 Artificial recharge and discharge .....	37
2.3.6 Origin of salinity of Crau aquifer .....	38
<b>Chapter 3 METHODOLOGIES.....</b>	<b>43</b>
<b>3.1 Methods .....</b>	<b>45</b>
<b>3.2 Hydrodynamic measurements .....</b>	<b>46</b>

---

<b>3.3</b>	<b>Geophysical investigation .....</b>	<b>52</b>
3.3.1	Electromagnetic (EM) mapping .....	53
3.3.2	The Electrical Resistivity Topography (ERT) .....	57
3.3.3	Applying geophysics to validate flow and transport modeling.....	59
3.3.4	Application to the study area.....	60
<b>3.4</b>	<b>Short-lived natural radioactive isotopes as tracers .....</b>	<b>63</b>
3.4.1	General introduction.....	63
3.4.2	Estimate of groundwater velocities using the decay of $^{222}\text{Rn}$ in a single well 63	
3.4.3	Estimate of groundwater discharge in to surface water using $^{222}\text{Rn}$ continuous monitor .....	70
<b>3.5</b>	<b>Numerical modeling of saltwater intrusion .....</b>	<b>76</b>
3.5.1	Introduction .....	76
3.5.2	Heterogeneity and variable-density flow .....	78
3.5.3	Governing equations .....	79
3.5.4	Numerical modeling of heterogeneity and variable-density flow .....	80
3.5.5	FEFLOW Code .....	83
<b>Chapter 4</b>	<b>RESULTS .....</b>	<b>85</b>
<b>4.1</b>	<b>Geophysics survey .....</b>	<b>87</b>
4.1.1	Electromagnetic mapping (EM34) .....	87
4.1.2	Electrical Resistivity Tomography (ERT).....	96
4.1.3	Partial conclusions.....	100
<b>4.2</b>	<b>Isotopic surveys .....</b>	<b>101</b>
<b>4.3</b>	<b>Groundwater numerical modeling .....</b>	<b>117</b>
4.3.1	Conceptual model.....	117
4.3.2	3D density-dependent flow model .....	119
4.3.3	Information on saltwater intrusion .....	122
<b>4.4</b>	<b>Coupling geophysical and isotopic approach to calibrate and validate saltwater intrusion modeling .....</b>	<b>126</b>

4.5	Effect of recharge and pumping on saltwater intrusion .....	138
	<b>GENERAL CONCLUSION.....</b>	<b>143</b>
	<b>Bibliography .....</b>	<b>149</b>
	<b>List of figures.....</b>	<b>165</b>
	<b>List of tables.....</b>	<b>171</b>
	<b>Annexes .....</b>	<b>173</b>
	<b>ABSTRACT.....</b>	<b>213</b>
	<b>RÉSUMÉ .....</b>	<b>213</b>
	<b>TÓM TẮT.....</b>	<b>214</b>



**Chapter 1**  
**INTRODUCTION**



## 1.1 General context

All around the Mediterranean Sea, saltwater intrusion is caused by overexploitation of fresh groundwater (Calvache and Pulido-Bosch, 1997, Duque et al., 2008, El Yaouti et al., 2009). Where groundwater is overexploitation from aquifers, water head gradients may cause the migration of sea water toward wells, making the freshwater unusable (Gimenez and Morell, 1997, El Yaouti et al., 2009).

The European Environment Agency has recognized that the problem of saltwater intrusion due to groundwater over-exploitation (Figure 1) is one of the major threats to coastal area freshwater resources in Europe (Scheidleger A et al., 2004). The salinization of the environment in coastal areas limits the supply of fresh water and damages areas of valuable land use (Vandenbohede et al., 2009). Activities such as agriculture are severely limited by the presence of saline soils. The world loses about 10 ha of arable land every minute, 3 ha of which are lost by salinization (Ghassemi et al., 1995). This is one of the main problems in arid zones leading to land desertification (Amezketta, 2006, Dahlhaus et al., 2010). These problems are increasing the importance of groundwater monitoring, management, and conservation to understand the origin and mechanisms of the salinization process for preventing further deterioration of groundwater resources.

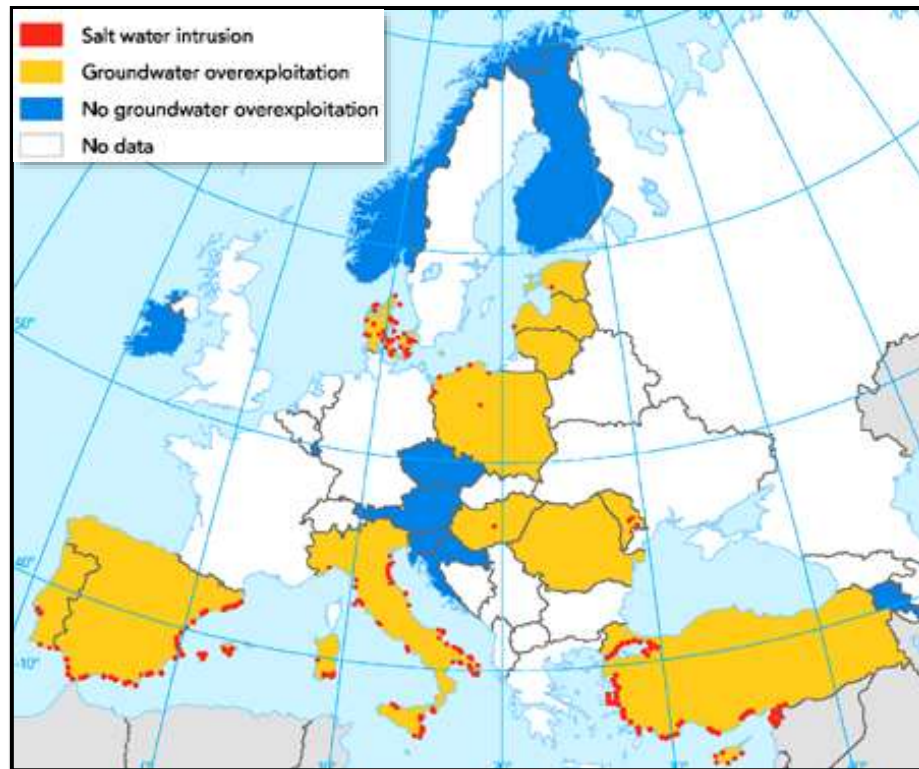


**Figure 1.** Saltwater intrusion due to groundwater overexploitation in Europe (EEA, 2005)

Many investigations have dealt with the origin of saltwater in coastal aquifer (Bear, 1999, Custodio, 2005) and discussed the following causes: overexploitation, dissolution of evaporate salts from geologic formations, saltwater spray on windy coastal strips, intense evapo-concentration of surface and phreatic water in dry climates, intense evaporation of outflowing groundwater in discharge areas and wetlands.

When considering saltwater intrusion in coastal areas by the interface between saltwater and freshwater, the problem can be conceptualize in two ways: Firstly, considering that both fluids are miscible and taking into account the existence of transition zone (Voss and Souza, 1987); secondly, an abrupt interface approximation (Bear and Verruijt, 1987, Duque et al., 2008) assuming that the freshwater and saltwater do not mix (are immiscible) and are separated by a sharp interface.

In case of an immiscible interface, salt water intrusion solution was first given for more than one century by the analytical solution approach of Badon-Ghyben (1889) and Herzberg (1901) and the single potential theory based on the Dupuis assumption given by Strack (1976). This mathematical solution can be used for hydrogeological homogeneous coastal aquifers and with a steady state flow condition. In case a mixing of saltwater and freshwater transition interface, a relatively complex approach based on the solution of the variable density flow in the dimension in both time and space (Voss and Souza, 1987, Bear, 1988, Holzbecher, 1998a, Kolditz et al., 1998). This variable density model represents the processes of saltwater intrusion in a more realistic way; not only for a homogeneous but also for a heterogeneous aquifer connect to the sea.

The Crau coastal aquifer is a delta in South-East of France, formed by alluvium of the ancient Durance, with area of 600 km<sup>2</sup>. The Crau is divided into two zones: the dry Crau with the Coussouls National Natural Reserve and the wet Crau with Vigueirat National Natural Reserve which is well-known as a rich ecosystem, hosting several endangered wildlife species and benefits from a strong natural area protection status. Moreover, the Crau aquifer provides the main resources domestic water for about 300,000 inhabitants, several industrial complexes and agriculture. The study area is one part of the Crau coastal aquifer, with a surface of 140 km<sup>2</sup> where the Crau aquifer is covered by the superficial layer of the Holocene deposits and the saltwater intrusion occurs in both groundwater and surface water.

## 1.2 Research objectives

This research focused on saltwater intrusion in a heterogeneous aquifer by using water monitoring and groundwater modeling. The main difficulty is to parameterize and calibrate/validate the variable-density modeling. This requires adequate information on aquifer parameters and concentration distribution in groundwater. To solve this problem, we propose

to use geophysical investigations to describe and image the transition zone of the freshwater/saltwater. Such investigations can help to setup and validate the variable-density flow models (Comte and Banton, 2007). Also we propose to use some natural radioactive isotopes (radon) as tracers to quantify water flows and calibrate the model.

### **1.3 Outline of thesis**

The thesis consists of five parts. A brief introduction is provided in first part to describe the general context and research objectives. Part two states the problematic of coastal aquifers and an overview of the study area. Part three provides a description of methods applied in this study, including electrical resistivity topography, electromagnetic, natural radioactive isotope and saltwater intrusion modeling. The results of these methods and of the numerical modeling are presented in Part four. Finally, Part five provides a general discussion and conclusion.



**Chapter 2**  
**SALTWATER INTRUSION**  
**INTO THE COASTAL AQUIFER**  
**AND THE STUDY AREA**



## 2.1 Hydrodynamics in coastal aquifers

### 2.1.1 Dynamic balance of fresh water and salt water in a coastal aquifer

The intrusion of seawater in coastal aquifers was first conceptualized independently by [Badon-Ghijben \(1889\)](#) and [Herzberg \(1901\)](#) assuming hydrostatic equilibrium, immiscible fluids and the existence of a sharp interface between fresh and saltwater in a homogeneous unconfined aquifer. They found that the depth of the freshwater–saltwater interface below sea level ( $z_s$ ) is shown in [Figure 2](#) and given by:

$$z_s = h_f \frac{\rho_f}{\rho_s - \rho_f} \quad (1)$$

Where  $\rho_f$  is the density of freshwater,  $\rho_s$  is the density of saltwater, and  $h_f$  is the elevation of the water table above sea level. When the equation is applied correctly, the estimated depth closely approximates the real one ([Cheng and Ouazar, 2004](#)); it is still widely used to simulate saltwater intrusion ([Essaid, 1992](#), [Cheng and Chen, 2001](#)) and, especially for educational purposes, to gain clear insight into the behavior of fresh and saline groundwater in coastal aquifer systems ([Essink, 2001](#), [Duque et al., 2008](#)). Due to molecular diffusion and hydrodynamic dispersion, fresh and salt water are actually miscible liquids: the contact between the two fluids is therefore a transition zone rather than a sharp interface ([Gambolati et al., 1999](#)). The situation is further complicated by the fact that the saltwater intrusion itself changes the fluid density, so that this parameter varies in space and time as a function of changes in concentration, temperature and pressure in the fluid. Furthermore, the porous medium itself is usually stochastically heterogeneous. In order to properly reproduce the mechanism of saltwater encroachment, a variable density flow and transport modeling approach is therefore currently adopted ([Voss and Souza, 1987](#), [Holzbecher, 1998a](#), [Koch and Zhang, 1998](#), [Bear, 1999](#), [Diersch and Kolditz, 2002](#)). The medium- and long-term effects of water management are difficult to foresee due to interaction between numerous elements and variables having different natures ([Bear, 1999](#), [Cheng and Ouazar, 2004](#), [Custodio, 2005](#)). Groundwater management thus requires the use of numerical models to test current and alternative exploitation scenarios taking into account technical aspects as well as economic, legal, social and political ones ([Bear and Verruijt, 1987](#), [Anderson and Woessner, 2002](#), [Bear, 2004](#)).

### 2.1.2 The pattern of fresh water flow in a coastal aquifer

In homogeneous media, the interface between salt and fresh water follow the Ghyben-Herzberg relation which assumes, under hydrostatic conditions, the weight of a unit column of freshwater extending from the water table to the salt-water interface is balanced by a unit column of salt water extending from sea level to that same point on the interface. Also, for every unit of groundwater above sea level there are 40 units of fresh water between sea level and the saltwater interface at depth.

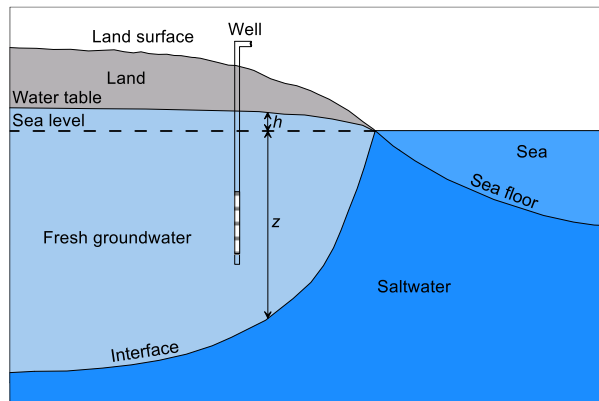


**Figure 2.** Interface between fresh water and salt water in a coastal aquifer in which the salt water intrusion is static (according to the Ghyben-Herzberg relation).

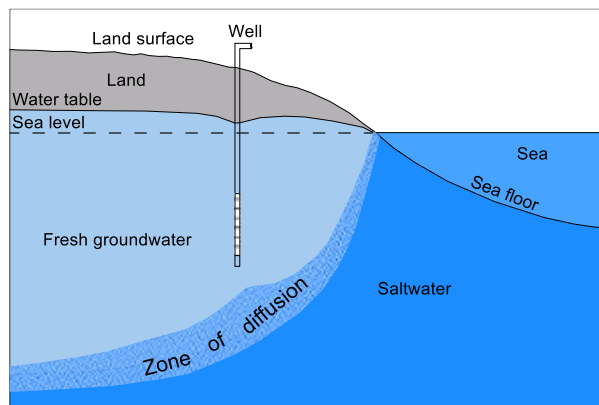


**Figure 3.** Circulation of salt water from the sea to the zone of diffusion and back to the sea in homogeneous coastal aquifer (Cooper, 1959).

This dynamic is more complex and very difficult to characterize and simulate when groundwater pumping through the freshwater lens induces a salt water upconing.

Although the presence of salinity in coastal aquifers has been widely studied, the source of this salinity remains in many cases unclear (Lloyd, 1992) Monitoring of saline domains is essential to determine and predict groundwater and soils deterioration, and assess the groundwater resources management in coastal aquifers. Monitoring involves designing a field survey strategy and methodology to obtain a reliable dataset (Melloul and Goldenberg, 1997).

Monitoring surveys can be implemented with direct (boreholes and sampling) or indirect (geophysical, geochemical or isotope survey) methods or a combination of both. Direct methods are generally expensive, especially for large study areas. It is in that context that inexpensive electrical techniques, such as the geophysical prospecting methods, are the most suitable (Land et al., 2004). With the development of computing science, we can characterize and predict saltwater intrusion with numerical modeling software such as SEAWAT, FEFLOW, SUTRA and FEMWATER.

In this research, the groundwater flow modeling will be validated using isotope measurements and geo-electrical investigations.

## 2.2 Effects of density in coastal groundwater

Many field and laboratory studies have shown that fluid density gradients caused by variation in concentration and/or temperature can play an important role in the transport of solutes in groundwater systems (Bear, 1988, Simmons et al., 2001). Simulation of density driven flow problems is very complicated due to the non-linear coupling between flow and transport equations and requires long computational time and/or powerful computer (Post et al., 2007, Ackerer and Younes, 2008). When corrections for density variations are ignored or not properly taken into account, misinterpretation of both groundwater flow direction and magnitude may result (Luszczynski, 1961, Post et al., 2007).

The hydraulic head is one of the most important metric in hydrogeology as it underlies the interpretation of groundwater flow patterns, the quantification of aquifer properties and the calibration of flow models (Post and von Asmuth, 2013). Hydraulic head observations in aquifers and surface water/sea water are very important to determine the interactions between groundwater and surface water bodies and research on salt intrusion. This parameter determined based on water level measurements in wells and piezometers.

### 2.2.1 Groundwater head of variable density

#### 2.2.1.1 Head and Pressure equation

Hydraulic head is a measure of mechanical energy per unit weight of water at everywhere within a groundwater aquifer. At any point 'i' in the groundwater body, hydraulic head can be quantified by the following equation:

$$h_i = z_i + \frac{P_i}{\rho_i g} \quad (2)$$

$h_i$  is the hydraulic head (m),  $z_i$  is the elevation head (m), represents the level of the well screen, and  $h_{p,i}$  the pressure head is the length of the water column in the well relative to  $z_i$ . For

stagnant water condition in the well,  $\rho_i$  is the density of water at the measurement point ( $\text{kg/m}^3$ ),  $g$  is the gravitational acceleration ( $\text{m/s}^2$ ), and the pressure  $P_i$  of the groundwater at the measurement point (Pa) is equal to the weight of the overlying water per unit cross-sectional area:

$$P_i = \rho_i g h_{p,i} \quad (3)$$

$h_{p,i}$  related to the pressure of the ground water at the well screen  $P_i$  or the height of the water column, by the following equation:

$$h_{p,i} = \frac{P_i}{\rho_i g} \quad (4)$$

Substituting equation (3) into equation (2), we will have:

$$h_i = z_i + h_{p,i} \quad (5)$$

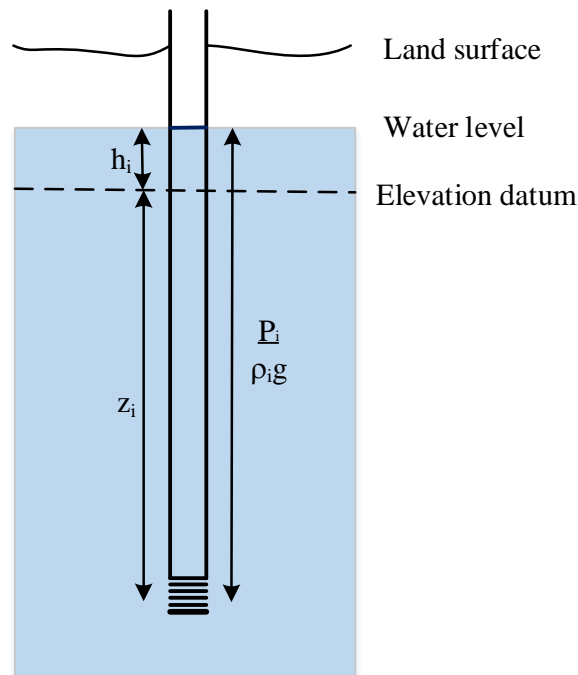


**Figure 4.** Schematic representation of a piezometer in a groundwater system with a constant density (edited from Musczynski,1961 and Post, 2013).

The absolute pressure  $P_{abs}$  is the sum of the atmospheric pressure and the groundwater pressure:

$$P_{asb} = P_{atm} + P_i \quad (6)$$

In groundwater of constant-density, water table is defined as the surface where the absolute pressure equals the atmospheric pressure,  $P_{asb} = P_{atm}$  and  $P_i = 0$ . With the equation(5),  $h_i = z_i$ , therefore, water table measured in situ equals the hydraulic head at the depth of water table. In this case, if all heads are compare to the same reference datum and groundwater have the same density  $\rho$ , hydraulic head could be compare directly to define the flow direction, groundwater will flow along the hydraulic head gradient from high to low hydraulic head.

If groundwater system with  $\rho$  varies over an area or with depth, value of  $h_{p,i}$  do not correctly represent partially variations of pressure  $P$  or the same  $P$  can correspond to different values of  $h_{p,i}$  depending on groundwater density. The concept of point-water head have been used (Luszczynski, 1961) as water level in a well filled with water coming from a point in an aquifer and which is sufficient to balance the pressure in the aquifer at that point. Therefore, density corrections must be made to the head that is measured in a well (Fetter, 2001) so the density of water in each piezometer must be estimated.

### 2.2.1.2 The fresh-water head

The fresh water head at any point in the ground is defined (Luszczynski, 1961, Acworth, 2007) as the head that would be developed in a variable density system if the pressure at the piezometer intake was generated by an equivalent column of fresh water. In other words, this point is defined as the water level in a well filled with fresh water from that point to a level high enough to balance the existing pressure at that point. Therefore, for the waters that have higher salinity contents than fresh water, the fresh water head will be higher than the point-water head and if we are in a fresh water aquifer, all point water heads are also fresh water heads. Figure 5 shows the head relationship in water of variable density for point-water head and fresh-water head in an unconfined aquifer with saline water overlain by fresh water. The fresh-water head is:

$$h_{f,i} = \frac{P_i}{\rho_f g} + z_i \quad (7)$$

$$h_{f,i} = \frac{\rho_i}{\rho_f} h_i - \frac{(\rho_i - \rho_f)}{\rho_f} z_i \quad (8)$$

Where  $\rho_f$  is the density of freshwater, normally taken as 998.3 or 1000kg/m<sup>3</sup>.

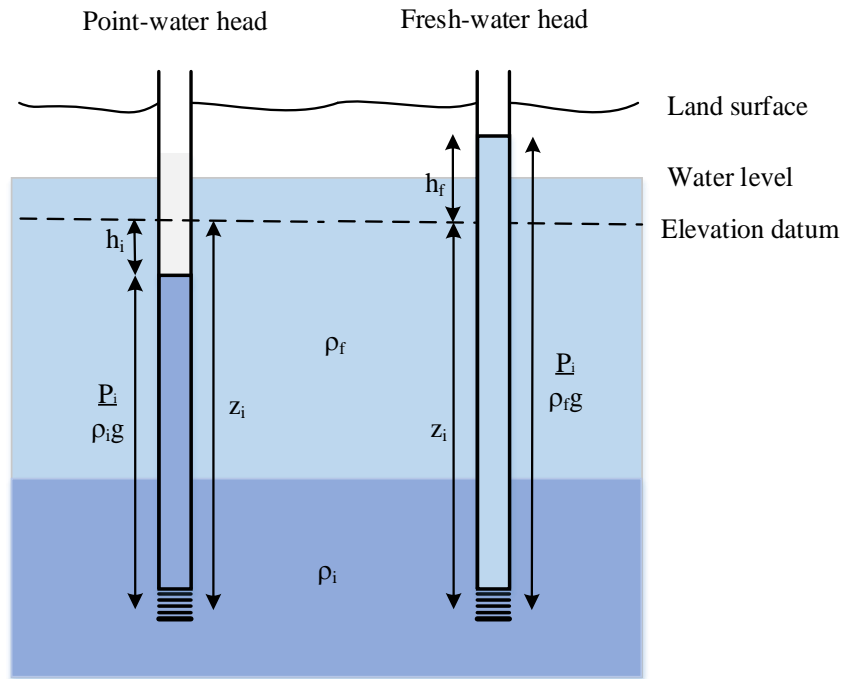


**Figure 5.** Schematic representation of head definitions in variable-density groundwater systems (modified from Muszynski 1961). Lightest shading corresponds to fresh water and darker shading represents increasing salinity.

### 2.2.2 Variable-density flow

Fluid flow is classified as variable-density flow if the flow pattern is affected by density differences in the fluid system, mainly influenced by temperature and salinity (Holzbecher, 1998b). Some other scientists use the term as “density-driven flow” or “density-dependent flow”.

#### Darcy’s Law

Actually, flow in aquifer cannot be directly measured. Darcy’s law is used to define the relation between specific flow and hydraulic head which can be measured.

$$\vec{q} = -K\nabla h \quad (9)$$

Where:  $\vec{q}$  denotes specific discharge (volume of fluid per unit cross-sectional area of porous medium per unit time, m/s) and also call as Darcy velocity

$K$  is hydraulic conductivity or permeability (m/s), and considered as isotropic, i.e. constant in all directions  $x,y,z$ .

$\nabla h$  is the hydraulic gradient, which is the driving force of groundwater flow per unit weight of groundwater (dimensionless).

Darcy's law in three dimensions could be written as follow:

$$\begin{aligned}q_x &= -K_x \frac{\partial h}{\partial x} \\q_y &= -K_y \frac{\partial h}{\partial y} \\q_z &= -K_z \frac{\partial h}{\partial z}\end{aligned}\tag{10}$$

The equation (9) is a simplified form of general physical law for fluid flow in a porous medium, which also applies to variable-density fluids (Bear, 1988, Post et al., 2007):

$$\vec{q} = -\frac{k}{\mu} (\nabla P - \rho \vec{g})\tag{11}$$

and in three dimensions

$$\begin{aligned}q_x &= -\frac{k_x}{\mu} \frac{\partial P}{\partial x} \\q_y &= -\frac{k_y}{\mu} \frac{\partial P}{\partial y} \\q_z &= -\frac{k_z}{\mu} \left( \frac{\partial P}{\partial x} + \rho g \right)\end{aligned}\tag{12}$$

Where  $k_x$ ,  $k_y$ ,  $k_z$ , are the principal directional permeabilities in the  $x$ ,  $y$ ,  $z$  directions ( $m^2$ ), a property of the porous medium;  $\mu$  is dynamic viscosity ( $kg/m/s$ ) of the groundwater;  $P$  is fluid pressure ( $kg/m/s^2$ ),  $\rho$  is fluid density ( $kg/m^3$ ) and  $g$  is the gravitational acceleration ( $m/s^2$ ).

From equation (11) shows the two basic driving forces for groundwater flow should be know:  $\nabla P$  and  $\rho \vec{g}$ . This is the main reason why quantification of groundwater flow from field data, which normally occurs in the form of head measurements requires a special treatment (Post et al., 2007). In this case, it is necessary that the hydraulic head refers to the same density, normally to the density of freshwater. Combining equation (7) and equation (12) gives the following:

$$\begin{aligned}
q_x &= -\frac{k_x \rho_f g}{\mu_f} \frac{\mu_f}{\mu} \frac{\partial h_f}{\partial x} = -K_{fx} \frac{\partial h_f}{\partial x} \\
q_y &= -\frac{k_y \rho_f g}{\mu_f} \frac{\mu_f}{\mu} \frac{\partial h_f}{\partial y} = -K_{fy} \frac{\partial h_f}{\partial y} \\
q_z &= -\frac{k_z \rho_f g}{\mu_f} \frac{\mu_f}{\mu} \left[ \frac{\partial h_f}{\partial z} + \left( \frac{\rho - \rho_f}{\rho_f} \right) \right] = -K_{fz} \left[ \frac{\partial h_f}{\partial z} + \left( \frac{\rho - \rho_f}{\rho_f} \right) \right]
\end{aligned} \tag{13}$$

With this equation,  $K_{fx}$ ,  $K_{fy}$ ,  $K_{fz}$  (m/d) are freshwater hydraulic conductivity in the principal directions  $x$ ,  $y$ ,  $z$ . It is assumed here that salinity variations have a negligible effect on  $\mu$  so that  $\mu_f/\mu \approx 1$ , which is a very good approximation for most practical applications. The difference between  $K_f$  and field-measured values of hydraulic conductivity, which are for ambient values of  $\mu$  and  $\rho$ , is much smaller than the uncertainty associated with this parameter. Therefore, in the equation for two components  $x$  and  $y$ , no special correction of existing hydraulic conductivity is required. Whereas in vertical flow component, the term  $\frac{\rho - \rho_f}{\rho_f}$  involving local groundwater variable-density is needed (Post et al., 2007). This equation is used in most of well-known variable-density flow and transport code such as FEFLOW (Holzbecher, 1998a, Kolditz et al., 1998, Diersch and Kolditz, 2002) or SEAWAT (Guo et al., 2002).

### Horizontal flow component:

When using equations (10) and (13) to calculate horizontal flow, it is very important that the freshwater head gradient (or pressure gradient) is evaluated using freshwater heads at the same depth (Post et al., 2007). In variable-density groundwater, freshwater head may vary with depth, even for hydrostatic conditions (Fetter, 2001). Therefore, all the measurements are taken from piezometers with screens at different depths, fresh water heads need to be calculated at a suitable reference depth and with the same density. At a point  $i$ , the pressure at reference depth  $P_r$  has a relation to pressure measured at screen  $P_i$  as follow:

$$P_r = P_i - g \int_{z_i}^{z_r} \rho dz = P_i - \rho_a g (z_r - z_i) \tag{14}$$

Where  $\rho_a$  is average density between measurement point  $z_i$  and the reference level  $z_r$ .

$$\rho_a = \frac{\rho_r + \rho_i}{2} \tag{15}$$

A correction of density between screen depth  $z_i$  at point  $i$  to reference depth  $z_r$  needs to be done. In a variable-density aquifer, water with low density (fresh water) floats on water with higher density (saltwater). From equation (8) and (14), we obtain the corresponding freshwater head at  $z_r$  ( $h_{f,r}$ )

$$h_{f,r} = z_r + \frac{P_r}{\rho_f g} = z_r + \frac{\rho_i}{\rho_f} (h_i - z_i) - \frac{\rho_a}{\rho_f} (z_r - z_i) \quad (16)$$

Horizontal component flow then could be calculated from the horizontal gradient as in the following:

$$\begin{aligned} q_x &= -K_f \frac{\Delta h_f}{\Delta x} \\ q_y &= -K_f \frac{\Delta h_f}{\Delta y} \end{aligned} \quad (17)$$

### 2.2.2.1 Density estimates

Groundwater density is an important parameter in the interpretation of flow patterns in coastal aquifer. The fluid density can be estimated from the fluid electrical conductivity (EC) obtained using a standard fluid electrical conductivimeter (Acworth, 2007). This method is extremely practical because measurements are cheap and easily performed (Post, 2012). Relationship can be established between electrical resistivity, solute concentration and density. Such relationship have been developed for coastal areas and sand aquifers (Stuyfzand, 1989):

$$\rho = 1000 \times \left( 1 + 0.805 \times TDS - 6.5 \times 10^{-6} \times (T - 4 + 220 \times TDS)^2 \right) \quad (18)$$

Where:  $T$  is the fluid temperature ( $^{\circ}\text{C}$ ) and  $TDS$  is the total dissolved solids (kg/kg).  $TDS$  can be converted from resistivity with the conversion factor for natural waters (usually between 0.55 and 0.75). This can be approximated from the formula following (Stuyfzand, 1989):

$$TDS = 0.69778 \times 10^{-6} \times EC_{20} \quad (19)$$

Where:  $EC_{20}$  is the fluid conductivity in  $\mu\text{S}/\text{cm}$  at temperature  $20^{\circ}\text{C}$ . Since conductivity varies with temperature, it is necessary to correct the readings for changes in temperature. Most instruments contain circuits that automatically compensate for temperature and correct the readings to a standard  $25^{\circ}\text{C}$ . Therefore, it is necessary to account for this temperature difference using the relationship formular given by Stuyfzand:

$$EC_{20} = EC_{25} \times \left( 1 + 0.23 \times (T_{20} - T_{25}) \right) \quad (20)$$

This equation, for a 5°C change, becomes  $EC_{20} = EC_{25} \times 0.85$ .

Water density can be also estimated on the basis of EC, temperature and pressure using the ‘UNESCO-1980’ equation of state of seawater (Unesco. et al., 1981).

$$\rho(S, t, p) = \frac{\rho(S, t, 0)}{\left[ 1 - \frac{p}{K(S, t, p)} \right]} \quad (21)$$

Where:  $\rho$  is the density ( $\text{kg/m}^3$ ) of sea water at practical salinity  $S$ , temperature  $t$  ( $^{\circ}\text{C}$ ) and pressure  $p$  (dBar),  $K$  is the secant bulk modulus relates the change in pressure to the change in volume. The practical salinity  $S$  base on the conductivity and is a function of the conductivity ratio ( $R$ ).

$$R = \frac{EC_{(S,t,p)}}{EC_{(35,15,0)}} \quad (22)$$

in which  $EC_{(S,t,p)}$  is the electrical conductivity of sea water at salinity  $S$ , temperature  $t$  and pressure  $p$ , and  $EC(35,15,0)$  is the electrical conductivity of standard sea water of practical salinity 35, at 15°C and at atmospheric pressure.

This approach can be considered to be a refinement of the approach of Stuyfzand. After the comparison between these approach (Post, 2012), the relationship given by Stuyfzand is better to predict the densities at low salinities ( $EC < 30$  mS/cm).

## 2.3 The Crau aquifer and study area

### 2.3.1 Introduction

The Crau coastal plain is a paleo-delta of the Durance River, located in the South-East of France, East of the present delta of the Rhône River, which is also known under the name of Camargue. The Crau aquifer delimited by Alpilles mountains in the North and by the Mediterranean sea in the South, forming a triangular area of about 600  $\text{km}^2$  between Arles, Salon-de-Provence and Fos. The aquifer is mostly recharged by direct infiltration of rainfall, irrigation practices and lateral groundwater flows. The irrigation of about 15,000 ha of meadow is done using water from the Durance supplied by a dense network of channels (Oliosio et al., 2013). Groundwater naturally discharges into the marshes and the Rhône River. Intensive withdrawal occurs from pumping wells. The Crau aquifer is the main resource of domestic water for more than 300,000 inhabitants. It is important to notice that there is no natural river over the Crau plain and that all the surface water transfers occur through artificial canals.

In this study, our approach was applied on an area of about 140 km<sup>2</sup>, is situated in downstream part of the Crau coastal plain, what is now called “Study area” shown in Figure 6).

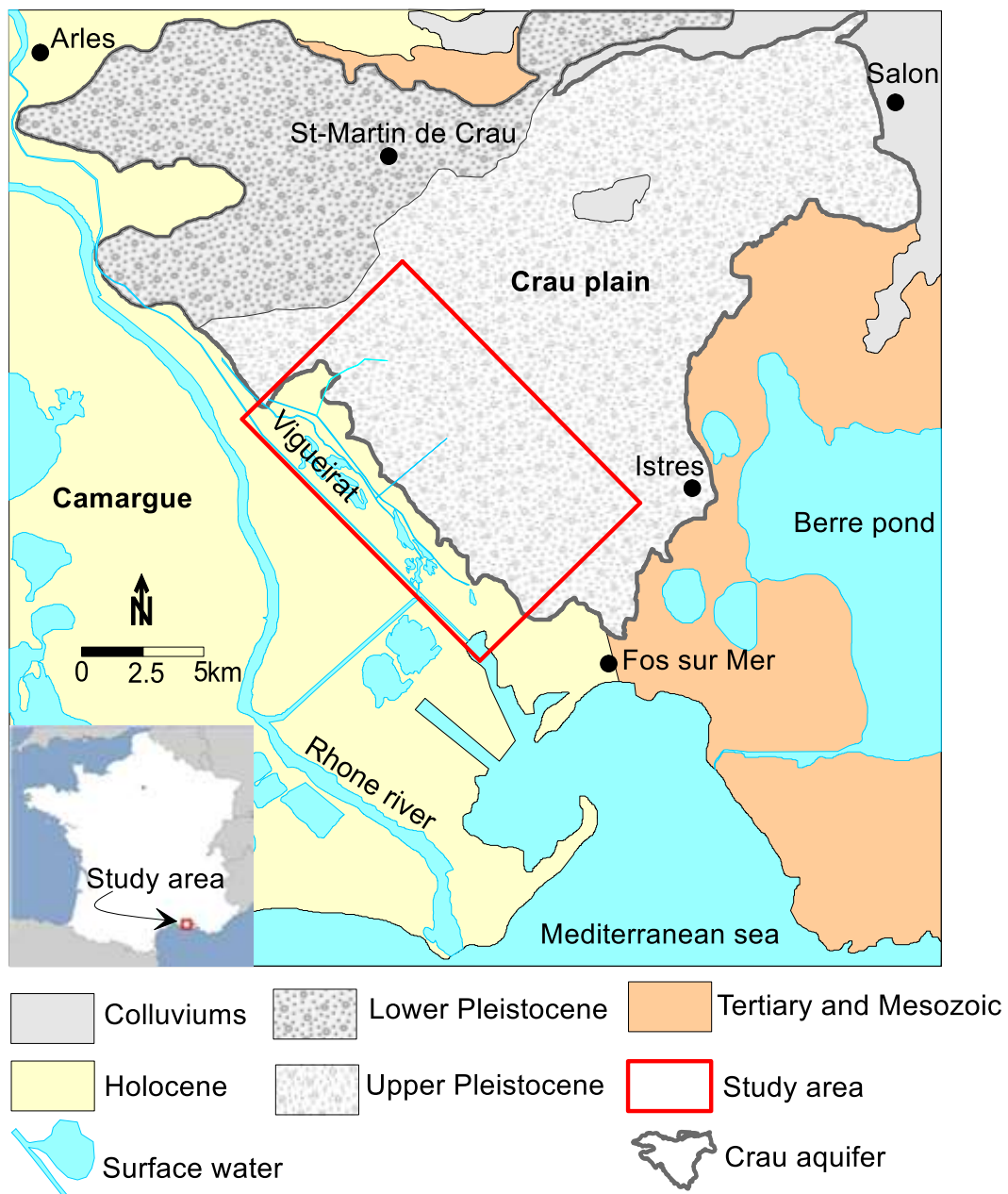


**Figure 6.** Location of Crau coastal plain and the study area. Limit of the Crau aquifer and lower/upper Pleistocene (Albinet M. et al., 1969)

The study area was considered a suitable case of study area because: (i) it is an important aquifer in the South of France, highly vulnerable to salinization due to its coarse nature; (ii) groundwater salinity problems have occurred due to a great number of groundwater extraction wells for irrigation and the changes in the water management; (iii) the groundwater abstraction for domestic/industrial use caused significant variation of water heads; (iv) a dataset over a 20 year period is available for the site.

### 2.3.2 Geological and hydrogeological setting

The Crau delta is filled with quaternary deposits lying on very thick marl substratum of Pliocene age. The Crau aquifer constitutes an unconfined aquifer mainly formed during the Pleistocene and Quaternary period, by a procreation of sedimentary bodies contributed by gravels alluvium of Durance River (E. Colomb and Roux, 1986). This aquifer presently outcrop in the Crau plain and progressively southwestwards to 50m below sea-level oh the coastline (de Montety et al., 2008) and continue to the continental shelf edge (around 30km from the shoreline) and thickness varies from 10 to 70m (Boyer et al., 2005), represented in cross-sections A-A' and C-C' (Figure 8 and Figure 10). Different geological zones can be distinguished corresponding to different times and origins of deposits (Figure 7). The lower Crau or "Old Crau", mainly represented by Arles Crau, is issued from deposits from the lower Pleistocene (from -2,000,000BP to -600,000BP). The main deposit of the lower Pleistocene is gravels of quartzite and limestone with a yellow matrix of sand and clay. The "Young Crau" is issued from deposits from the second part of the Pleistocene (upper Pleistocene): from -600,000BP to -100,000BP for the Luquier Crau, mainly of Riss period, and -100,000BP to -10,000BP for the Miramas Crau, mainly of Würm period (E. Colomb and Roux, 1986). Both formations "Old Crau" and "Young Crau" have the general orientation NE-SW. The gravel and pebbles from Alps having variable lithology, with dominant contribution of magmatic rock is the main component of the deposits. They are locally cemented and constitute a conglomerate or associated to a matrix of finer materials (silty sand), which is locally called "taparas". This formation has a variable thickness from few meters in the area of ledge (Aulnes and Entressen ponds) up to more than 50m in river paleo-channels area (East of St Martin de Crau) and average from 10-20m in the center (Roure S et al., 2004). It is very heterogeneous with lateral distribution due to shifts in the course of the Durance River.

The superficial layer (upper part of the Holocene Rhone deposits) is made of clay and silt with sand interlayers, heterogeneous and very low permeable (Boyer et al., 2005). This layer deposited during the early stage of the transgression (18000 to 6000 BP) and thickness varies from 0m at the limit of Crau aquifer to around 30m in Camargue area.

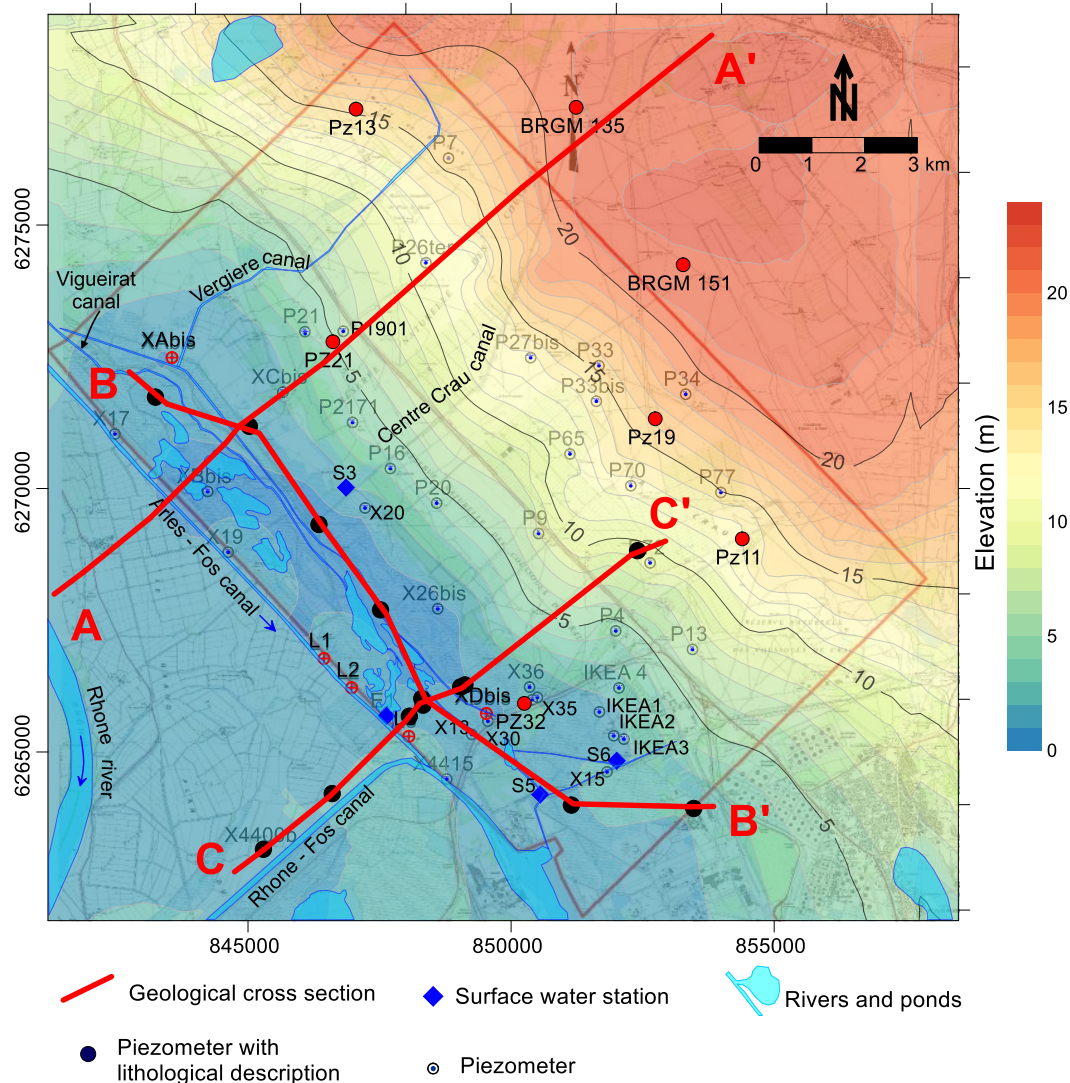


**Figure 7.** Location of geological formations and cross sections and topography map

Due to the alluvial placer dynamic, hydraulic conductivity ( $K$ ) is very variable. The value of  $K$  of Crau aquifer varies according to grain size, from  $4.0 \times 10^{-5}$  and  $1.6 \times 10^{-2}$  m/s by “Bureau de Recherches Géologiques et Minières, France” (BRGM, 1995), between  $1.6 \times 10^{-5}$  and  $1.8 \times 10^{-2}$  m/s (Simmarano, 2012) and between  $1 \times 10^{-5}$  and  $8 \times 10^{-2}$  m/s (INRA, 2013). Location of measured and calculated hydraulic conductivities in previous studies shown in Figure 11 and distribution of  $K$  modeled from INRA (2013) shown in Figure 12. The transmissivity could be very high in the area of Miramas, up to  $10^{-1}$  m<sup>2</sup>/s, and between  $5 \cdot 10^{-3}$  and  $5 \cdot 10^{-1}$  m<sup>2</sup>/s elsewhere (SAFEGE, 2006). The specific yield was calculated by BRGM (1995) from 0.1 to 0.5, with an average value of 0.15.

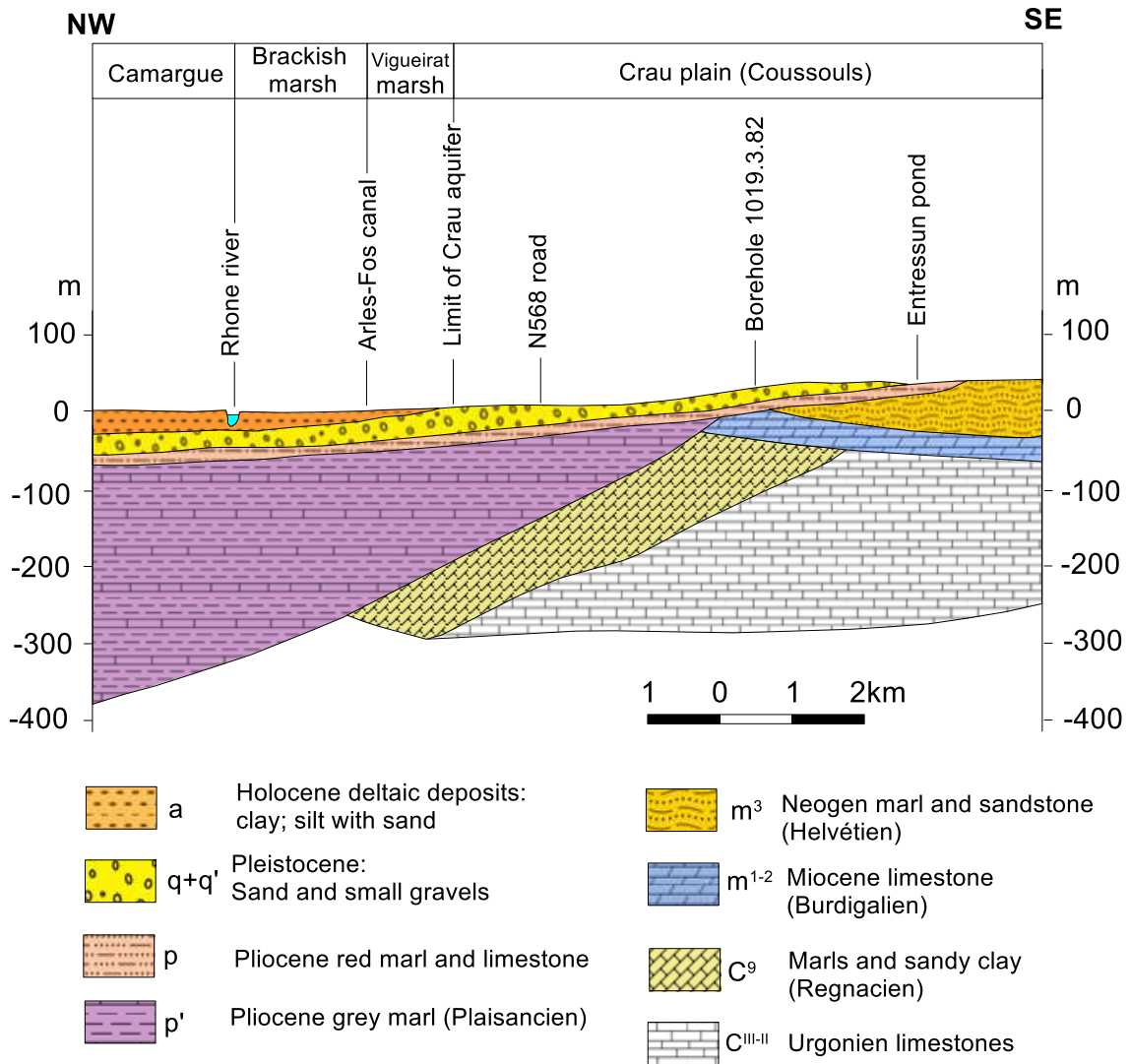


Figure 8. Geological cross section A-A' (Figure 14) (BRGM, edited)

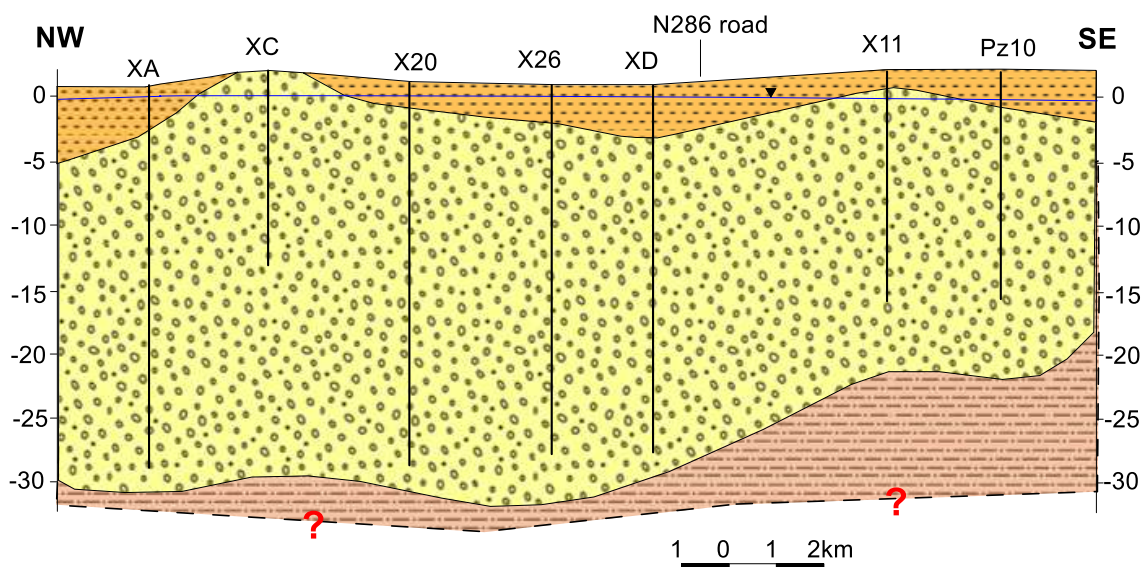
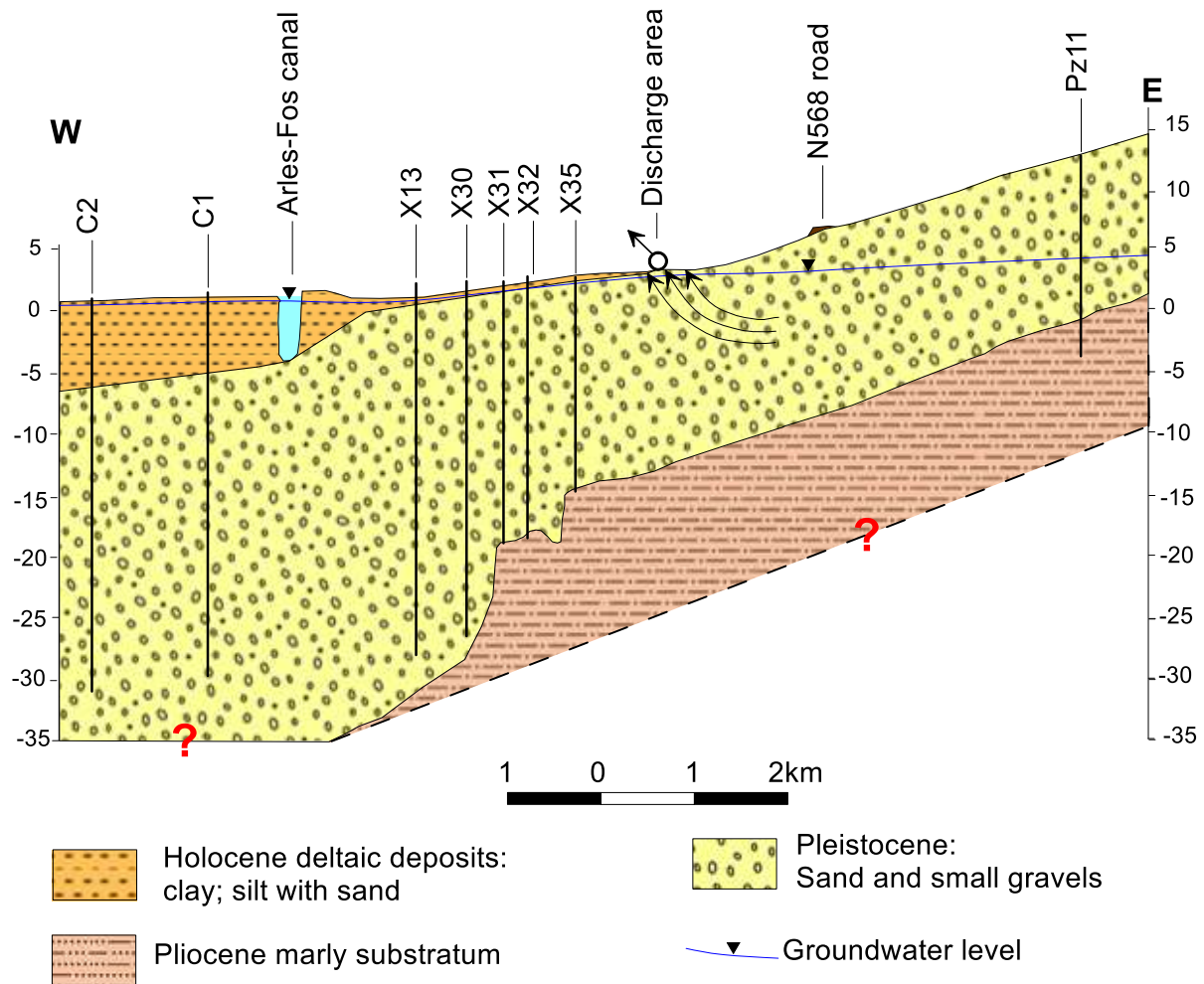


Figure 9. Hydrogeological cross section B-B' (BRGM, edited)



**Figure 10.** Schematic hydrogeological cross section C-C' (BRGM, edited)

The Crau aquifer is globally unconfined, but becomes semi-confined to confined in the marsh area of Vigueirat and Landre ponds, due to the presence of semi-pervious material (Rhône River sediment and lacustrine deposits). This material has low hydraulic conductivity (between  $3.7 \times 10^{-5}$  and  $8.7 \times 10^{-3}$  m/s) and its thickness in the study area varies from 0m at the limit of Crau aquifer to more 7m near Arles-Fos canal. The specific yield of aquifer obtained from pumping tests is in the range of 0.01 to 0.18 attesting the unconfined to semi-confined (leaky) behavior of aquifer.

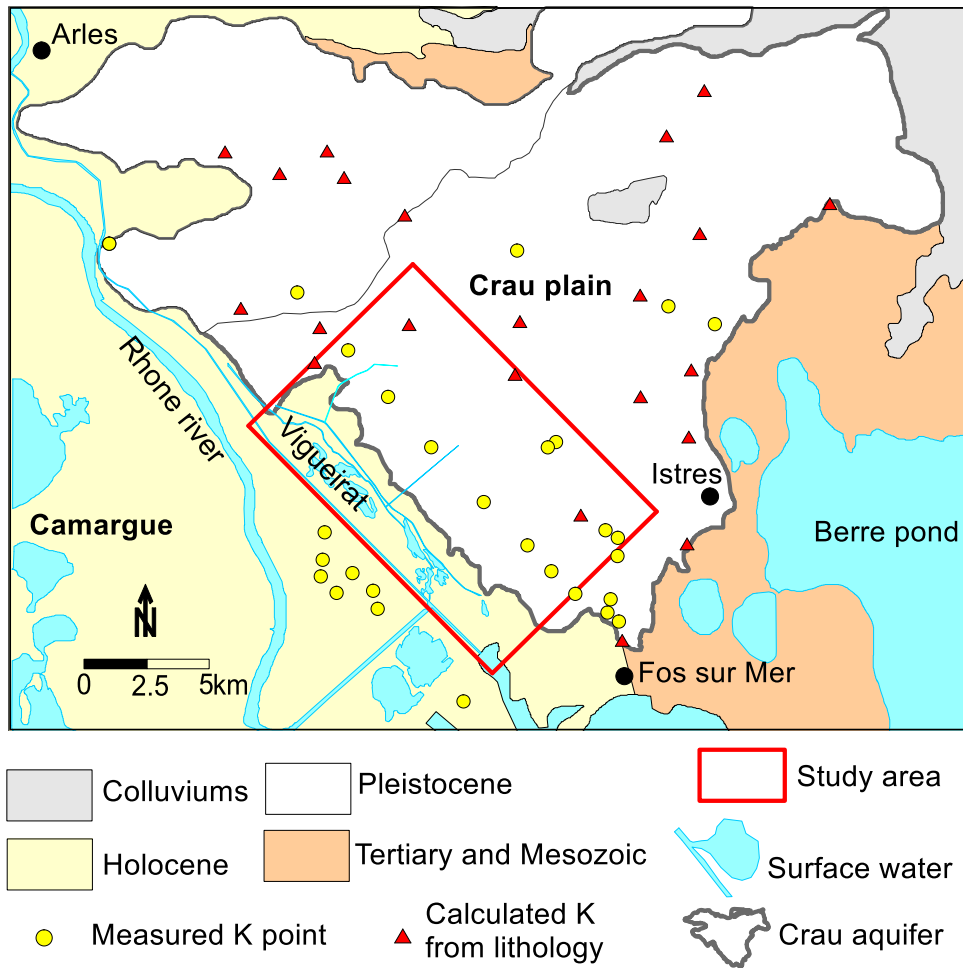


Figure 11. Available hydraulic conductivity in Crau aquifer (yellow point measured by BRGM and red point calculated from lithological data by Simmarano, 2012)

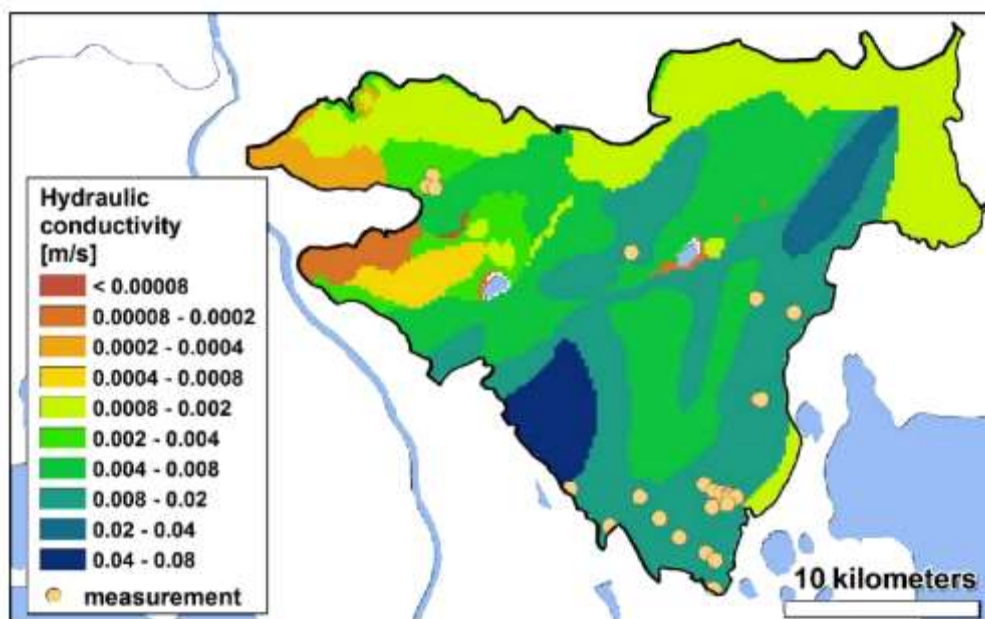


Figure 12. Hydraulic conductivity distribution from INRA, 2013

The hydraulic head is about 7.5 - 8.0 m.asl in the north-eastern area and decreases to south-western with a mean hydraulic gradient of 2-3‰.

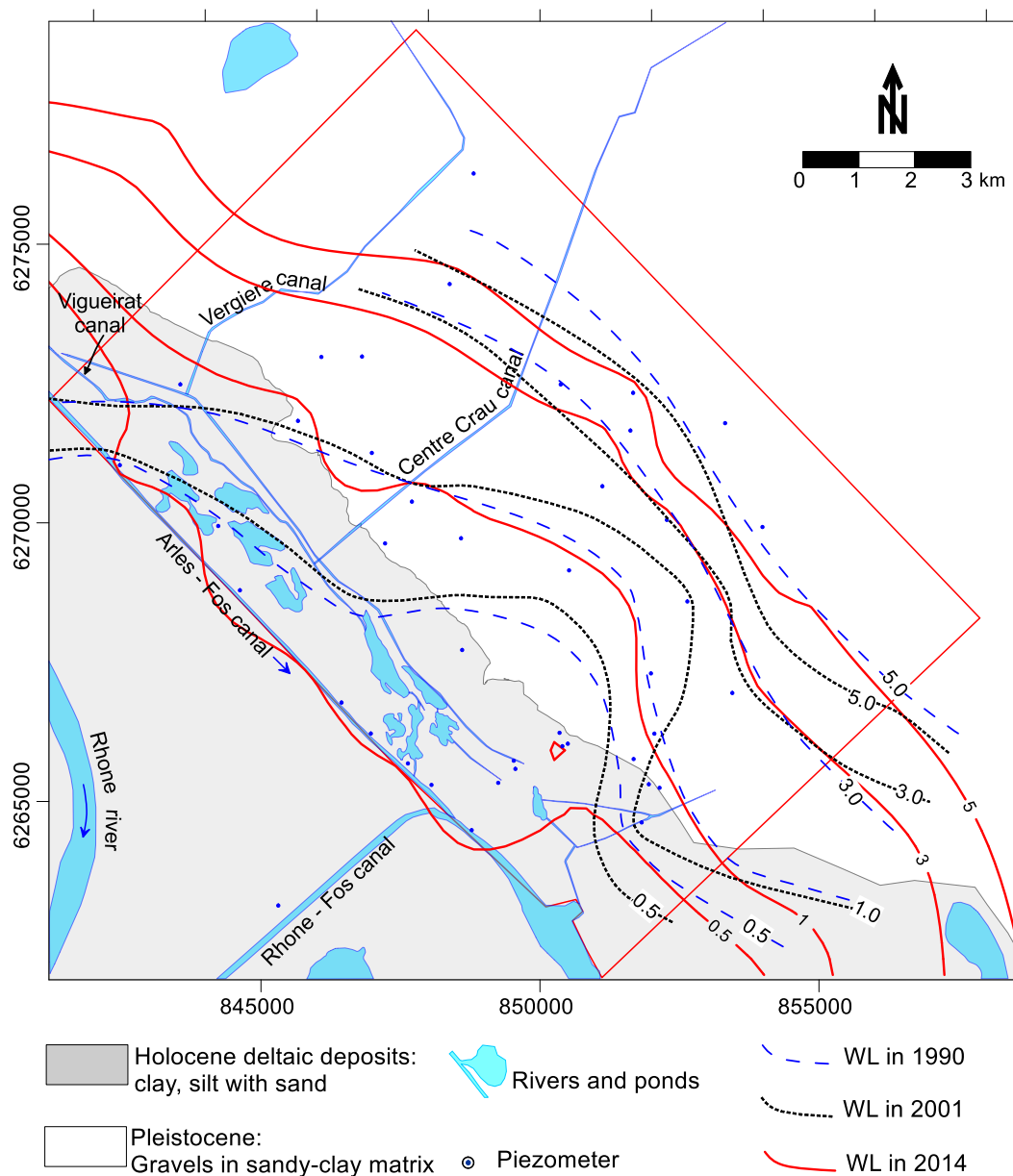


Figure 13. Water level distribution from 1990 to 2014. Data in 1990 and 2001 from SAFEGE (2004)

### 2.3.3 Topography

The Crau delta extends North to Alpilles reliefs, East to the Rhône River and Camargue and West to limestone outcrops of Miramas and Istres area. It is an alluvial plain with a mean slope of 0.4% to South-West, which is also the general trend of groundwater flow.

In study area, the depositional have a slight slope and divides this the studied sector into two parts, high elevation part in upstream area with elevation varies from 5m in center to 20m

in north-east. From center to downstream area, the elevation is lower than 5m and less than 2m in marsh area (Figure 14).

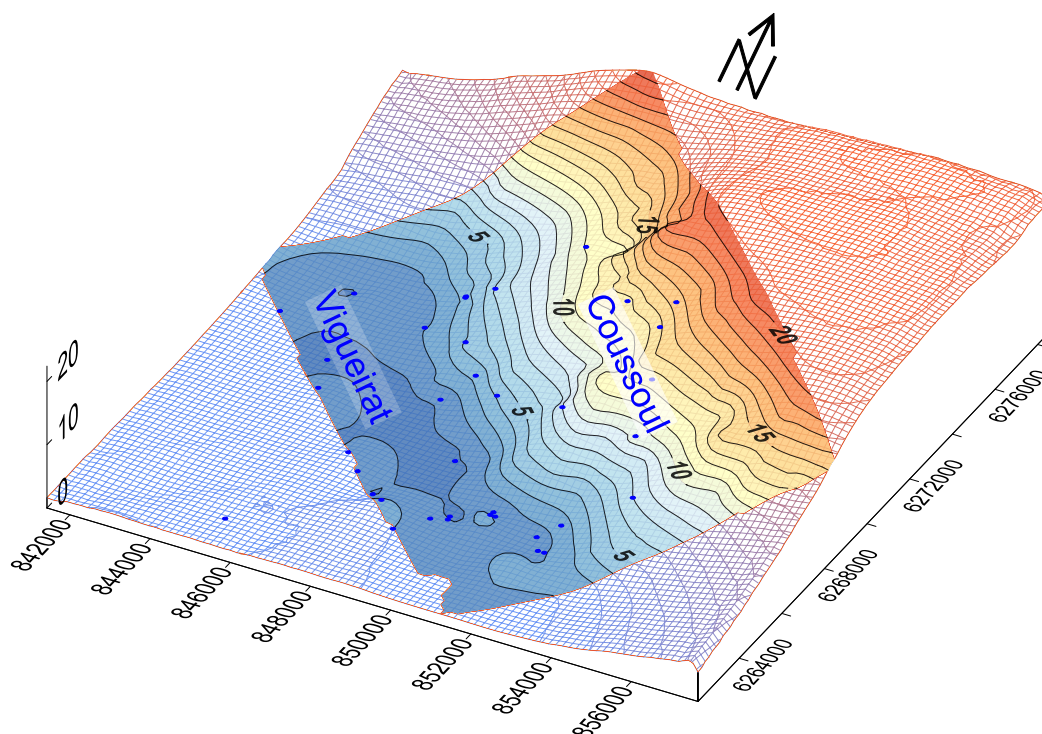
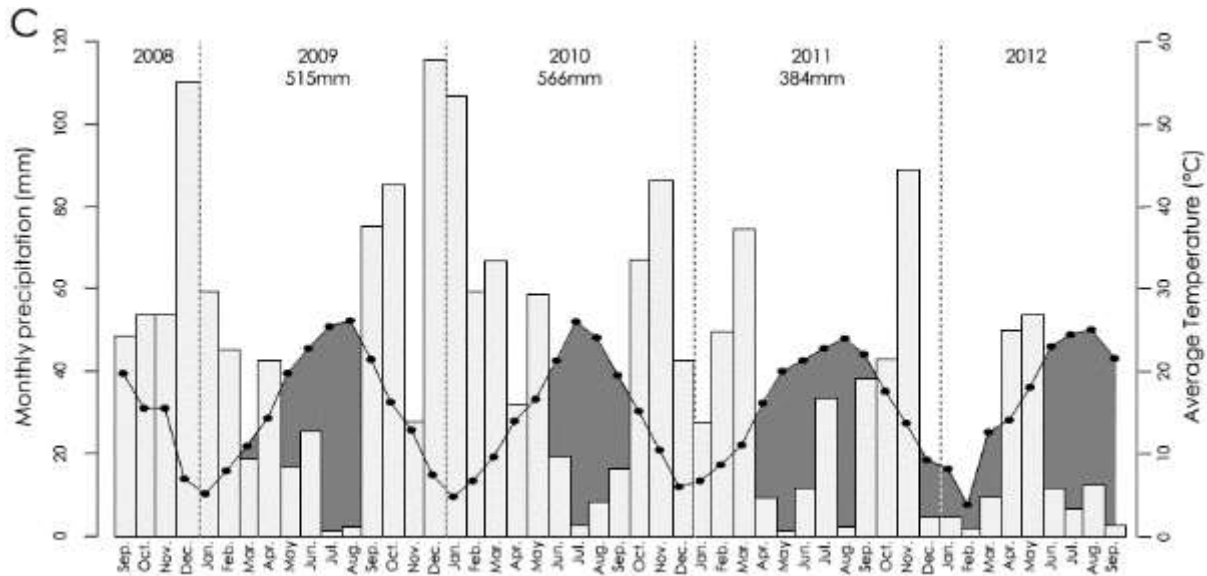


Figure 14. Topography of study area

### 2.3.4 Climate

The Crau has a meso-Mediterranean climate characterized by two periods: the dry season with a 3-months summer drought, from June to the end of August, a mild winter (average temperature of 7°C and rare frosts). Annual rainfall is 400 to 600 mm, mainly occurring in autumn (50%), and December-January period (up to 120mm/month). The number of sunshine hours is high (>2800) and the wind very frequent and strong. This wind is an essential component of the Crau climate, with 300 days of wind per year, including 70 days with wind speeds higher than 20 km/h, mainly caused by the Mistral which is a north/north-westerly wind taking place in the Rhone corridor. This wind is cold and dry which increases soil desiccation and sunlight and lowers winter temperatures. The means temperature varies from 5°C in December to 27°C in June and August and average is 15-16°C. In dry Crau (Coussouls), the gravels accumulate heat during the day therefore temperature is higher than which in wet Crau (Vigueirat). Another major component of the Mediterranean climate is the high inter-annual variability. For example, between 1997 and 2006, the southern meteorological station of Crau area recorded an average yearly precipitation of 561 mm but with a minimum of 394 mm and a maximum of 823 mm. The inter-annual variability is illustrated by the ombrothermic diagram (Bagnouls and Gausson, 1953) (Figure 15). From this diagram, the period which temperature

higher than precipitation, represent a dry period and inversely, the rest are humid periods. It shows that 2010 and 2011 were rather humid compared to 2012. Despite its relatively small size, a significant environmental condition gradient occurs from North to South and is reflected by a phonological time lag of approximately 5 to 10 days (phonological events occur earlier in southern areas) (Bourelly et al., 1983).



**Figure 15.** Monthly rainfall (bars) and monthly temperature (dots) from Istres station. The grey filled parts shown the dry periods using the ombrothermic diagram from Bagnouls, 1953 (data from INRA)

### 2.3.5 Artificial recharge and discharge

The recharge of the Crau aquifer (550 km<sup>2</sup>) highly depends on the irrigation of around 15,000 ha of orchards and meadow from water of Durance River supplied through a dense network of canals which control the surface flows system. The contribution of irrigation to the recharge is estimated between 50% and 80% of the total recharge of aquifer depending on the estimation method (Saos JL et al., 2006, Oliosio et al., 2013) and the rest of recharge from rainfall. Groundwater in Crau aquifer is globally freshwater and greatly abstracted for domestic and industries.

In the studied area, 79 pumping wells have been found, including 8 municipal pumping stations and 71 private wells which provide about 965 m<sup>3</sup>/h for domestic supply, more than 1050 m<sup>3</sup>/h for industrial complexes and about 410 m<sup>3</sup>/h for agricultural activities (Annex 4). The total withdrawal reaches about 56,000 m<sup>3</sup>/day. Municipal and irrigation wells are mainly located North-East of the area (upstream of study area) and have screen depths varying between less than 10 m.asl to more than 20 m.asl (Figure 16).

Irrigation activities are mostly in the center and North of area (dry Crau), with about 1000 ha of orchards and take irrigation water from groundwater during the dry season (March to September).

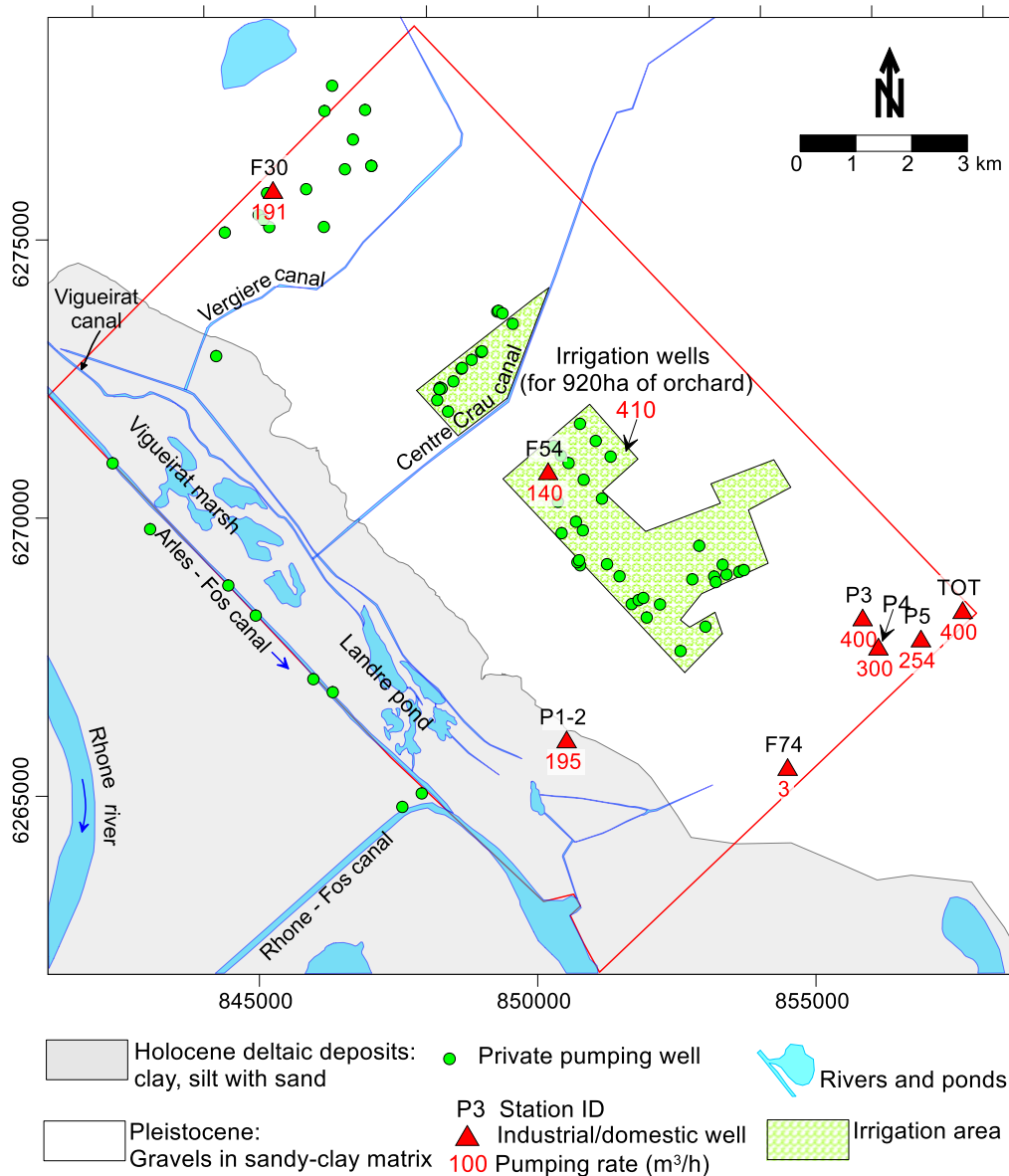


**Figure 16.** Groundwater exploitation activities in study area (sources from Safeg, Symcrau and INRA)

### 2.3.6 Origin of salinity of Crau aquifer

The origin of salinity of groundwater have been introduced in many guidelines (FAO, 1997, Bear, 1999) and applied in difference coastal aquifers and difference formations (Pulido-Leboeuf et al., 2003, Wang and Jiao, 2012, Khaska et al., 2013). Several sources of salinity have been identified: general mixing process of shallow karst waters with deep saline fossil waters (Khaska et al., 2013) or infiltrated into the confined basal (Wang and Jiao, 2012), by evaporating seawater and formed sedimentary deposits (Pulido-Leboeuf et al., 2003) or from

upcoming of underlying saltwater bodies by overexploitation of freshwater (Vengosh et al., 1999).

In Rhone river delta, saltwater origin and evolution of Rhone delta plain have dealt in several researches (L'Homer et al., 1981, Vella et al., 2005, de Montety et al., 2008). In the study of Vella (2005), a radiocarbon chronology was used for the accumulation of Holocene sedimentary bodies (unconfined aquifer) and morphology of mouth lobes. These sediment bodies correspond to the sea-level rise around 6000 years BP and the Pleistocene surface topography (Figure 17). According to the evolution of past coastline, the study area is situated near the shoreline existing between 2400 to 4000 years BP.

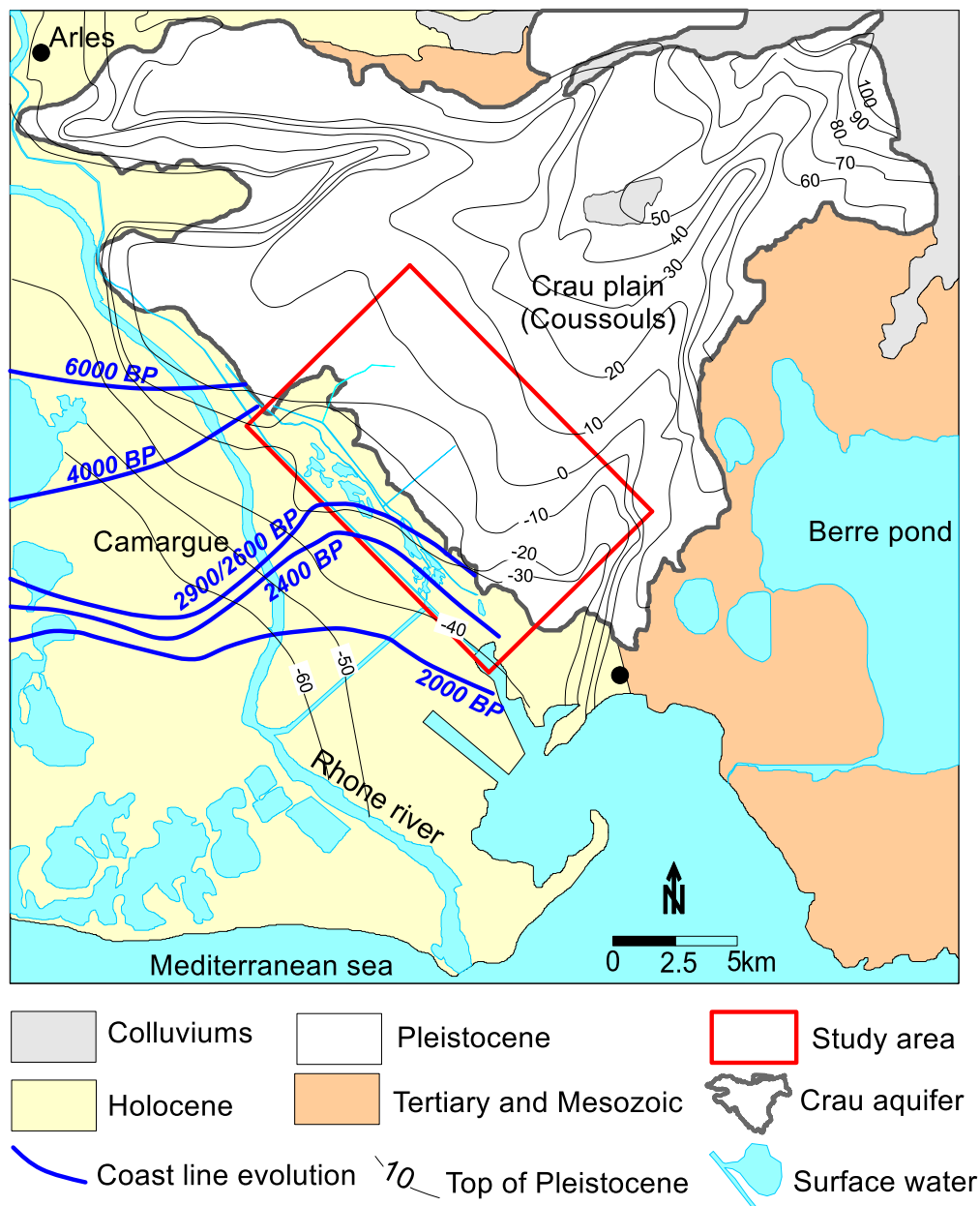


**Figure 17.** Comparison of the delta lobes progradation (Vella et al., 2005) and the Pleistocene gravel isobaths (Roure S et al., 2004).

In the later researches, De Montety (2008) defined the sources of salinity in groundwater of confined Pleistocene aquifer in Rhone delta which is separated from seawater by an impermeous layer. This aquifer is shown on Figure 18. A natural tracer characterization was carried out on a monitoring network through Crau and Camargue plain and samples of Mediterranean seawater and Rhone River water. Isotopic and hydrochemical investigations confirmed that the strong salinities in groundwater of this gravel aquifer are due to mixing between Mediterranean seawater and freshwater from Rhone River and Crau aquifer. The percentage of seawater in groundwater increases from north to south and reaches up to 98% in the most southern part of this aquifer. This study also shown that the salinity of the aquifer has strongly increased since 1970 possible due to the increasing of exploitation activities in this aquifer.

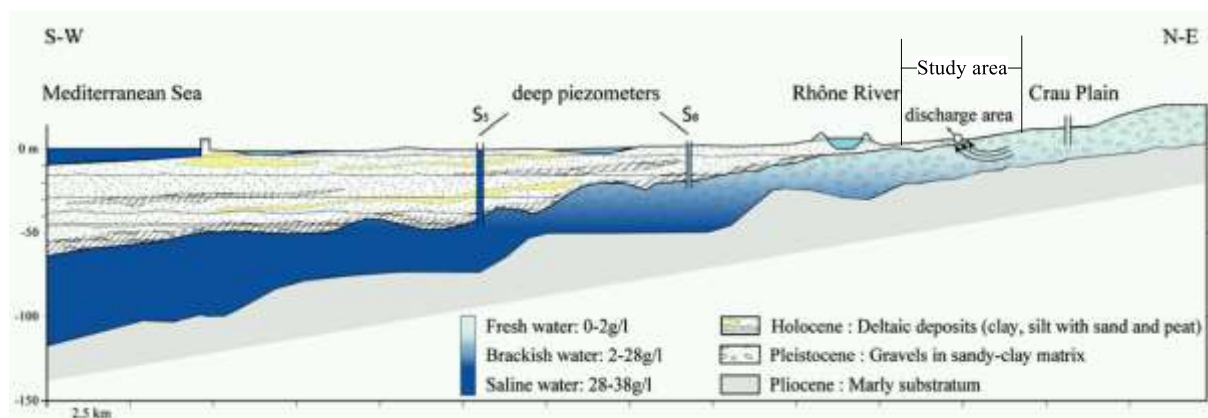


**Figure 18.** Schematic cross-section of the investigation in studies of De Montety (2008)

In study area, salinity of groundwater have been observed during the period 1982-2005 with observation for every 2-3 months and from 2006 until now, very few data are available and missing in several years (2007-2010). Based on these observations, a salinity evolution was created as in Figure 19. The contour map show a saltwater intrusion to NE direction in the downstream part of study area. In sector along N286 road, landward displacement of saltwater front of  $Cl=10g/l$  was about 1200m during 1990-2001 (more than 100m/year) and around 1000m from 2001-2014 (average 75m/year).

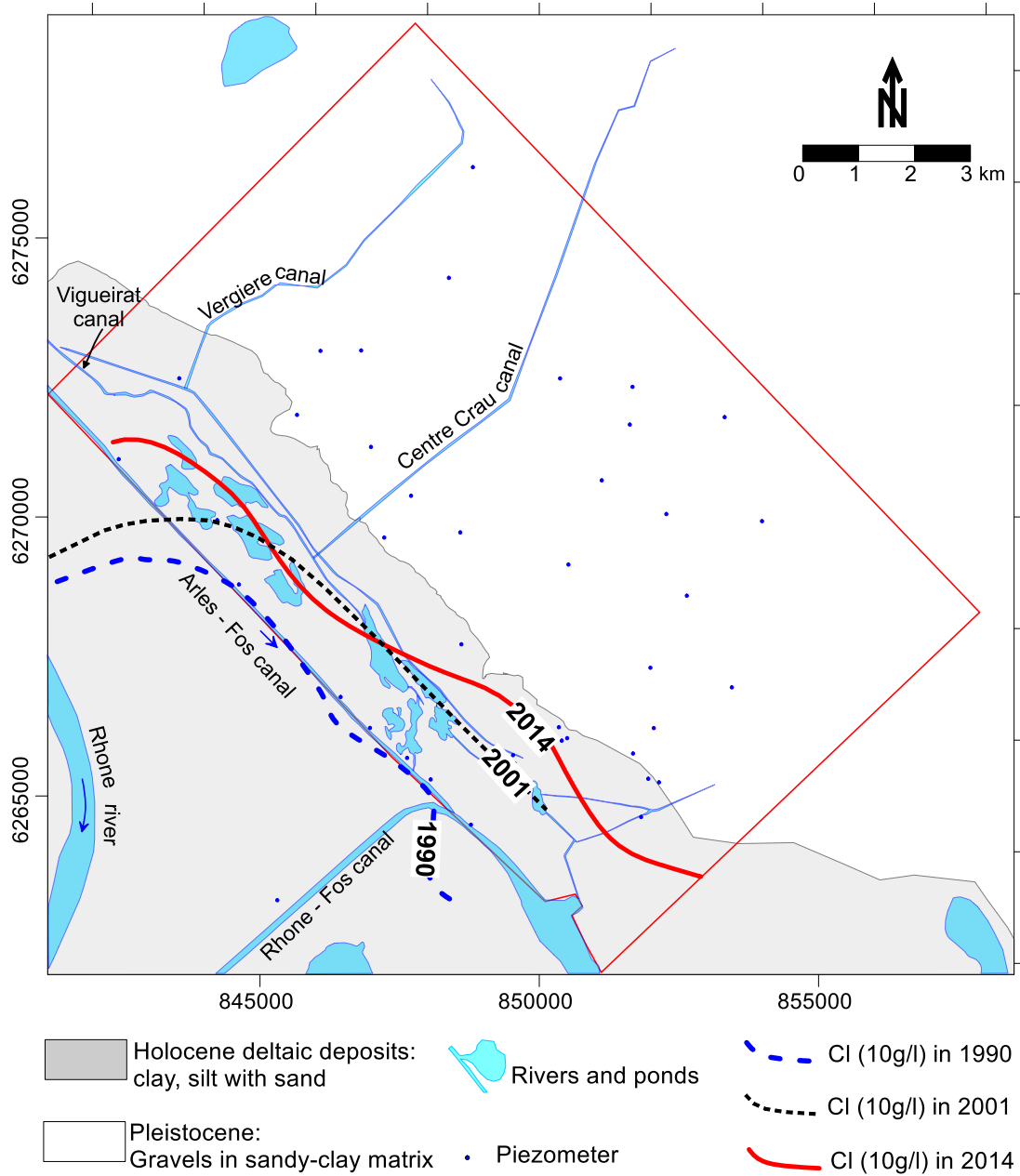


**Figure 19.** Salinity evolution from 1990 to 2014. Observation data of 1990 and 2001 from [SAFEGE](#). Data of 2014 were measured on 24/10/2014 at 10m below groundwater surface.



**Chapter 3**  
**METHODOLOGIES**



### 3.1 Methods

The research focuses on the constraints related to the modeling of groundwater in the coastal downstream part of the Crau aquifer. In such aquifer, the concomitant presence of freshwater and saltwater modifies flow patterns typically represented by the Darcy equation. Works on these groundwater are difficult because of the influence of salinity on properties (density and permeability) and the complex mathematical representation of the flow equations. Moreover, the influence of heterogeneities makes the model parameterization and calibration more difficult.

To help such works, we propose to combine four methods:

- (i) Hydrodynamic measurements to precise the boundary conditions, including two different measurements:
  - Monthly water head measurements for a period more than one year to determine hydraulic head gradient, then groundwater flow direction and velocity.
  - Continuous recording of hydraulic head, temperature and salinity for a long period to compare and validate to simulations.
- (ii) Geophysical investigations to provide information about concentration distribution in groundwater (by the mean of electrical resistivity distribution) and validate the model, including two different methods:
  - Electrical resistivity tomography (ERT) to provide continuous characterization of subsurface electrical conductivity,
  - Electromagnetic (EM) to mapping terrain conductivity.
- (iii) Isotope measurements to quantify groundwater velocity and discharge and validate the simulated flow, including two different experiences:
  - $^{222}\text{Rn}$  (Radon) monitoring in canals and ponds water to estimate groundwater discharge to surface water,
  - Decay of  $^{222}\text{Rn}$  in single wells to estimate groundwater flow rate (Darcy velocity) in aquifer,
- (iv) 3D numerical modeling to simulate flow and saltwater intrusion into this coastal aquifer.

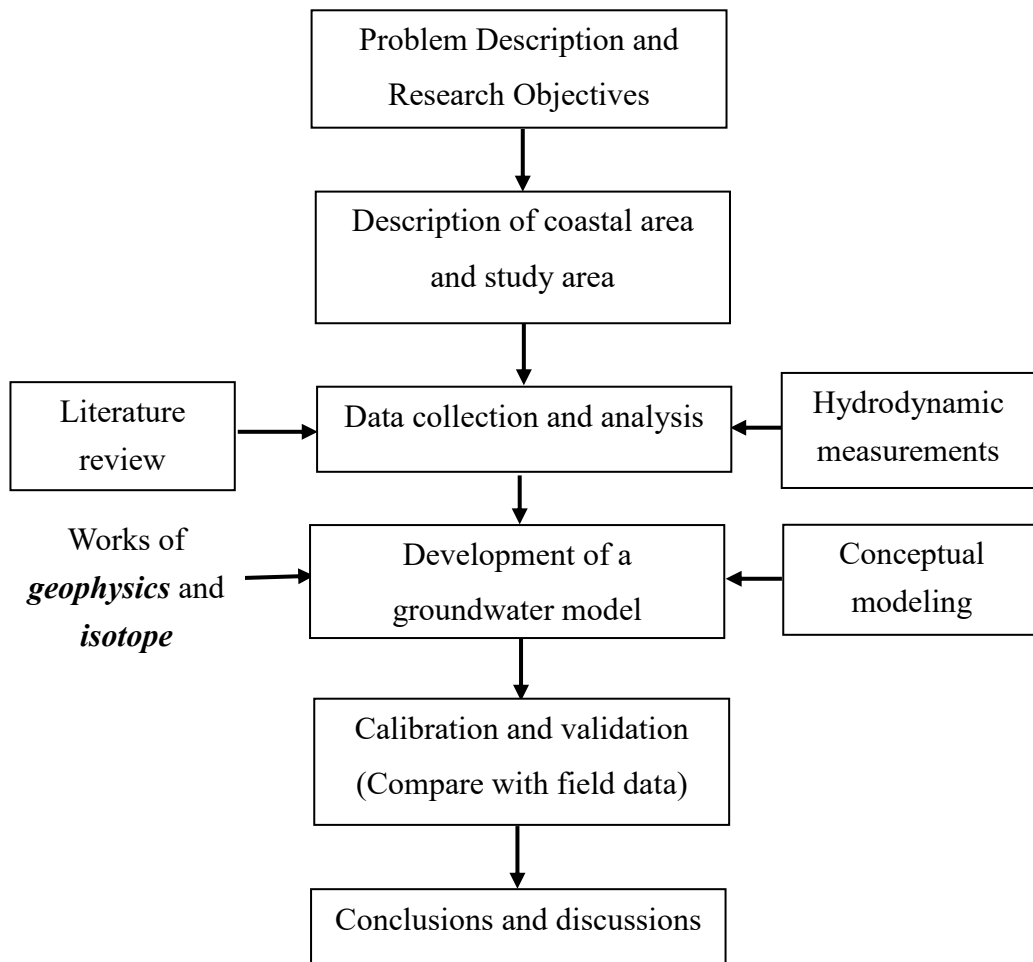


Figure 20. Methodology flowchart of the study

## 3.2 Hydrodynamic measurements

Water level data in aquifers, surface water and sea water are very important in studying movement of groundwater as discussed in section 2.2. These data need to be interpreted with relation to water density.

### 3.2.1.1 Water level measurements

In this study, 45 points (including 28 piezometers, 16 wells and 1 surface water station) have been chosen to observe water level, electrical conductivity and temperature (location of these piezometers shown in Figure 21). Most of the piezometers have been constructed from the 1980s, with some replacements after 2000s, and 9 new piezometers were added in 2009 in the marsh area around the canals and ponds. Depth of piezometers and wells varies between 7 and 32 m (piezometers and wells information in Annex 1, geological and technical logs in and Annex 6). All the wells are less than 15m depth and located in dry Crau part while most of piezometers are deeper than 15m and located around the marsh area. Monthly observations have been done during one year, from April 2013 to March 2014. All investigation data on water level, electrical conductivity and temperature are shown in Annex 2.

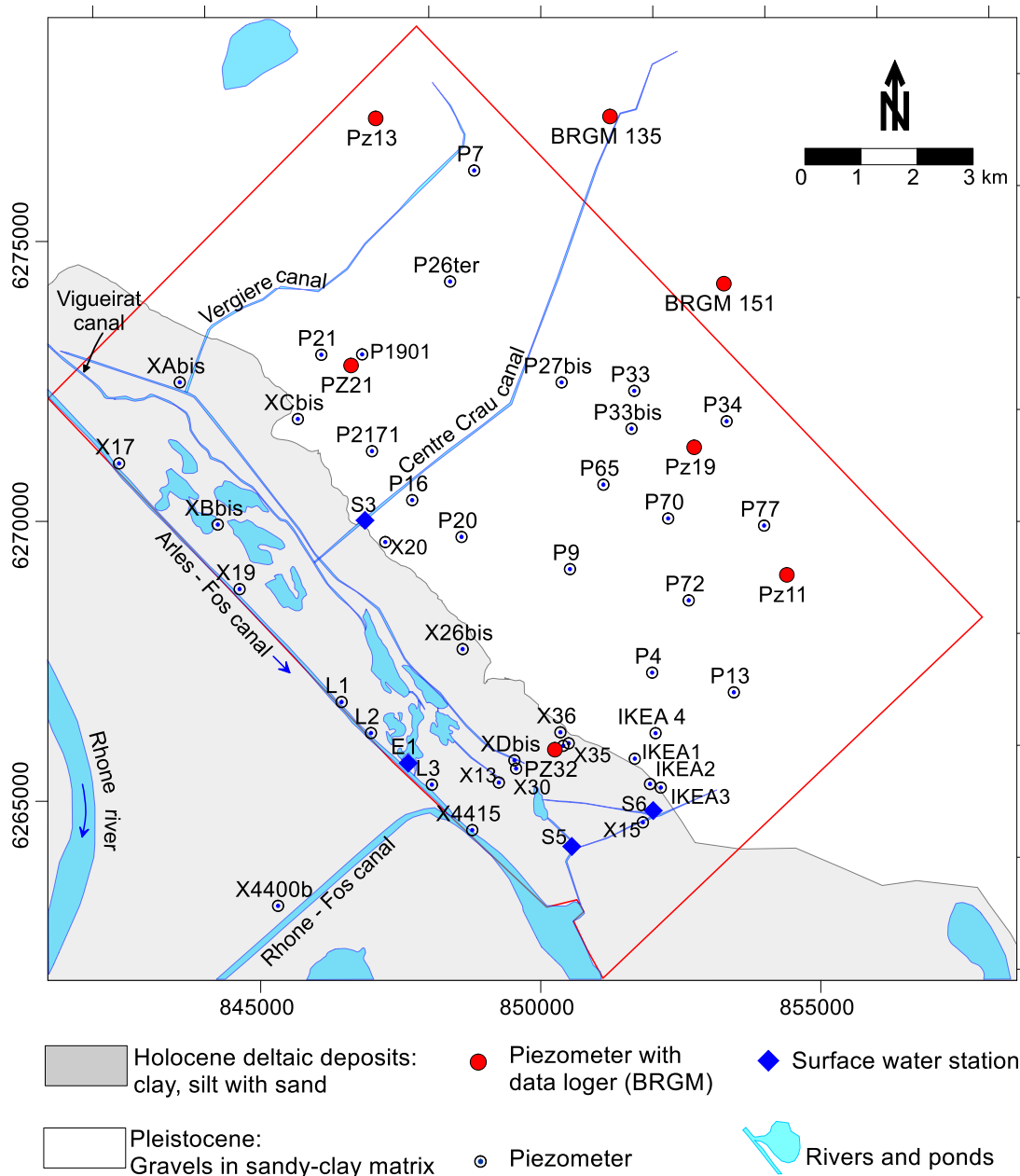


**Figure 21.** Location of groundwater and surface water observation points in study area

All geological logs show that the aquifer is unconfined, but semi-confined to confined aquifer in the marsh area of Vigueirat and Landre (NW-SE boundary of area) due to the present of the semi-pervious covers.

### 3.2.1.2 Salinity in wells

According to previous works, the main physical-chemical characteristics of groundwater were defined through electrical conductivity surveys, water head measurements and analysis of water samples. The distribution of saltwater (Figure 19) from 1990 and 2014 campaigns shows that seawater intrusion globally comes from SW to NE.

Electrical conductivity has been measured in wells and piezometers at the same time than water levels at the depth of 10 m below groundwater level. This aquifer shows a very high variability in EC (Figure 22). The direction of EC gradient is similar to the one of water level, i.e. from NE to SW. EC is lower than 1000  $\mu\text{S}/\text{cm}$  in NE and center of area and more than 50,000  $\mu\text{S}/\text{cm}$  in the SW. Beside these measurements, three campaigns have been organized to measure EC profile (every meter) in piezometers from the salty zone. EC profiles are shown in Annex 3.

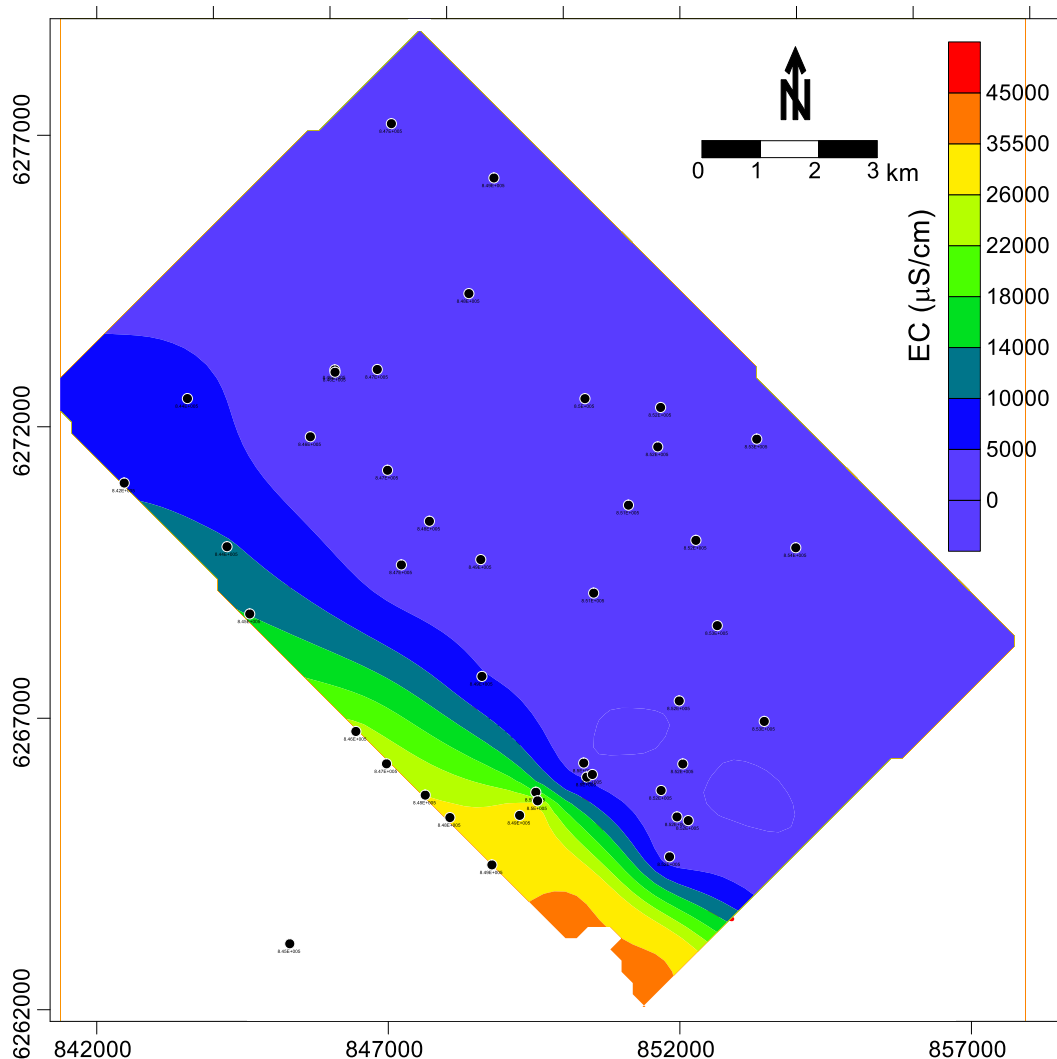


**Figure 22.** Electrical conductivity distribution in wells and piezometers at 10m bellow groundwater surface (data on 24/10/2013)

Electrical conductivity has been measured at different depths in observation wells of sector 1 (i.e. along the road N286) and sector 2 (i.e. along the Arles-Fos canal; Figure 23). Data show that the EC comes from south west to north east. Along the Arles-Fos canal, groundwater is salty with the chloride isoline of 15 g/l varying from -10 m.asl (in well X4415) to -18 m.asl. But along road D286, EC at -18 m.asl in borehole X35 is below the limit of 22, 3 mS/cm.

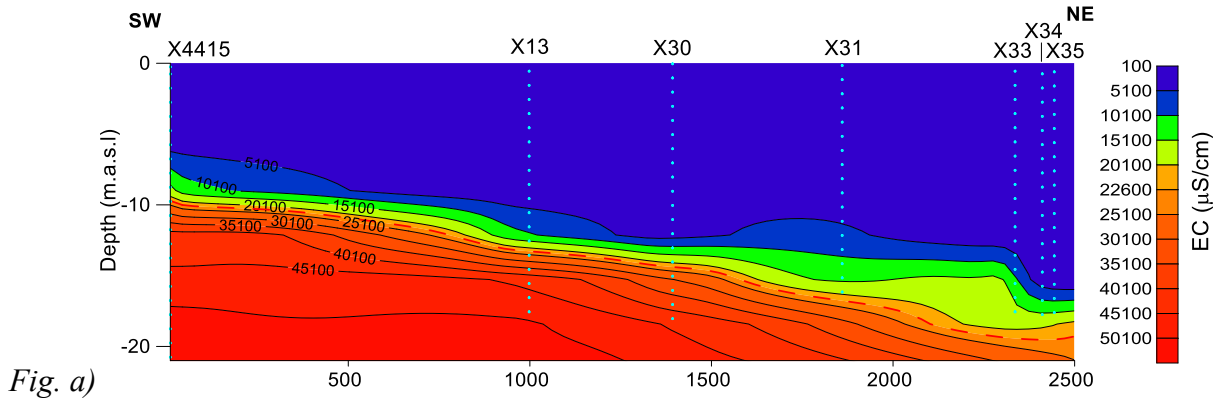


Fig. a)

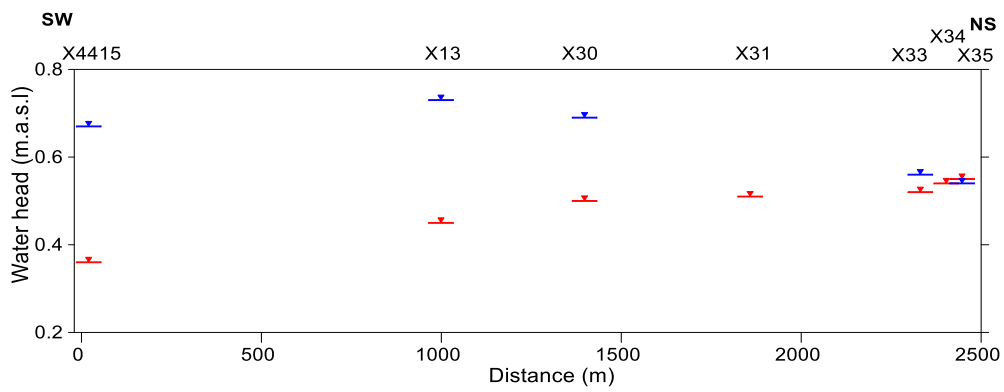


Fig. b)

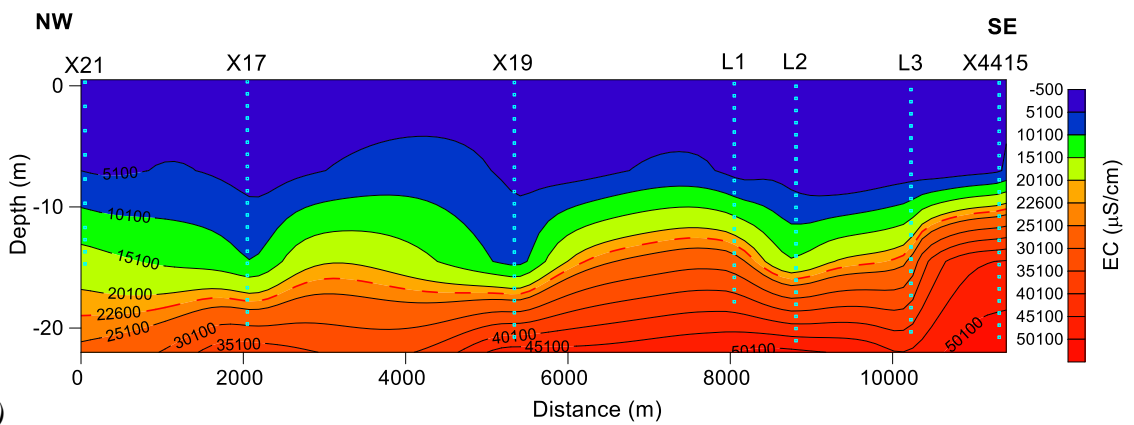


Fig. c)

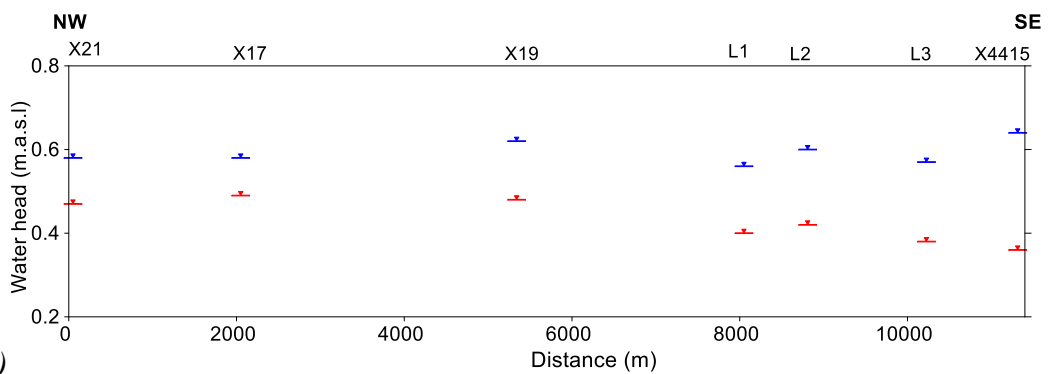


Fig. d)

**Figure 23.** Electrical conductivity distribution along the road N286 (a) and along Arles-Fos canal (c). Water level measurement in piezometers (red) and hydraulic head with the correction of density (blue) along the road N286 (b) and along the Arles-Fos canal (d)

All EC measurements show that groundwater has to be considered as density variable and need to use a correction of water level with density. For each piezometer, water density has been calculated by Stuyfzand's equation (1989).

**Table 1.** Water density in piezometers and water level with density correction (freshwater head)

<b>Well</b>	<b>Temperature <math>T</math> <math>^{\circ}C</math></b>	<b>Average EC in well (<math>\mu S/cm</math>)</b>	<b>Average density <math>\rho</math> <math>kg/m^3</math></b>	<b>WL measured <math>h_i</math> <math>m.asl</math></b>	<b>Fresh water head <math>h_f</math> <math>m</math></b>
<b>XA</b>	15.8	8658	1004.18	0.61	0.73
<b>XC</b>	16.3	797	999.44	0.89	0.88
<b>X17</b>	17.7	9288	1004.20	0.49	0.58
<b>XB</b>	15.7	7171	1002.95	0.5	0.56
<b>X19</b>	17.8	18150	1009.34	0.48	0.76
<b>P21</b>	19.2	578	998.81	1.4	1.40
<b>P21 Bis</b>	19.2	768	998.91	1.42	1.40
<b>P1901</b>	18.6	760	999.02	1.84	1.84
<b>P2171</b>	18.9	625	998.89	1.5	1.50
<b>P16bis</b>	19.5	707	998.81	0.75	0.75
<b>X20bis</b>	16.1	1461	999.83	0.7	0.70
<b>P20</b>	19.2	540	998.79	0.89	0.89
<b>P9</b>	17.5	642	999.16	0.89	0.89
<b>X26bis</b>	15.2	9824	1004.95	0.6	0.75
<b>P13</b>	18.1	668	999.10	2.67	2.67
<b>P72</b>	17.2	700	999.24	1.67	1.67
<b>P70</b>	17.4	475	999.09	2.48	2.48
<b>P33</b>	16.7	557	999.25	4.24	4.24
<b>P33bis</b>	16.9	549	999.21	3.53	3.53
<b>P27bis</b>	17.6	685	999.16	3.82	3.82
<b>P26ter</b>	18.2	921	999.18	4.39	4.39
<b>X36</b>	16.5	780	999.40	0.53	0.52
<b>XD</b>	16.6	23688	1011.34	0.53	0.860
<b>X4415</b>	16.6	29380	1014.78	0.36	0.69
<b>L1</b>	16.4	17348	1008.57	0.4	0.57
<b>L2</b>	16.4	13652	1005.55	0.45	0.60
<b>L3</b>	14.5	18934	1009.65	0.38	0.59
<b>X13</b>		25556	1013.21	0.45	0.81
<b>X30</b>	17.1	21664	1010.42	0.5	0.78
<b>X33</b>	16.2	4986	1001.87	0.52	0.56
<b>X35</b>	16.9	2284	1000.07	0.55	0.55
<b>IKEA 1</b>	17.5	328	998.99	0.771	0.76

Well	Temperature $T$ °C	Average EC in well ( $\mu\text{S/cm}$ )	Average density $\rho$ $\text{kg/m}^3$	WL measured $h_i$ m.asl	Fresh water head $h_f$ m
IKEA 2	17.8	600	999.08	0.826	0.82
IKEA 3	22.1	722	998.25	0.86	0.84
IKEA 4	17.5	642	999.16	1.092	1.09
X23	17.1	1550	999.71	0.74	0.73
X4400b	19.8	48800	1027.00	-0.58	-0.56
C3	18.5	52500	1026.18	0.24	1.00
C4	18.5	41700	1020.58	0.14	0.74
X15	15.3	782	999.59	1.46	1.45
P34	16.8	477	999.19	7.97	7.97

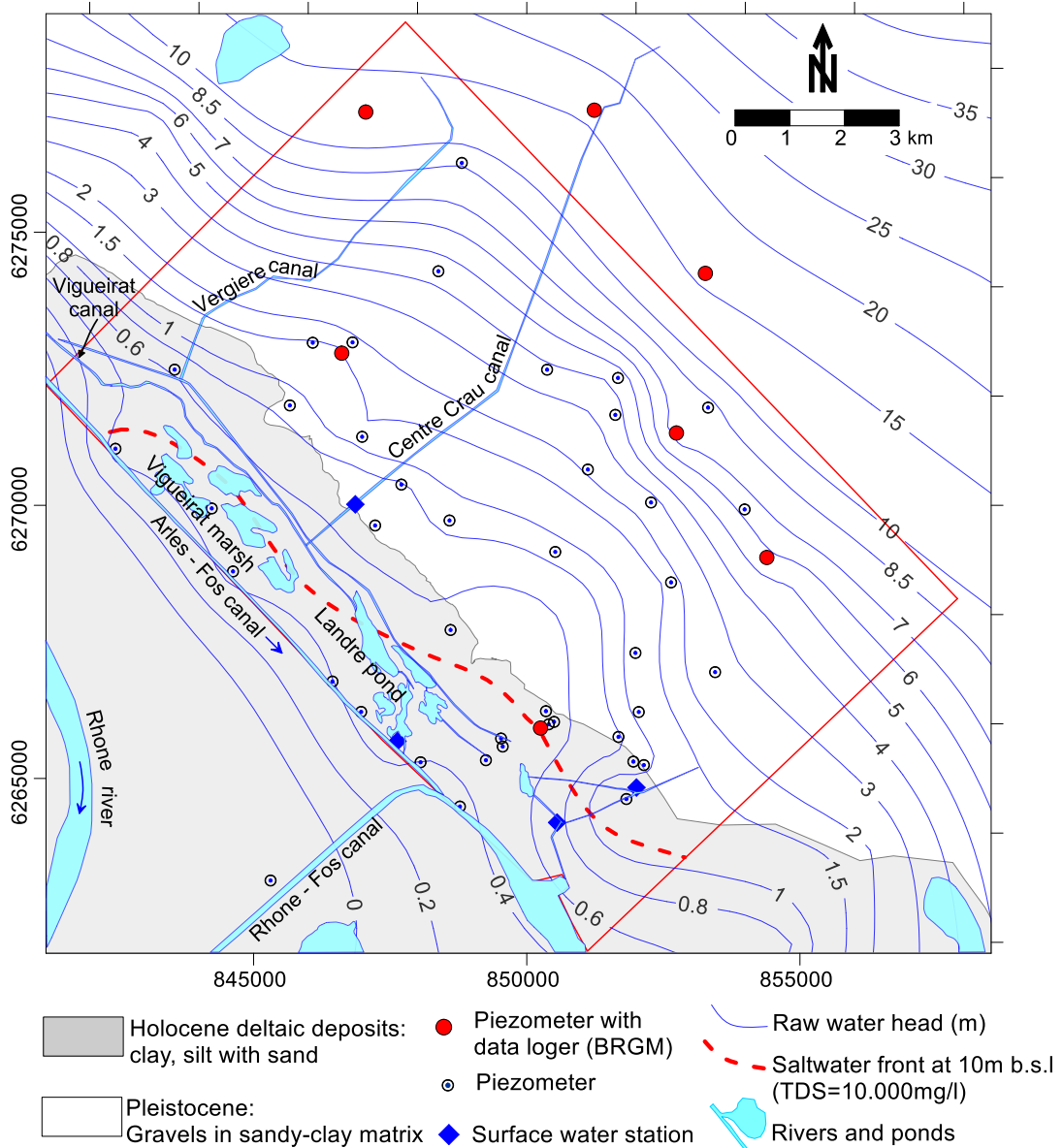
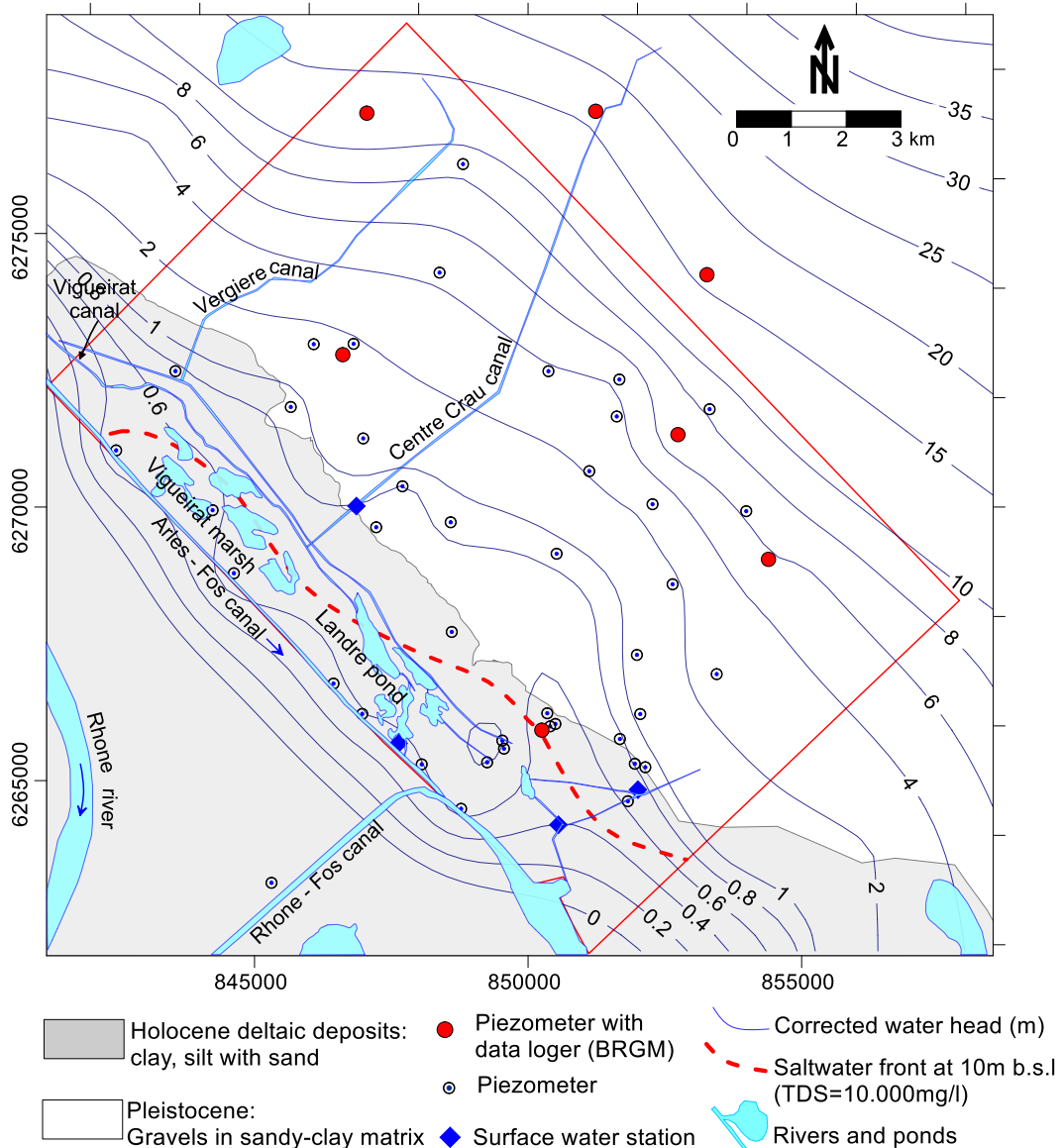


Figure 24. Location of observation points and water level map (raw data of 24/10/2013)



**Figure 25.** Hydraulic head map with density correction (data on 24/10/2013)

According to hydraulic head contour maps with density correction (Figure 25), groundwater flow directions are from the NE to SW. The hydraulic head on the NE boundary is about 10.0 m.asl and around 0.3 – 0.5 m.asl in the SW boundary; the average hydraulic gradient is about 2 – 3‰.

### 3.3 Geophysical investigation

Usual process to study coastal aquifer includes geology (lithology, geometry ...) and hydrogeology (water table and salinity distribution ...). However these methods are time consuming. For this reason such data are often limited. In the other hand, geophysical methods can be very relevant and valuable. Indirect information obtained from geophysical investigation can help to understand geology and hydrogeology combined with direct information. Nowadays,

the two most common methods used to study saltwater intrusion are electromagnetic (EM) (Goldman et al., 1991, Frohlich et al., 1994, Kafri and Goldman, 2005, Abdalla et al., 2010) and electrical resistivity tomography (ERT) (Acworth and Dasey, 2001, Batayneh, 2006, de Franco et al., 2009, Comte et al., 2010).

### **3.3.1 Electromagnetic (EM) mapping**

#### *3.3.1.1 Introduction*

One of the most popular geophysical methods currently used to provide information about the spatial variation of soil properties is EM induction (Triantafilis and Monteiro Santos, 2013). EM methods were originally developed for mine exploration and have been widely used over the last decades for groundwater investigations (Fitterman and Deszcz-Pan, 2004). These techniques have been described in geophysical handbooks and scientific papers (McNeill, 1980, Stewart, 1982, Stewart and Gay, 1986, Borne, 1990, Triantafilis et al., 2003, Santos, 2004). This technique is widely used for engineering purposes (McNeill, 1980) and is cost effective and reliable. Then, despite the qualitative nature of the provided information, this method is widely applied for hydrogeological and environmental investigations. Many applications of electromagnetic surveys have been applied for resources management in coastal aquifer (Stewart, 1982, Goldman et al., 1991, Frohlich et al., 1994)

With the development of the EM31 and the EM34-3 (Geonics Ltd) it is possible to map terrain conductivity virtually as fast as the operators can walk and at low costs. The interpretation of EM data by using some modeling programs is qualitative even their inversion can be done for layered models.

#### *3.3.1.2 Principle of operation*

In this study, we employed an EM34-3 of Geonics (Figure 26) to directly measure bulk conductivity. This equipment consists of two coils. One is the transmitter which is energized with an alternating current at a specific frequency and other is the receiver. The transmitter creates a magnetic field in the subsurface while the receiver detects and records the magnetic field. These two coils can be operated with different spacing of 10, 20 and 40 m to vary the depth of exploration. Changing the orientation of transmitter/receiver loops from the vertical to the horizontal (Figure 27) also varies the depth of exploration by increasing the 70% response from 0.75 to 1.5 time the intercoil spacing (McNeill, 1980). The use of different intercoil spacing with different frequencies (6400, 1600 and 400 Hz) and different loops orientation vertical and horizontal allows to construct an image of subsurface electrical conductivity distribution from 7.5 meters to a maximum of 60 meters (Santos, 2004).

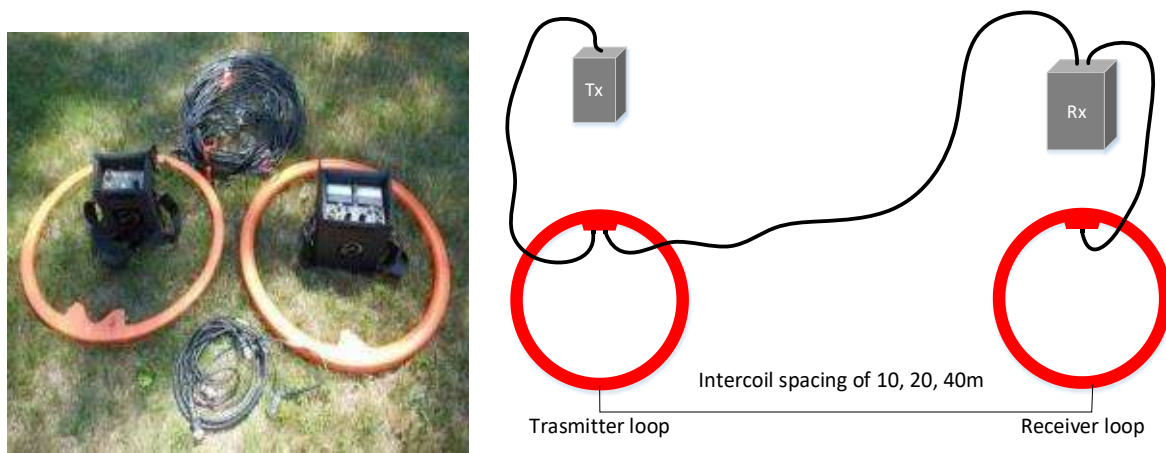


Figure 26. Geonics Electromagnetic EM34-3 instrument applied in study area

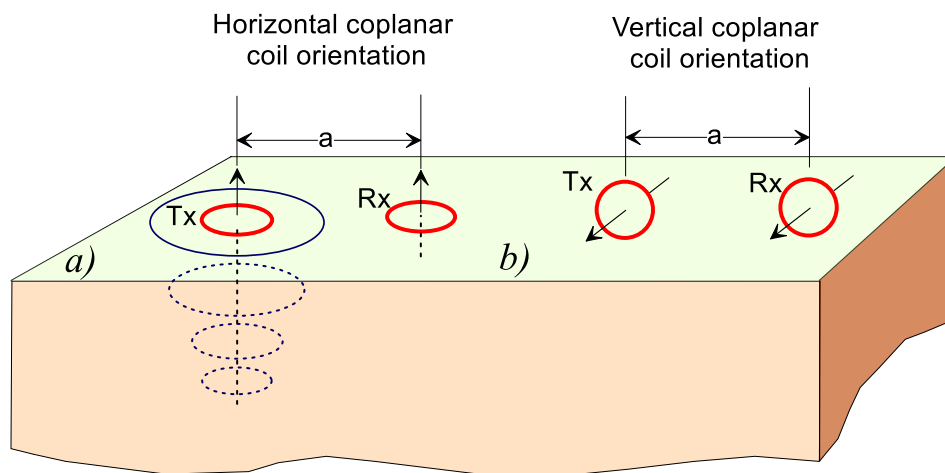


Figure 27. Relative response versus depth for

(a) vertical dipoles and (b) horizontal dipoles

Consider to Figure 28, in which a transmitter coil  $T_x$  energized with an alternating current at an audio frequency, is placed on the earth and a receiver coil  $R_x$  is located a short distance  $s$  away. The time-varying magnetic field arising from the alternating current in the transmitter coil induces very small currents in the earth which generates a secondary magnetic field  $H_s$  which is sensed, together with the primary field,  $H_p$ , by the receiver coil. In general this secondary magnetic field is a complicated function of the intercoil spacing  $s$ , the operating frequency,  $f$ , and the ground conductivity  $\sigma$ . Under certain constraints, technically defined as “operation at low values of induction number”, the secondary magnetic field is a very simple function of these variables. These constraints are incorporated in the design of the EM31 and EM34-3 whence the secondary magnetic field is shown to be

$$\frac{H_s}{H_p} \cong \frac{i\omega\mu_0\sigma s^2}{4} \tag{23}$$

Where:

$H_s$ : secondary magnetic field at the receiver coil

$H_p$ : primary magnetic field at the receiver coil

$$\omega = 2\pi f$$

$f$  = frequency (Hz)

$\mu_0$  = permeability of free space

$\sigma$  = groundwater conductivity (mho/m)

$s$  = intercoil spacing (m)

$$i = \sqrt{-1}$$

The ratio of the secondary to the primary magnetic field is now linearly proportional to the terrain conductivity, a fact which makes it possible to construct a direct-reading, linear terrain conductivity meter by simply measuring this ratio. Given  $H_s/H_p$  the apparent conductivity indicated by the instrument is defined from equation as

$$\sigma_s = \frac{4}{\omega\mu_0 s^2} \left( \frac{H_s}{H_p} \right) \quad (24)$$

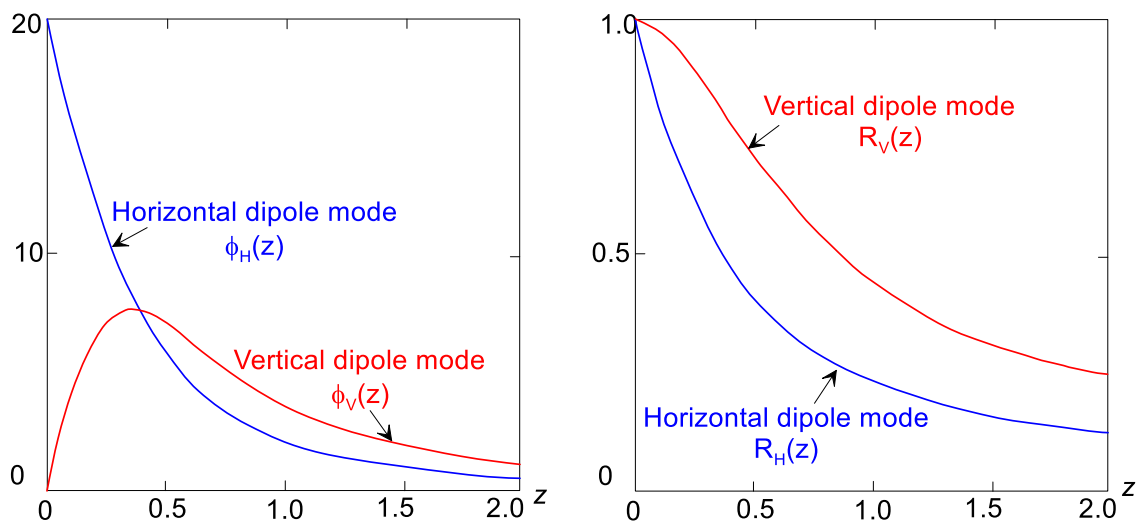


**Figure 28.** Comparison of relative responses for vertical and horizontal dipole modes. Note x axis = depth/intercoil spacing. (reproduced from McNeill, 1986)

### 3.3.1.3 Interpretation

Usually the interpretation of the EM34-3 data is qualitative. One-dimensional modeling or inversion is possible (Santos et al., 2002).

A mesh of prismatic blocks centered at each measurement point, as is usual in three-dimensional modeling, make up the earth model. The program inverts all the data set jointly, using the cumulative response (McNeill, 1980) approach at each site of the grid of measurements to calculate the forward response and derivatives. Spatial smoothness constraints are introduced during the inversion procedure in order to construct a conductivity model, which represents the main features contained in the data. Two inversion algorithms are given by Sasaki. The least square solution of such a non-linear smoothing problem is (Sasaki, 1989):

$$\left[ (J^T J + \lambda C^T C) \right] \delta p = J^T b \quad (25)$$

And in the second algorithm (Sasaki, 2001), the equation is :

$$\left[ (J^T J + \lambda C^T C) \right] \delta p = J^T b + \lambda C^T C (p - p_0) \quad (26)$$

Here  $\delta p$  is the vector containing the corrections applicable to the model parameters,  $p_0$  is a reference model,  $b$  is the vector of the differences between the logarithm of the observed and the calculated  $\sigma_a$ ,  $J$  is the Jacobian matrix, the superscript  $T$  is the transpose operation and  $\lambda$  is a Lagrange multiplier that controls the amplitude of the parameter corrections and the elements of the matrix  $C$  are the coefficients of the values of the roughness in each parameter which is defined in term (Sasaki, 1989). Although the final result obtained applying such a method is only a rough approach of a three-dimensional model and, for this reason it is designated as quasi-three-dimensional model, it can be very useful in the global interpretation of surveys.

Therefore, we have some difference methods of interpretation:

- i) Direct interpretation using multiple EM readings at selected locations –  
Using (empirical) formulae – Using EMIX34 computer software
- ii) Analysis of relative readings (shows area of saline water and fresher water)
- iii) Correlation of results with other more direct techniques:
  - Salinity profiles from boreholes on same island
  - Salinity profiles from islands with similar geology
  - Electrical resistivity soundings

### 3.3.2 The Electrical Resistivity Topography (ERT)

#### 3.3.2.1 Introduction

Electrical resistivity (ER) is one of the main properties adapted to hydro-geophysical studies (Gu erin, 2005). The resistivity of rocks is affected by different factors (Matsui et al., 2000): porosity, pore fluid resistivity, water saturation, water content by volume and clay content.

Electrical resistivity tomography (ERT, also called Direct Current – DC Resistivity Imaging) is now one of the most popular geophysical techniques that has been rapidly developed and widely used in the last few decades to map the electrical resistivity of the subsurface (Griffiths and Barker, 1993, Loke and Barker, 1996, Zarroca et al., 2011). The advantage of this method is the quality of the electrical resistivity data obtained with relatively high spatial resolution (Bauer et al., 2006) and the possibility to obtain continuous coverage of the underground in 2D and 3D spaces (Batayneh et al., 2010).

#### 3.3.2.2 Principle of operation

Using ERT for investigation of seawater intrusion is effective because the presence of salt increases the bulk electrical conductivity of the soil.

The multi-electrode resistivity technique consists in using a multi-core cable with as many conductors as electrodes plugged into the soil. Electrical current ( $I$ ) is injected in two electrodes and potential difference ( $V$ ) is measured on two other electrodes (Figure 29). The various combinations of transmitting (A,B) and receiving (M,N) pairs of electrodes construct the mixed sounding/profiling section, with a maximum investigation depth which mainly depends on the total length of the cable. Based on the potential differences and the used electrode configuration (e.g. Wenner, Schlumberger), an apparent resistivity can be calculated.

The fundamental physical law used in resistivity surveys is Ohm's Law that governs the flow of current in the ground. The equation for Ohm's Law in vector form for current flow in a continuous medium is given by

$$J = \sigma E \quad (27)$$

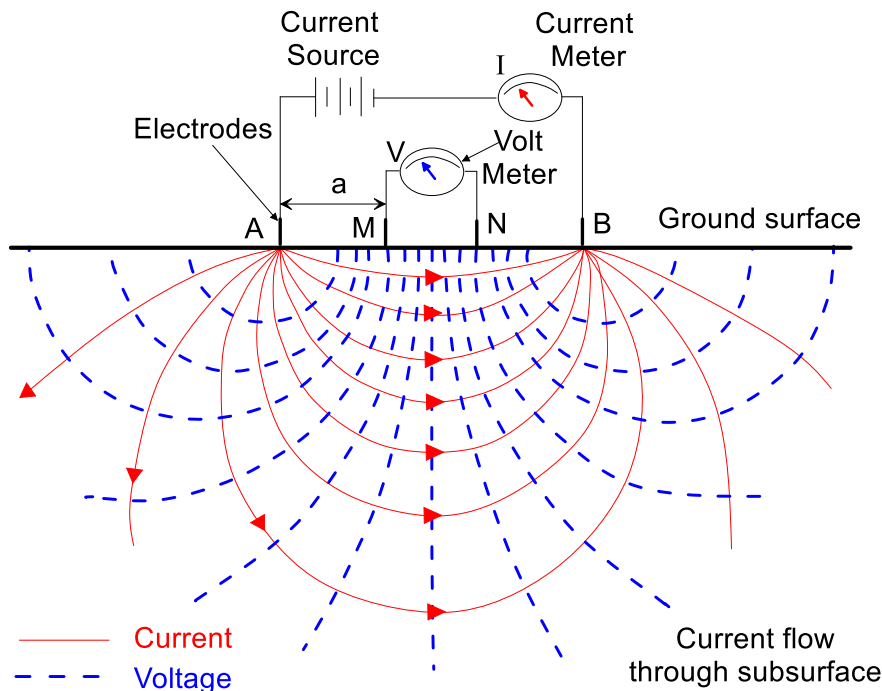


**Figure 29.** Principle of electrical resistivity tomography (ERT) measurement. Note : Band I indicates an electrical current (A) and V indicates the potential difference (V) which is measured by this method.

Where:  $\sigma$  is the conductivity of the medium,  $J$  is the current density and  $E$  is the electric field intensity. In geophysical surveys the medium resistivity  $\rho$ , which is equals to the reciprocal of the conductivity ( $\rho=1/\sigma$ ), is more commonly used. The relationship between the electric potential and the field intensity is given by

$$E = -\nabla\Phi \tag{28}$$

Combining equations, we get

$$J = -\nabla\Phi\sigma \tag{29}$$

In almost all surveys, the current sources are in the form of point sources. In this case, over an elemental volume  $\Delta V$  surrounding the a current source  $I$ , located at  $(x_s, y_s, z_s)$  the relationship between the current density and the current (Dey and Morrison 1979a) is given by

$$\nabla \cdot J = \left( \frac{I}{\Delta V} \right) \delta(x-x_s) \delta(y-y_s) \delta(z-z_s) \tag{30}$$

where  $\delta$  is the Dirac delta function. This equation can then be rewritten as

$$-\nabla \cdot [\sigma(x, y, z) \nabla \phi(x, y, z)] = \left( \frac{I}{\Delta V} \right) \delta(x-x_s) \delta(y-y_s) \delta(z-z_s) \tag{31}$$

This is the basic equation that gives the potential distribution in the ground due to a point current source. A large number of techniques have been developed to solve this equation. This is the “forward” modeling problem, i.e. to determine the potential that would be observed over a given subsurface structure. Fully analytical methods have been used for simple cases, such as a sphere in a homogenous medium or a vertical fault separating two areas each with a constant resistivity. For an arbitrary resistivity distribution, numerical techniques are more commonly used. For the 1-D case, where the subsurface is restricted to a number of horizontal layers, the linear filter method is commonly used (Koefoed and Dirks, 1979). For 2-D and 3-D cases, the finite-difference and finite-element methods are the most versatile. In Chapter 2, we will look at the use of a forward modeling computer program for 2-D structures.

From the current ( $I$ ) and potential ( $\phi\Delta$ ) values, an apparent resistivity ( $\rho_a$ ) value is calculated.

$$\rho_a = k \frac{\Delta\Phi}{I} \quad (32)$$

$$k = \frac{2\pi}{\left( \frac{1}{r_{C1P1}} - \frac{1}{r_{C2P1}} - \frac{1}{r_{C1P2}} + \frac{1}{r_{C2P2}} \right)} \quad (33)$$

$k$  is a geometric factor that depends on the arrangement of the four electrodes. Resistivity measuring instruments normally give a resistance value,  $R = \Delta\phi/I$ , so in practice the apparent resistivity value is calculated by

$$\rho_a = kR \quad (34)$$

The calculated resistivity value is not the true resistivity of the subsurface, but an “apparent” value that is the resistivity of a homogeneous ground that will give the same resistance value for the same electrode arrangement. The relationship between the “apparent” resistivity and the “true” resistivity is a complex relationship. To determine the true subsurface resistivity from the apparent resistivity values is the “inversion” problem.

### 3.3.3 Applying geophysics to validate flow and transport modeling

Ground water validation is one of the most challenging issues facing modelers and hydrogeologists (Hassan, 2004). Model quality mainly depends on previous characterization of subsurface environment which requires extensive borehole drilling that can adversely affect the geologic integrity of the site or be prohibitively expensive. Therefore, uncertainty is always inherent in the model and requires a validation procedure which is performed calibration and sensitivity analysis was described in section 4.4.

Model calibration is classically done by doing many repeated runs of the numerical model in which aquifer structure, parameters and boundary conditions are modified until obtain an acceptable match between observed (or expected) and computed hydraulic heads and concentration distribution.

The validation of variable-density flow models simulating seawater intrusion in coastal aquifers requires not only head observations but also information about concentration distribution in groundwater (Comte, 2008). Therefore, by combining head with salinity and flow rate observations, the parameters became much better constrained (Shoemaker, 2004, Carrera et al., 2010)

But in fact, the use of concentration distribution is not as simple as it might look which caused by salt water circulation within the well (Carrera et al., 2010) because of the difference between measured salinity profiles and actual width of the mixing zone (Tellam et al., 1986).

In the last decades, many studies has been done to solve the difficulties of concentration data, which using electrical conductivity (EC) measurement, normally from geophysics (Batayneh, 2006, Comte and Banton, 2007, Jin et al., 2008, de Franco et al., 2009, Nguyen et al., 2009, Batayneh et al., 2010, Comte et al., 2010, Ramalho et al., 2013)

### **3.3.4 Application to the study area**

#### *3.3.4.1 EM method*

Two campaigns of EM surveys have been conducted (Figure 32) in marsh area around the saltwater front which was defined by electrical conductivity measurements (discussed in sections 2.3.6 and 3.2). Principle EM profile with regard to saltwater front is shown in Figure 30. The first campaign have been carried out in four sectors northeastern side of the canal Colmatage (sectors 1-4) and the second campaign in eight sectors on the other side of canal (sectors 5-12). The transmitter-receiver separation was 10m (EM34-10) and 20m (EM34-20) with both vertical dipole (VD) and horizontal dipole (HD). Distance between sectors varies from about 600 m to 11 km. 480 points where measured with EM34-10, 853 points with EM34-20 and 30 points with EM34-40 (Table 6). The topography in marsh area is flat at a level between 0-1 m.asl in the marsh zone and 2-3 m.asl in the sector 1-4. In several sectors, some measurements with an intercoil separation of 40m (EM34-40) have been added in order to image the apparent electrical conductivity distribution at the difference depths. These surveys have covered distances of more than 20km (Figure 31).

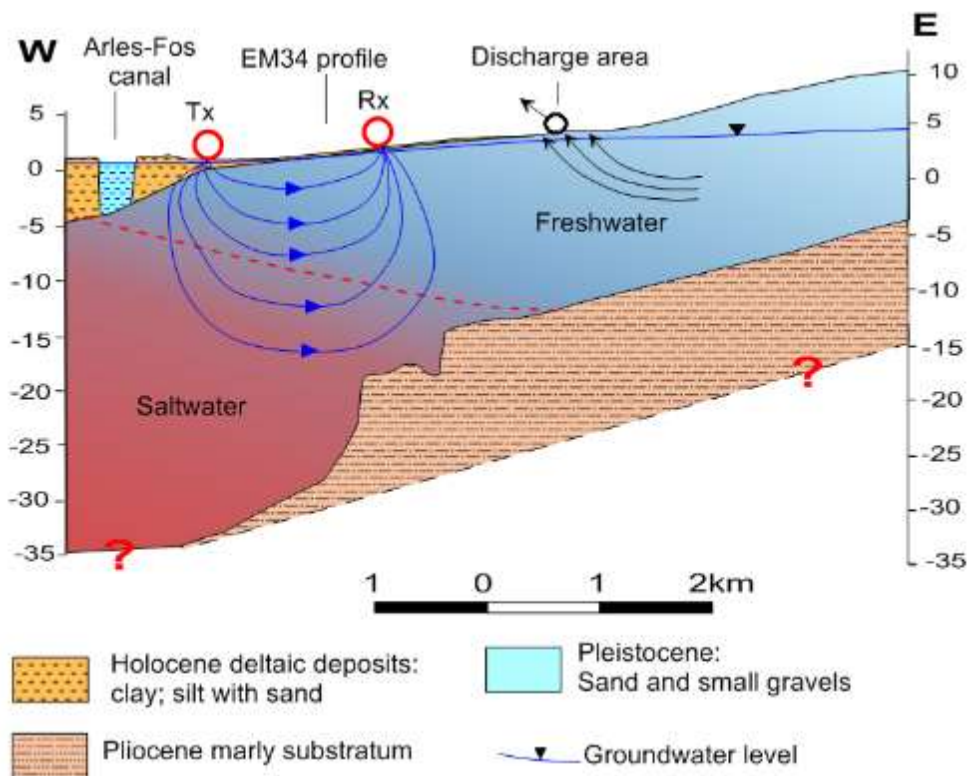


Figure 30. Principle of EM34 profile with regard to interface between fresh and salt water. This cross section along the Pissarote secteur.

Table 2. EM34 profiles

Sector	Location	Distance (m)	Measurements (point)	
			EM34-10	EM34-20
1	Center Crau (nearby P21, P21bis)	1,600	90	73
2	Along Center Crau canal	909		22
3	Nearby X20 piezometer	1,153		32
4	Nearby X26 piezometer	1,235	29	36
5	Northern of Vigueirat	1,977	57	57
6	Center of Vigueirat, nearby XB	2,028		40
7	Center of Vigueirat, nearby X19	1,426	33	33
8	Southern of Vigueirat	2,598		121
9	Sector Pissarotte, nearby X13, X31-X35	2,236	117	96
10	Sector Tonkin	2,599	28	83
11	Along Colmatage canal	5,849		107
12	Along canal Arles-Fos	6,800	126	153
	<b>Total</b>	<b>30,410</b>	<b>480</b>	<b>853</b>



Figure 31. EM34 measurement in study area

3.3.4.2 ERT method

ERT has been applied in three profiles, with two profiles T1 and T2 orientated perpendicularly to the saltwater-freshwater interface to evaluate the electrical measurement and profile T3 in the center of study area to determine the geological structure (Figure 32). The profiles were collected with a multi-electrode ABEM Lund Imaging System.

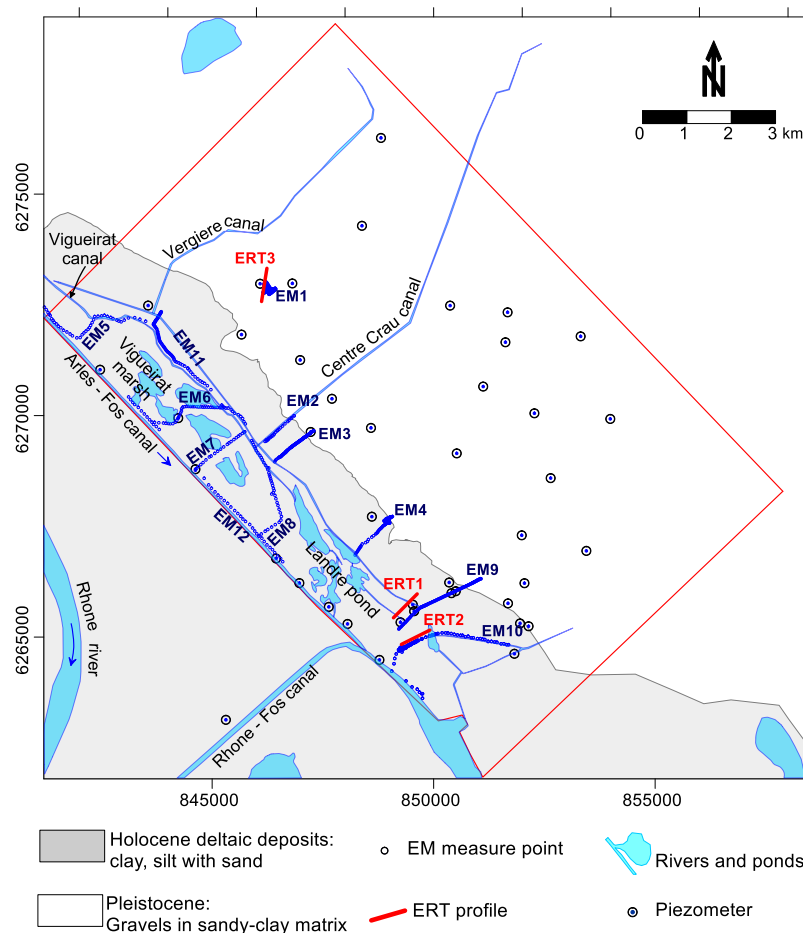


Figure 32. Position of electrical resistivity topography (ERT) sectors and electromagnetic (EM34) measurement points

### 3.4 Short-lived natural radioactive isotopes as tracers

#### 3.4.1 General introduction

Natural  $^{222}\text{Rn}$  was used as a good groundwater tracer of submarine groundwater discharge because of its conservative nature (inert), short half-life (half-life = 3.824 days) comparable to the time scale of circulation in many coastal settings, easiness in measurement and high abundance in groundwater compared to surface waters (Moore, 2000, Burnett and Dulaiova, 2003, Dulaiova et al., 2005). The  $^{222}\text{Rn}$  concentration in groundwater is in radioactive equilibrium with  $^{226}\text{Ra}$  and the equilibrium value depends on the  $^{226}\text{Ra}$  content and specific surface area of the constituents of the aquifer. Using these characteristics, aquifers can be classified according to their  $^{222}\text{Rn}$  concentrations (Hamada, 2000). In addition, radon can be used to estimate groundwater flow rate in wells (Hamada, 2000, Schubert et al., 2011) and groundwater discharge to seawater, lakes or marshes. In many recent researches, radon was used to map groundwater discharge points in surface waters (Dimova and Burnett, 2011).

In this research, we applied radon as a tracer to estimate the discharge of groundwater in to surface water and groundwater velocities.

#### 3.4.2 Estimate of groundwater velocities using the decay of $^{222}\text{Rn}$ in a single well

##### 3.4.2.1 Introduction

Groundwater velocities and directions can be estimate from the movement of a tracer between two measure points, such as common salt, bromide, chloride, rhodamine, various fluorocarbons, radioactive components and dyes.... Application of tracers is very useful because of their low susceptibility to adsorption or ion exchange on aquifer materials. Then groundwater velocities can be calculated by using Darcy's law (Millham and Howes, 1995, Fetter, 2001). This equation supposes the hydraulic gradient between two groundwater measure piezometers is constant. In coastal aquifer with density variations by mixing of saltwater and freshwater makes the tracer analyses more sensitive and should be use with care (Mongelli et al., 2013). Moreover, this application requires groundwater wells separated by distance comparable to the distance over which significant changes of the aquifer can be expected (Schubert et al., 2011). This method has certain disadvantages, such as the difficulty of installation measuring device into a well, the tracer can change the natural hydro-geochemical conditions. Therefore, a natural tracer such as  $^{222}\text{Rn}$  can be used to solve these problems (Cook et al., 1999, Hamada, 2000, Schubert et al., 2011).

##### 3.4.2.2 Methodology

In the aquifer, when groundwater flows in to a well, radon decay is no longer balanced by decay of  $^{226}\text{Ra}$ . Activity of radon therefore decreases with time following an exponential law:

$$C_{ww}^t = C_{gw}^\infty e^{(\lambda t)} \quad (35)$$

where lambda ( $\lambda$ ) is the radon decay constant ( $2.1 \times 10^{-6} \text{ s}^{-1}$ ) and  $C_{ww}^t$  is the radon concentration in well water after time  $t$  has elapsed since the moment the water entered the well. The water residence time in the well and the radon deficit  $C_{ww}^t / C_{gw}^\infty$  of ground water depends on the radius  $r$  of the well and on the velocity of the groundwater flow.

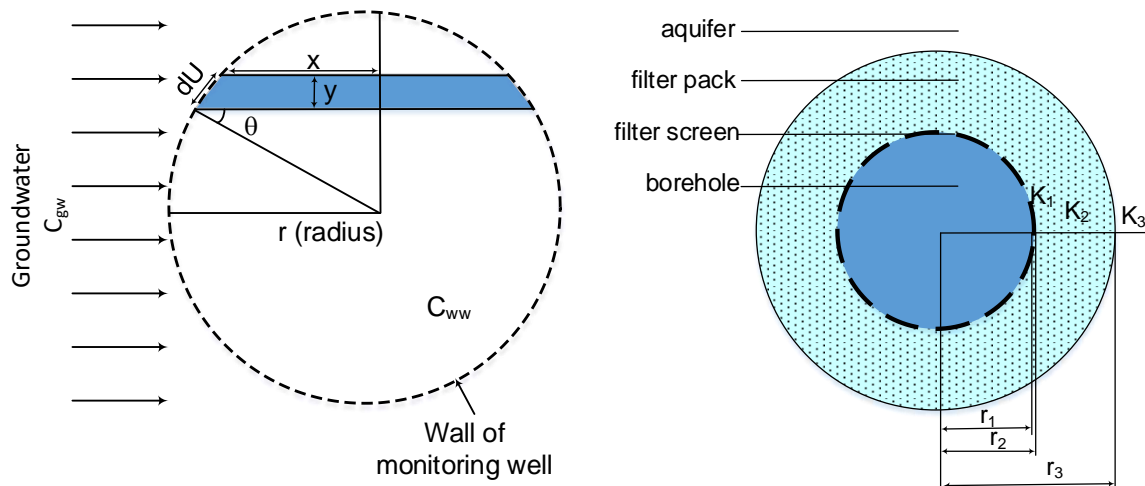


**Figure 33.** (left) Schematic sketch of a subarea (modified after Schubert [2011] and Hamada [2000]), (right) schematic horizontal cross section of a screen borehole with filter pack (Schubert [2011])

Hamada (2000) divided a cross section of well into sub minute areas  $dA$  (Figure 33) with the amount of  $^{222}\text{Rn}$  can be quantified as follows

$$dC_{ww}^t dA = r \cos \theta d\theta \int_0^t C_{gw}^\infty e^{-\lambda t} v_{ww} dt \quad (36)$$

The total amount of  $^{222}\text{Rn}$  for the complete cross section of well per unit length is calculated from Eq.(36) with  $\theta$  from  $-\pi/2$  to  $\pi/2$  as:

$$C_{ww}^t = \frac{1}{\pi r^2} \int_{-\pi/2}^{\pi/2} r \cos \theta d\theta \left( -\frac{1}{\lambda} C_{gw}^\infty v_{ww} \left( e^{-\lambda 2r \cos \theta / v_{ww}} - 1 \right) \right) \quad (37)$$

Then the radon deficit in well water can be therefore calculated as

$$\frac{C_{ww}^t}{C_{gw}^\infty} = \frac{v_{ww}}{\pi \lambda r} \int_{-\pi/2}^{\pi/2} \left( 1 - e^{-\lambda 2r \cos \theta / v_{ww}} \right) \cos \theta d\theta \quad (38)$$

The advantage of Schubert approach is take in to account the different hydraulic conditions in the aquifer and well including filter screen and filter pack, which was not considered by Hamada, given by a horizontal convergence factor  $\alpha$  (Drost et al., 1968) with the relationship

$$v_{gw} = v_{ww} / \alpha \quad (39)$$

with

$$\alpha = \frac{8}{\left(1 + \frac{K_3}{K_2}\right) \left\{ 1 + \left(\frac{r_1}{r_2}\right)^2 + \left[ \frac{K_2}{K_1} \left(1 - \frac{r_1}{r_2}\right)^2 \right] \right\} + \left(1 - \frac{K_3}{K_2}\right) \left\{ \left(\frac{r_1}{r_3}\right)^2 + \left(\frac{r_2}{r_3}\right)^2 + \frac{K_2}{K_1} \left[ \left(\frac{r_1}{r_3}\right)^2 - \left(\frac{r_2}{r_3}\right)^2 \right] \right\}} \quad (40)$$

where  $K_1$ ,  $K_2$ ,  $K_3$  is hydraulic conductivity of filter screen, filter pack and aquifer respectively,  $r_1$ ,  $r_2$  is the inside and outside radius of the filter screen and  $r_3$  is radius of the borehole.

If the monitoring well is an open borehole without filter screen and filter pack, the coefficient  $\alpha = 2$ . In case of an unpacked well or packed by the same material of the aquifer, then this coefficient can be calculated as

$$\alpha = \frac{4}{1 + \left(\frac{r_1}{r_2}\right)^2 + \left[ \frac{K_2}{K_1} \left(1 - \frac{r_1}{r_2}\right)^2 \right]} \quad (41)$$

### 3.4.2.3 Field investigations

In order to estimate groundwater velocity in the research area, we have adapted a protocol modifying the methods of Schubert et al 2011. The selected piezometers have been chosen located in difference locations in the interested zone near the fond of saltwater intrusion. These piezometers have different depths to the bottom of aquifer (from 15m in XC to 24.2m in L3 and 30m in these others) and well screen distributed of all the depth (from 1-2m of on top steel protection casing to the bottom). Lithology and well construction information of these piezometers are shown in Annex 3.

In this research, a vertical heterogeneous distribution of the aquifer and variable-density have been considered, which was not done by previous studies. Depending on the depth of piezometers and density distribution, three samples in each piezometers (XD, X20, X26, L3),

two samples in well XC and one sample in XA were taken and analyzed (Figure 34). The shallower sample consists in freshwater (with EC less than 1 mS/cm at average depth of 5 to 8m from the surface). The intermediate sample were taken in the layer corresponds to the saltwater front (at depth of 15 to 17m from the surface) and the deepest samples were taken at depth where groundwater effected by saltwater intrusion (at average depth of 21 to 22m from the surface).

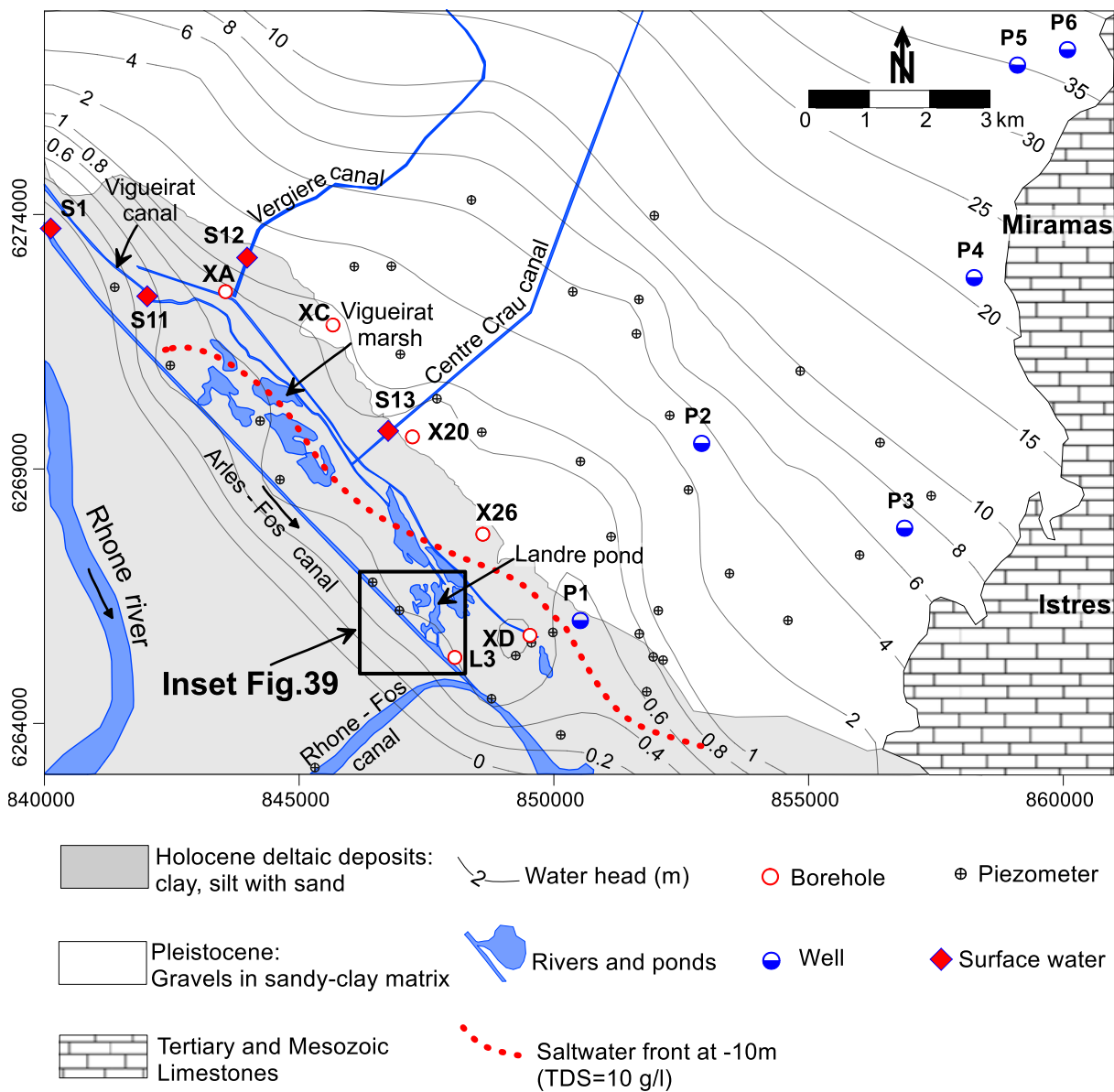


**Figure 34.** Radon monitoring locations, including Radon sampling in continue pumping wells, in piezometers and in surface water.

**Table 3.** Summary of results of regular measurements of  $^{222}\text{Rn}$  from groundwater samples in selected piezometers for estimation of groundwater flow (detailed information of piezometers is shown in Annex 1)

Sample /Well name	X	Y	Altitude of piezometer casing <i>m</i>	Sampling date	Depth from piezometer casing <i>m</i>	Depth from sea level <i>m</i>	EC $\mu\text{S}/\text{cm}$	T $^{\circ}\text{C}$	$^{222}\text{Rn}$ $\text{Bq}/\text{m}^3$	+/- ( $2\sigma$ ) $\text{Bq}/\text{m}^3$	
X26	848605	6267718	1.23	05/03/2014	8	-6.77	$C_{ww}$	893	15.4	9328	283
							$C_{gw}$	857	15.8	10854	313
							$C_{ww}$	1140	15.4	12040	366
							$C_{gw}$	1150	15.9	11354	448
							$C_{ww}$	17460	15.5	6632	285
							$C_{gw}$	20800	16.2	7978	323
XD-I	849530	6265731	1.12	21/05/2014	5	-3.88	$C_{ww}$	955	14	6921	238
							$C_{gw}$	1098	14.7	8842	328
							$C_{ww}$	8170	14	2401	130
							$C_{gw}$	8600	15.2	8689	274
							$C_{ww}$	39800	15	6878	265
							$C_{gw}$	47000	15	9809	289
XD-II	849530	6265731	1.12	06/11/2014	5	-3.88	$C_{ww}$	1060	16.8	8196	195
							$C_{gw}$	1168	16.4	9144	210
							$C_{ww}$	7480	15.8	3853	123
							$C_{gw}$	8650	15.3	6603	189
							$C_{ww}$	37500	15.5	7407	195
							$C_{gw}$	45500	15.1	7951	214
XC	845663	6271829	2.26	06/11/2014	5	-2.74	$C_{ww}$	739	17.6	8295	182
							$C_{gw}$	749	20.7	10264	206
							$C_{ww}$	760	17.4	10945	231
							$C_{gw}$	760	16.2	10810	218
XA	843555	6272484	1.19	24/09/2014	7	-5.81	$C_{ww}$	932	16.5	5728	175
							$C_{gw}$	929	15.6	11694	256
X20	847224	6269630	1.39	13/11/2014	7	-5.61	$C_{ww}$	790	16.5	7758	306
							$C_{gw}$	649	16.6	10167	228
							$C_{ww}$	654	16.4	10016	191
							$C_{gw}$	616	16.5	10491	232
							$C_{ww}$	713	16.6	8751	180
							$C_{gw}$	745	16.7	9943	198
L3	848056	6265296	2.69	13/11/2014	7	-4.31	$C_{gw}$	4590	16.4	4561	76
							$C_{ww}$	3950	15.1	7713	189
							$C_{gw}$	13850	15.3	3919	130
							$C_{ww}$	16610	14.5	4586	152
							$C_{gw}$	40200	15.1	2790	116
							$C_{ww}$	48900	14.7	5126	162

**Table 4.** Summary of results of  $^{222}\text{Rn}$  analysis from groundwater in continue pumping wells

Sample	Exploitation station	Lat.	Long.	Sampling date	EC	T	$^{222}\text{Rn}$	+/-
					$\mu\text{S}/\text{cm}$	$^{\circ}\text{C}$	$\text{Bq}/\text{m}^3$	$(2\sigma)$ $\text{Bq}/\text{m}^3$
P1	Pissarotte	850661	6266209	27/03/2013	817	16.6	8506	231
P2	Vallignette	852901	6269502	24/07/2012	980	18.2	9475	152
P3	Fanfarigoule	856885	6267836	27/03/2013	716	17.0	2681	124
P4	Caspienne	858250	6272759	27/03/2013	749	16.6	8829	236
P5	BMW	859100	6276936	27/03/2013	653	16.6	5921	180
P6	Sulauze	860082	6277239	27/03/2013	726	17.1	2604	113

For selected piezometers, electrical conductivity and temperature have been measured before and after water sampling. The evaluation of groundwater velocity was done for three water depths. Knowing the depth of the bottom of the piezometer and the water level and the distribution of salinity, the water column was divided in three segments. The shallower sample was taken at the mean depth of the freshwater zone, with lower shallower segment, the intermediate to the mean depth of the intermediate segment in the changing zone of EC, and the deepest sample in the middle of the deeper segment with high EC. Purges of the different column segments were done successively at the same intermediate positions. The operations done in the field followed basically this scheme:

1. The piezometric head and the water depths have been measured and recorded
2. The volume of water in the piezometer was calculated.
3. The height of the water column was divided in three parts, at equal distances.
4. The 12V pump was lowered until the mean depth of the shallower segment. The pump was attached slowly to one end of a 23m-long hose in Nalgene and the nominal flow rate of the pump is about 2 liter / minute to avoid the contamination with fresh groundwater.
5. The other end of the hose was introduced into the bottom of a 2.5 liter-glass bottle.
6. The pump was activated and the volume of the bottle was filled with incoming groundwater.

7. The time necessary to fill the bottle (filling time) was measured.
8. The volume of water into the bottle was renovated without removing the hose, with the pump continuously pumping for another filling time.
9. In the discharged water the temperature and the conductivities were measured with a probe.
10. When the second filling time was reached (and the renovation of the water volume achieved), the hose was gently removed from the bottle while the pump was continuously pumping.
11. As soon as the hose was out of the bottle, the pump was switched to off, a water volume of 5 ml was removed from the bottle with a syringe and the lid of the bottle was closed. The removal of this 5 ml volume is necessary to compensate thermal expansion of groundwater sample.
12. The time of collection was recorded for radon decay correction.
13. The operations were repeated for the mean depths of the second and third segments.
14. The hose was not emptied in between the sample collections, to avoid degassing.

After collections of the stagnant water in the piezometer, we proceeded with the collection of the sample after purge.

1. We raised the pump at the depth of the shallower sample.
2. We pumped at least three times the volume of the shallower water segment.
3. Then we sampled groundwater as described in points 5 to 12.
4. The pump was then lowered to the depth of the intermediate sample and purge was done for a volume of three times the intermediate water segment.
5. Then we sampled groundwater as described in points 5 to 12.
6. The pump was then lowered to the depth of the deepest sample and purge was done for a volume of three times the deeper water segment.

### 3.4.3 Estimate of groundwater discharge in to surface water using $^{222}\text{Rn}$ continuous monitor

#### 3.4.3.1 Introduction

The observed enrichment of radon in groundwater relative to the surface water bodies helps to understand the groundwater-seawater interactions occurring in a wide range of time scales. Because the  $^{222}\text{Rn}$  concentrations in surface waters are low and due to its short half-life, large volume water are required for the measurement of  $^{222}\text{Rn}$  and hence in situ monitoring is highly essential (Jacob et al., 2009).

For the in situ measurement of  $^{222}\text{Rn}$  in the coastal area, surface water will continuously pumped from the same depth and sprayed as a jet into an air-water exchanger (Figure 35). The radon is thus stripped out from the water and recirculates through a closed air loop via a desiccant tube into a single-detector system (a Rad7 system, DurrIDGE Inc.). The purpose of the desiccant is to absorb moisture, as detection efficiency decreases at higher humidity. The equilibrium of  $^{222}\text{Rn}$  between the liquid and gaseous phase is established within 30min. The radon monitor uses a high electric field above a silicon semiconductor detector at ground potential to attract the positively charged polonium daughter,  $^{218}\text{Po}^+$  (half-life = 3.1min; alpha energy = 6.00MeV) and  $^{214}\text{Po}^+$  (half-life = 164 $\mu$ min; alpha energy = 7.67MeV), which are counted as a measure of  $^{222}\text{Rn}$  concentration in air. An air filter at the inlet of the radon monitor prevents dust particles and charged ions from entering into alpha detector. The ions are collected in energy specific windows which eliminate interference and maintain very low background.  $^{222}\text{Rn}$  activities are expressed in Bq/m<sup>3</sup> (disintegration per second per m<sup>3</sup>) with 2 $\sigma$  uncertainties. In order to get acceptable precision,  $^{222}\text{Rn}$  activity at each location was counted for two hours (three cycles of counting) after attaining equilibrium. At room temperature, as the radon in air is about four times more than that in water at equilibrium, the measured radon concentrations in air are corrected accordingly.

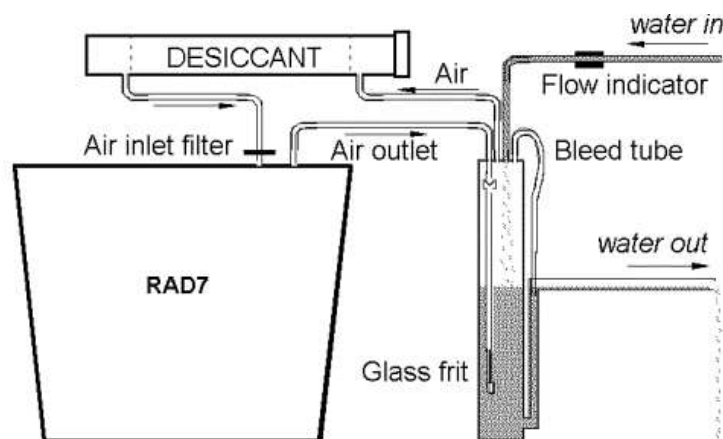


**Figure 35.** Diagrammatic view of experimental setup for single RAD-7 exchanger continuous radon-in-water monitor. (Burnett et al., 2001, Dulaiova et al., 2005)

In order to triple the time resolution, the continuous radon monitor system was connected to 2 or 3 radon detectors (Figure 36)

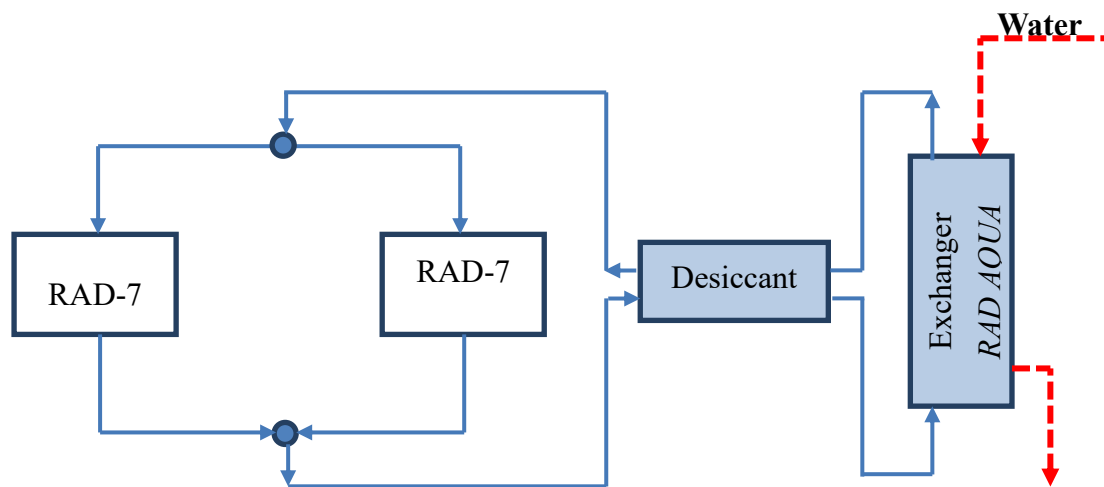


**Figure 36.** A simplified sketch of an equilibrium radon measurement system. Lines shown represent the water pumped through the exchanger by a submersible pump (dashed) and a closed air loop (solid) that flow through a parallel monitor system of RAD-7 (Dulaiova et al., 2005).

#### 3.4.3.2 Method

Estimating groundwater discharge approach is based on a radon model which was first given by Cable and then applied and developed by many other studies (Cable et al., 1996, Burnett et al., 2001, Burnett and Dulaiova, 2003, Lambert and Burnett, 2003, Oliveira et al., 2006, Dimova et al., 2013). This model is a mass balance box of all radon input and output to the ponds including diffusion across the sediment-water interface which relevant to all groundwater sink and source (Figure 37).

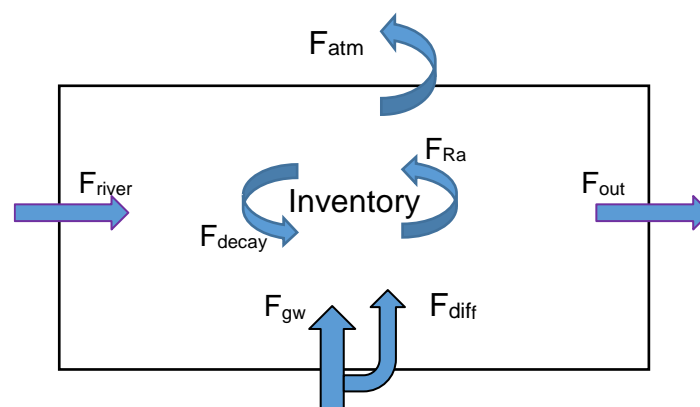


**Figure 37.** Schematic of the radon mass balance box model (edited from Natasha [2013])

Base on this model, applied to the research area of Crau-Vigueirat system and assuming steady-state condition, the equation of radon mass balance may be written as:

$$F_{river} + F_{diff} + F_{Ra} + F_{gw} = F_{decay} + F_{air} + F_{out} \quad (42)$$

In this equation, all radon fluxes can be calculated or measured except radon flux in ground water  $F_{gw}$  due to groundwater discharge into the ponds which is the unknown radon flux that we are interested on. The other fluxes are determine and calculate as follows.

$F_{river}$  is radon flux in the river water,  $F_{river} (Bq/m^2/d) = Rn_{river} * Q_{river} / S$ , where  $Q_{river}$  is the river water flow and  $S$  is the surface of the pond.

$F_{diff}$  is the radon flux produced by sediments diffusion. This term is important because it provides a constant radon input through the sediment interface even if no groundwater discharge occurs.

$F_{Ra}$  is the flux produced by disintegration of the dissolved  $^{226}\text{Ra}$  calculated as follow

$$F_{Ra} = I^{226}\text{Ra} \times \lambda_{222} \quad (43)$$

where  $I^{226}\text{Ra}$  is the inventory of  $^{226}\text{Ra}$  in the water column, therefore, water depth needed to be measure.

$F_{air}$  is the flux of radon lost to the atmosphere and was evaluated using the gas transfer velocity ( $k$ ) approach. A recent study (Cockenpot et al., 2015) about radon degassing in the nearby Berre Pond has shown that the relationships between wind and gas transfer velocity  $k$  modeled with a variety of methods fits statistically the experimental relation:

$$k_{660} = 0.0033u^3 + 5.4 \quad (44)$$

where  $k_{660}$  is the gas transfer velocity (cm/h) or radon, normalized to  $\text{CO}_2$  at  $20^\circ\text{C}$  for brackish waters and  $u$  is the wind velocity (m/s) measured at 10m above ground. The gas transfer velocity can be determine using the relationship of McIntyre (1995) obtained experimentally for freshwaters:

$$k_{600} = 0.45u^{1.6} (Sc/600)^{-0.5} \quad (45)$$

where  $Sc$  is the Schmidt number, corresponding to the ratio between kinetic viscosity and molecular diffusivity of radon, that in the case of freshwater is divided by 600 ( $Sc$  for  $\text{CO}_2$  in freshwater at  $20^\circ\text{C}$ ). The kinetic viscosity is the ratio between absolute viscosity and density. We calculated absolute viscosity with the equation of (Seeton, 2006) molecular diffusivity with the equation of Peng et al. (1974). The atmospheric flux can be calculated with the approach of McIntyre (1995):

$$F_{air} = k_{600} (Rn_{ave} - \delta Rn_{air}) \quad (46)$$

where  $Rn_{ave}$  and  $Rn_{air}$  are the average  $Rn$  activities in the ponds waters and in the air,  $\delta$  is the Ostwald coefficient. The Ostwald coefficient is calculated using the Bunsen coefficient, obtained using the equation of Schubert et al 2012, which takes into account the effects of salinity on radon solubility.

$F_{decay}$  is the radon inventory

$$F_{decay} = I^{222} Rn \times \lambda_{222} \quad (47)$$

$$I^{222} Rn = Rn_{ave} \times h \quad (48)$$

where  $Rn_{ave}$  is the average  $Rn$  concentration measured in the pond.

$F_{out}$  is output flux obtained by multiplying the measured radon activity at the outlet with the total water outflow.

The time evolution of radon input from the rivers into the ponds can be modelled using the usual differential equation:

$$dRn / dt = F_{river} + F_{diff} + F_{Ra} + F_{gw} - F_{decay} - F_{air} - F_{out} \quad (49)$$

This equation can be rearranged to separate variables and integrated imposing as boundary condition that the radon activity at time  $t=0$  is the one of the river inputs ( $Rn_{river}$ ).

$$Rn(t) = c_2 / c_1 + (Rn_{river} - c_2 / c_1) \exp(-c_1 t) \quad (50)$$

where:

$$c_1 = \lambda_{Rn} h + k \quad (51)$$

and

$$c_2 = k Rn_{air} \alpha + F_{gw} + F_{diff} + F_{Ra} - F_{out} \quad (52)$$

### 3.4.3.3 Results of field investigation

Two field monitoring surveys have been done in April, 2014 with one sector along the canal Arles-Fos and other survey have been measured in Landre pond), field survey measurements shown in Table 5 and Figure 34.

To determine radon activities in surface water, an automatic continuous measuring system on a small boat have been setup and surveyed with an average speed of 3-4km/h. Surface water samples have been collected at a depth interval of 1m from the various locations along the canal and in the lake and pump to air-water exchanger system (Figure 38). By this system, radon will stripe out from the water and circulate through a close air-loop including with a desiccant to absorb moisture, and then go into a radon monitor system (including 3 parallel RAD-7 monitors).

At the same frequency of 5minutes, a coordination have been selected using a GPS equipment and water physical parameters such as temperature, electrical conductivity (EC) have been measured.

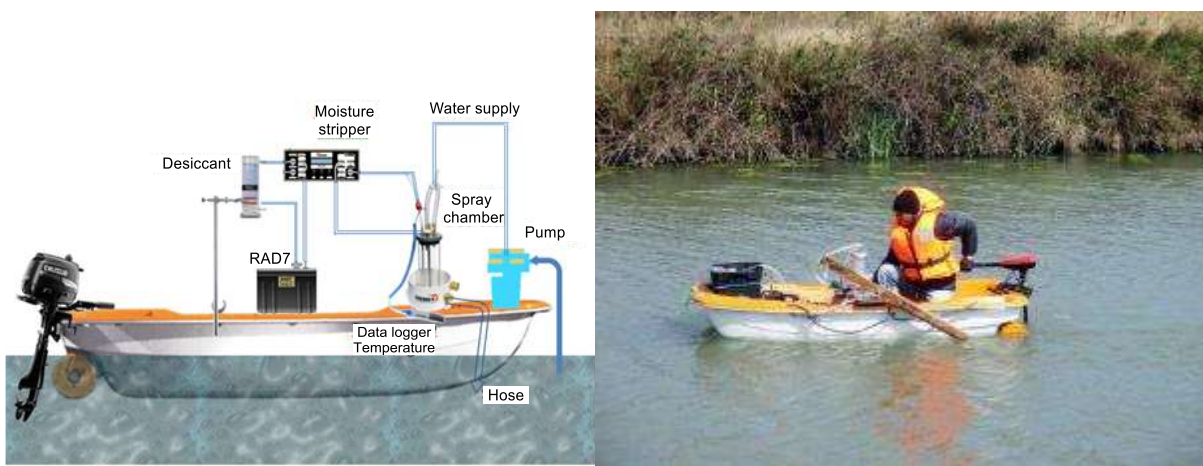


Figure 38. Operational conguration of the continuous  $^{222}\text{Rn}$  monitoring system (left) and field campaign in study area (right)

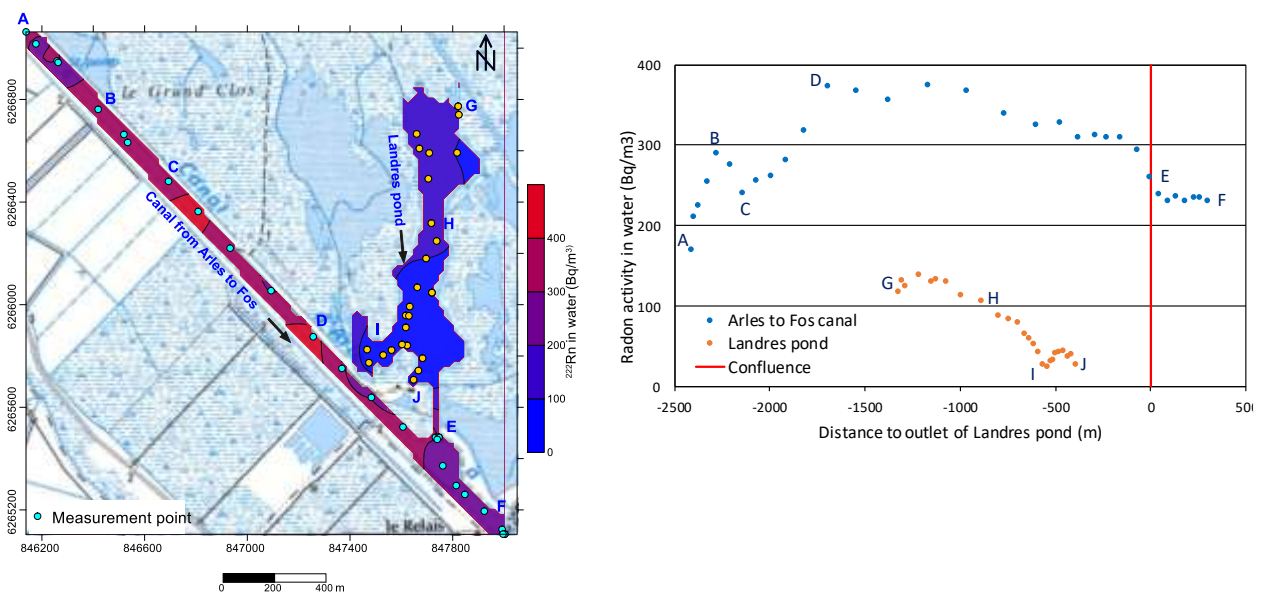


Figure 39. Track map of surface water radon measurements (left) and tracer distribution of  $^{222}\text{Rn}$  (right) in Arles-Fos canal (blue circles) and Landre pond (orange circles) in April, 2014

**Table 5.** Radon activities in surface water in the Crau area. X and Y are coordinates according to Lambert 93 projection. **st.**, radon measurement points with the boat maintained in a stable location. **av.**, average radon activities during continuous radon measurement done on a boat transect. Coordinates are centroids of several consecutive points during navigation.

Station	Location	X	Y	Date	EC	T	<sup>222</sup> Rn	+/- (2σ)
				2014	μS/cm	°C	Bq/m <sup>3</sup>	Bq/m <sup>3</sup>
<b>Arles - Fos canal</b>								
S1	st. Mas Thibert	839760	6274350	01/09	659	21.5	415	39
				24/09	695	19.3	-	-
S2	av. Ligagneau	843154	6267142	24/03	871	13.6	312	47
S3	av. Ligagneau – Galejon	847281	6265851	24/03	855	13.7	349	24
				st. Galejon (Landre				
S4	outlet)	847710	6265520	24/03	810	13.4	238	25
	av. Landre - le							
S5	Relais	847886	6265301	24/03	829	13.5	253	42
S6	st. Le Relais	847970	6265120	24/03	829	13.5	203	12
				01/09	683	21.0	178	20
				23/09	660	19.5	231	23
<b>Landre Pond</b>								
S7	st. Outlet of Landre pond (no outflow)	847710	6265520	01/09	615	20.3	-	-
				23/09	635	18.2	11	5
				23/09	631	18.1	13	7
S8	av. Southern Landre	847631	6265735	25/03	911	12.2	40	12
S9	av. Central Landre	847830	6266054	25/03	791	12.4	78	14
S10	av. Northern Landre	847786	6266608	25/03	788	12.7	111	17
<b>Canals entering the Landre pond</b>								
S11	st. Vigueirat canal	842040	6272630	23/09	650	19.3	172	26
S12	st. Vergiere canal	843690	6273090	23/09	700	17.1	495	36
				06/11	752	12.6	770	58
S13	st. Centre Crau canal	846650	6269850	23/09	570	17.4	82	19
				06/11	759	12.1	156	28

## 3.5 Numerical modeling of saltwater intrusion

### 3.5.1 Introduction

Generally, “a model is a representation of an object, system, or idea in some form other than the entity itself” (Leendertse, 1981). The use of groundwater models is prevalent in the field of environmental science. Models have been applied to investigate a wide variety of hydrogeological conditions. More recently, groundwater models are being applied to predict the transport of contaminants or saltwater intrusion for risk evaluation.

In general, models are conceptual descriptions or approximations that characterize physical systems using mathematical equations. By mathematically representing a simplified version of a hydrogeological system, reasonable alternative scenarios can be predicted, tested, and compared. The applicability or usefulness of a model depends on how closely the mathematical equations approximate the physical system being modeled. In order to evaluate the applicability or usefulness of a model, it is necessary to have a thorough understanding of the physical system and the assumptions embedded in the derivation of the mathematical equations.

Groundwater models describe the groundwater flow and transport processes using mathematical equations based on certain simplifying assumptions. These assumptions typically involve the direction of flow, geometry of the aquifer, the heterogeneity or anisotropy of sediments or bedrock within the aquifer, the contaminant transport mechanisms and chemical reactions. Because of the simplifying assumptions embedded in the mathematical equations and the many uncertainties in the values of data required by the model, a model must be viewed as an approximation and not an exact duplication of field conditions. Groundwater models, however, even as approximations are a useful investigation tool that groundwater hydrologists may use for a number of applications.

Application of existing groundwater models include water balance (in terms of water quantity), gaining knowledge about the quantitative aspects of the unsaturated zone, simulating of water flow and chemical migration in the saturated zone including river-groundwater relations, assessing the impact of changes of the groundwater regime on the environment, setting up/optimizing monitoring networks, and setting up groundwater protection zones.

It is important to understand general aspects of both groundwater flow and transport models so that application or evaluation of these models may be performed correctly.

The protocol to set up a numerical modeling include 4 main steps (Anderson and Woessner, 2002), such as (i) define objectives, (ii) build and revise a conceptual modeling, (iii) develop a numerical modeling and (iv) calibrate and validate model.

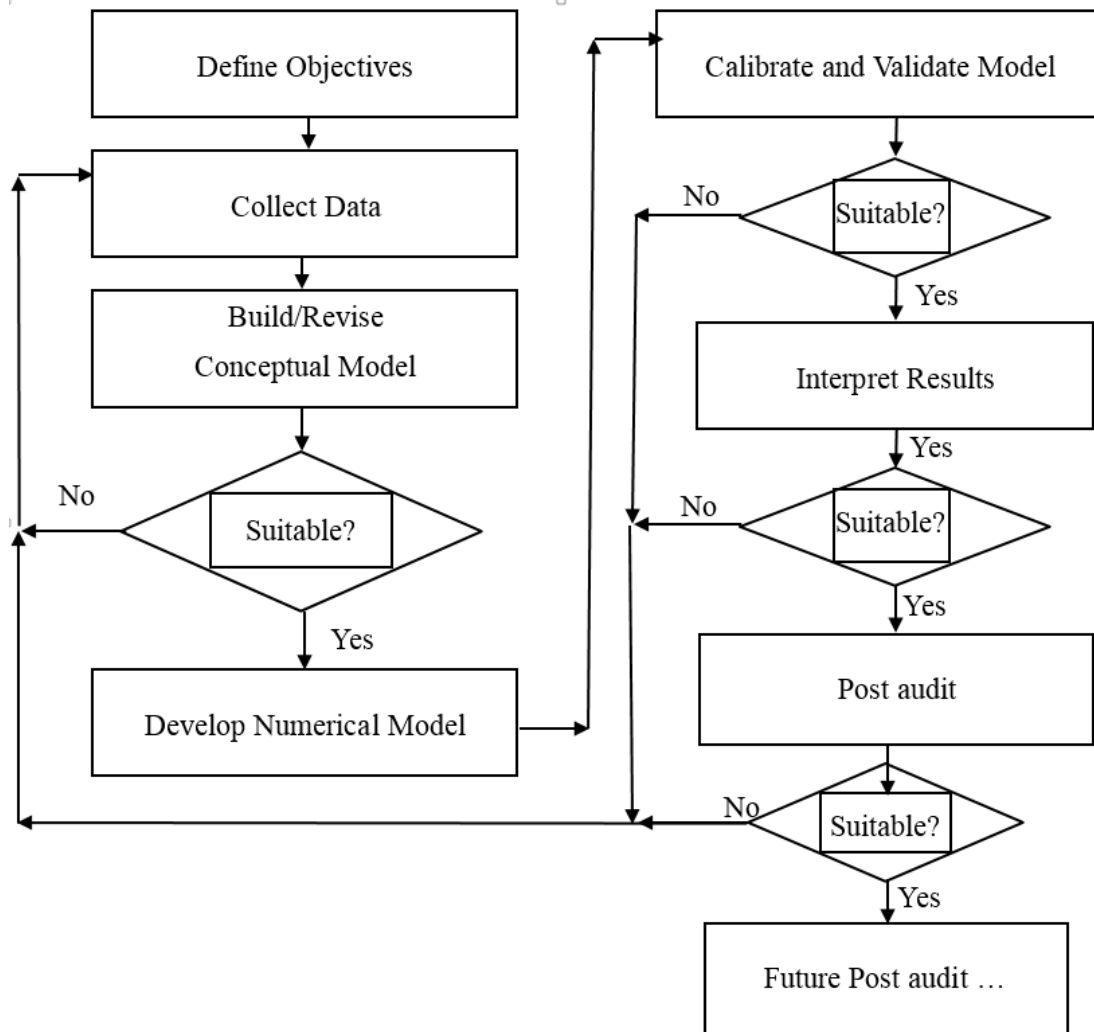


**Figure 40.** Protocol of building a groundwater modeling (Anderson and Woessner, 2002)

In certain hydrogeological situations such as seawater intrusion, radioactive waste disposal, groundwater contamination and geothermal energy production, fluid density variations occur because of changes in solute or colloidal concentration, temperature and pressure of groundwater (Simmons et al., 2001). Field and laboratory studies have shown that groundwater dynamics are strongly influenced by density differences producing convective current (Kolditz et al., 1998). The stratification is the main cause of the instability (free convection) which enhances hydrodynamic mixing of the high density with the lower density. Many mathematical and numerical models have been used to predict the location and movement of saltwater interface (Abd-Elhamid and Javadi, 2011) and some of them considered the dependence on fluid density (Voss and Souza, 1987, Holzbecher, 1998a, Frolkovič and De Schepper, 2000, Simmons et al., 2001). These models can be categorized as sharp interface or dissipative interface models depends on the method of treating the interface.

### 3.5.2 Heterogeneity and variable-density flow

#### 3.5.2.1 Heterogeneity

Soil structure is the arrangement of soil particles at various scales, mainly depends on soil properties such as bulk density, porosity, penetration resistance, hydraulic conductivity (Seger et al., 2009). In practical, geologic systems are not really homogeneous or uniform, it is variable by space and time and very difficult to characterize (Besson et al., 2004). Therefore, single-number representations of porous media are not correct to the reality but widely accepted to simplify and ignore the limitation of characterize and observe soil properties in actual formations over large spatial scales. Several studies have shown that the solute transport in porous media is controlled by the spatial variations in heterogeneous conductivity field (Dagan, 1989). This concept could be reach with the stochastic approach using a model where the input parameters are considered to be random spatial function with an associated probability density function (Neuman et al., 1987, Dagan, 1989, Tompson and Gelhar, 1990). This approach could be support and validate by accurate field analyses and data collection. After validations stochastic approaches can provide a quantitative description of soil properties over large spatial scales and account for the inherent spatial variability.

#### 3.5.2.2 Variable-density

When density differences are significant, solute transport is the result not only of forced convection (advection) and dispersion/diffusion but also of free convection. Almost researches of solute transport in groundwater have focused on transport that occurs mainly by forced convection. Most mass transport studies in groundwater have focused on transport that occurs primarily by force convection (Simmons et al., 2001). This conclusion have been confirmed in case of surface water/groundwater interaction in a stably-stratified fresh surface/salt groundwater interface (Massmann et al., 2006). Several studies have investigated the error introduced by adopting the sharp interface approximation and to correct the Ghyben-Herzberg estimate of the interface depth (Pool and Carrera, 2011).

Numerous studies have used this approach in groundwater flow and solute transport modeling (Shikaze et al., 1998, Zhang et al., 1998, Simmons et al., 2001, Qahman and Larabi, 2006, Lin et al., 2009, Pool and Carrera, 2011, Webb and Howard, 2011, Xu et al., 2013) and shown that the magnitude of horizontal flow velocity, the solute transport rate and density difference between the contaminant solution and the ambient groundwater influenced the stability of the plumes.

### 3.5.2.3 Variable-density flow in heterogeneity systems

In variable-density flow systems, heterogeneity in hydraulic properties can perturb flow over many length scales (Simmons et al., 2001). Several studies have been done from the year of 1980s to examine the way in which heterogeneity in hydrogeological properties can affect the variable-density instabilities. The first studies have been applied to multiple hydraulic conductivity layer models to show that when increase the number of layers, the system approached the behavior of an equivalent anisotropic, homogeneous single layer (Mckibbin and O'Sullivan, 1980). Then, several experimental and numerical investigations of variable-density groundwater flow in homogeneous, layered and lenticular media has been applied by Schincariol and concluded that more anisotropic and heterogeneous permeability field will make more dampening of instability growth (Schincariol et al., 1997). After an numerical study, (Shikaze et al., 1998) suggested that heterogeneity can enhance plume migration rates or dissipate them. Heterogeneity is important because it is the triggering mechanism for the onset of instabilities and control the instabilities to grow or decay (Simmons et al., 2001). Variable-density flow and solute transport are most sensitive to the medium, which are properties that can be determined more accurately than the geometry and hydraulic properties of the fracture network, which have a smaller impact on density-driven transport (Graf and Therrien, 2007).

### 3.5.3 Governing equations

The governing equations of variable-density groundwater flow and solute transport are described in detail in many studies by (Voss and Souza, 1987, Bear, 1988, Diersch, 1988, Stuyfzand, 1989, Holzbecher, 1998a, Guo et al., 2002).

Groundwater modeling begins with a conceptual understanding of the physical problem. The next step in modeling is translating the physical system into mathematical terms. In general, the results are the familiar groundwater flow equation and transport equations. The governing flow equation for three-dimensional saturated flow in saturated porous media is:

$$\frac{\partial}{\partial x} \left( K_{xx} \frac{\partial h}{\partial x} \right) + \frac{\partial}{\partial y} \left( K_{yy} \frac{\partial h}{\partial y} \right) + \frac{\partial}{\partial z} \left( K_{zz} \frac{\partial h}{\partial z} \right) - Q - S = S_s \frac{\partial h}{\partial t} \quad (53)$$

Where,

$K_{xx}$ ,  $K_{yy}$ ,  $K_{zz}$  = hydraulic conductivity along the  $x,y,z$  axes which are assumed to be parallel to the major axes of hydraulic conductivity;

$h$  = piezometric head;

$Q$  = volumetric flux per unit volume representing source/sink terms;

$S_s$  = specific storage coefficient defined as the volume of water released from storage per unit change in head per unit volume of porous material.

The transport of solutes in the saturated zone is governed by the advection dispersion equation which for a porous medium with uniform porosity distribution is formulated as follows:

$$\frac{\partial c}{\partial t} = -\frac{\partial}{\partial x_i}(cv_i) + \frac{\partial}{\partial x_i}\left(D_{ij}\frac{\partial c}{\partial x_j}\right) + Rc \quad i, j = 1, 2, 3 \quad (54)$$

where,

$c$  = concentration of the solute;

$Rc$  = sources or sinks;

$D_{ij}$  = dispersion coefficient tensor;

$v_i$  = velocity tensor.

An understanding of these equations and their associated boundary and initial conditions is necessary before a modeling problem can be formulated. Basic processes, that are considered, include groundwater flow, solute transport and heat transport. Most groundwater modeling studies are conducted using either deterministic models, based on precise description of cause-and-effect or input-response relationships or stochastic models reflecting the probabilistic nature of a groundwater system.

The governing equations for groundwater systems are usually solved either analytically or numerically. Analytical models contain analytical solution of the field equations, continuously in space and time. In numerical models, a discrete solution is obtained in both the space and time domains by using numerical approximations of the governing partial differential equation. Various numerical solution techniques are used in groundwater models. Among the most used approaches in groundwater modeling, three techniques can be distinguished: Finite Difference Method, Finite Element Method, and Analytical Element Method. All techniques have their own advantages and disadvantages with respect to availability, costs, user friendliness, applicability, and required knowledge of the user.

### 3.5.4 Numerical modeling of heterogeneity and variable-density flow

The mathematical or the numerical models are usually based on the real physics the groundwater flow follows. These mathematical equations are solved using numerical codes such as MODFLOW, FEFLOW, GMS, SUTRA, etc. Various types of numerical solutions like the finite difference method (FDM) and the finite element method (FEM).

The FDM is the oldest and is based upon the application of a local Taylor expansion to approximate the differential equations. The FDM uses a topologically square network of lines to construct the discretization of the partial differential equation (PDE).

The FEM is a numerical technique for finding approximate solutions to boundary value problems for differential equations. It uses variation methods (the calculus of variations) to minimize an error function and produce a stable solution. Analogous to the idea that connecting many tiny straight lines can approximate a larger circle, FEM encompasses all the methods for connecting many simple element equations over many small subdomains, named finite elements, to approximate a more complex equation over a larger domain.

However simulation codes called finite elements (FE) are in fact hybrid models using the FE technique for the spatial resolution and the FD technique for time-resolved (Voss and Souza, 1987, Simmons et al., 2001).

Flow simulation densitaires involves solving coupled flow and transport, because the transport influences the flow (convection) and the influence of flow transport (advection). Equations must be solved simultaneously by an iterative process given time step. The velocity field at the required resolution Darcy transport results from the resolution of the flow (the pressure) at the previous iteration. Once stabilized for a given time step (called convergence model) solution, the iterations are carried forward to the next time step.

The modeling of variable density flow has been addressed by numerous authors and a number of codes were developed to simulate variable-density groundwater systems.

For hydrogeological modeling, simulation densities particular phenomena related to transport salt (eg. Seawater intrusion) or heat (eg. Geothermal), the most widely used codes which have the subject of numerous publications, both in theory and in applied fields (Kumar, 2004). The main models are presented below in chronologic order:

1. *SUTRA (2-D Saturated/Unsaturated Transport Model)*

SUTRA (1984) is a 2D groundwater saturated-unsaturated transport model, a complete saltwater intrusion and energy transport model. SUTRA simulates fluid movement and transport of either energy or dissolved substances in a subsurface environment. SUTRA employs a two-dimensional hybrid finite-element and integrated finite-difference method to approximate the governing equations that describe the two interdependent processes that are simulated: (1) fluid density dependent saturated or unsaturated groundwater flow and either (2a) transport of a solute in the groundwater, in which the solute may be subject to equilibrium adsorption on the porous matrix and both first-order and zero-order production or decay, or (2b) transport of thermal energy in the groundwater and solid matrix of the aquifer.

## 2. SEAWAT (3-D Variable-Density Ground-Water Flow) and MODFLOW

The SEAWAT (2002) program was developed by U.S. Geology Survey (USGS) to simulate three-dimensional, variable density, transient ground-water flow in porous media. The source code for SEAWAT was developed by combining MODFLOW and MT3DMS into a single program that solves the coupled flow and solute-transport equations. The program has been used to study on brine migration in continental aquifers, saltwater intrusion in coastal aquifers. The SEAWAT code follows a modular structure, and thus, new capabilities can be added with only minor modifications to the main program. SEAWAT reads and writes standard MODFLOW and MT3DMS data sets, although some extra input may be required for some SEAWAT simulations. This means that many of the existing pre- and post-processors can be used to create input data sets and analyze simulation results. Users familiar with MODFLOW and MT3DMS should have little difficulty applying SEAWAT to problems of variable-density ground-water flow.

## 3. FEFLOW (Finite Element Subsurface Flow Simulation System)

FEFLOW is a finite-element package for simulating 3D and 2D fluid density coupled flow, contaminant mass (salinity) and heat transport in porous and fractured media. It is capable of computing (Diersch, 2014):

- Groundwater systems with and without free surfaces (phreatic aquifers, perched water tables, moving meshes);
- Problems in saturated-unsaturated (variable-saturation zones);
- Variable-density (salt intrusion) and variable-temperature transport phenomena (thermohaline flows);
- Complex geometric and parametric situations.

The package is fully graphics-based and interactive. Pre-, main- and post processing are integrated. There is a data interface to GIS (Geographic Information System) and a programming interface. The implemented numerical features allow the solution of large problems. Adaptive techniques are incorporated.

### 3.5.5 FEFLOW Code

FEFLOW has been used to simulate groundwater flow/discharge and solute transport for both steady state and transient conditions by matching computed and measured piezometric levels (Padilla et al., 2008) and determine the transaction between salt water and fresh water of this coastal alluvial area (Padilla et al., 2008, Allow, 2011) and (Barazzuoli et al., 2008). The conceptual model was based on steady-state flow and transient solute transport (Barazzuoli et al., 2008, Padilla et al., 2008). Steady-state flow will be calibrated by using water level during 2012-2013 and collected data from piezometric wells. Using the flow model to calculate the interaction between groundwater and surface water (Hu and Jiao, 2010); (Faye et al., 2001); (Padilla et al., 2008) and solute transport model will be calibrated using the salinity observed in control wells near the coastal wedge of the aquifer (Cronin et al., 2000). The computed head and salinity distribution will be compared with the control wells to calibrate the model and computed velocity and flow direction together will be calibrate with isotopic data measurements which will be done on boreholes (Faye et al., 2001, Vaidote Jakimavičiūtė - Maselienea, 2006); (Schubert et al., 2011).

For theoretical and practical information concerning the use of FEFLOW and the solution of equations, the reader can refer to the respective manuals (Diersch, 1988, Diersch et al., 2011a, Diersch et al., 2011b).

The basic mass conservation equation of a fluid in a variably saturated media is given by

$$S_o \cdot s(\psi) \frac{\partial \psi}{\partial t} + \varepsilon \frac{\partial s(\psi)}{\partial t} + \nabla q = Q \quad (55)$$

The fluid motion is described by the Darcy equation written in this form

$$q = -K_r(s)K(\nabla h + \chi e) = -K_r(s)K[\nabla \psi + (1 + \chi)e] \quad (56)$$

In equations (55) and (56):

$h = \psi + z$  is hydraulic head;

$\psi$  = pressure head, ( $\psi > 0$  saturated medium,  $\psi \leq 0$  unsaturated medium);

$s(\psi)$  saturation, ( $0 < s \leq 1$ ,  $s = 1$  if medium is saturated)

$q$  = Darcy flux vector

$z$  = elevation above reference datum

$t$  = time

$S_o = \varepsilon\gamma + (1-\varepsilon)r$  is specific storage due to fluid and medium compressibility,

$\varepsilon$  = porosity

$\gamma$  = fluid compressibility

$r$  = coefficient of skeleton compressibility

$K_r(s)$  = relative hydraulic conductivity ( $0 < K_r \leq 1$ ,  $K_r = 1$  is saturated  $t s = 1$ )

$K$  = tensor of hydraulic conductivity for the saturated medium (anisotropy)

$\chi$  = buoyancy coefficient including fluid density effects

$Q$  = specific mass supply,

The finite element formulation of the mass balance equation can be written as

$$\int_{\Omega} w S_o s(\psi) \frac{\partial \psi}{\partial t} + \int_{\Omega} w \varepsilon \frac{\partial s}{\partial t} - \int_{\Omega} q \cdot \nabla w = \int_{\Omega} w Q - \int_{\Gamma} w q_n \quad (57)$$

And with equation (\*\*\*) as

$$\begin{aligned} & \int_{\Omega} w S_o s(\psi) \frac{\partial \psi}{\partial t} + \int_{\Omega} w \varepsilon \frac{\partial s}{\partial t} + \int_{\Omega} \nabla w \cdot [K_r(s) K \cdot \nabla \psi] \\ & = \int_{\Omega} w Q - \int_{\Gamma} w q_n - \int_{\Omega} \nabla w \cdot [K_r(s) K \cdot (1 + \chi) \mathbf{e}] \end{aligned} \quad (58)$$

Where  $w$  is a test function and  $q_n$  corresponds to the normal fluid flux directed positive outward on  $\Gamma$ .

Geolithological, hydrogeological and hydrochemical data can be carried out in a GIS environment (ArcView, MapInfo, Surfer...) that is totally interfaced with FEFLOW. This is very useful in the development of the conceptual model, in the creation of the numerical model and in the analysis of simulation results.

# **Chapter 4**

## **RESULTS**



## 4.1 Geophysics survey

The main objectives of geophysical methods are saline intrusion mapping and aquifer characterization (depth of aquifer/water head, spatial dimensions and properties of geological formations).

In order to interpret the indirect geophysical measurements, a comparison have been done between geophysical data and lithological information from boreholes and water level, electrical conductivity measurements from piezometers in this area.

### 4.1.1 Electromagnetic mapping (EM34)

After two campaigns of EM survey, 12 profiles of EM34 have been done (Figure 32 and Table 2) in the marsh area, with 10 profiles perpendicular with salt-freshwater limit and two others along the canals. The spatial distribution of apparent soil electrical conductivity ( $\sigma_a$  - mS/m) of EM34-20 have been compared with a spatial distribution of electrical conductivity (EC) measurements from in pore water at 10 m depth. The small  $\sigma_a$  (<30 mS/m) characterize the freshwater zone in the center and northeast of Crau. In the zone along the Colmatage canal in center of marsh area,  $\sigma_a$  varies from 30-80 mS/m characterize a saline intrusion zone, equivalent to EC from 6000-18000  $\mu\text{S}/\text{cm}$ . In the southwest area,  $\sigma_a$  is very high (>100 mS/m) characterize the saltwater zone.

The EM34 data have been interpreted by using the software EM4Soil - a software package which was developed to enable the inversion of electromagnetic (EM) conductivity data  $\sigma_a$  acquired at low induction numbers (EMTOMO, 2015). The inversion algorithm is based upon the Occam regularization method (Sasaki, 1989, Sasaki, 2001) was described and applied in several studies (Santos et al., 2010, Triantafilis and Monteiro Santos, 2013, Triantafilis et al., 2013). With the inverse model, EM34 apparent conductivity ( $\sigma_a$ ) were inverting using a 1-D spatially constrained algorithm for quasi-3D conductivity imaging, then a map of spatial distribution of estimated electrical conductivity  $\sigma$  have been done would help to better understand in term of geology (structure, lithology,...) and hydrogeology (saline groundwater interface, ...).

The first campaign, studying the thickness and geometry of depositional systems, using intercoil spacing of 10 and 20 m, has been applied on 4 sectors in the NE of the Colmatage canal. This sector contains freshwater and is far from salt-freshwater limit as determined by electrical conductivity measured in piezometers. The second campaign have been developed around the salt intrusion zone described by previous studies (SAFEGE, 2004, SAFEGE, 2006). This campaign was dedicated to understand the current distribution of salt and brackish water in this aquifer.

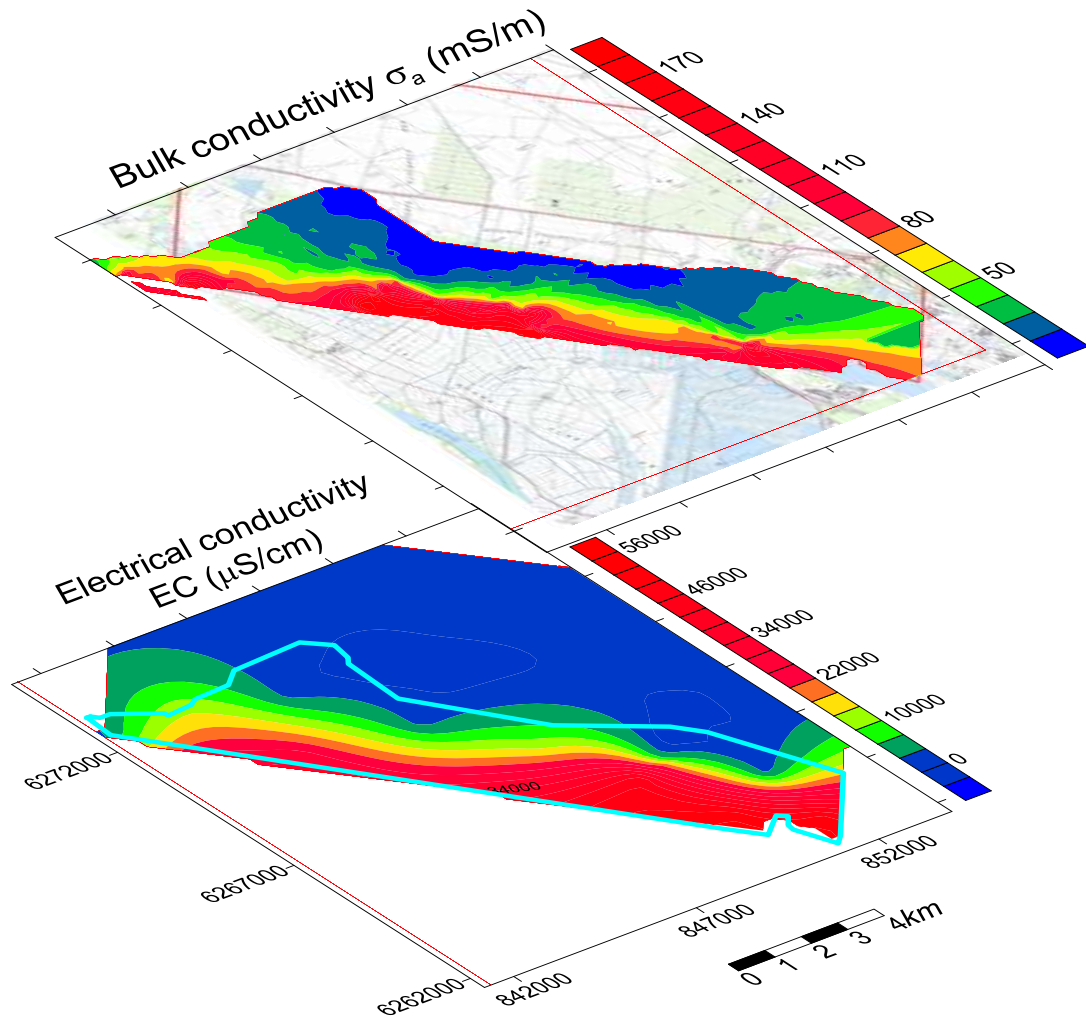


**Figure 41.** Spatial distribution of appaeent electrical conductivity  $\sigma_a$  (mS/m) with EM34-20m HDM (upper) and electrical conductivity  $EC_e$  ( $\mu\text{S}/\text{cm}$ )in groundwater at -10m depth from groundwater level in piezometers (lower), red and blue colors represent the conductive and resistive layers, respectively.

**Table 6.** EM-34 survey measurement statistics

Sensor	Readings	Mean+1std dev.	Std dev.	Min	Max
VDM-10m	435	77.38	64.83	7.13	201.30
HDM-10m	435	29.17	24.74	3.80	93.34
VDM-20m	774	58.99	38.30	10.50	198.07
HDM-20m	774	60.12	48.75	9.70	232.65
VDM-40m	30	62.32	13.65	49.00	112.60
HDM-40m	30	42.97	2.87	38.60	48.00

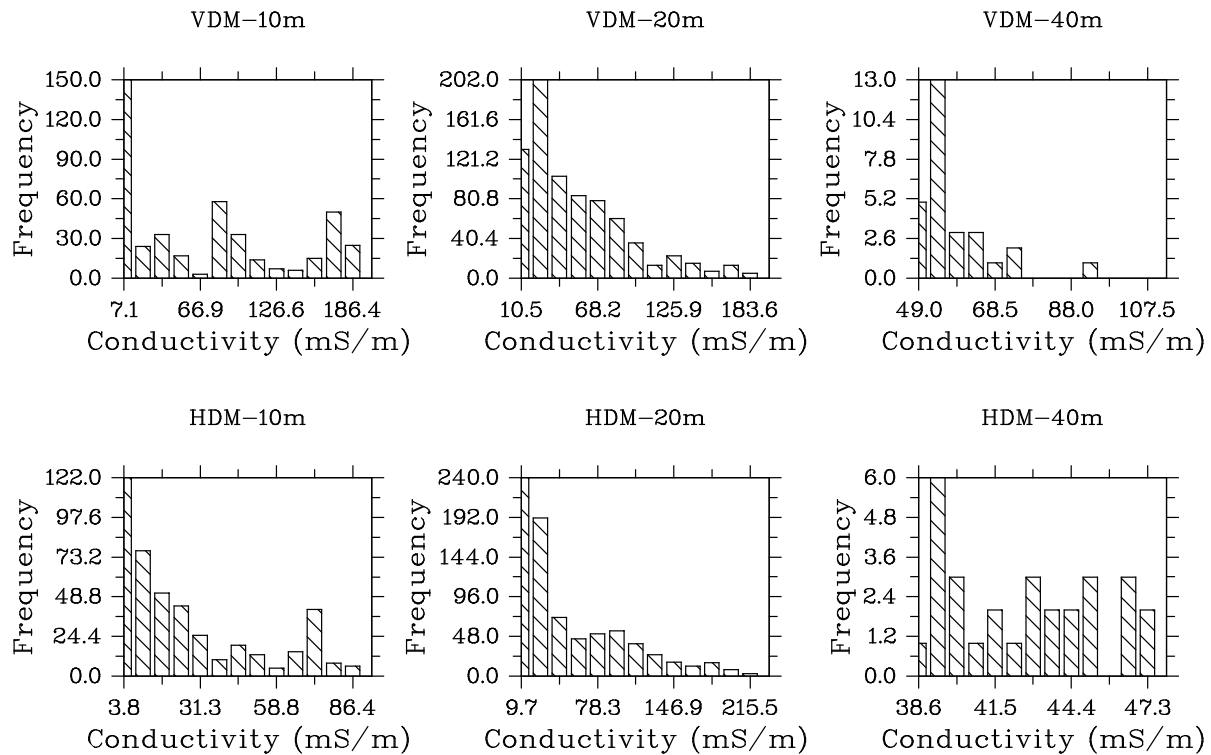


**Figure 42.** EM34 data statistic of all measurements .

To interpret the spatial distribution of electrical conductivity  $\sigma$  within these sectors, one campaign of electrical conductivity  $EC_e$  profiling in boreholes has been done at the same period of geophysical campaign (electrical conductivity logs for each piezometer are shown [Annex 3](#)). Two perpendicular sectors of  $EC_e$  have been investigated, one along the road N286 (with X4415, X13, X30, X31, X33, X34, X35) ([Figure 43.a](#)) and the other along the canal from Arles-Fos (X21, X17, X19, L1, L2, L3, X4415) ([Figure 44.a](#)). On both profiles, spatial distribution of  $EC_e$  is clear. Spatial maps of estimated  $\sigma$  from electromagnetic EM34 ([Figure 43.b](#) and [Figure 44.b](#)) were compared to the spatial maps of  $EC_e$ . The spatial, vertical distribution of  $EC_e$  measured in piezometers ([Figure 43.a](#)) shows that the saltwater comes from SW to NE. Saltwater (with  $EC_e > 2250$  mS/m) from -10 m in X4415, and from -14 m in X13 but in X33,  $EC_e$  at -20 m is only 2030 mS/m. The spatial distribution map of  $\sigma$  ([Figure 43.b](#)) shows a similar pattern with higher conductivity in the SW, and decrease to the NE. High value of electrical conductivity  $\sigma > 150$  mS/m is observed at about 10 m depth in X13 but disappears even at -20 m depth in X31.

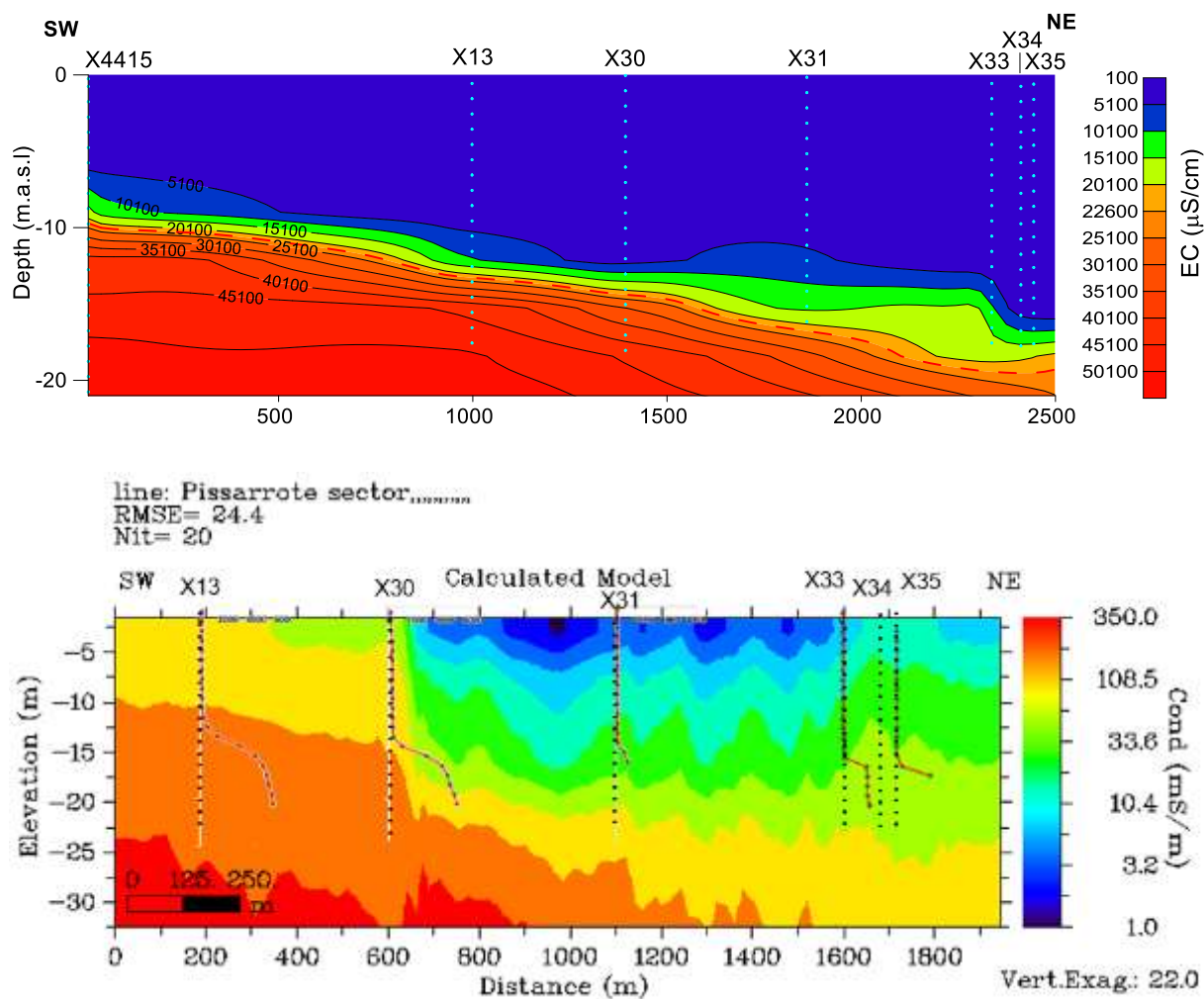


**Figure 43.** Spatial distribution of a. electrical conductivity water in piezometers (EC<sub>e</sub> - μS/cm) and b. estimated electrical conductivity from EM34 apparent electrical conductivity (σ<sub>a</sub> - mS/m) in sector EM9 (Pissarrote)

It is similar for the sector along the Arles-Fos Canal. A spatial distribution of  $\sigma$  was obtained from the apparent survey electricity with root mean square error (RMSE) of 28.0%. The 2-D estimated  $\sigma$  profile shows that the higher  $\sigma$  are distributed in SE and decrease to NW direction. From Figure 44.a the depth of saline groundwater with EC<sub>e</sub> > 2250 mS/m have been found at 14 m depth in L1 and are not present in X21 (at 18m). Comparing the pattern of two sectors, the saline groundwater zone from Figure 44 has the pattern of  $\sigma > 150$  mS/m and fresh water zone with  $\sigma$  between 5 and 40 mS/m. From the pattern of the distribution of the estimated electrical conductivity and electrical conductivity of water in piezometers from Figure 43 and Figure 44, the inverse models compared favorably with the electrical conductivity profiles obtained from piezometer measurements. It is obvious that the distribution of  $\sigma$  confirms the presence of saline groundwater.

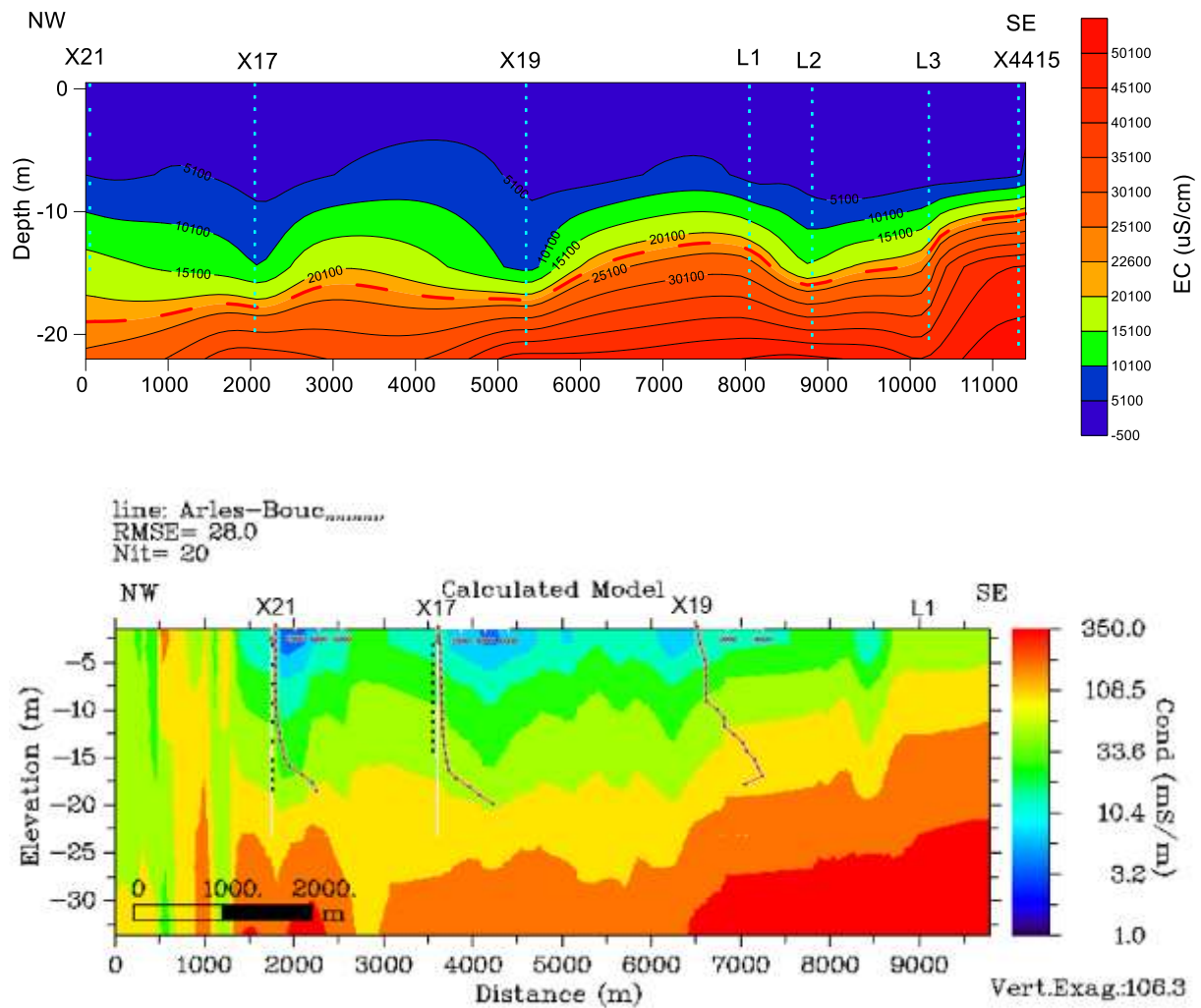
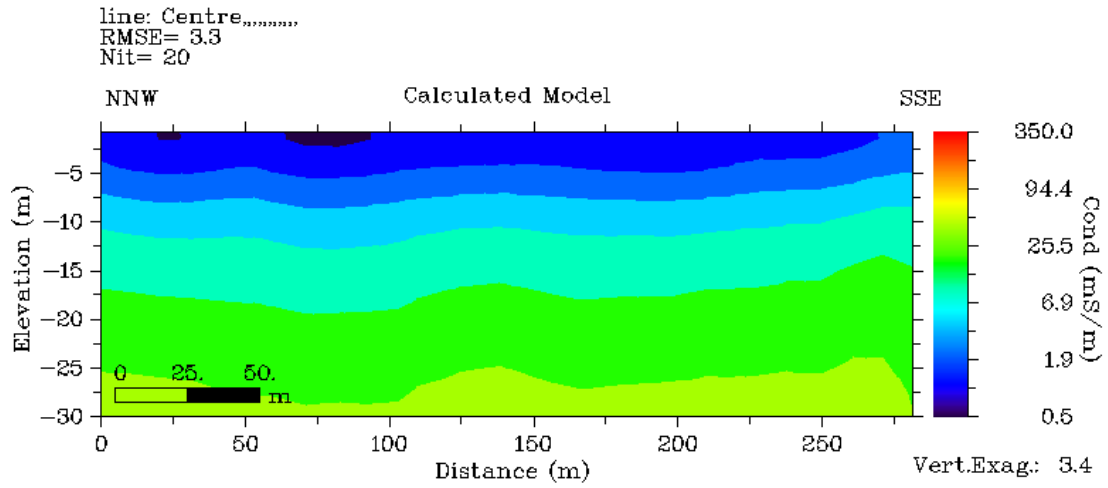
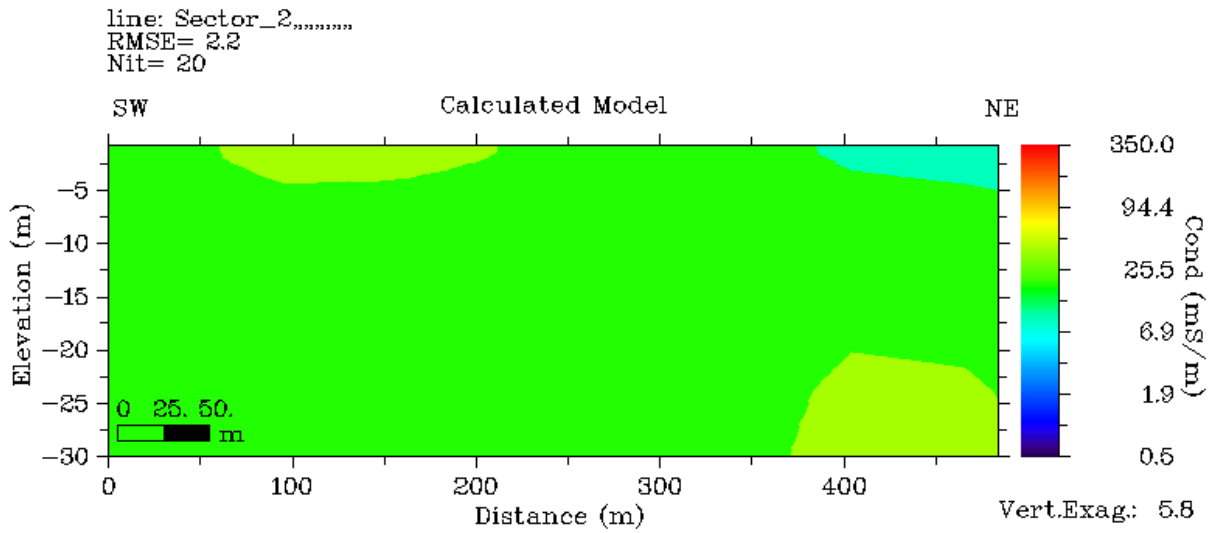


**Figure 44.** Spatial distribution of a. electrical conductivity water in piezometers ( $EC_e$  -  $\mu\text{S/cm}$ ) and b. estimated electrical conductivity from EM34 apparent electrical conductivity ( $\sigma_a$  -  $\text{mS/m}$ ) in sector EM12 along the canal from Arles-Fos

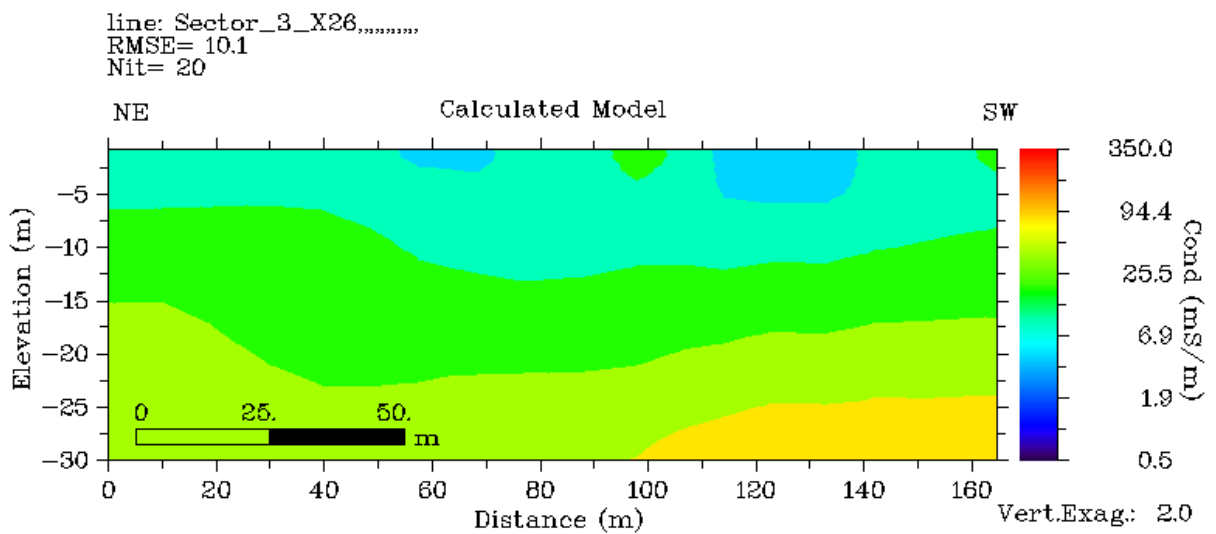
**Figure 45** shows the 2-D cross sections of  $\sigma$  along NNW-SSE direction (Figure 32) with EM1, EM2, EM3, EM4 in the NE of the Colmatage, EM5, EM6, EM7, EM8 in the Vigueirat reserve area, EM10 in Tonkin and EM11 along Colmatage canal in center of marsh area (location of EM sectors shown in Figure 32).



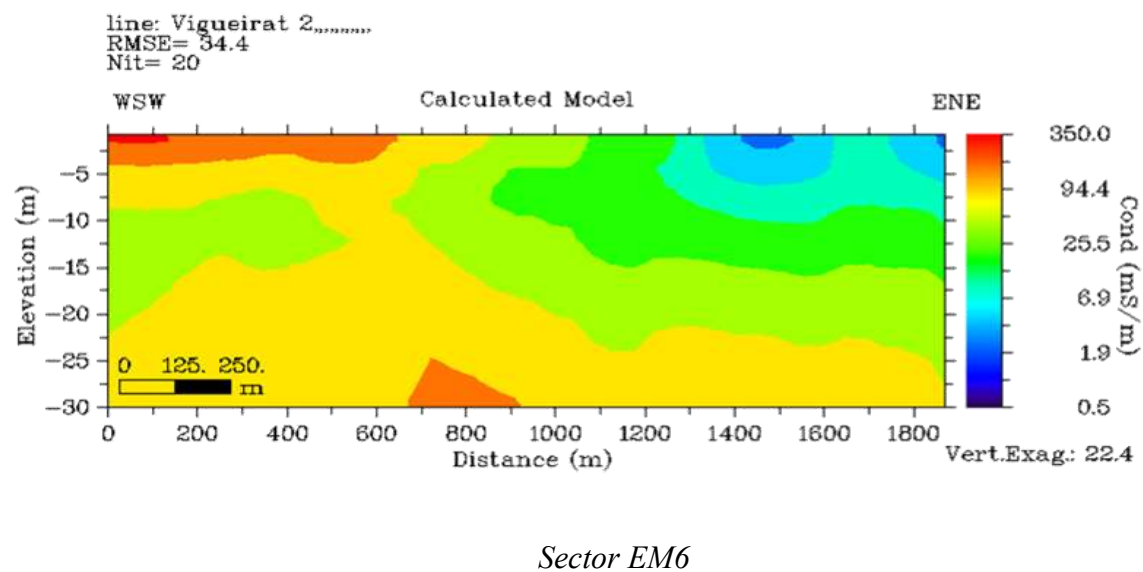
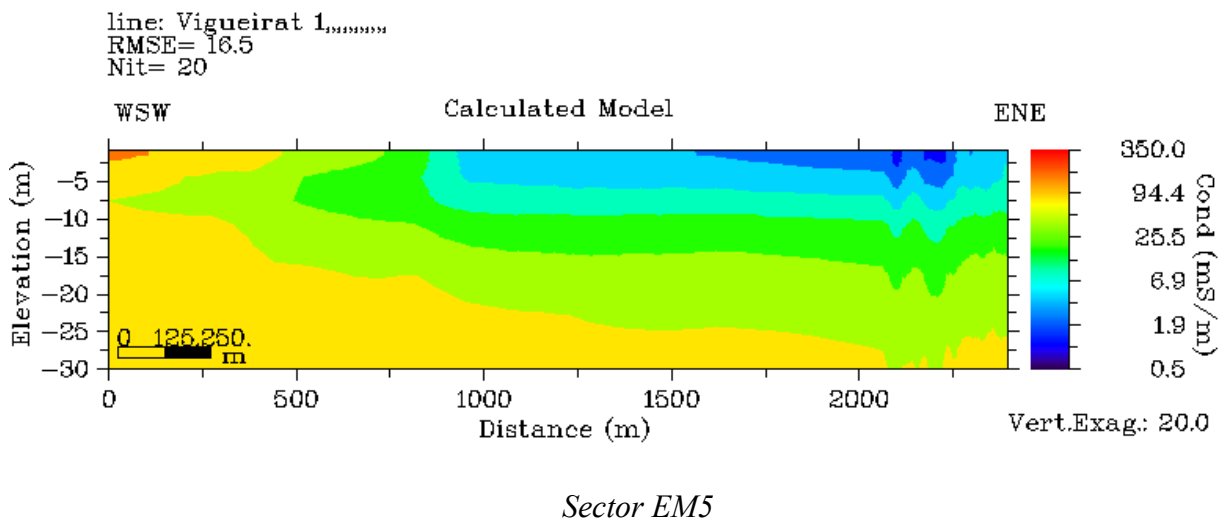
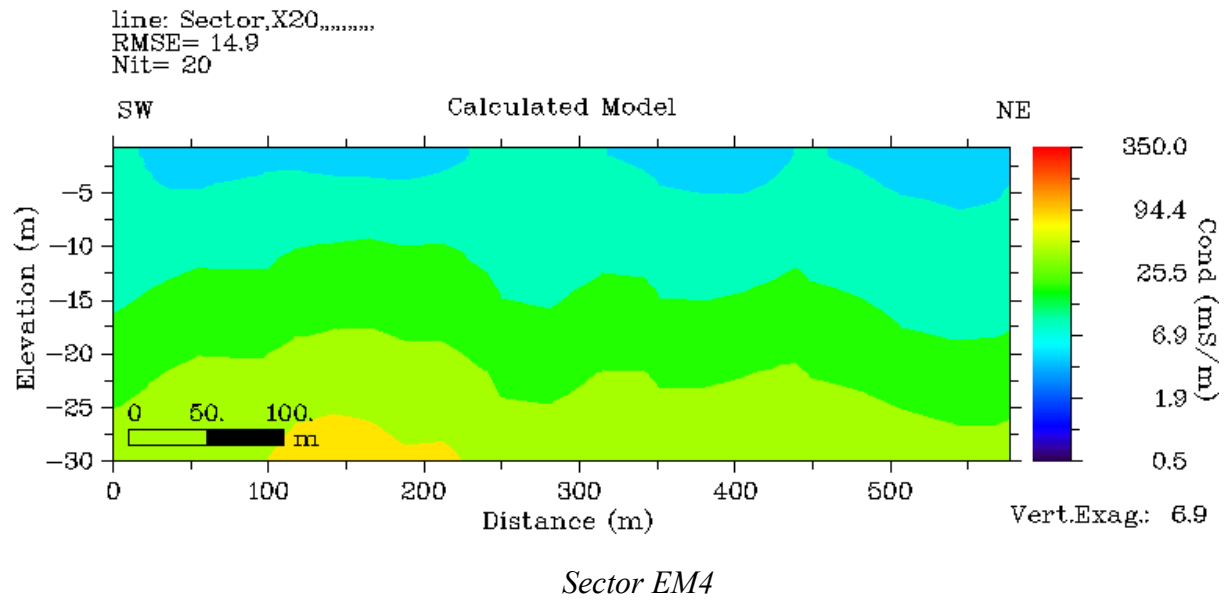
*Sector EM1*

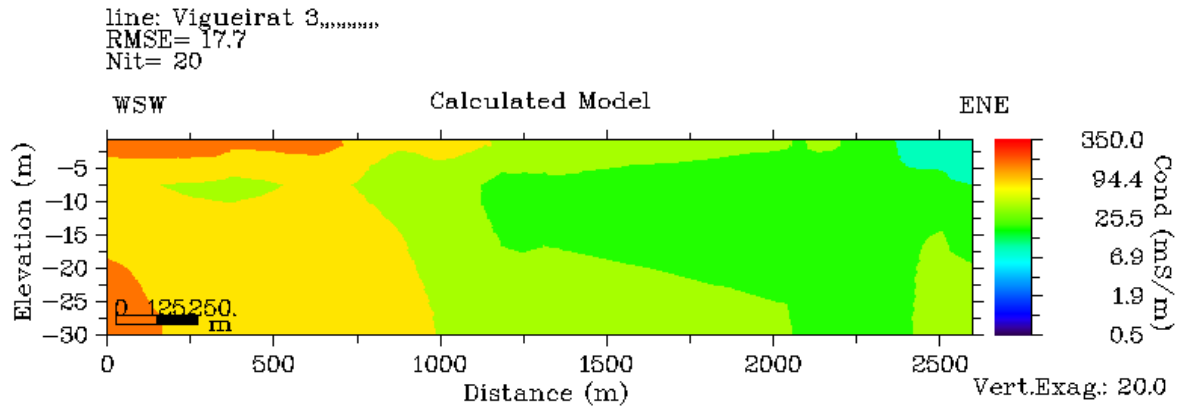


*Sector EM2*

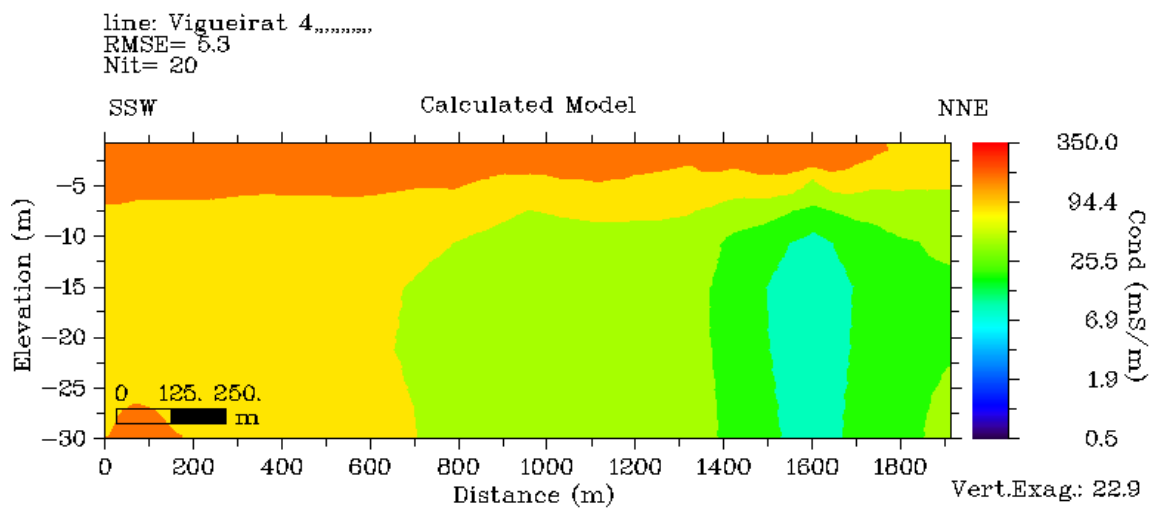


*Sector EM3*

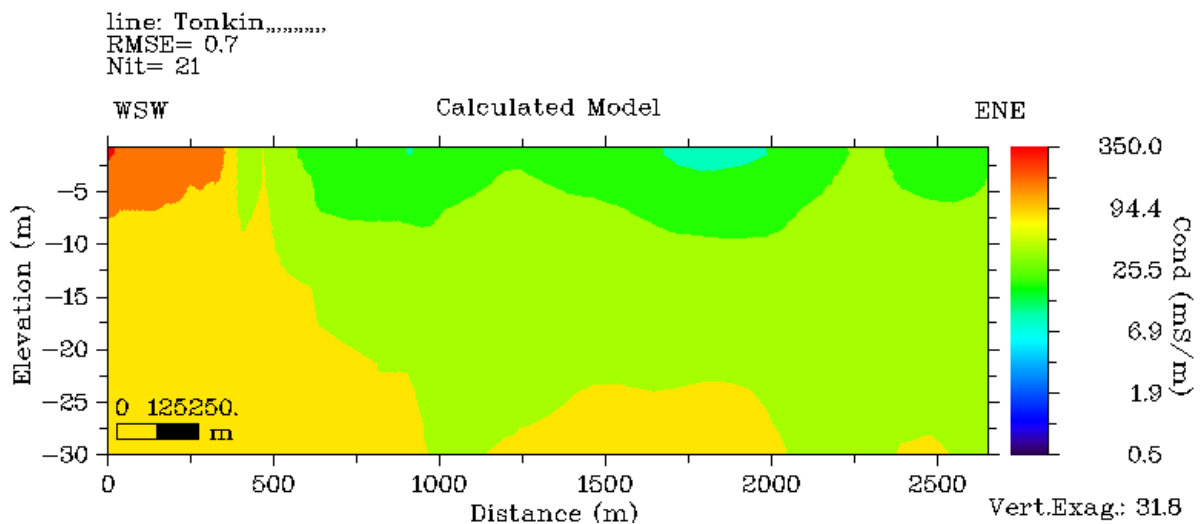




Sector EM7



Sector EM8



Sector EM10

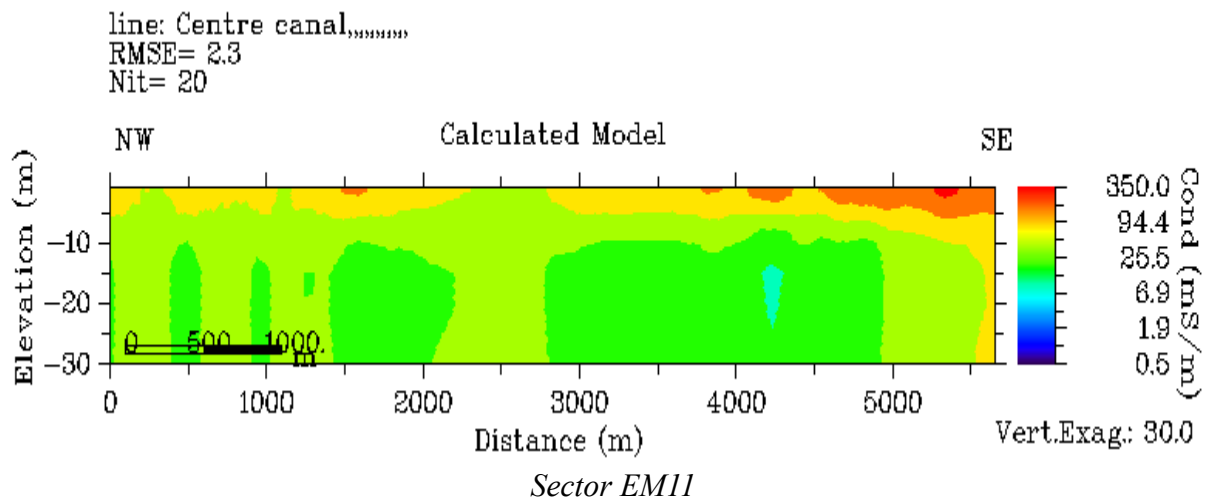


**Figure 45:** Plot of 2-D cross section of estimated electrical conductivity ( $\sigma$  - mS/m) from a joint inversion of EM34 apparent electrical conductivity ( $\sigma_a$  - mS/m) data using a 1-D laterally constrained algorithm for quasi-3-D conductivity imaging along 10 sectors (sectors 1-12, locations of sectors shown in Figure 32)

In sector 1, the small  $\sigma$  (less than 2 mS/m) have been found from top to about 4 m depth. One can distinguish the water table in the aquifer (water table in Pz21 is 3.15 m). In some sectors,  $\sigma$  of the top soil (few meters depth) is very high ( $\sigma > 150$  mS/m) and compares to the values of  $EC_e$  smaller than 20 mS/m (fresh water). These zones coincide with the clay layer described in piezometers XB, X19, L1 and XA (sectors 6, 7, 8 and 12). In sector Vigueirat 2 (sector 5, Figure 45), sector Tonkin (sector 12, Figure 45) and sector along the Colmatage Canal in center of the marsh (sector 10, Figure 45),  $\sigma$  of topsoil is high in some place ( $\sigma > 300$  mS/m) and coincide with brackish surface water ( $EC_e$  is up to 700 mS/m). The electrical conductivity is high in some places because: 1) water table is very low about 0.3 m to 0.7 m from the surface; 2) saltwater table is shallow (less than 10 m); 3) surface water is not connected to pond or canals and 4) effect of evapo-transpiration that concentrates salt in water. In comparison, the saturated sand and gravels layer with fresh water ( $EC_e < 200$  mS/m) is characterized by  $\sigma$  ranging between 5 and 40 mS/m (sectors 1, 3, 4 and 6, Figure 45).

In sector EM12 along the Arles to Fos canal, the value of RMSE is 28% and could be due to the low resolution of  $\sigma_a$  along this sector. The sector is too long (>10km), and data of EM34 is discontinue in some parts because of the security regulation of Vigueirat (cows and bulls grazing).

Despite these comparisons and validations, electrical conductivity  $\sigma$  appears to sign the presence of saltwater and the difference of lithology. Therefore, the spatial distribution of  $\sigma$

from quasi 3-D imaging have been done to validate and calibrate at difference depths the saltwater model (Figure 63 and Figure 64).

Figure 64 shows the spatial pattern of estimated electrical conductivity from EM34 data at difference depths. All distributions show a high conductivity zone in the southwestern part of the area. These conductive zone can potentially present saltwater intrusion. Coupled with 2-D cross sections (Figure 43, Figure 44 and Figure 45), interpretation for the different depth has been done. With the respect to soil type and conductivity, the depth of clay layer and the interface of salt-fresh water have been determined.

#### 4.1.2 Electrical Resistivity Tomography (ERT)

Three ERT profiles (SW-NE oriented) were measured. Profiles T1 (Pissarotte sector) and T2 (Tonkin sector) were located SW of area, perpendicularly to the saltwater-freshwater limit. T3 profile was done in the center of area to determine the geological features (Figure 32). Investigations were done with a multi-electrode ABEM Lund Imaging System, with inter-electrode spacing of 5m.

Inversion of the measured apparent resistivity  $\rho_a$  was carried out to estimate the real resistivity of the soil with the software package RES2DINV (v.3.5, Geotomo Software). The software constructs a resistivity model of the subsurface based on iterative smoothness-constrained least squares inversion (Loke and Barker, 1996).

##### 4.1.2.1 Saline intrusion mapping

Profile 1 is located perpendicular on the limit between saltwater and freshwater (SAFEGE, 2004, SAFEGE, 2006). It shows (Figure 46) a high contrast of electrical resistivity. Below 30 m depth, very low resistivity (a few ohm.m) are observed and probably interpreted as the substratum of clays and marl of Pliocene. Between 20-30 m depth, resistivity varies between 10 and 40 ohm.m that reflects salt and brackish water coming from SW to NE. At about 5 to 20 m depth, higher resistivity ( $> 40$  ohm.m) are observed, reflecting the aquifer of gravel with freshwater/brackish water. The shallow part of the profile (up to 5 m) shows low resistivity corresponding to superficial Holocene sediments made of sandy clay. Low resistivity may also result from the increase of salt content due to evaporation (transpiration). High resistivity zone in the shallow part is due to the channel fresh water.

Profile 2 was orientated perpendicular to saltwater limit to characterize the distribution of saltwater and clay. Electrode e spacing was 5 m giving a total length of 320 m. The obtained RMS was 11%. This profile shows resistivity lower than 20 ohm.m in the first 7 m depth that can be attributed to clay or shallow saltwater. As for sector 1, below 25-30 m depth, very low resistivity (few ohm.m) is observed corresponding to the substratum of clays and marl of

Pliocene. Between 7 and 25 m depth, resistivity varies from 20 to more than 100 ohm.m. This resistive, heterogeneous layer corresponds to sand and gravel sediments with fresh or brackish water.

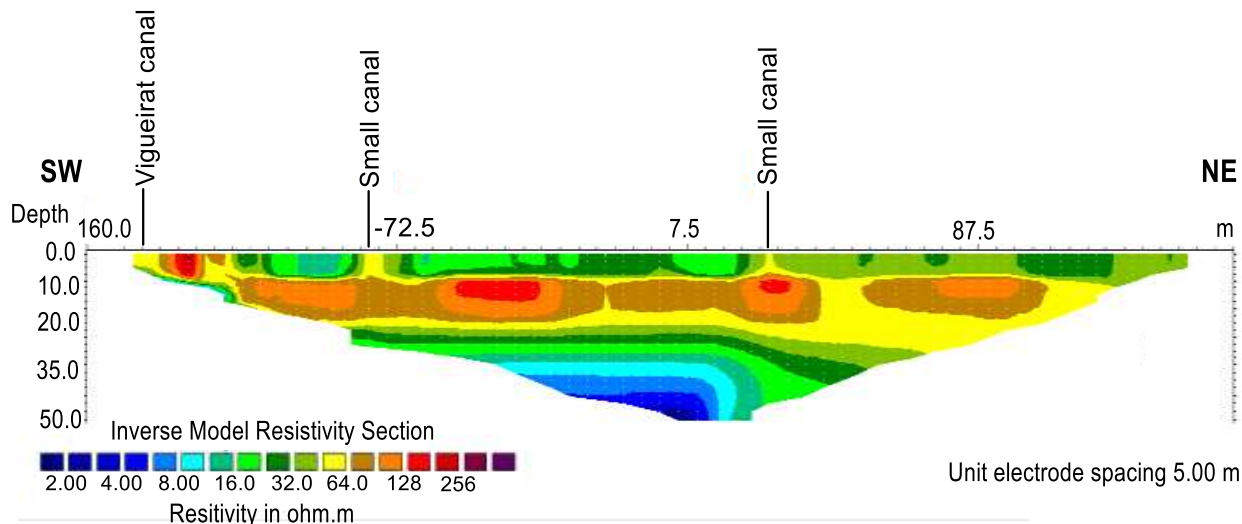


Figure 46. 2-D electrical resistivity tomography on section 1 (Figure 32)

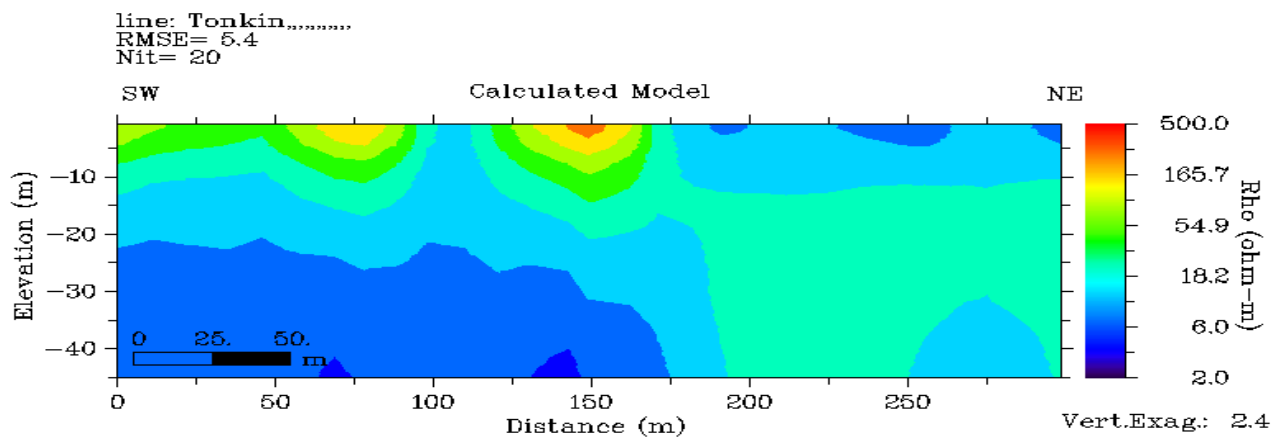
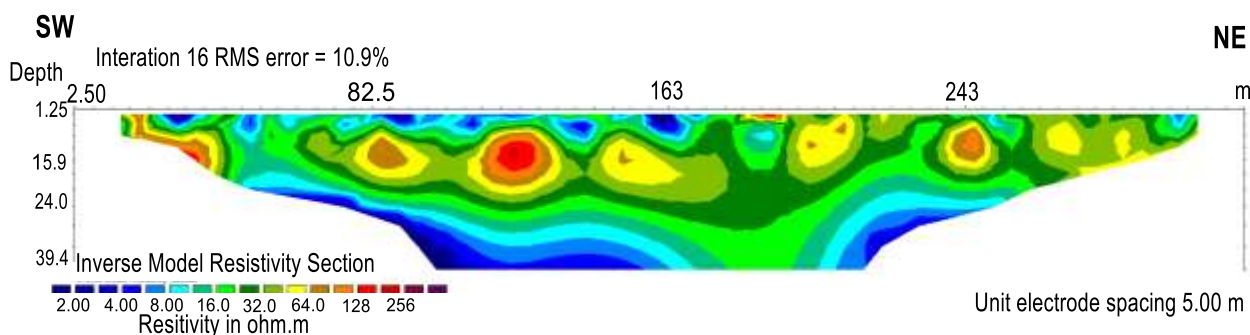
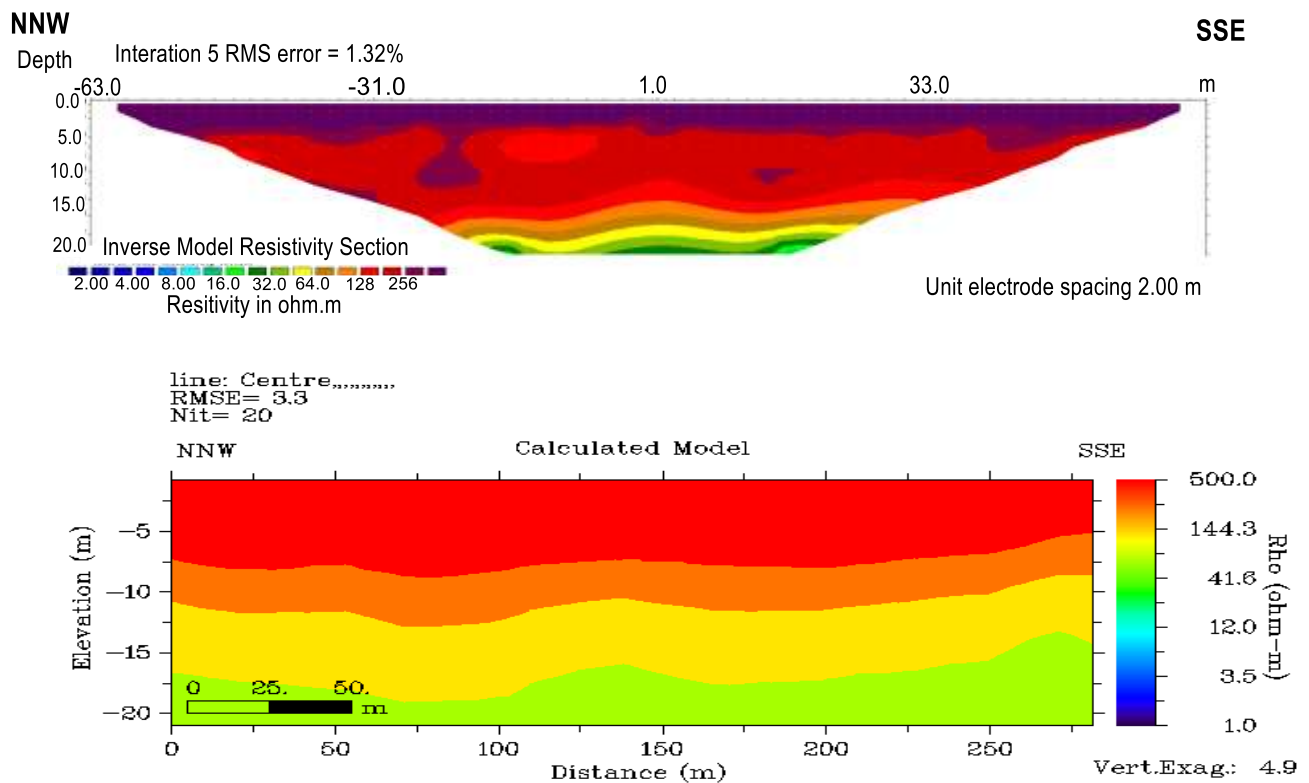


Figure 47. 2-D electrical resistivity tomography (ERT) (upper) and electromagnetic (EM34) (lower) in the sector Tonkin.

#### 4.1.2.2 Piezometric heads and aquifer geometry

Profile 3 was also oriented SW-NE and located in the center of the area. Electrodes were spaced 2m, giving a total length of 128 m. RMS is 10.9%. Profile (Figure 47.a) shows high resistivity on the top (up to 4 m), with resistivity higher than 300 ohm.m maybe related to the sandy, unsaturated zone (water level in Pz21 nearby the profile is 3.15 m). This high resistivity of the top coincides with the one ( $> 400$  ohm.m) observed into EM34 investigations (Figure 47.b). Between 5 m and 15 m, the intermediate resistivity, from 100 to 250 ohm.m, could correspond to the saturated fresh water zone. ERT results are comparable with EM survey. Deeper than 15 m, a small resistivity (varying from 15 to 100 ohm.m) may correspond to clay-rich sediments or saltwater. Compared to electrical conductivity of pore water measured in Pz21, values of ECe in groundwater until 19m are stable and about 65-80mS/m (fresh water). Moreover, according to geological description in Pz21, below 15.4m depth, the lithology changes from gravels, pebbles and sand of Pleistocene to marl, gravel and clay of Pliocene.



**Figure 48.** 2-D electrical resistivity tomography (ERT) (upper) and electromagnetic (EM34) (below) of sector 3 in center research area.

Interpretations of results can be summarized as follows: (i) the resistivity of sandy gravelly aquifer is strongly governed by the salinity of water; (ii) the resistivity of the top of the profiles is influenced by the clay content salt concentration due to evaporation (transpiration).

### 4.1.2.3 Aquifer porosity

The porosity was estimated using Archie's law. The relationship between bulk resistivity of a saturated porous medium  $\rho_r$  (ohm.m) and its porosity  $\phi$  and resistivity of pore water  $\rho_w$  (Ohm.m) is expressed by Archie's equation (Archie, 1942)

$$\rho_r = \rho_w \frac{a}{\phi^m} = F \rho_w \quad (59)$$

And similar for the bulk electrical conductivity ( $\sigma$ ) and pore water conductivity ( $\sigma_w$ )

$$\sigma_r = \sigma_w \frac{\phi^m}{a} = \frac{\sigma_w}{F} \quad (60)$$

where  $F = a/\phi^n$  (Humble formula, in (Winsauer et al., 1952) is an intrinsic parameter representing the micro-geometry of the material;  $m$  and  $a$  are dimensionless material-dependent empirical factors;  $m$  is known as the cementation index and  $a$  is the coefficient of pore tortuosity. For unconsolidated sandstone formation, parameters  $a$  and  $m$  can be set to 0.81 and 2 respectively (Winsauer et al., 1952), then  $F=0.81 \phi^2$ .

Figure 49 compares the vertical electrical conductivity profile of borehole XD and the ERT profile 1 near to this piezometer.

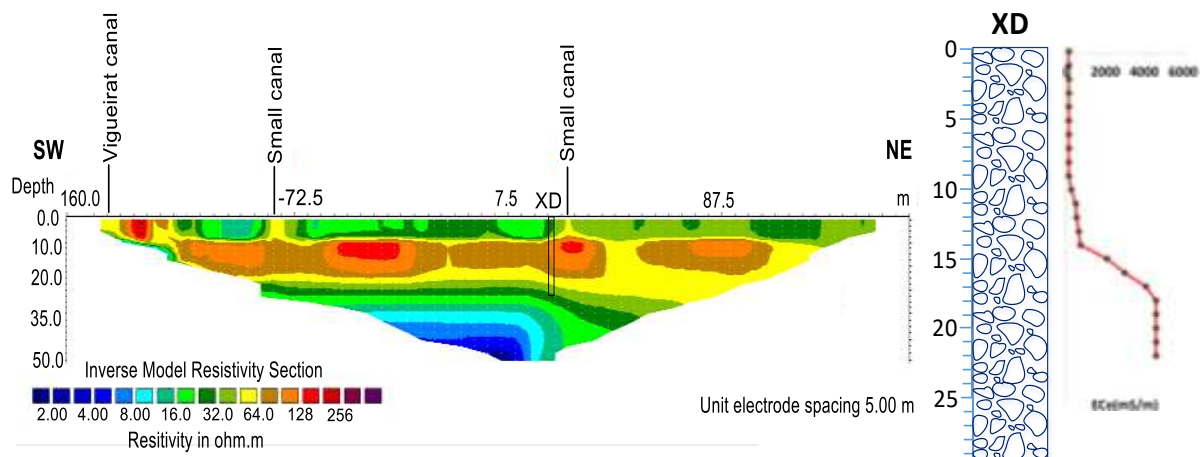


**Figure 49.** (left) ERT profile (with location of XD borehole) and (right) vertical distribution of electrical conductivity in pore water of XD

The porosity calculated using Archie's law varies from 4% to more than 30% on top, with an average of 11.5%. This value is comparable to the one related in other research on Crau aquifer (Olioso et al., 2013). The very high porosity between 0 and 8 m depth correspond to high content of clay constituting the Holocene sediment. The porosity values at some depth are quite small (about 4-5%) that can be explained conglomerate (cemented sand and gravels).

**Table 7.** Porosity values estimated by Archie's law with  $a=0.81$  and  $m=2$ . Example for piezometer XD.

ID	Depth	Bulk electrical resistivity (ohm.m)	Water conductivity (mS/m)	Porosity (%)
1	0-6	60	102.4	36.3
2	6-8	100	107.8	27.4
3	8-10	120	233	17.0
4	10-12	120	508	11.5
5	12-14	120	694	9.9
6	14-16	120	2980	4.8
7	16-18	120	4600	3.8
8	18-20	100	4600	4.2
9	20-22	100	4600	4.2
10	22-24	50	4600	5.9
11	24-28	50	4600	5.9
12	28-30	35	4600	7.1

#### 4.1.3 Partial conclusions

Resistivity distributions from EM and ERT methods show four different layers. i) A superficial unsaturated layer made of coarse sand and gravel (thickness of about 6 m) in the northeastern part of marsh area (center of research area) with very low  $\sigma < 2$  mS/m (sector 1, Figure 45.a); ii) a saturated coarse sand and gravel layer with fresh water where  $\sigma$  ranges from 2 to 30 mS/m (sector 1-5, Figure 45); iii) a superficial fine sand and clay layer found in marsh area where  $\sigma$  varies from 100 to more than 300 mS/m (sector 5-12, Figure 45) and iv) a conductive ( $\sigma > 80$ mS/m) coarse sand and gravel layer saturated by brackish or saltwater observed between 3-7 and 30 m depth in sector Pissarotte and between 15-20 and 30 m depth in Vigueirat area (sector 5, 6, 7, 8 and 10, Figure 45, Figure 43 and Figure 44).

The electrical conductivity of aquifer increases with depth and towards SW due to saltwater. The most conductive area is found in sector Pissarotte (Figure 43) and in sector along the Arles-Fos canal (Figure 44) with  $\sigma > 150$  mS/m at a depth less than 10 m. This characteristic is observed for all other sectors in the marsh area (Figure 45).

The variation of electrical conductivity also corresponds to the variation of lithology. The thickness of superficial fine sand and clay layer increases to SW from 0 m in center to 5-7 m along the Arles-Fos canal. On the other hand, water level decreases to SW from 2-3 m in the NE of marsh area to 0.3-0.7 m SW of marsh. Therefore the thickness of high conductive (low resistivity) superficial layer also increases to SW due to: i) influence of clay content and ii) increase of dissolved salt due to evaporation.

## 4.2 Isotopic surveys

*Using radon-222 to study coastal groundwater/surface-water interaction in the Crau coastal aquifer (southeastern France)*

**Adriano Mayer, Bach Thao Nguyen & Olivier Banton**

**Hydrogeology Journal**  
Official Journal of the International Association of Hydrogeologists

ISSN 1431-2174

Hydrogeol J  
DOI 10.1007/s10040-016-1424-9



 Springer

Author's personal copy

Hydrogeol J  
DOI 10.1007/s10040-016-1424-9

PAPER

## Using radon-222 to study coastal groundwater/surface-water interaction in the Crau coastal aquifer (southeastern France)

Adriano Mayer<sup>1</sup> · Bach Thao Nguyen<sup>1</sup> · Olivier Banton<sup>1</sup>Received: 31 October 2015 / Accepted: 21 April 2016  
© Springer-Verlag Berlin Heidelberg 2016

**Abstract** Radon has been used to determine groundwater velocity and groundwater discharge into wetlands at the southern downstream boundary of the Crau aquifer, southeastern France. This aquifer constitutes an important high-quality freshwater resource exploited for agriculture, industry and human consumption. An increase in salinity occurs close to the sea, highlighting the need to investigate the water balance and groundwater behavior. Darcy velocity was estimated using radon activities in well waters according to the Hamada “single-well method” (involving comparison with radon in groundwater in the aquifer itself). Measurements done at three depths (7, 15 and 21 m) provided velocity ranging from a few mm/day to more than 20 cm/day, with highest velocities observed at the 15-m depth. Resulting hydraulic conductivities agree with the known geology. Waters showing high radon activity and high salinity were found near the presumed shoreline at 3,000 years BP, highlighting the presence of ancient saltwater. Radon activity has also been measured in canals, rivers and ponds, to trace groundwater discharges and evaluate water balance. A model of the radon spatial evolution explains the observed radon activities. Groundwater discharge to surface water is low in pond waters (4 % of total inputs) but significant in canals (55 l/m<sup>2</sup>/day).

**Keywords** Radon · Salinization · Salt-water/fresh-water relations · France

✉ Adriano Mayer  
adriano.mayer@univ-avignon.fr

<sup>1</sup> Department of Hydrogeology - UMR 1114 EMMAH UAPV INRA UAPV, University of Avignon, Campus Jean-Henri Fabre, 301 rue Baruch de Spinoza, BP 21239, 84916 Avignon Cedex 9, France

### Introduction

Shi and Singh (2003) estimated that by 2050, 72 % of the world population would live in coastal zones with a rapidly increasing demand in water supply. In this perspective, coastal groundwater is considered today as a strategic resource for future urban development, agriculture and industry. Coastal groundwater resources have been therefore the focus of a large number of studies, including characterization of resources, modeling, vulnerability assessment and prediction (Werner et al. 2013). In many cases, seawater intrusion is the main process responsible for degradation of groundwater quality in coastal zones. A good example of an aquifer vulnerable to salinization is the Crau aquifer, close to the Mediterranean Sea in southern France (Fig. 1). Today, this aquifer provides a high quality water for about 300,000 inhabitants, 57,036 ha of farming land (INRA 2013), about 5,000 ha of protected natural area (Coussouls National Reserve) and several industrial complexes (industrial harbor of Marseille). Groundwater induces diffuse springs all along the Viguierat wetland/marsh (Fig. 1), which is a fragile humid ecosystem (Ramsar and Natura 2000 site). The spring water is drained to canals (Viguierat, Vergiere and Centre-Crau canals, Fig. 1) that enter the wetland area and contribute to the regulation of its salinity and water level.

Groundwater salinity in the Crau aquifer has been constantly monitored since 1984. Although an increase in salinity has been observed close to the Viguierat wetland system, the salt-water front seems relatively stable over time. This nearly steady-state condition could however change in the near future due to the increasing exploitation rate of this water resource, sea-level rise and change in groundwater recharge, as discussed by Oliso et al. (2013), and also in response to the general global-change scenario as discussed by Holman et al. (2012). Quantification of groundwater flows in this setting is

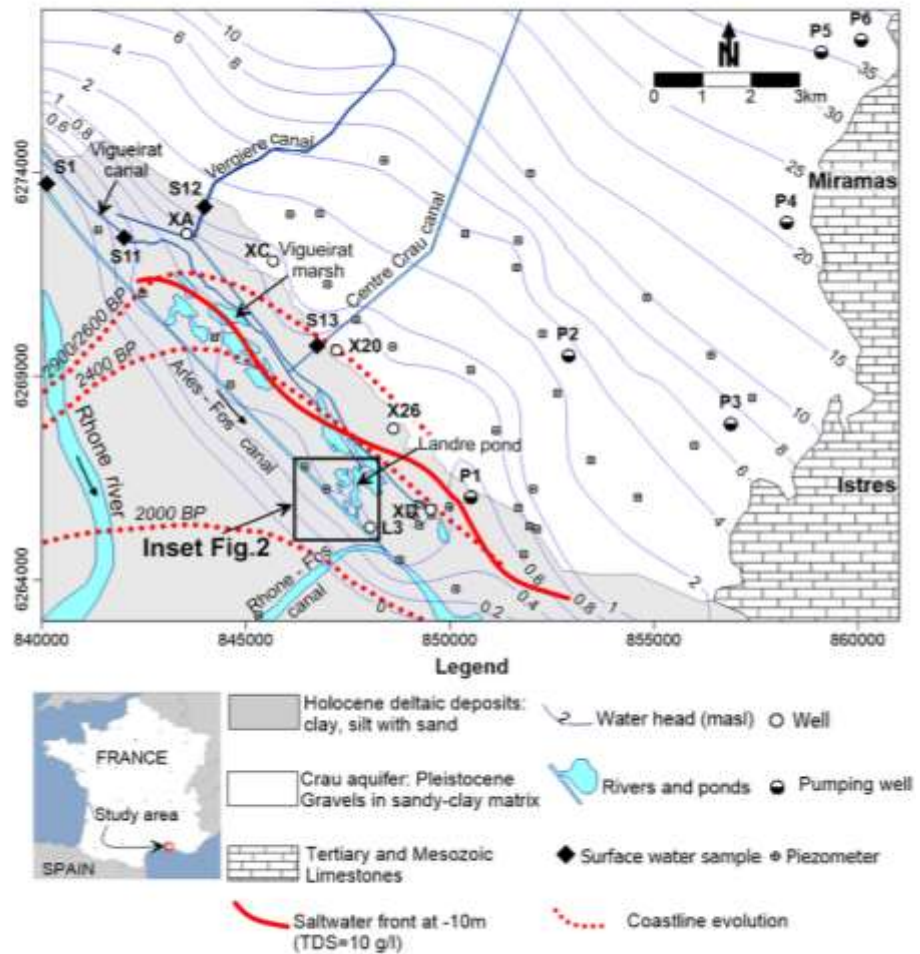
Published online: 11 May 2016

Springer

Author's personal copy

Hydrogeol J

**Fig. 1** Geological sketch map of the south-west termination of the Crau aquifer. Water-table contour lines (fine black lines) were obtained from piezometric surveys done during this study. The limit of the saltwater front (thick black line) was obtained from electrical conductivity logs. Evolution of past coastline (dotted lines) are redrawn after Vella et al. (2005). Positions of surface-water samples S7–S9 (in the inset) are shown in Fig. 2



therefore an important step toward the management of groundwater resource, i.e. its survey, control and optimization.

In this study, radon activity in groundwater was used to assess groundwater flow rates, hydraulic conductivities and groundwater-to-surface-water fluxes downstream of the Crau aquifer. Radon ( $^{222}\text{Rn}$ ) is a radioactive gas produced by the decay of radium ( $^{226}\text{Ra}$ ). In groundwater, radon activity originates essentially from  $^{226}\text{Ra}$  adsorbed on mineral surfaces in the aquifer with little contribution from dissolved  $^{226}\text{Ra}$ . Natural radon is a good groundwater tracer because of its inert chemical behavior, its elevated concentrations in groundwater and its “lack of memory” after a few days (half-life=3.824 days). Several recent studies also used radon activity surveys in surface water to localize and quantify groundwater discharges into rivers, lakes, lagoons and the sea (e.g. Dimova et al. 2013; Rodellas et al. 2012; Stieglitz et al. 2013). Radon may also be used to estimate groundwater velocity by comparing radon activity in well waters and in groundwater found in the aquifer, according to the “single-well test” (Hamada 2000; Schubert et al. 2011). Aquifer hydraulic

conductivities were calculated using the radon-determined groundwater velocities and the observed hydraulic gradients.

### Study area

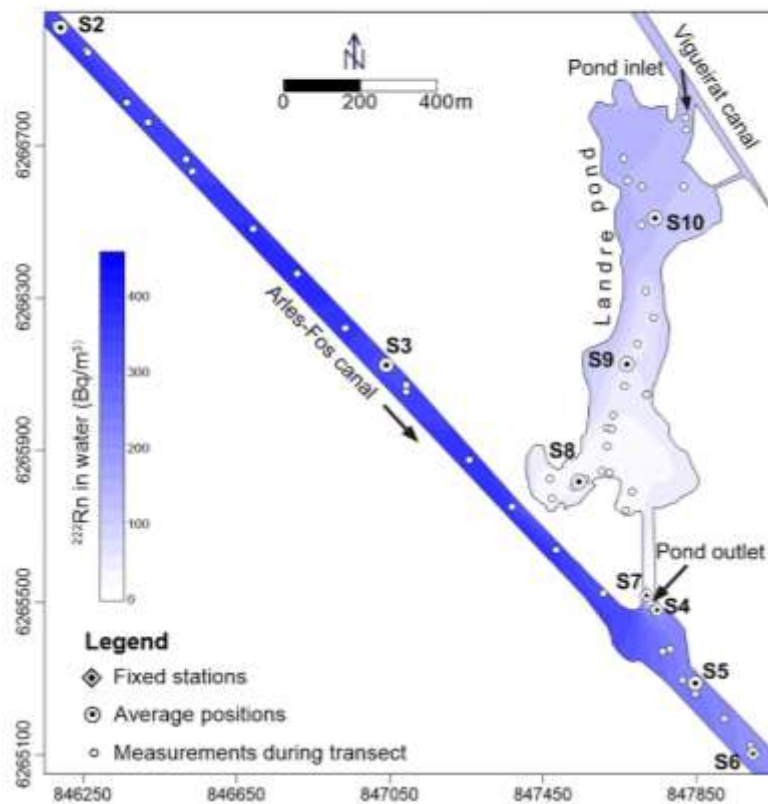
The study area is the downstream, coastal part of the Crau aquifer (southeastern France, Fig. 1), located to the east of the Rhône River delta (Camargue National Park). The Crau aquifer corresponds to the 600 km<sup>2</sup> paleo-delta of the Durance River, extending between the cities of Arles, Salon-de-Provence and Fos-sur-mer (Boyer et al. 2005; De Montety et al. 2008; Molliex et al. 2013). This study focused in particular on the SW downstream part of this aquifer, on an area of about 140 km<sup>2</sup> (Fig. 1) where the aquifer is partially affected by saltwater intrusion.

The aquifer is made of Quaternary coarse-grain deposits lying on a Pliocene marl substratum (Vella et al. 2005). The depositional age of the sediments varies between 2.0 and 0.6 million years (Ma) in the western side (ancient Crau), between

Author's personal copy

Hydrogeol J

**Fig. 2** Enlarged inset of Fig. 1. Activity of radon measured in surface water in the Arles-Fos canal and in Landre Pond during navigation. Fixed stations S1–S10 are radon measurement points with the boat maintained in a stable location (counting time of 45 min). Average positions are the centroids of several consecutive points of continuous radon measurement done during a boat transect. White dots represent positions reached during transects and 15-min integrated measurements. Average radon activities are reported in Table 1



0.6 and 0.1 Ma in the eastern area (recent Crau), and between 100 and 10 ka in the north-east sector (town of Miramas).

The deposits are mainly composed of gravels and pebbles from the Alps, having variable lithology, with dominant contributions of magmatic rocks (granites). Locally these sediments are partially cemented (conglomerates) or associated to a matrix of finer materials (silty sand). The thickness of the deposit is variable, from a few meters to 50 m in river paleo-channels (Roure et al. 2004). In the studied sector, the depositional surfaces have a slight slope to the southwest, which is also the general trend of groundwater flow. Due to the alluvial placer dynamic, the hydraulic conductivity ( $K$ ) is very variable. Estimates of  $K$  range between  $4.0 \cdot 10^{-5}$  and  $1.6 \cdot 10^{-2}$  m/s (BRGM 1995) and between  $1 \cdot 10^{-5}$  and  $8 \cdot 10^{-2}$  m/s (INRA 2013). Resulting transmissivity generally varies between  $5 \cdot 10^{-3}$  and  $5 \cdot 10^{-1}$   $\text{m}^2/\text{s}$ .

The Crau aquifer is commonly unconfined, but becomes semi-confined to confined in the marsh area of Vigueirat and Landre ponds (Fig. 1), due to the presence of semi-pervious material (Rhône river sediments and lacustrine deposits). Thickness of this material varies from 0 to 7 m and its hydraulic conductivity ( $K$ ) is between  $3.7 \cdot 10^{-5}$  and  $8.7 \cdot 10^{-3}$  m/s (INRA 2013). The specific yield of the aquifer, obtained from pumping tests, is in

the range of 0.01–0.18, attesting to the unconfined to semi-confined (leaky) behavior of the aquifer.

The hydraulic head is about 7.5–8.0 m above sea level (a.s.l.) in the north-eastern area and decreases to the west with a mean hydraulic gradient of 2–3 ‰.

The aquifer is recharged by rainfall and irrigation water. About 15,000 ha of meadow are irrigated with water from the Durance River through a dense network of channels, while about 5,000 ha of orchards are irrigated using local groundwater. Irrigation is estimated to contribute 50–80 % of the total recharge. Rainfall mainly occurs during December and January while irrigation mainly occurs during summer. Groundwater discharges into the ponds of the Vigueirat Natural Reserve and likely into the Rhône River. The aquifer is subject to intensive water withdrawal that reaches about 56,600  $\text{m}^3/\text{day}$ . Part of this exploitation is used for irrigation and partially returns into the aquifer.

The study area is bordered by the Arles-Fos canal that is supplied by freshwater from the Rhône River and constitutes a stable boundary condition. Groundwater locally presents significant salinity that may have different origins. One of them is the digging of the industrial harbour of Fos-Marseille, during which the Rhône and Crau deposits were removed, causing the direct contact of the fresh groundwater with seawater. Another source of salinity is the important evaporation

occurring at the Vigueirat-Landre ponds/marshes, which increases the salt content of the subsurface water. Finally, a salt-water origin may be the ancient shoreline that was north of the Vigueirat ponds 2,000 years ago (Fig. 1).

## Methods

Radon activity was measured in water using RAD7 radon monitors (DurrIDGE Co. Inc.) and RAD H<sub>2</sub>O and a RAD-AQUA water exchanger. For surface waters (canals and ponds) that have typically low radon activities, the sensitivity of the system was increased using two parallel RAD7 monitors connected in closed loop with the water-gas exchanger RAD-AQUA, as in other studies (Dulaiova et al. 2005). The water was pumped at a flow rate of 4.5 l/min and injected into the water-gas exchanger. Radon activity in the air-loop between the gas-exchanger and the two RAD7 monitors reaches equilibrium with radon dissolved in water after an equilibration time (Dulaiova et al. 2005; Dimova et al. 2009). For the

continuous radon survey (gray scale in Fig. 2), since the radon activities are low (Landre Pond, 11–111 Bq/m<sup>3</sup>), the measured activity approached (within the error  $2\sigma = 16\text{--}50\%$ ) the final equilibrium value after 15 min counting-time. For the stationary measurement points reported in Fig. 2 and Table 1, 45-min measurements were integrated in fixed positions to obtain more precise results and closer to the final equilibrium value. The radon activity of water is then calculated knowing the radon activity in the air-loop and the radon partition coefficient (Ostwald coefficient), which depends on temperature and salinity (Schubert et al. 2011). Radon in the air loop is determined from decay of daughter isotope <sup>218</sup>Po (polonium-218). All devices were installed on a small boat equipped with a global positioning system (GPS) and an electrical conductivity (EC) and temperature data logger. The system allows continuous measurements in a fixed position or during navigation.

For groundwater (observation wells and pumping wells) that has typically much higher radon activity, 2.5 l of water samples were collected and analyzed in the laboratory with the

**Table 1** Radon activities in surface water in the Crau area. *X* and *Y* are coordinates according to Lambert 93 projection

Station	Location	<i>X</i>	<i>Y</i>	Date in 2014	EC (μS/cm)	<i>T</i> (°C)	<sup>222</sup> Rn activity (Bq/m <sup>3</sup> )	± (2σ)
<b>Arles - Fos canal</b>								
S1	st. Mas Thibert	839,760	627,435	01/09	659	21.5	415	39
				24/09	695	19.3	–	–
S2	av. Ligagneau	843,154	626,714	24/03	871	13.6	312	47
S3	av. Ligagneau - Galejon	847,281	626,585	24/03	855	13.7	349	24
S4	st. Galejon (Landre outlet)	847,710	626,552	24/03	810	13.4	238	25
S5	av. Galejon - Le Relais	847,886	626,530	24/03	829	13.5	253	42
S6	st. Le Relais	847,970	626,512	24/03	829	13.5	203	12
				01/09	683	21	178	20
				23/09	660	19.5	231	23
<b>Landre Pond</b>								
S7	st. Outlet of Landre Pond (no outflow)	847,744	626,558	01/09	615	20.3	–	–
				23/09	635	18.2	11	5
				23/09	631	18.1	13	7
S8	av. Southern Landre	847,631	626,573	25/03	911	12.2	40	12
S9	av. Central Landre	847,830	626,605	25/03	791	12.4	78	14
S10	av. Northern Landre	847,786	626,661	25/03	788	12.7	111	17
<b>Canals entering the Landre Pond</b>								
S11	st. Vigueirat canal	842,040	627,263	23/09	650	19.3	172	26
S12	st. Vergiere canal	843,690	627,309	23/09	700	17.1	495	36
				06/11	752	12.6	770	58
S13	st. Centre Crau canal	846,650	626,985	23/09	570	17.4	82	19
				06/11	759	12.1	156	28

st. radon measurement points with the boat maintained in a stable location. av. average radon activities during continuous radon measurement done on a boat transect. Coordinates are centroids of several consecutive points during navigation

Author's personal copy

Hydrogeol J

RAD7–RAD H<sub>2</sub>O system. Groundwater was sampled from six municipal pumping wells (Fig. 1; Table 2) and six observation wells located near the ponds (Table 3). Four of these wells (XA, XC, X20, X26) are situated upstream of the saltwater front and two (XD and L3) downstream of it. The saltwater front is here defined as the position of groundwater having EC higher than 22 mS/cm (15 g/l) at –10 m (depth) from soil surface (this value is conventionally used by the Marseille Industrial Harbor Authority to monitor the position of the saltwater front in local groundwater).

To assess groundwater velocity (here, this is the Darcy velocity as used by previous authors and not the mean pore velocity) using radon, the method of Schubert et al. (2011) was adapted. The basic principle of this method is that inside an observation well, dissolved radon is no longer supplied by the decay of <sup>222</sup>Ra adsorbed on mineral surfaces of the aquifer, therefore, water in the well has a lower radon activity in respect to that in the groundwater outside of the well. Neglecting degassing, the steady-state radon activity in the well water depends on the initial activity of the groundwater coming from the aquifer and the water residence time in the well. The water residence time in the well depends on the velocity of groundwater in the aquifer and on the hydraulic characteristics of the well. Velocity of groundwater in the aquifer can thus be estimated by comparing radon activity in well water with that in the aquifer. The latter may be obtained by sampling water after a complete purge of the well. According to Schubert et al. (2011), groundwater velocity (Darcy velocity) is calculated from the ratio of the measured activity of water in the well ( $C_{ww}$ ) to that in aquifer ( $C_{gw}$ ):

$$\frac{C_{ww}}{C_{gw}} = \frac{v}{\pi \lambda r} \int_{-\pi/2}^{\pi/2} \left(1 - e^{-\lambda 2r \cos \theta / v_{ww}}\right) \cos \theta d\theta \quad (1)$$

where  $\lambda$  is the radon decay constant,  $v_{ww}$  is the velocity of water in the well,  $r$  is the well radius (3 cm in this case) and  $\theta$  the variable of integration. This integral is solved by an iterative, numerical approach to obtain  $v_{ww}$ . The value of  $C_{gw}$  was obtained by measuring activity in well water after a complete purge, i.e. after complete renewal of the water volume in the well.

In addition, this study attempts to highlight the effects of aquifer heterogeneity and the freshwater/saltwater interface by repeating the measurements of  $C_{ww}$  and  $C_{gw}$  at three depths. For this purpose, a series of wells was selected, situated near the front of the saltwater intrusion (Figs. 1 and 2). Before collection of the water samples, the water table and well depths were measured. The depths of sample collection were defined by dividing the water column into three regularly spaced depth intervals. The water samples were taken in the middle (at mean depth) of each interval (i.e. at 1/6, 3/6 and 5/6 of the well water column). The range of mean depths of sample collection was 5–8 m for the shallow interval, 15–17 m for the intermediate interval, and 21–22 m for the deep interval. When the well is located above the saltwater front, as for X26, XD and L3, the intermediate interval is close to the freshwater/saltwater interface. In these cases, the deep interval is located within saltwater, whereas the shallow interval is always in freshwater, i.e. above saltwater.

The water samples for  $C_{ww}$  were collected first. To collect samples at the three depth intervals, the intake of the pump was lowered at the requested depth starting from the shallower interval to avoid water mixing. The water was pumped at a rate of 2 l/min into a 2.5-l bottle. To minimize degassing, the sample bottle was kept upright and the bottle was filled from the bottom to the top. The water volume in the bottle was renewed one time to assure that the sampled water was not degassed.

After that, water was sampled to measure  $C_{gw}$ . The intake pump was lowered at the same depths as for  $C_{ww}$ , starting from the shallow interval. Before collecting the sample, the water-volume of the depth-interval of the well was purged three times at a rate of 2.5 l/min. It was considered that the aquifer permeability in front of the tested interval is sufficient to supply water and that the pumping rate is low enough to prevent water coming from shallower or deeper intervals. It was assumed therefore that the permeability is sufficient to maintain a linear sub-horizontal flow during purging as it is in natural conditions. Finally, the sample for  $C_{gw}$  was collected; also, in this case, water was renovated one time in the bottle to minimize degassing.

**Table 2** Radon activities in groundwater from continuously exploited wells of the Cnu aquifer.  $X$  and  $Y$  as in Table 1

Well	Location	$X$	$Y$	Date	EC ( $\mu$ S/cm)	$T$ ( $^{\circ}$ C)	<sup>222</sup> Rn activity ( $Bq/m^3$ )	$\pm (2\sigma)$ ( $Bq/m^3$ )
P1	Vallignette	852,901	626,950	24/07/2012	980	18.2	9,480	152
P2	Fanfarigoule	856,885	626,784	27/03/2013	716	17	2,680	124
P3	Sulauze	860,082	627,724	27/03/2013	726	17.1	2,600	113
P4	Caspienne	858,250	627,276	27/03/2013	749	16.6	8,830	236
P5	Pissarote	850,661	626,621	27/03/2013	817	16.6	8,510	231
P6	BMW	859,100	627,694	27/03/2013	653	16.6	5,920	180

Author's personal copy

Hydrogeol J

**Table 3** Radon activities in groundwater at different depths in wells at the south-western rim of the Crau aquifer:  $X$  and  $Y$  as in Table 1.  $C_{sw}$ , radon activity in well water;  $C_{gw}$ , radon activity in groundwater after purge and renewal of well water

Well	$X$	$Y$	Elevation of well casing (m asl)	Date in 2014 (dd/mm)	Sample depth from well casing (m)	Sample level relative to sea level (m)		EC ( $\mu$ S/cm)	$T$ ( $^{\circ}$ C)	$^{222}\text{Rn}$ activity ( $\text{Bq/m}^3$ )	$\pm (2\sigma)$ ( $\text{Bq/m}^3$ )
X26	848,605	626,772	1.23	05/03	8	-6.77	$C_{sw}$	893	15.4	9,330	283
							$C_{gw}$	857	15.8	10,900	313
					17	-15.77	$C_{sw}$	1,140	15.4	12,000	366
							$C_{gw}$	1,150	15.9	11,400	448
					22	-20.77	$C_{sw}$	17,460	15.5	6,630	285
XD-I	849,530	626,573	1.12	21/05	5	-3.88	$C_{sw}$	20,800	16.2	7,980	323
							$C_{gw}$	955	14.0	6,920	238
							$C_{sw}$	1,098	14.7	8,840	328
					15	-13.88	$C_{sw}$	8,170	14.0	2,400	130
							$C_{gw}$	8,600	15.2	8,690	274
XD-II	849,530	626,573	1.12	06/11	21	-19.88	$C_{sw}$	39,800	15.0	6,880	265
							$C_{gw}$	47,000	15.0	9,810	289
					5	-3.88	$C_{sw}$	1,060	16.8	8,200	195
							$C_{gw}$	1,168	16.4	9,140	210
					15	-13.88	$C_{sw}$	7,480	15.8	3,850	123
XC	845,663	627,183	2.26	06/11	21	-19.88	$C_{sw}$	8,650	15.3	6,600	189
							$C_{gw}$	37,500	15.5	7,410	195
					5	-2.74	$C_{sw}$	45,500	15.1	7,950	214
							$C_{gw}$	739	17.6	8,900	182
					13	-10.74	$C_{sw}$	749	20.7	10,300	206
XA	843,555	627,248	1.19	24/09	7	-5.81	$C_{sw}$	760	17.4	10,900	231
							$C_{gw}$	760	16.2	10,800	218
							$C_{sw}$	932	16.5	5,730	175
							$C_{gw}$	929	15.6	11,700	256
					7	-5.61	$C_{sw}$	790	16.5	7,760	306
X20	847,224	626,963	1.39	13/11	7	-5.61	$C_{sw}$	649	16.6	10,200	228
							$C_{gw}$	654	16.4	10,000	191
					15	-13.61	$C_{sw}$	616	16.5	10,500	232
							$C_{gw}$	713	16.6	8,750	180
					21	-19.61	$C_{sw}$	745	16.7	9,940	198
L3	848,056	626,530	2.69	13/11	7	-4.31	$C_{sw}$	679	16.7	10,600	212
							$C_{gw}$	4,590	16.4	4,560	76
							$C_{sw}$	3,950	15.1	7,710	189
					15	-12.31	$C_{sw}$	13,850	15.3	3,920	130
							$C_{gw}$	16,610	14.5	4,590	152
		$C_{sw}$	40,200	15.1	2,790	116					
		$C_{gw}$	48,900	14.7	5,130	162					

To compute groundwater velocity  $v_{gw}$  from  $v_{wsm}$  the  $v_{wsm}$  value was divided by a geometric correction coefficient  $\alpha$  to take into account the convergence of water streamlines into the well. The value of  $\alpha$  was calculated according to Cook et al. (1999) and the reference therein:

$$\alpha = \frac{4}{1 + \left(\frac{r_1}{r_2}\right)^2 + \left[\frac{K_2}{K_1} \left(1 - \frac{r_1}{r_2}\right)^2\right]} \quad (2)$$

In Eq. (2),  $K_1$  is the hydraulic conductivity of the filter screen,  $K_2$  is the hydraulic conductivity of the aquifer,  $r_1$  is the inside radius of the filter screen,  $r_2$  is the well radius. Assuming that the permeability of the well screen is much higher than the permeability of the aquifer, and that the well is constructed without a filter pack, the  $\alpha$  coefficient has a value of 2.

## Results and discussion

### Radon in surface water

Table 1 reports the results of in-situ measurements of radon activity at fixed stations and average activities measured during navigation on two transects, in the Arles-Fos canal and in the Landre Pond (Fig. 2). Activities measured during the transect surveys are mapped in Fig. 2. Radon activity in the Arles-Fos canal measured in March 2014 and September 2014 results elevated, suggesting that a significant groundwater discharge occurs into this canal. The magnitude of this discharge will be discussed later. Near the outlet of the Landre Pond (station S4, Galejon) the activity in the Arles-Fos canal is lower, probably because of dilution with low-radon water flowing from Landre Pond. Downstream of the Landre outlet (S5 and S6) the activity remains low. Repeated measurement

Author's personal copy

Hydrogeol J

at S6 returned fairly constant radon activity during three campaigns despite different meteorological conditions (including windy conditions in September 2014). This suggests that radon activity in this canal approaches a steady state in the area of S6.

The radon activity of Landre Pond water (S7–S10, Fig. 2) decreases from the northern input canals (Vigueirat Canal) to the southern outlet of the Pond of the Galejon. The regular decrease in activity with the distance suggests that no groundwater discharge occurs into the pond. The very low activity measured at the outlet (S7, 11–13 Bq/m<sup>3</sup>) was obtained during a period of no water flow.

The canals of Vigueirat (S11), Vergiere (S12) and Centre Crau (S13) also yield elevated radon activity, in particular the Vergiere canal (495–770 Bq/m<sup>3</sup>). These canals certainly contain a significant amount of “recent” (few days) groundwater discharged by the network of streams draining the Crau aquifer. In parallel with the measurements of radon activity, the water flow rates of Vigueirat, Vergiere and Centre Crau canals were estimated by measuring the water velocity and their cross sectional areas. The flow rates in these canals were respectively 1.04, 1.22 and 0.75 m<sup>3</sup>/s.

### Radon in groundwater

Salinity and radon data shown on Fig. 3 and Tables 2 and 3 indicate that radon activity in shallow and intermediate groundwater far from the saltwater interface (wells XC, XA, X20) is rather constant with a value in the range 10–11 kBq/m<sup>3</sup>. This constant activity implies that the aquifer is quite homogeneous in terms of radon production rate, i.e. amount of <sup>226</sup>Ra adsorbed on mineral surfaces and the surface/volume ratio of the aquifer matrix.

The three municipal pumping wells located in the eastern area—P4 (Caspienne), P5 (Pissarotte) and P1 (Valignette)—however, yielded slightly lower activity

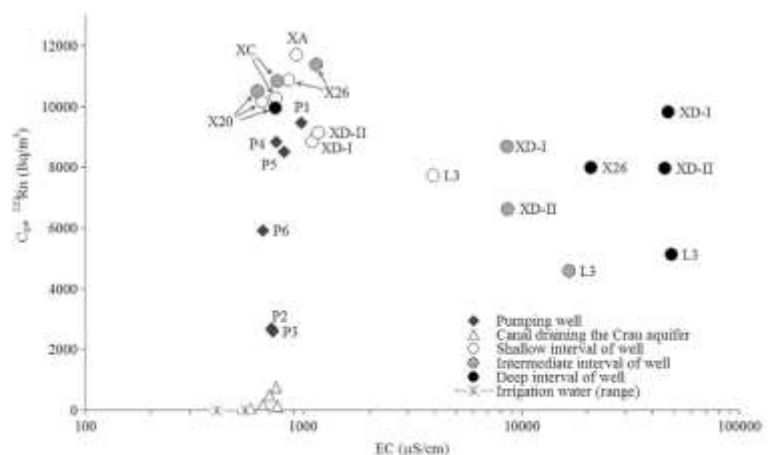
(9 kBq/m<sup>3</sup>). The reason for this low activity is probably the larger size of the sediment grains and the lack of fine sediments near these wells, which implies a lower specific surface (surface/volume) and consequently lower amount of adsorbed <sup>226</sup>Ra (and thus also lower <sup>222</sup>Rn) for the same water volume. Valignette and Pissarotte pumping wells, which have respectively the lowest and the highest water extraction-rate in this group, yield respectively the highest and the lowest radon activity.

On the other hand, samples P6 (BMW), P2 (Fanfarigoule) and P3 (Sulauze) clearly have lower radon activities. Two reasons may be proposed for this: mixing with rapidly infiltrated irrigation waters and/or groundwater flowing from the nearby limestone aquifer.

The first possibility is suggested by the lower EC value of irrigation water used in this zone (0.4–0.6 mS/cm). In Fig. 3, the position of the samples P6 (BMW), P2 (Fanfarigoule) and P3 (Sulauze) in the diagram may suggest that these waters could result from mixing between Crau groundwater (11 kBq/m<sup>3</sup>, 1 mS/cm) and irrigation waters depleted in radon by atmospheric degassing (~0 kBq/m<sup>3</sup>, 0.4–0.6 mS/cm). Radon supplied by adsorbed <sup>226</sup>Ra in the aquifer would however reset the activity to a near secular equilibrium value in of about three radon half-lives (11.4 days); therefore, the infiltration of irrigation water should occur within a few days to be able to keep the low radon activities. This possibility seems corroborated by the presence of highly permeable sediments in these zones and by the rapid fluctuations of the water table observed during irrigation.

On the other hand, mixing with groundwater from the limestone reservoir is also a possibility, as Mesozoic limestone occurs near these wells (Fig. 1) and a few meters underneath the well bases. Mesozoic limestone often yields radon activity in the range of 2,000–4,000 Bq/m<sup>3</sup> (Graves 1987), as in the Fanfarigoule and Sulauze wells. Limestone is probably the dominant lithology of the Crau deposits in this area.

**Fig. 3** Radon activity and electrical conductivity (EC) in groundwater of the Crau aquifer and in the surface water of Vigueirat, Vergier and Central Crau canals. Irrigation waters are reported as a range of EC, assuming that they do not contain a significant radon activity



Springer

Groundwater activities,  $C_{gw}$ , measured in wells located around the ponds are reported in Table 3 and discussed with respect to water depth. All shallow samples (depth 5–8 m), beside the southernmost well L3, have EC lower than 1 mS/cm and thus are not affected by saltwater intrusion. These samples yielded radon activities  $C_{gw}$  in the range 9–11 kBq/m<sup>3</sup>, barely lower than the activity observed in wells far from the ponds. Samples affected by minor salinization such as XD and L3 (having EC of 1.1 and 4 mS/cm respectively) also have slightly lower radon activity (about 8–9 kBq/m<sup>3</sup>). The radon activity measured at XD in November 2014 is similar to the one obtained in May within counting uncertainty ( $2\sigma$ ).

For the intermediate interval (15–17 m depth), the wells affected by minor or no saltwater intrusion yielded again the typical radon equilibrium activity of 11 kBq/m<sup>3</sup>. Two samples having higher salinity, XD and L3, yielded instead significantly lower radon activities (4–9 kBq/m<sup>3</sup>) similarly to the  $C_{gw}$  of the shallow saline waters.

Finally, for the deep layer (21–22 m depth), it is observed that the well X20, not affected by saltwater intrusion, yielded the same value of equilibrium activity as in the shallow level. It may be concluded that the aquifer areas far from the salinization areas are vertically homogeneous in terms of adsorbed <sup>226</sup>Ra and radon release efficiency. The wells affected by salinity always yielded lower activities (5 to 8 kBq/m<sup>3</sup>), except the sample XD collected in May 2014, which will be discussed later. These lower values of  $C_{gw}$  are compatible with an ion-exchange process implicating substitution of radium with sodium, as typically occurring at salinity in the range 6–10 ‰. In open-system condition, the substitution depletes aquifer minerals of adsorbed radium, lowering the radon equilibrium activity.

The deep samples collected in XD in May 2014 yielded  $C_{gw}$  values approaching the maximum equilibrium activity despite its high salinity (EC = 47 mS/cm). At this level of salinity, radium is thought to be completely desorbed from the aquifer matrix (Lazar et al. 2008) and thus radon activity was expected to be much lower. To explain the high equilibrium activity occurring at high salinity it is suggested that the saltwater/freshwater interaction at the salinity front did not remove a significant amount of radium from the aquifer and that the saltwater intrusion is older than a few thousand years.

Radium desorption may have occurred in nearly closed-system conditions. Desorbed radium may thus have remained in groundwater as a dissolved ion or co-precipitated in an insoluble mineral phase (barium sulfate or iron hydroxide). Unfortunately, <sup>226</sup>Ra in groundwater was not measured to verify whether the radon activity in this well is supplied by dissolved <sup>226</sup>Ra rather than an insoluble mineral phase. In addition, the radium lost by leaching may have been regenerated by new decay of parent <sup>230</sup>Th contained in the aquifer mineral. Considering the <sup>226</sup>Ra half-life of 1.6 ky, the intrusion of saltwater should be older than a few <sup>226</sup>Ra half-lives to be able to

regenerate <sup>226</sup>Ra in the aquifer (about 5,000 years). Such age is consistent with the evolution of the seashore during the last millennia as described by Vella et al. 2005 (Fig. 1), showing that the studied area was situated near the shoreline a few thousand years ago. Thus, the observed salinity in the well XD could be a residue of ancient seawater and not current seawater intrusion into the aquifer.

The time variability of  $C_{gw}$  in the intermediate and deep layers of XD between May and November 2014 may have several explanations. Harris et al. (2006) observed seasonal differences that were interpreted as differential water extraction rates from primary vs. secondary veins in the aquifer just before sample collection. Mullinger et al. (2009) suggested for similar radon variability an effect of water-table fluctuations related to rainwater infiltration. Kasztovszky et al. (2000) also observed a variability in radon activity, even at the diurnal time scale, interpreted to result from water-table fluctuations perturbing the water pathway between radon sources in the aquifer and the well. Since water-table fluctuations in XD are in fact observed (and related to water extraction-rate in the nearby well of Pissarotte), the favored explanation is that radon time-variability in this well is due to different groundwater pathways in response to water-table fluctuations.

In the northern sector (wells XA, XC and X20),  $C_{gw}$  is about 11 kBq/m<sup>3</sup>, barely lower than the highest  $C_{gw}$  measured in the Crau aquifer (X26, 12 kBq/m<sup>3</sup>), which suggests that <sup>226</sup>Ra in the northern zone has not been “leached” by seawater intrusions during the last millennia. This result is also in agreement with the evolution of the seashore proposed by Vella et al. (2005) for which the position of the shoreline 5,000 years ago was south of these wells.

#### Groundwater velocity from radon measurements

The radon activities measured in well waters ( $C_{ww}$ ) are presented in Table 3, Figs. 3 and 4 for the three depth intervals, while calculated groundwater velocities are presented in Table 4.

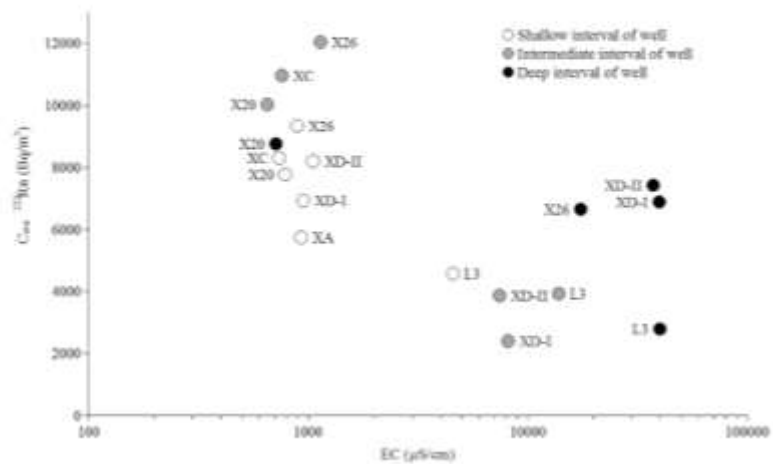
In the shallow interval (5–8 m), the difference in activity before ( $C_{ww}$ ) and after ( $C_{gw}$ ) the purge is large, indicating that groundwater velocity is low. This result agrees well with the nature of the sediments in the upper part of the deposits. Well logs made around the ponds indicate that the aquifer is partially confined by less permeable sediments of the Rhône River, mixed with lacustrine deposits. The lowest velocities (XA and L3, Table 4) are obtained for the wells situated on the two opposite sides of the study area (Fig. 1). Water level in these wells merges with the water level in the pond.

For the intermediate interval (14–17 m), in the northern sector, the radon activities before and after the purge are almost identical, implying high groundwater velocities. These

Author's personal copy

Hydrogeol J

**Fig. 4** Radon activity and electrical conductivity (EC) of well waters of the Crau aquifer, sampled before well purge



high velocities are explained by a much higher permeability, i.e. by the presence of coarse-grain material corresponding to alluvial pebbles and gravels. Another reason for the high groundwater velocity may be the rise of the saltwater interface—the more elevated the saltwater interface, the thinner the freshwater layer. Velocity must thus increase to accommodate the thinning of the freshwater cross-section. The salinity interface in X26 and X20 occurs at depths of 17 and 21 m

respectively, just below the depths obtained for the maximum velocities. For XC, the saltwater interface has not been found because this well reaches only 13 m depth; however, since in the nearby XA well the saltwater interface is at 12 m depth, it is assumed that in XC, slightly upstream relative to XA, the saltwater interface is somewhat lower than 13 m depth.

Well L3, located within the saltwater intrusion (Fig. 1), shows moderate velocities (Table 4) in agreement with a water

**Table 4** Groundwater velocity and permeability estimated from radon data and piezometric gradient, according to the data in Table 3.  $V_{gw}$  is the calculated groundwater velocity. Ranges (min-max) are estimated on the basis of  $2\sigma$  errors of groundwater radon activity measurements

		Piezometric gradient (per mille)	Sample depth (m)	$V_{gw}$ (cm/day)		Hydraulic conductivity (m/day)	
				Min	Max	Min	Max
Northern sector							
XA	Sept. 2014	0.36	7	0.25	0.30	7	8
XC	Nov. 2014	0.29	5	0.9	1.3	29	45
			13	8	–	270	–
X20	Nov. 2014	0.19	7	0.7	1.1	34	56
			15	2.6	46	140	2,400
			21	1.3	2.6	70	140
X26	March 2014	0.07	8	1.1	2.5	150	350
			17	21	–	3,000	–
			22	0.8	2.2	120	320
Southern sector (saltwater intrusion)							
L3	Nov. 2014	0.29	7	0.36	0.43	12	15
			15	1.0	2.5	34	85
			21	0.3	0.4	10	13
XD	May 2014	0.35	5	0.7	1.3	20	37
			15	0.11	0.14	3	4
			21	0.5	0.8	14	22
			21	0.5	0.8	14	22
XD	Nov. 2014	0.35	5	1.4	3.7	41	100
			15	0.3	0.4	9	12
			21	1.8	13.2	52	380
			21	1.8	13.2	52	380
XD	Average May–Nov. 2014	0.35	5	1.1	2.5	30	71
			15	0.2	0.3	6	8
			21	1.2	7.0	33	200

Author's personal copy

table essentially controlled by surface waters (Arles-Fos Canal and Vigueirat Marsh). A minor increase in velocity occurs in the intermediate interval, as observed in the northern wells; also in this case, the increase in velocity is accompanied by a sudden increase in salinity in the interval below. On the other hand, the well XD yields the lowest velocity in the intermediate interval for which a probable reason is that XD is located in the water divide area (or stagnation point) of the groundwater capture zone of the Pissarotte pumping well (average pumping rate of 2,600 m<sup>3</sup>/day). On this downstream boundary of the pumping well capture zone, velocity becomes zero (stagnation). The measurement made in May 2014 clearly reflects the existence of stagnant groundwater in the intermediate interval. For November 2014 velocity is somewhat higher in XD, probably due to the displacement of the stagnation point after the period of high water-pumping rate. For the deeper interval, radon data suggest that, except for XD, groundwater velocity is lower than in the intermediate layer.

**Estimate of hydraulic conductivity**

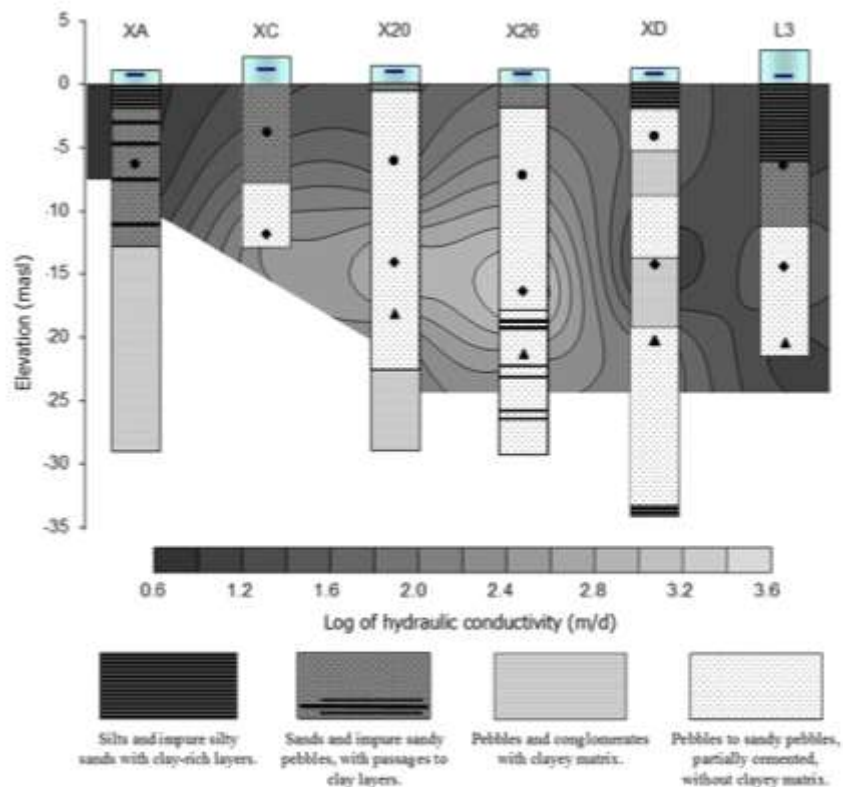
Table 4 and Fig. 5 present the values of hydraulic conductivity (*K*) calculated as the ratio between the (Darcy) groundwater velocity obtained from radon activity and the hydraulic gradient. The calculation assumes that groundwater flow is

horizontal (no vertical component) and that the hydraulic gradient is constant at any depth, i.e. flow is two-dimensional (2D). The hydraulic gradient was determined from the water-table map drawn using 45 water level measurements in piezometers (locations on Fig. 1). Measurements have been corrected for density changes in the water column due to water salinity; for X20 and X26, located in the central zone, the hydraulic gradient is very low (0.07–0.19 ‰, against 0.35 ‰ at the border).

The high hydraulic conductivity found in the intermediate interval indicates that this interval is very permeable, i.e. probably composed of very coarse material. The top of the Rhône River gravels, mapped by Vella et al. (2005), corresponds to the high-permeability intermediate interval found with radon in this study.

The value of *K* in the shallow interval is much lower and is consistent with the occurrence of fine sediments of the Rhône River mixed with lacustrine deposits. A monotonic increase in *K* value is observed in the shallow depth interval from north to south in the sequences XA, XC, X20 and X26. For XD, estimates of *K* are given for May and November 2014, and averaged in Fig. 5. For both estimates, the intermediate interval appears to be less conductive; however, as discussed in the preceding, these estimates are probably influenced by the variable hydraulic gradient near the pumping station (water-table

**Fig. 5** Hydraulic conductivity (m/day) in the Crau aquifer obtained from radon data and piezometric gradients. Well data are obtained from the BRGM website (BRGM 2015). Circles, diamonds and triangles (black symbols) indicate depths of shallow, intermediate and deep samples in wells, respectively. Blue horizontal segments indicate elevation of the water table with respect to sea level



Author's personal copy

Hydrogeol J

depression and hydraulic-gradient inversion). For this specific location, it is probably not correct to calculate  $K$  using a hydraulic gradient that is not determined at the same time as the radon sample collection. Figure 5 shows the extrapolation of hydraulic conductivities obtained with radon-determined velocities and hydraulic gradient. The spatial distribution of  $K$  values well agrees with the geology known from well logs. High-permeability zones are found at depths corresponding to unconsolidated pebbles and sands.

Estimate of groundwater discharge into ponds

Radon activity was used to estimate an overall mass balance in Landre Pond. The radon mass balance imposes that the total input of radon equals the total output of radon. For the Crau-Vigueirat system, and assuming steady-state condition, the radon mass balance may be written as:

$$F_{river} + F_{diff} + F_{Ra} + F_{gw} = F_{decay} + F_{air} + F_{out} \quad (3)$$

In this equation, all radon fluxes can be calculated or measured except the radon flux  $F_{gw}$  due to groundwater discharge into the ponds, which is the flux of interest here. The values of all variables used in this calculation are summarized in Table 5.

$F_{river}$  is the radon flux from the river (Bq/day),  $F_{river} = Rn_{river} \cdot Q_{river}$  where  $Q_{river}$  is the river water flow occurring in the three canals (Vigueirat, Centre Crau and Vergiere) and evaluated at  $3 \text{ m}^3/\text{s}$ .  $Rn_{river}$  is the weighted average radon activity measured in the canals. The flux  $F_{river}$  accounts for 72.8 MBq/day.

The term  $F_{diff}$  is the radon flux produced by sediments diffusion and is important because it provides a constant radon input through the sediment interface even in the absence of groundwater discharge. The value of  $F_{diff}$  ( $2.2 \text{ Bq/m}^2/\text{day}$ , i.e.  $2.1 \text{ MBq/day}$  for the total pond surface of  $0.95 \text{ km}^2$ ) comes from a previous study (Radakovitch et al. 2007; GIZCAM 2009) made on sediments having similar origin and permeability in a nearby zone (Vaccares).

$F_{Ra}$  is the flux produced by disintegration of the dissolved  $^{226}\text{Ra}$ . This flux accounts for  $0.9 \text{ Bq/m}^2/\text{day}$ , i.e.  $0.9 \text{ MBq/day}$  for the total pond and has been calculated as  $I^{226}\text{Ra} \cdot \lambda_{222}$ , where  $I^{226}\text{Ra}$  is the inventory of  $^{226}\text{Ra}$  in the water column, using a water column height ( $h$ ) of  $0.5 \text{ m}$  and a  $^{226}\text{Ra}$  activity of  $10 \text{ Bq/m}^3$  as measured in Vaccares Pond (Radakovitch et al. 2007; GIZCAM 2009).  $F_{decay}$  is calculated as  $I^{222}\text{Rn} \cdot \lambda_{222}$ , where  $I^{222}\text{Rn}$  is the radon inventory, calculated as  $Rn_{ave} \cdot h$ , where  $Rn_{ave}$  is the average radon concentration measured in the pond ( $76 \text{ Bq/m}^3$ , 26 individual measurements in the pond averaged with 15–30 % error). The calculation obtains  $F_{decay} = 6.6 \text{ MBq/day}$ .

**Table 5** Constants used to estimate groundwater seepage into Landre Pond and radon mass balance

Parameter	Term	Value	Error	Units
Constants used to calculate groundwater seepage into Landre Pond				
Volume of pond	$V$	0.48		$\text{Mm}^3$
Surface of pond	$S$	0.95		$\text{km}^2$
Fresh water input from canals to pond	$Q$	3.0		$\text{m}^3/\text{s}$
Average $^{226}\text{Ra}$ activity in Landre Pond water	$^{226}\text{Ra}$	10		$\text{Bq/m}^3$
Average $^{222}\text{Rn}$ activity in Landre pond water	$Rn_{ave}$	76		$\text{Bq/m}^3$
Average $^{222}\text{Rn}$ activity in groundwater	$Rn_{gw}$	10		$\text{kBq/m}^3$
Average $^{222}\text{Rn}$ activity in canals and rivers	$Rn_{river}$	280		$\text{Bq/m}^3$
Average $^{222}\text{Rn}$ activity in air	$Rn_{air}$	5		$\text{Bq/m}^3$
Wind velocity	$u$	6.0		$\text{m/s}$
Gas transfer velocity	$k_{600}$	1.46	$\pm 0.18$	$\text{cm/h}$
Radon mass balance of Landre Pond				
$F_{river}$		73		$\text{MBq/day}$
$F_{diff}$		2.1		$\text{MBq/day}$
$F_{Ra}$		0.9		$\text{MBq/day}$
Total $^{222}\text{Rn}$ input fluxes (beside groundwater)		76		$\text{MBq/day}$
$F_{decay}$		-6.6		$\text{MBq/day}$
$F_{out}$		-3.5		$\text{MBq/day}$
$F_{air}$		-105	$\pm 13$	$\text{MBq/day}$
Total $^{222}\text{Rn}$ output fluxes		-115	$\pm 13$	$\text{MBq/day}$
Imbalance due to groundwater $^{222}\text{Rn}$ flux		39	$\pm 13$	$\text{MBq/day}$
Integrated groundwater seepage into Landre Pond		45	$\pm 15$	$\text{l/s}$

The flux of radon to the atmosphere  $F_{air}$  will be discussed in detail as this flux is very important for radon mass balance. This flux was evaluated using the gas transfer velocity ( $k$ ) approach. A recent study (Cockenpot et al. 2015) on radon degassing in the nearby Berre Pond has shown that the relationship between wind and gas transfer velocity  $k$  fits the experimental relation:

$$k_{660} = (0.0033 \pm 0.0008)u^3 + (5.4 \pm 0.6) \quad (4)$$

where  $k_{660}$  is the gas transfer velocity (cm/h) of radon, normalized to  $CO_2$  at 20 °C for brackish waters and  $u$  is the wind velocity (m/s) measured at 10 m above ground. To compare models of radon degassing,  $k$  was also calculated with the commonly used relationship of MacIntyre et al. (1995), also obtained experimentally:

$$k_{660} = 0.45u^{1.6}(Sc/600)^{-0.5} \quad (5)$$

where  $Sc$  is the Schmidt number, corresponding to the ratio between kinematic viscosity and molecular diffusivity of radon, that in the case of freshwater is divided by 600 ( $Sc$  for  $CO_2$  in freshwater at 20 °C). The kinematic viscosity is the ratio between dynamic viscosity and density. Dynamic viscosity was calculated with the equation of Seeton (2006) and molecular diffusivity with the equation of Peng et al. (1974).

Knowing the value of  $k_{660}$ , the atmospheric flux was finally calculated with the relation (MacIntyre et al. 1995):

$$F_{air} = k(Rn_{ave} - \delta Rn_{air}) \quad (6)$$

where  $Rn_{ave}$  and  $Rn_{air}$  are the average radon activities in the ponds waters and in the air, and  $\delta$  is the Ostwald coefficient. The Ostwald coefficient is calculated using the Bunsen coefficient obtained using the equation of Schubert et al. (2011), which takes into account the effects of salinity on radon solubility. The value of  $k$  is either  $k_{660}$  for brackish water determined using the relationship of Cockenpot et al. (2015; Eq. 4) or  $k_{660}$  calculated according to MacIntyre et al. (1995; Eq. 5).

The velocity of the wind was obtained from the meteorological station of Istre airbase located in the vicinity. The average wind velocity in the area during the 2 days preceding the radon measurements was 6 m/s. This 2-day period is close to the water residence time calculated as  $\tau = V/Q$ , where  $V$  is the volume of the ponds and  $Q$  is the total water inflow from canals and rivers (3 m<sup>3</sup>/s). The residence time is 1.78 days assuming that the water mass balance is in steady state during this time, i.e. that no significant variation of water volume occurs during this period.  $Rn_{air}$  is assumed to be 5 Bq/m<sup>3</sup>, as measured in the Vaccares Lagoon by Radakovitch et al. (2009) and also as an average value in the Berre Lagoon by Cockenpot et al. (2015; Table 5). The average radon activity measured in the ponds ( $Rn_{ave}$ ) is 76 Bq/m<sup>3</sup>. Finally, the  $F_{air}$

value was calculated as 91–118 MBq/day using the  $k_{660}$  calculated as in Cockenpot et al. with its incertitude (Eq. 4). The  $F_{air}$  calculated using the  $k_{660}$  of MacIntyre et al. (1995; Eq. 5) is 99 MBq/day, thus falling within the results of the model of Cockenpot et al. (2015).

The radon output flux  $F_{out}$  due to the water leaving the pond through the Landre outlet is obtained by multiplying the measured radon activity at the outlet of the pond ( $13 \pm 7$  Bq/m<sup>3</sup>) by the total water outflow. The latter was calculated as the sum of all water inputs into the ponds corrected for evaporation, which assumes steady-state condition in terms of water volume over the pond surface. The total water input to the pond is the sum of river and canal inputs (3.01 m<sup>3</sup>/s), groundwater (initially assumed to be negligible) and rainfall cumulated during the water residence period preceding the radon measurements (12 mm rainfall from 21 to 23 March 2014, equivalent to a total rainfall input of +0.07 m<sup>3</sup>/s). The evaporation during the same period is 0.027 m<sup>3</sup>/s. Hourly data used to calculate the cumulated rainfall and evaporation have been obtained by the INRA station of Salon de Provence. The total radon loss at the outlet of the pond is 3.49 MBq/day.

Using Eq. (3), the total daily inputs into the ponds, beside groundwater, account for 76 MBq/day and the total outputs account for 101–128 MBq/day, assuming the atmospheric flux model of Cockenpot et al. (2015) with its analytical uncertainty (Table 5). The imbalance due to the  $F_{gw}$  is thus 26–52 MBq/day. Assuming finally that the groundwater radon activity is 10 kBq/m<sup>3</sup> (from well data), the vertical water seepage necessary to support the radon flux  $F_{gw}$  is 2.7–5.5 mm/day, e.g. 2.7–5.5 l/m<sup>2</sup>/day. This seepage over the pond area corresponds to a total groundwater discharge of  $2.5 \cdot 10^3$  to  $5.2 \cdot 10^3$  m<sup>3</sup>/day or 30–60 l/s. Such groundwater flow accounts for about 1–2 % of the total freshwater input from canals (3.0 m<sup>3</sup>/s). This flux is thus negligible in terms of water supplied to the pond and corroborates the initial assumption of no groundwater flux for the calculation of  $F_{out}$ . The total uncertainty in the final mass balance is difficult to estimate since the calculation is strongly dependent on the model of  $k$  and of the steady-state condition. The groundwater discharge remains however negligible over the range of  $F_{air}$  deduced from the model uncertainty (Table 5) and represents, in any case, the largest flux affecting the radon mass-balance of the Landre Pond (91 % of total output flux).

#### Evolution of radon inputs into the pond

To verify the low  $F_{gw}$  flux into the pond, the time-evolution of radon activity in the pond was modeled using the measured input and output fluxes. In particular, the aim was to verify whether the activity in water calculated at the residence-time

of the pond matches the average activity measured near the outlet of the pond. The time evolution of radon input from the rivers into the pond can be modeled by means of the usual differential equation:

$$\frac{dRn}{dt} = F_{river} + F_{diff} + F_{Ra} + F_{gw} - F_{decay} - F_{air} - F_{out} \quad (7)$$

This equation can be rearranged to separate variables and integrated, imposing as boundary condition that the radon activity at time  $t = 0$  is one of the river inputs ( $Rn_{river}$ ), which renders the following:

$$Rn(t) = \frac{c_2}{c_1} + \left( Rn_{river} - \frac{c_2}{c_1} \right) \cdot e^{(-c_1 \cdot t)} \quad (8)$$

where  $c_1 = \lambda_{222} \cdot h + k$  and  $c_2 = k \cdot Rn_{air} \delta + F_{gw} + F_{diff} + F_{Ra} - F_{out}$

In Eq. (8), the  $k$  value calculated as in Cockenpot et al. (2015) was used. The radon activity calculated for the water residence-time  $\tau$  of 1.78 days is  $43 \text{ Bq/m}^3$ . This result is within the average activity of  $40 \pm 12 \text{ Bq/m}^3$  measured in the southern side of the pond, near the outlet and confirms that Eq. (4), with the assumptions made previously, well describes the radon evolution in the pond and that no significant groundwater discharge to the pond occurs. The equation also well predicts the pattern of radon activity in the pond, with upstream high values and downstream low values. The final equilibrium activity value would be  $24\text{--}27 \text{ Bq/m}^3$ , therefore water reached 93 % of its final radon equilibrium activity near the outlet of the pond.

Equation (8) was also used to constrain the piston velocity  $k$  necessary to reduce radon activity from the value observed in the canals ( $280 \text{ Bq/m}^3$ ) to the one observed near the outlet of Landre Pond ( $40 \text{ Bq/m}^3$ ) after a water residence time of 1.78 days. The obtained value of  $k$  is  $1.58 \text{ m/day}$ . This value is probably a better estimate of  $k$  since it does not rely on wind-dependent equations (Eqs. 4 and 5).

#### Groundwater discharge into Arles-Fos canal

The Arles-Fos canal is excavated to the limit between the Holocene Rhône sediments and the Crau formation. The depth of the canal (more than 2 m, with a water height of about 1.7 m) is sufficient to intercept the upper part of the coarse material of the Crau aquifer (thickness of sandy silt being 2 to 3 m as indicated by well logs); therefore, a significant input of groundwater is expected into the canal. The high radon activity measured in the canal ( $312 \text{ Bq/m}^3$ ) suggests that a significant groundwater discharge indeed occurs. The groundwater flux necessary to support the observed radon activity in the canal was calculated, assuming that the measured activity is steady state, i.e. the radon lost by degassing and decay are

compensated by groundwater discharge, diffusion and radium decay:

$$F_{diff} + F_{Ra} + F_{gw} = F_{decay} + F_{air}$$

For this calculation,  $F_{diff}$  and the activity of  $^{226}\text{Ra}$  as in the previous section were assumed, and a canal water column of 1.8 m for radium and radon inventories in the canal were also assumed.  $F_{air}$  was calculated as in the previous section. The  $F_{gw}$  necessary to support radon activity in the canal is then  $548 \text{ Bq/m}^2/\text{day}$ . This flux does not generate the high activity in the canal ( $312 \text{ Bq/m}^3$ ) but corresponds to the flux requested only to maintain a stationary radon activity. The corresponding groundwater seepage is  $5.5 \text{ cm/day}$ , which compares well with the groundwater velocity obtained measuring radon in wells with the method of Schubert et al. (2011). The calculated groundwater discharge into the canal is  $55 \text{ l/m}^2/\text{day}$ .

#### Conclusions

Radon has been used to assess groundwater velocities in the Crau aquifer to highlight the pattern of groundwater discharge and to constrain the water-mass balance at the downstream boundary of the Crau aquifer (Vigueirat-Landre ponds). Groundwater Darcy velocities have been measured using the method proposed by Schubert et al. (2011). The measurements were repeated at three depth intervals in wells situated close to the saltwater interface (salinity front). Darcy velocities are in the range of a few cm/day to more than 20 cm/day. The results highlight the existence of high groundwater velocity (few m/day) at a depth of about 14 m below surface in the central part of the study area. These high velocities, related to a low hydraulic gradient, imply the existence of a highly permeable layer at this depth. Such a highly conductive layer is supported by the presence of pebbles and uncemented coarse sediments as described by well logs. Hydraulic conductivities were also calculated as the ratio between the groundwater velocity and the piezometric gradient. Shallower and deeper intervals provide lower velocities. This characterizes the less permeable sediments indicated by the well logs: fine sediments of the Rhône River at shallow level and cemented conglomerates at deeper level. Reduced velocities are also observed in zones of low hydraulic gradient due to the effect of water pumping. The high velocities may also be related to the reduction in the freshwater thickness due to saltwater intrusion. All these results show that measurements of radon activity provide very relevant information. For example, such evaluation of groundwater velocity and hydraulic conductivity may help to calibrate and validate groundwater models.

Surveys of radon in surface waters suggest that no significant discharges of groundwater occur in the ponds of Vigueirat and Landre. Radon activity in the ponds appears to

be essentially controlled by upstream inputs from canals and minor rivers draining the Crau. Groundwater inputs to the ponds are less than 4 % of the total input. The calculated change of radon activity through the system compares well with the measured water activity at the pond outlet. The good match between calculated and observed data, as well as the distribution of radon in the pond, indicates that the pond and aquifer behave as a simple system in a nearly steady-state condition. This result corroborates the observed stability of the saltwater front in the area and may also be used to validate groundwater models.

On the other hand, high radon activities were observed in the Arles-Fos canal, which intercepts coarse material of the Crau aquifer. This implies that groundwater discharge must occur in this canal, also corroborating the high groundwater velocity found in some of the wells. The order of magnitude of groundwater seepage necessary to explain the radon activity in the canal is consistent with the groundwater velocity calculated with the radon method in the wells.

Radon appears to be an effective tracer to quantify water balance at the scale of coastal pond–aquifer systems. The measurements of radon activity in well groundwater and in surface water provide very relevant information for understanding groundwater behavior, as well as for developing, calibrating and validating groundwater flow models. In this respect, and in this setting, radon seems to be a better tracer for surface (river) water inputs into ponds than electrical conductivity and temperature.

**Acknowledgements** This work has been supported by the Ministry of Training and Education of France and Vietnam (French-Vietnamese co-operation). We thank ‘Grand Port de Marseille’ and ‘Syndicat Mixte de Gestion de la Nappe Phréatique de la Crau’ for data provided and ‘Reserve Naturelle des Marais du Viguiat’ for access to sites.

## References

- Boyer J, Duval C, Le Strat P, Gensous B, Tesson M (2005) High resolution stratigraphy and evolution of the Rhône delta plain during Postglacial time, from subsurface drilling data bank. *Mar Geol* 222–223:267–298
- BRGM (1995) MARTCRAU: actualisation du modèle de la nappe de la Crau [Update of the Crau aquifer model]. Report 94-D-211, BRGM, Orléans, France, 73 pp
- BRGM (2015) Dossiers sur le sous-sol (BSS) [Records on the basement (BSS)]. <http://infoterre.brgm.fr/dossiers-sur-le-sous-sol-bss>. Accessed Oct 2015
- Cockenpot S, Claude C, Radakovitch O (2015) Estimation of air-water gas exchange coefficient in a shallow lagoon based on  $^{222}\text{Rn}$  mass balance. *J Environ Radioact*. doi:10.1016/j.jenvrad.2015.02.007
- Cook PG, Love AJ, Dighton JC (1999) Inferring ground water flow in fractured rock from dissolved radon. *Ground Water* 37(4):606–610
- De Montety V, Radakovitch O, Vallet-Coulomb C, Blavoux B, Hermitte D, Valles V (2008) Origin of groundwater salinity and hydrogeochemical processes in a confined coastal aquifer: case of the Rhône delta (southern France). *Appl Geochem* 23(8):2337–2349
- Dimova N, Burnett WC, Lane-Smith D (2009) Improvements in the automated analyses of radon ( $^{222}\text{Rn}$ ) and thoron ( $^{220}\text{Rn}$ ) in water. *Environ Sci Technol* 43(22):8599–8603
- Dimova NT, Burnett WC, Chanton JP, Corbett JE (2013) Application of radon-222 to investigate groundwater discharge into small shallow lakes. *J Hydrol* 486:112–122
- Dulaiova H, Peterson R, Burnett WC, Lane-Smith D (2005) A multi-detector continuous monitor for assessment of Rn-222 in the coastal ocean. *J Radioanal Nucl Chem* 263:361–365
- GIZCAM (2009) Constraints, limits and perspectives for integrated coastal zone management in the Rhône River delta. Liteau 2 final report, Tour du Valat, Arles, France
- Graves B (ed) (1987) Radon, Radium and Other Radioactivity in Groundwater. Lewis Publishers, Chelsea, Michigan
- Hamada H (2000) Estimation of groundwater flow rate using the decay of Rn-222 in a well. *J Environ Radioact* 47:1–13
- Harris SA, Billmeyer ER, Robinson MA (2006) Evaluation of repeated measurements of radon-222 concentrations in well water sampled from bedrock aquifers of the Piedmont near Richmond, Virginia, USA: effects of lithology and well characteristics. *Environ Res* 101:323–333
- Holman IP, Allen DM, Cuthbert MO, Goderniaux P (2012) Towards best practice for assessing the impacts of climate change on groundwater. *Hydrogeol J* 20:1–4
- INRA (2013) Sustainable use of irrigation water in the Mediterranean region. Report D5.3, SIRRIMED. [http://www.sirrimed.org/catalogo/d4\\_4\\_d4\\_5\\_model\\_adaptation\\_coupling\\_v03.pdf](http://www.sirrimed.org/catalogo/d4_4_d4_5_model_adaptation_coupling_v03.pdf). Accessed Oct 2015
- Kaszovszky Z, Sajo-Bobus L, Fazekas B (2000) Parametric changes of radon ( $^{222}\text{Rn}$ ) concentration in ground water in northeastern Hungary. *J Environ Radioact* 49:171–180
- Lazar B, Weinstein Y, Paytan A, Magal E, Bruce D, Kolodny K (2008) Ra and Th adsorption coefficients in lakes: Lake Kinneret (Sea of Galilee) “natural experiment”. *Geochim Cosmochim Acta* 72(14–72):3446–3459
- MacIntyre S, Wanninkhof R, Chanton JP (1995) Trace gas exchange across the air-sea interface in freshwater and coastal marine environments. In: Matson PA, Harriss C (eds) *Methods in ecology - Biogenic trace gases: measuring emissions from soil and water*. Blackwell Science, Oxford, pp 52–97
- Molliex S, Siame LL, Bourlés DL, Bellier O, Braucher R, Clauzon G (2013) Quaternary evolution of a large alluvial fan in a periglacial setting (Crau Plain, SE France) constrained by terrestrial cosmogenic nuclide ( $^{10}\text{Be}$ ). *Geomorphology* 195:45–52
- Mullinger NJ, Pates JM, Binley AM, Crook NP (2009) Controls on the spatial and temporal variability of  $^{222}\text{Rn}$  in riparian groundwater in a lowland Chalk catchment. *J Hydrol* 376:58–69
- Olifoso A, Lecerf R, Baillieux A, Chanzy A, Ruget F, Banton O, Lecharpentier P, Trolard F, Cognard-Planq A-L (2013) Modelling of drainage and hay production over the Crau aquifer for analysing impact of global change on aquifer recharge. *Procedia Environ Sci* 19:691–700
- Peng TH, Akatashi TT, Broecker WS (1974) Surface radon measurements in the north Pacific Ocean Station Papa. *J Geophys Res* 79: 1772–1780. doi:10.1029/JC079i012p01772
- Radakovitch O, Mayer A, Garcia Orellana J, Garcia Solsona E, Claude C, Masque Barri P, Chauvelon P, Ollivier P (2007) Submarine groundwater discharge estimates on coastal waters based on  $^{222}\text{Rn}$  measurements. Proceedings of 38th IAGLR Congress, Istanbul, April 2007, 698 pp
- Radakovitch O, Mayer A, Chauvelon P, Vallet-Coulomb C, Claude C, Parisot JC, Hermitte D (2009) Groundwater inputs in the Vaccares lagoon (South France) estimated from  $^{222}\text{Rn}$  budget. ECOCLR: 4th European Congress on Lagoon Research, Montpellier, France, December 2009

*Author's personal copy*

Hydrogeol J

- Rodellas V, Garcia-Orellana J, Garcia-Solsona E, Masqué P, Domínguez JA, Ballesteros BJ, Mejias M, Zarroca M (2012) Quantifying groundwater discharge from different sources into a Mediterranean wetland by using  $^{222}\text{Rn}$  and  $\text{Ra}$  isotopes. *J Hydrol* 466–467:11–12
- Rouze S, Duvail C, Aunay B, Le Strat P (2004) Geodynamique des Systemes Plio-quaternaires des Nappes Alluviales de la Plaine de la Crau [Geodynamic of the Plio Quaternary systems of the Alluvial sediments of the Crau plain]. BRGM report, RP-53088-RR, BRGM, Orléans, France
- Schubert M, Brueggemann L, Knoeller K, Schirmer M (2011) Using radon as an environmental tracer for estimating groundwater flow velocities in single-well tests. *Water Resour Res* 47(3). doi:10.1029/2010WR009572
- Seeton CJ (2006) Viscosity–temperature correlation for liquids. *Tribol Lett* 22:67–78. doi:10.1007/s11249-006-9071-2
- Shi H, Singh A (2003) Status and interconnections of selected environmental issues in the global coastal zones. *AMBIO* 32(2):145–152. doi:10.1579/0044-7447
- Stieglitz TC, van Beek P, Souhaut M, Cook PG (2013) Karstic groundwater discharge and seawater recirculation through sediments in shallow coastal Mediterranean lagoons, determined from water, salt and radon budgets. *Mar Chem* 156:73–84
- Vella C, Fleury TJ, Raccasi G, Provensal M, Sabatier F, Bourcier M (2005) Evolution of the Rhone delta plain in the Holocene. *Mar Geol* 222–223:235–265
- Werner AD, Bakker M, Post VEA, Vandenbohede A, Lu C, Amie-Ashtiani B, Simmons CT, Baery DA (2013) Seawater intrusion processes, investigation and management: recent advances and future challenges. *Adv Water Resour* 51:3–26

### 4.3 Groundwater numerical modeling

#### 4.3.1 Conceptual model

##### 4.3.1.1 Geometry and structure

The study area is the downstream part of the Crau coastal plain, and has an area of about 140 km<sup>2</sup>. It includes the marsh area of the Vigueirat Natural Reservation (Wet Crau) and one part of the irrigation zone of the Coussouls natural reserve zone (Dry Crau). The main structural and hydrogeological characteristics of the Crau aquifer are known through the geological information and the lithological descriptions from 45 borehole logs. Two main geological units are considered: the Holocene clay and sandy clay layer and the Pleistocene conglomerate of sand, clay and gravels (Figure 50 and Figure 52). Hydraulic parameters of the aquifer are considered heterogeneous taking into account available data.

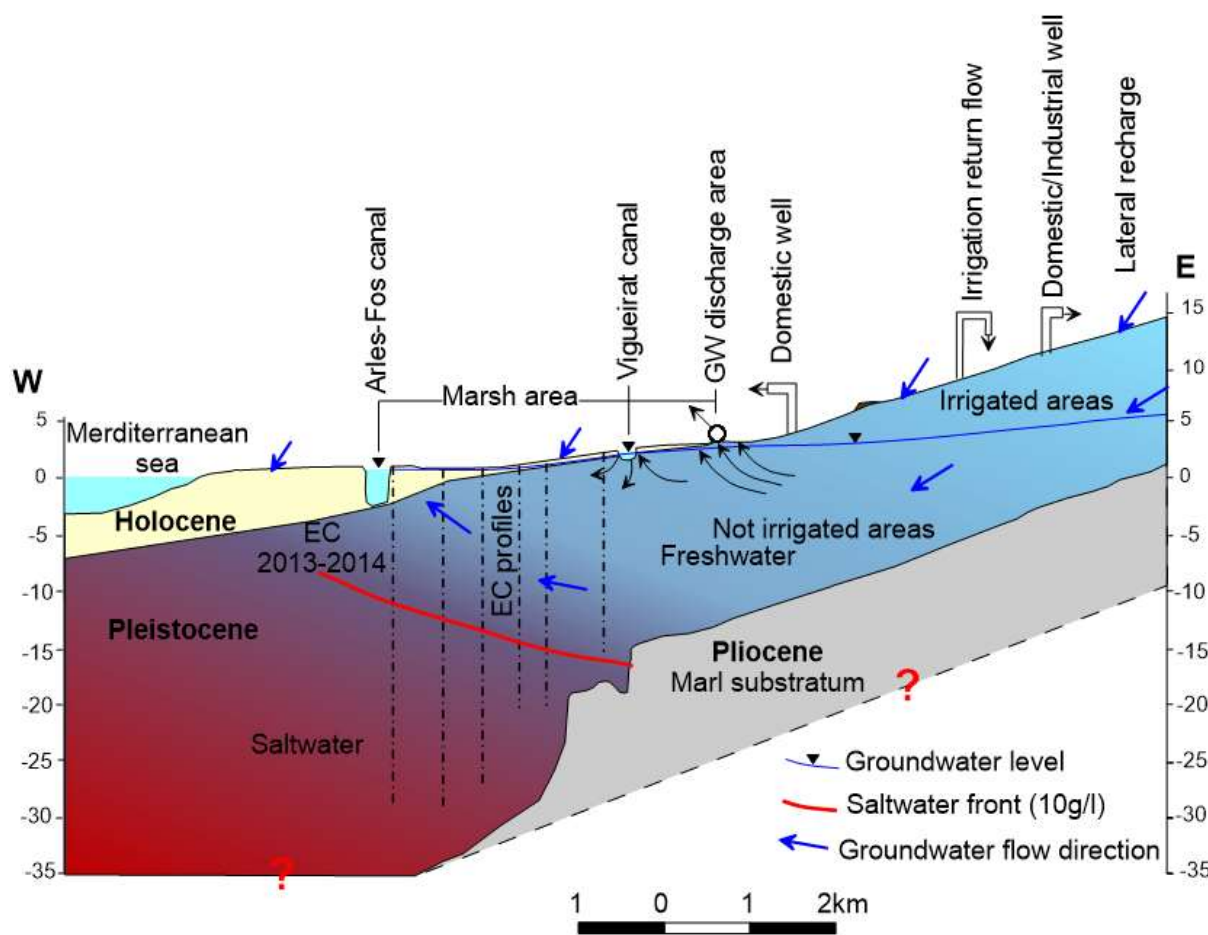


Figure 50. Conceptual model based on geological and hydrodynamic data.

The topography shown in (Figure 14) is based on kriged information from 203 boreholes/wells and national geodesic points (<http://geodesie.ign.fr/>). The main geometric-structural and hydrogeological characteristics of the study area (Figure 50) were based on

geological and lithological descriptions of boreholes and results of geophysics surveys (3 ERT profiles and 12 EM profiles). The digital elevation model (DEM) of each layer surface was interpolated by ordinary kriging.

#### 4.3.1.2 *Water table*

Until now, more than 60 observation wells have been set in this area by difference organizations. Most of observation wells have been installed since the 1980 years and surveyed with monthly measurement data. From 1999, BRGM continuously surveyed groundwater with data loggers (Pz32, Pz9, Pz11, Pz13, Pz21). Data are available from ADES database (<http://www.ades.eaufrance.fr>). We monthly measured water heads in 45 boreholes (Figure 21) from March 2013 to March 2014 during geophysical and geochemistry studies. Measured water levels have been converted to equivalent freshwater levels (section 3.2). A maximum correction of about 0.33m was done on piezometer XD (Table 1). The resulting hydraulic head map shows a global NE-SW flow direction (Figure 25).

In study area, the aquifer is unconfined to semi-confined in the marsh area due to the clayey layer with very low permeability (semi-pervious or impervious material). Aquifer is mostly recharged by the direct infiltration of rainfall and water flowing from upstream zone (N-E area). The natural outflow of the aquifer discharges into the canal system, but also by evapotranspiration and pumping wells. Part of groundwater flows out of study area to SW direction.

#### 4.3.1.3 *Salinity of groundwater*

Due to the good correlation between electrical conductivity and chloride concentration (Bear, 1988, Stuyfzand, 1989, Post, 2012), EC could be used to survey saltwater intrusion. Groundwater chlorine concentration was studied by electrical conductivity measurements in boreholes and surface waters of canals and ponds. The distribution of electrical conductivity has been discussed in section 3.2 (Figure 23 and Annex 3). The highest electrical conductivity are observed in the marsh area, on the S-W part of study area, along the Arles-Fos canal. The EC measurement varies in space and depth. The highest values, about 54mS/cm, have been observed into piezometer XD.

#### 4.3.1.4 *Exchange with surface water*

The water level in canal and pond have been observed automatically in 4 points (S2, S3, S5, S6) and measure manual at two point E1 and E2. From the observation data, water level in boreholes is little higher than in surface water. This seams indicate that groundwater discharges to surface water but with a very low flow rate. Results from radon survey have been used to

quantify the exchange between surface water and groundwater. From these results, groundwater discharge to canals and ponds is  $55 \text{ l/m}^2/\text{day}$ .

#### 4.3.1.5 Role of recharge

Recharge from rainfall is taken into account in the model as inflow applied on the top layer. This recharge was computed with time step of 10 days from 2000 to 2010 by the STICS crop model developed by INRA (Brisson N., 2009). This calculation has been calibrated and simulated with the help of Baillieux A. (INRA, 2013). The average recharge used into the model ranges between 0 and 2 mm/day, with an average value of about 0.6 mm/day.

#### 4.3.1.6 Importance of pumping wells

Pumping wells are included in the model as boundary conditions. Well screens were set as indicated by the technical description of the well. Some of them are multi-layer wells. Annex 4 and Figure 51 provide information and location of pumping wells area. 8 wells are owned and operated by municipalities or industries with abstraction rate of about  $40,388 \text{ m}^3/\text{day}$  and 71 private wells with average pumping of  $15,640 \text{ m}^3/\text{day}$  mainly for irrigation.

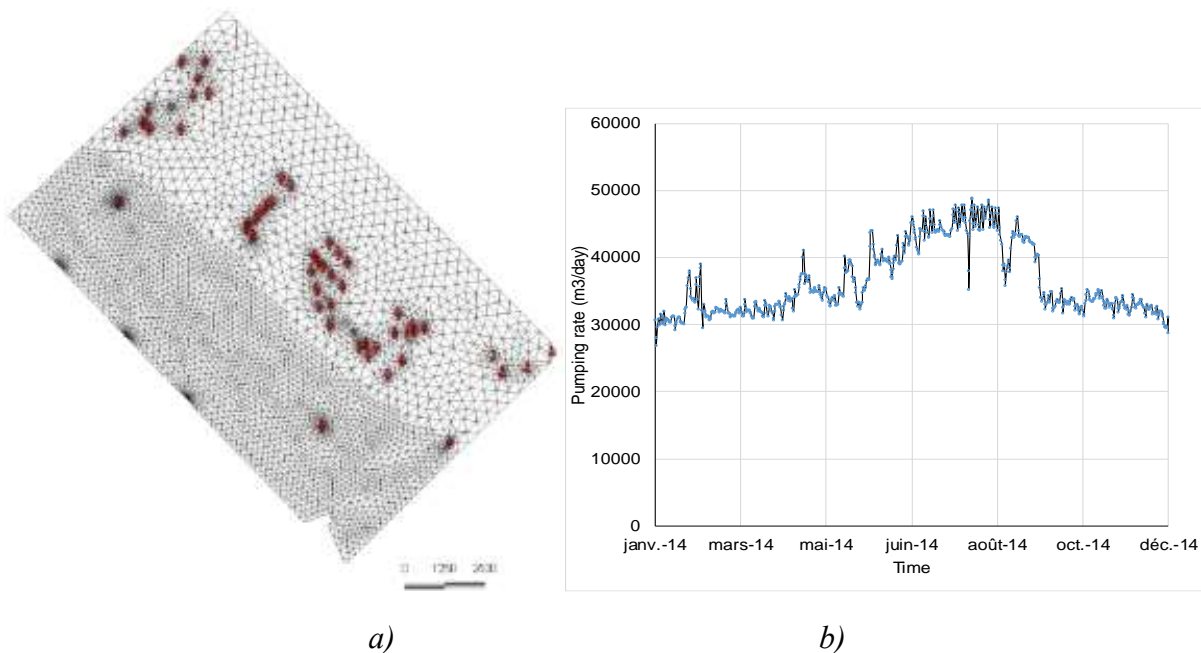


**Figure 51.** a) Pumping wells location in modeling b) total daily pumping rate (data in 2014)

### 4.3.2 3D density-dependent flow model

Despite previous studies and existing data, there are still remaining unknowns about the behavior of groundwater flow in Crau aquifer. Developing a 3D density dependent flow numerical model will help to integrate all the available information and experiment results to better understand the groundwater dynamic and its effect on saltwater intrusion. Before building

model, all input parameters such as initial water heads, hydraulic conductivity, porosity, storativity and geometry of aquifer have to be collected. All layer properties were interpolated from this information using conventional kriging.

#### 4.3.2.1 Boundary conditions

The horizontal mesh refinement includes 150,285 elements and 81,840 nodes covering an area of about 140km<sup>2</sup>. A high degree of mesh refinement was adopted also along the boundaries and pumping/observation wells which were placed in the mesh as fixed nodes representing their true position. The elements dimensions range from less than 15m around the control points such as pumping wells and observation wells to about 70m in the marsh area or up to 200m in the rest area. This mesh has been built to have a good detail into both the pumping well area and the marsh one. The 3D numerical model (Figure 52) consists of 12 numerical layers subdividing the aquifer system made of sandy clay and sandy gravel. The bottom of layers was obtained by combining lithological descriptions from drilling well and results of the ERT and EM investigations. The upper layer, that appears in marsh SW area of study area, mainly consists of impermeable clay to sandy clay sediments with depth varying from 0 to 7m and hydraulic conductivity  $K$  of  $3.7 \times 10^{-5} - 8.7 \times 10^{-3}$  m/s. The specific yield of aquifer obtained from pumping tests is in the range of 0.01 to 0.18 attesting the unconfined to semi-confined (leaky) behavior of aquifer. It overlies the main aquifer layer consisting of sand, pebble and gravel sediments with sandy-clayey matrix that shows high lateral heterogeneity due to the shift of the Rhone River. In the studied sector, the depositional surfaces have a slight slope to South-West, which is also the general trend of groundwater flow. Due to the alluvial placer dynamic, hydraulic conductivity ( $K$ ) is very variable. Resulting transmissivity globally varies between  $5 \times 10^{-3}$  and  $5 \times 10^{-1}$  m<sup>2</sup>/s.

The system is constrained by boundary conditions: NW and SE boundaries were set as no-flow conditions. NE and SW boundaries were set as constant water head (Dirichlet type). NE boundary was considered as a constant water head according to the water table simulated by the model of Crau aquifer (INRA, 2013) and to observation wells (BGRM). The constant water head conditions applied along the SW boundary is set to the water levels measured in observation wells of this area. Along SW boundary and in marsh area, a system of drainage condition (Neumann type) represents draining canals of Arles-Fos, Vigueirat and Colmatage. The drain conductivity was assumed to be equal to the hydraulic conductivity of the clay and sandy clay layer. The groundwater recharge rate from irrigation and rainfall was specified in the model as a sink/source boundary condition. Input values were calculated by STICS model for each model elements with time step of 10 days (INRA, 2013). Discharge condition (flux boundary) was assigned for the pumping wells (10 municipal pumping wells and private irrigation wells).

Boundary conditions are summarized on Figure 52. In a variable-density flow model, concentrations along the boundaries are also required.

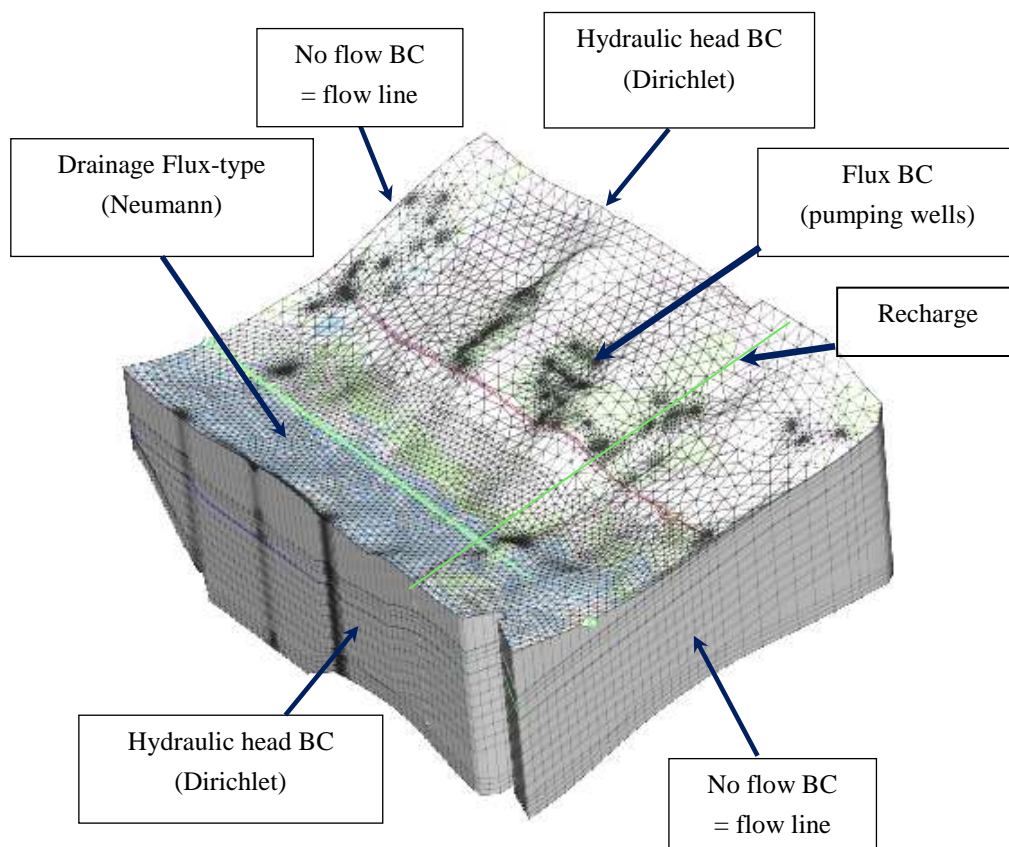


**Figure 52.** Boundary conditions

#### 4.3.2.2 Model parameters

Porosity of aquifer was specified in the range 0.038 and 0.17 with an average of 0.5 as estimated using Archie's law for difference depth (as discussed in 4.1.2).

The concentration of freshwater is 0 g/l and the density is 1000 kg/m<sup>3</sup>, and respectively of 35 g/l and 1.025 kg/m<sup>3</sup> for seawater. The longitudinal dispersivity is 0.35 m and transverse dispersivity is 0.003 m. The aquifer is mainly unconfined therefore specific yield is approximately equivalent to the storage coefficient and was set to 15%.

**Table 8.** Input parameters and boundary conditions applied to the model

Input variables		Numerical solution parameters	
Recharge (average) (mm/day)	0.6	Number of elements	150285
Pumping rates of all wells (m <sup>3</sup> /d)	56600	Number of nodes	81840
$\rho_s$ (kg/m <sup>3</sup> )	1025	Number of layers	15
$\rho_f$ (kg/m <sup>3</sup> )	1000	Area of model (km <sup>2</sup> )	140
$C_s$ (kg/m <sup>3</sup> )	35	Clay layer size (m)	0-7
<b>Estimated parameters and starting values</b>		Aquifer layer size (m)	9-28
$K_h$ of clay layer (m/s)	$3.7 \times 10^{-5}$ – $8.7 \times 10^{-3}$	Time step length (day)	< 1
$K_h$ of aquifer	$2.5 \times 10^{-4}$ – $1.2 \times 10^{-2}$		
$K_z / K_h$	0.1		
$S_y, S_s$ clay layer	0.001, $10^{-6}$		
$S_y, S_s$ aquifer	0.05, $10^{-5}$		
$\alpha_L, \alpha_T / \alpha_L$ (m)	10, 0.1		
n of clay	0.01		
n of aquifer	0.1		

Model is run in 2 modes: i) steady state condition of flow used to get suitable initial conditions (heads and concentrations) for the transient model; ii) transient simulation mode from 2004 to 2014. Simulated results were compared to water heads and electrical conductivities observed in boreholes (including 45 manual surveys and 4 continuous surveys).

### 4.3.3 Information on saltwater intrusion

Realistic models must include the three dimensions distribution of lithological units and their hydraulic properties (Günther et al., 2014). However, model parameters are never completely defined and always associated to uncertainties (Gunduz et al., 2004). Physical properties of aquifer such as hydraulic conductivity, porosity and storativity are the most important parameters for flow. With saltwater intrusion models, initial groundwater salinity is also required. The use of geophysics to provide information to model have been applied in many previous researches (Stewart, 1982, Borne, 1990, Buchanan and Triantafilis, 2009, Sirhan and Hamidi, 2012). For saltwater intrusion, geophysical data may be used through a coupled

hydrogeophysical inversion (Bouzouf et al., 2001, Comte and Banton, 2007, Comte, 2008, Capizzi et al., 2010, Comte et al., 2010, Herckenrath et al., 2013a, Herckenrath et al., 2013b). Additionally,  $^{222}\text{Rn}$  concentrations can be used as a natural tracer to estimate the groundwater flow velocity (Hamada, 2000, Schubert et al., 2011) and assess the groundwater discharge. Application of geophysical and isotopic studies, therefore can be combined to classical measurements of water heads and water salinity.

Petrophysical and geometric items are two separate groups of the relationships between geophysical models and hydrologic models. Petrophysical relationship describes the correlation between a geophysical parameter and a hydrologic variable or parameter (Herckenrath et al., 2013b). The common one is Archie's law (Archie, 1942) that describes the dependence of bulk electrical conductivity ( $\sigma$ ) to pore water conductivity ( $\sigma_w$ ) and porosity (see section 4.1.2).

Porosity of aquifer has been estimated by using results of inversed ERT model with application of Archie law. For model, we assumed that porosity are horizontally homogeneous and vertically heterogeneous, i.e. vertically distributed.

The second type of constraints coupling geophysics and hydrologic models is the geometric relationship describing the spatial characteristics of the subsurface. Geometric constraints are used to delineate geological units (elevation and thickness of layer) and spatial structure of heterogeneous aquifer properties.

The variation of electrical conductivity is also indicating the variation of the lithology. ERT and EM methods are successfully applied since the electrical conductivity is sensitive to both clay content and groundwater salinity (Goldman et al., 1991, Kafri and Goldman, 2005, Triantafilis and Lesch, 2005). The results of geophysics are described in section 1.1. Lithology can be divided in different units. A superficial unsaturated layer of coarse sand and gravel with a thickness about 6m is located in the NE marsh area (center of the study area) and shows very low  $\sigma < 2\text{mS/m}$  (sector EM1). The saturated coarse sand and gravel layer of freshwater with  $\sigma$  ranging from 2 to 30mS/m is found in the NE marsh area (sector EM1-EM5). A superficial fine sand and clay layer found in marsh area above the saltwater with a thickness increasing toward SW from 0 to 5-7 m along the Arles-Fos canal (sector EM5-EM12). This high conductive layer with  $\sigma$  from 100 to more than 300 mS/m is due to clay cation activity and dissolved salt resulting from evapotranspiration. Using the lithological information obtained from borehole and EM – ERT investigations, the 3D organization of lithology unit is as show in Figure 52.

#### 4.3.3.1 Hydraulic parameters estimated from geophysics and isotopes

For modeling, the most important parameters are the hydraulic conductivity and porosity. These parameters were estimated from the results of geophysics and isotope measurements.

The hydraulic conductivity was discussed in previous studies but these lasts do not provide enough information for the marsh area. The locations where of hydraulic conductivity values are available from previous and current studies are shown in Figure 53. We used the approach proposed by Schubert and Hamada (Hamada, 2000, Schubert et al., 2011) where groundwater (Darcy) flow velocity can be estimated by using the decay of  $^{222}\text{Rn}$  in single well (sections 3.4 and 4.2).

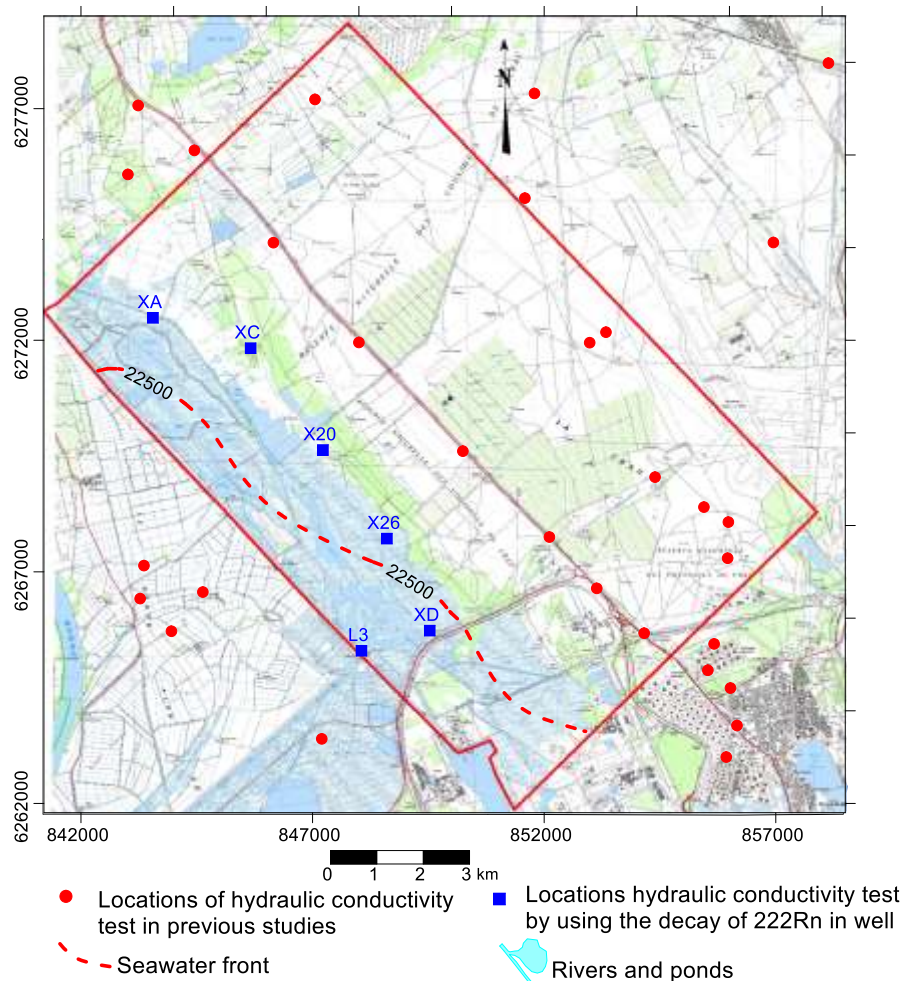


**Figure 53.** Locations of K value estimated from previous and current studies.

The groundwater velocity was estimated at three different depths in 6 boreholes and provided hydraulic conductivity using the water table gradient (Section 4.2 - Table 3). These estimated permeabilities have been used to calibrate the model. Spatial distribution of hydraulic conductivity was kriged using values of hydraulic conductivity.

#### 4.3.3.2 Estimation of groundwater electrical conductivity from geophysics

Using the distribution of  $\sigma$  obtained from EM and ERT, the electrical conductivity of groundwater  $\sigma_w$  was estimated using the equation of Archie (1942) as follow:



sediment bearing high conductivity of  $\sigma > 80\text{mS/m}$  are found at 3-7 m depth in the SW area (Pissarotte area) increasing to the depth of 15-20 m in Vigueirat area. In the middle of the marsh area, fresh water extends to the depth of 30 m. Saltwater intrusion thickness decreases from the SW limit of the study area to the center of the marsh area and intrusion disappears after the marsh area (sectors 5, 6, 7, 8 and 10 in Figure 45, Figure 43 and Figure 44). Groundwater EC increases with depth towards SW due to seawater intrusion and diffusion. The most conductive area is found in Pissarotte area (Figure 43) and along the Arles-Fos Canal (Figure 44) with  $\sigma > 150\text{mS/m}$  at less than 10m depth. This is observed in all other sectors of marsh area (Figure 45). Combining measurements of EC in boreholes and estimated EC from geophysics (using Archie's equation), the initial distribution of groundwater EC was computed.

#### **4.4 Coupling geophysical and isotopic approach to calibrate and validate saltwater intrusion modeling**

Model calibration is a very important step to ensure the accuracy of developed modeling. In this process, model parameters are adjusted until the simulated results (hydraulic heads, flow rates, concentrations) fit the observed data.

##### *4.4.1.1 Calibrating model using measurements from boreholes*

The model was first ran in steady state condition for the mean situation of March 2013 - March 2014 and calibrated with measured hydraulic heads and groundwater EC of 45 boreholes and 4 continuous surveys. All input parameters have been changed in their initial range using trial-and-error process until a steady state was reached. Calibration has been achieved modifying hydraulic properties and boundary conditions to fit the observed values of i) groundwater heads and ii) salinity concentration. The results shows a quite fair fit between observed and simulated water heads, as shown in Figure 55.

Errors between simulated and observed values water heads are small (from 0 to less than 1m) when compared to the hydraulic gradient and the dimension of aquifer. Note that observed heads vary from 0.5 in SW area to about 17m in NE area. The two sets of values are well correlated and close to the 1:1 line with RMS of 0.542 and an average absolute difference less than 0.5m. The highest difference is about 1m and obtained on Pz11 in the center of area.

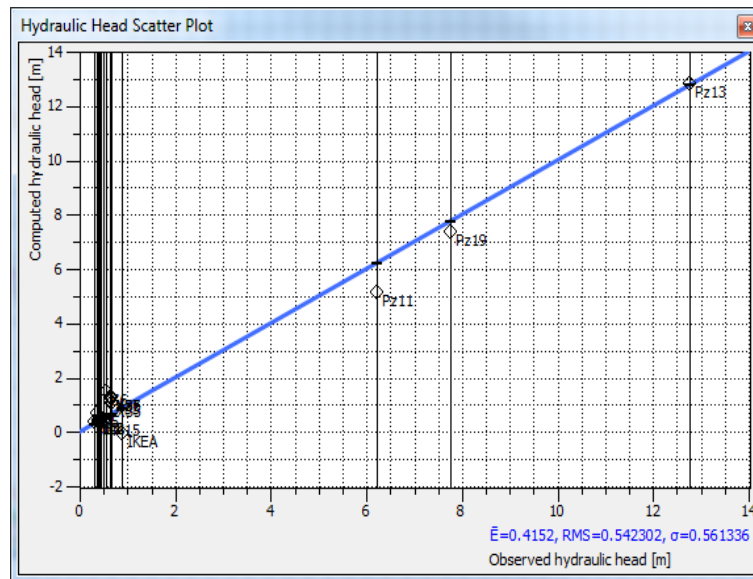


**Figure 55.** Comparison between observed and simulated water heads for the validation period from 3/2013 to 3/2014. Each value was extracted from the results according to daily frequency of sampling [m]

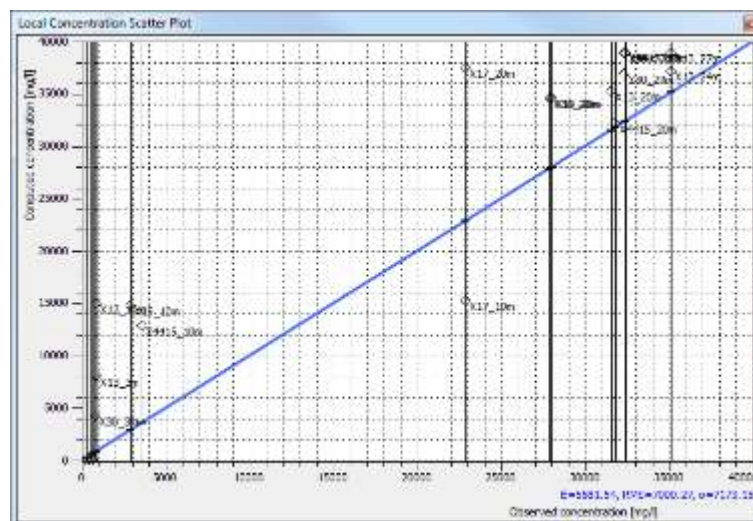


**Figure 56.** Comparison between observed and simulated of salt concentrations for the validation from 3/2013 to 2014[g/l].

**Figure 56** compares observed and simulated salt concentration of groundwater. The largest difference is observed in the saltwater-freshwater transition zone (in X17 at 10 m and 20 m depth). RMS for salt concentration is about 7000 mg/l with concentration observations from 500 to 36000 mg/l, giving an acceptable calibration.

The spatial distribution of hydraulic head shown on Figure 57 and salt concentration on Figure 58 are in agreement with field observations. The simulated results show the highest hydraulic gradient in the NE area and the lowest in the marsh zone with hydraulic head smaller

than 1.5m. In contrast, the highest salt concentrations in both observed and simulated distribution map are in the SW area and the salt water front close the marsh area.

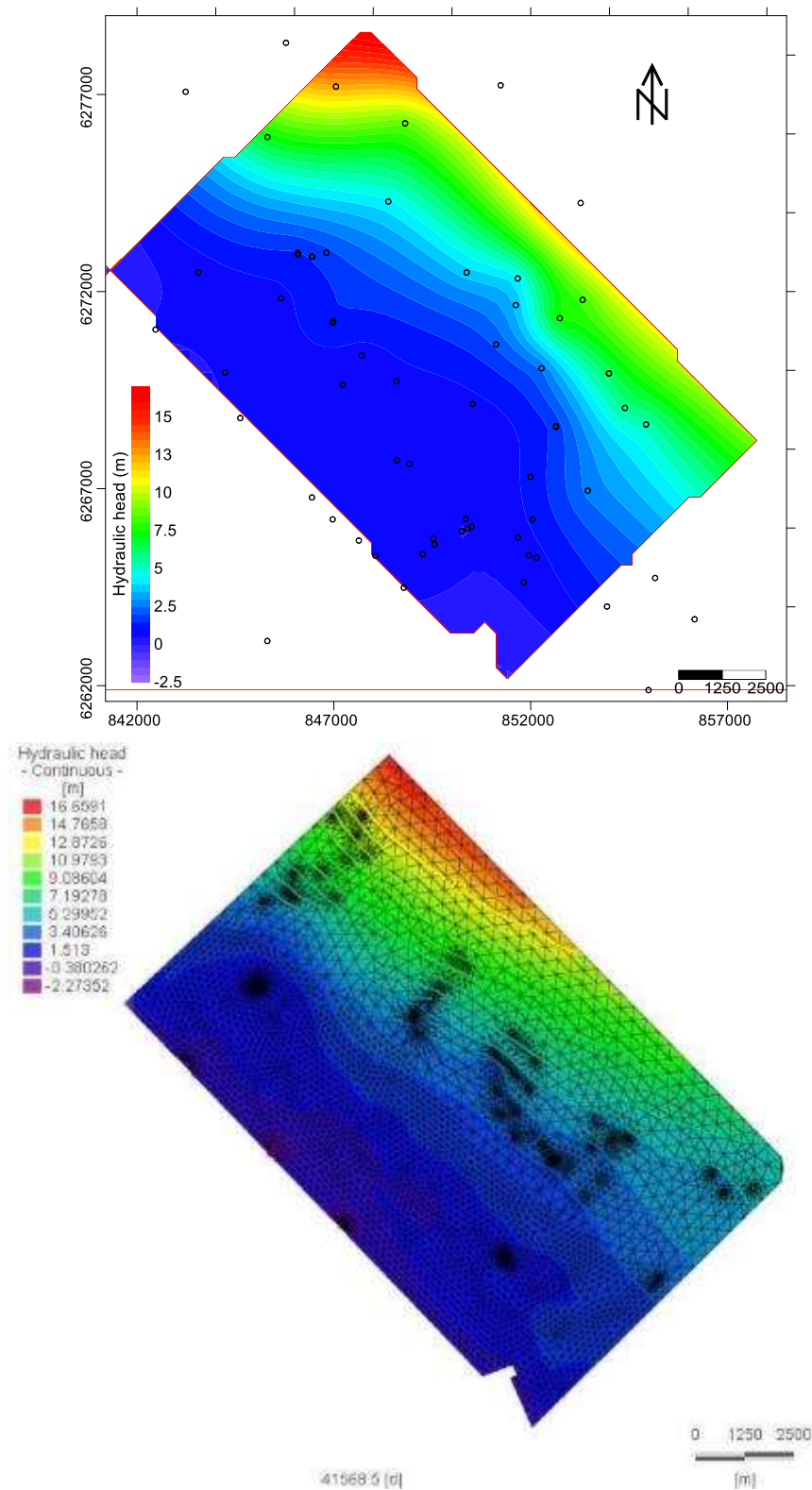


**Figure 57.** Comparison of hydraulic head between a) observation measurement in piezometer (black arrows are groundwater flow directions) and b) flow model results after calibration (hydraulic head contours in m) on 23/10/2013

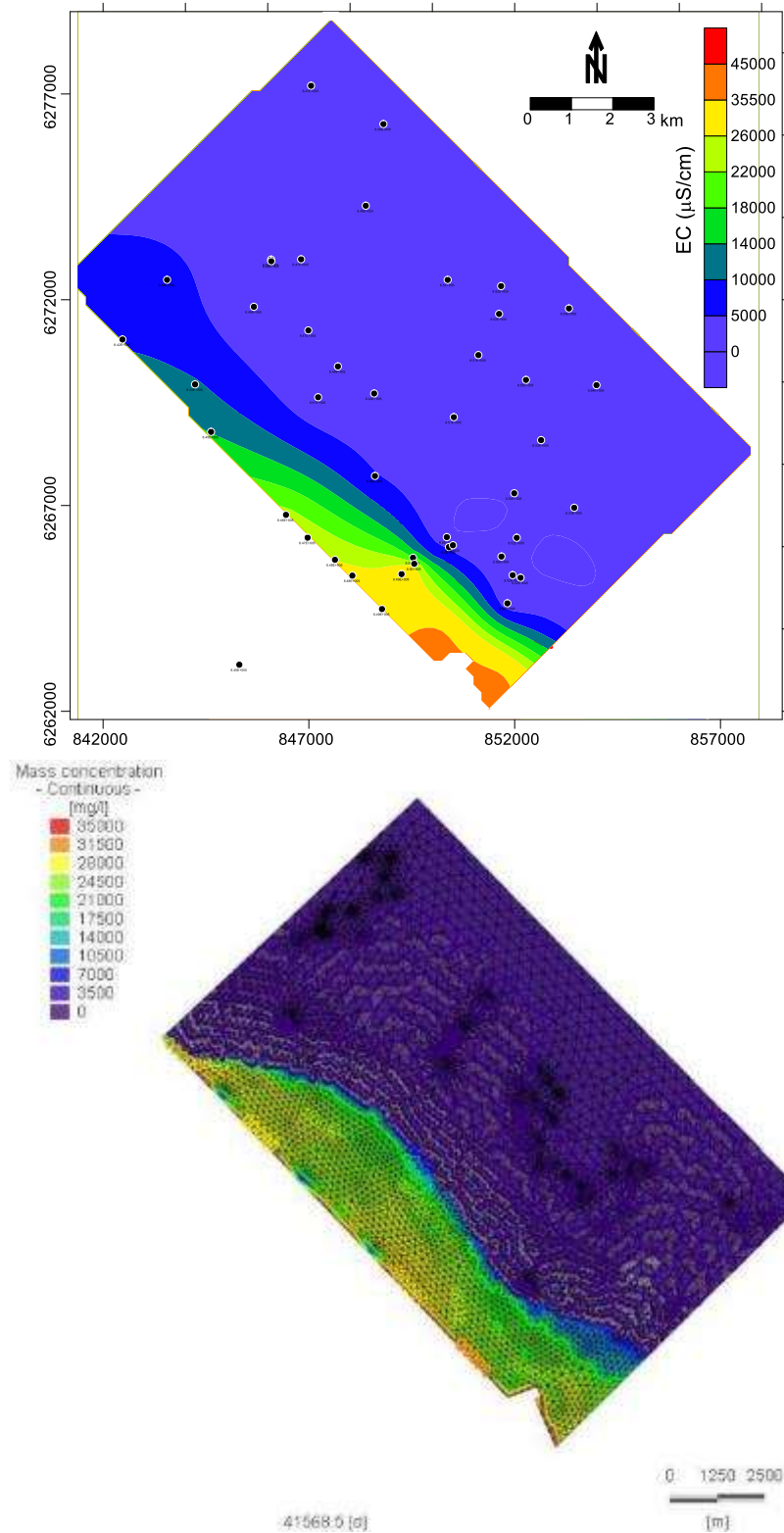


**Figure 58.** Comparison of spatial distribution of a) electrical conductivity of groundwater and b) calculated concentration at -10m asl (on 23/10/2013)

These calibrated results were used as initial condition for the transient state simulated over the 2004-2014 period. The pumping rates of the 10 municipal pumping wells were established on the records of the 2011-2014 period. For the unknown 2004-2010 period, we

assumed that the pumping rates are the same as those of 2011. A good agreement was globally achieved between simulated results and observed water heads (Figure 59) in continuous observation wells (Pz11, Pz13, Pz19 and Pz32; Figure 21).

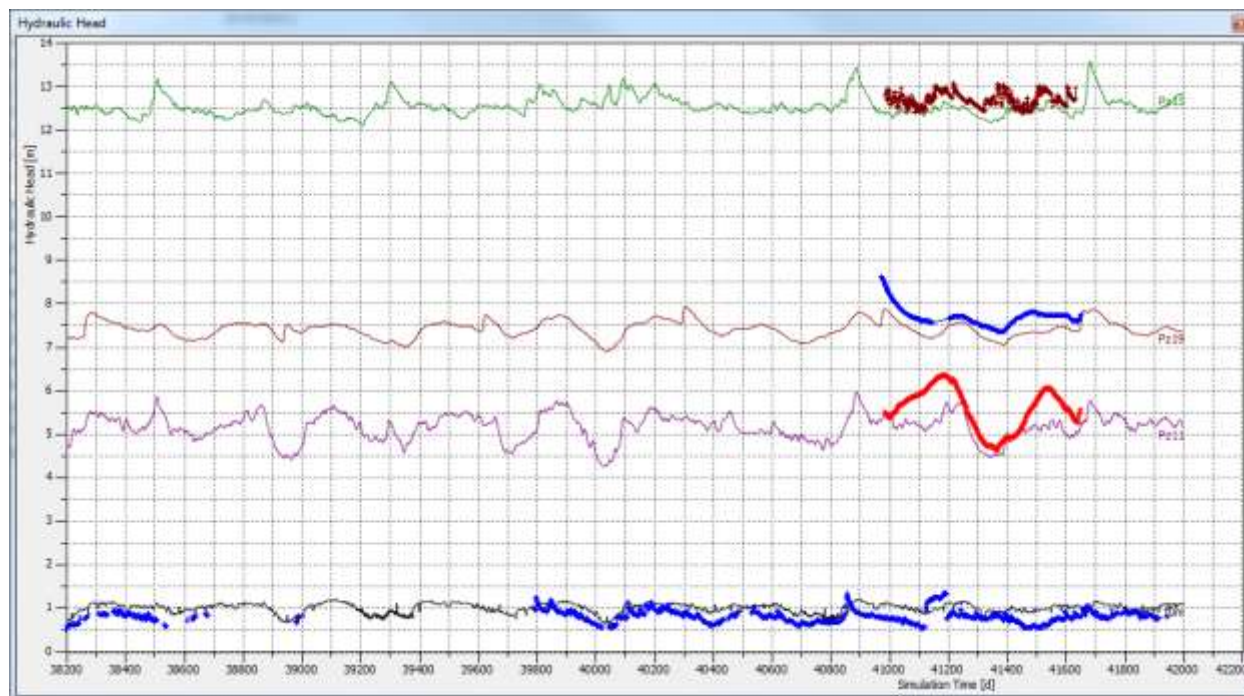


**Figure 59.** Evolution of the simulated and observed hydraulic heads during the 2004-2014 period

#### 4.4.1.2 Validation of simulated groundwater discharge using $^{222}\text{Rn}$

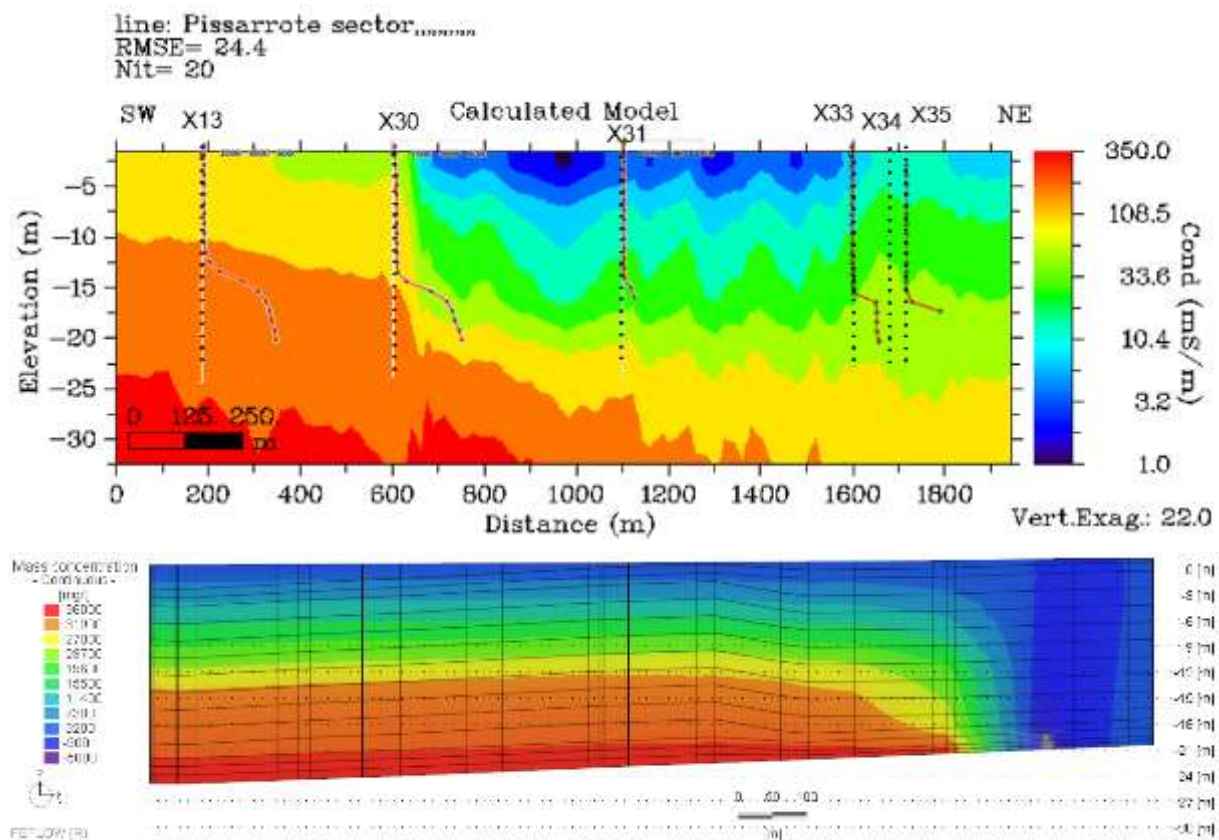
Groundwater discharge to surface water was estimated using  $^{222}\text{Rn}$  giving a value of  $55 \text{ l/m}^2/\text{day}$  for canal Arles-Fos and  $4\text{-}7 \text{ l/m}^2/\text{day}$  for the Landre pond. The total area of surface water systems have been simulated in saltwater modeling is  $2.38 \text{ km}^2$ , as detailed in Table 9. Total volume of groundwater discharge to surface water by this method was  $57,513 \text{ m}^3/\text{day}$ .

**Table 9.** Groundwater discharge to surface water estimated from  $^{222}\text{Rn}$  measurements.

No	Surface water	Seepage rate $\text{l/m}^2/\text{day}$	Area (sq km)	Discharge $\text{m}^3/\text{d}$
1	Arles-Fos canal	55	0.52	28,682.5
2	Colmatage canal	55	0.19	10,175.0
3	Vigueirat canal	55	0.19	10,241.0
4	Vigueirat pond	5.65	0.66	3,729.0
5	Landre pond	5.65	0.83	4,685.5
<b>Total</b>				<b>57,513.0</b>

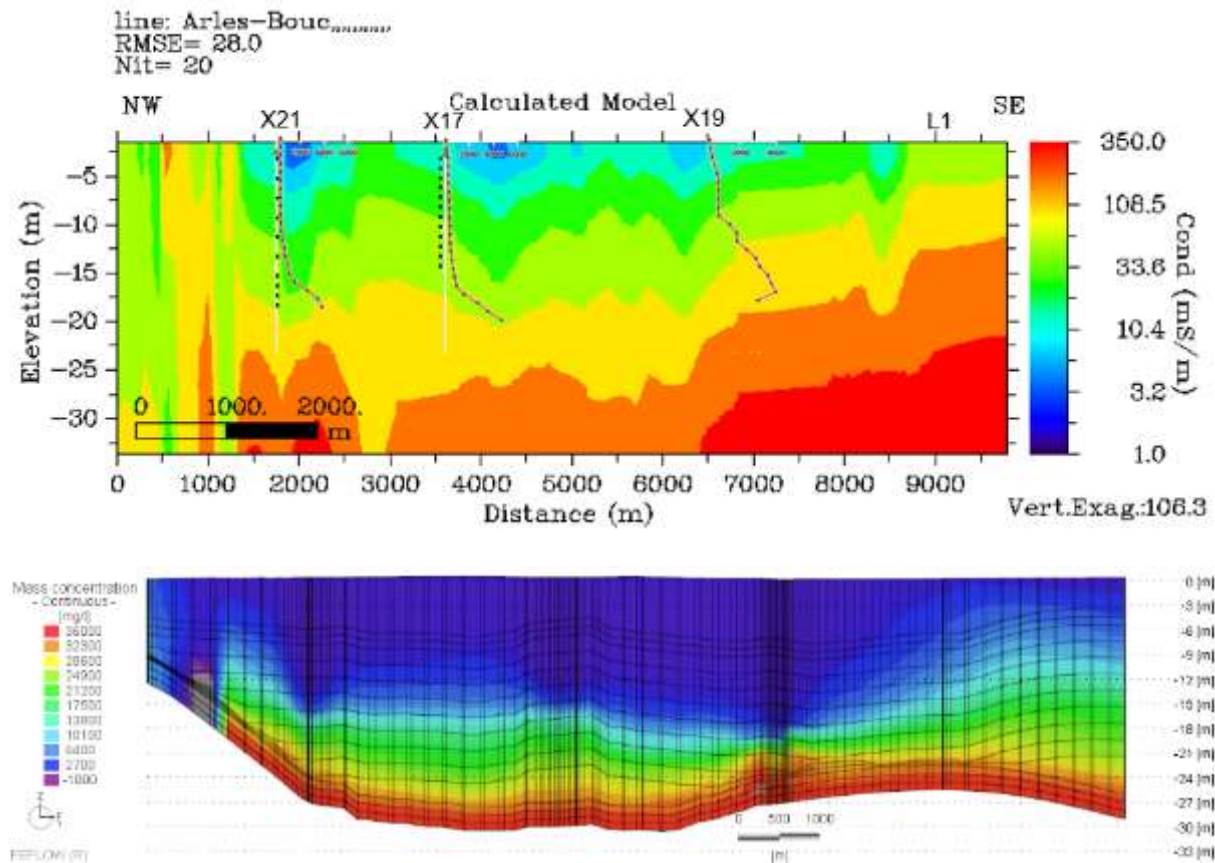
#### 4.4.1.3 Validation of saltwater intrusion using geophysics results

The simulated EC in Pissarotte area and along the Arles to Fos canal (Figure 60 and Figure 61) are consistent with observations. In Pissarotte area, results show a high conductivity zone. Near X1, this conductive zone distribute at about 13m of depth and shows EC over 200 mS/m. Upper this high conductive zone, conductivity varies from 80 mS/m to 200 mS/m with a thickness of about 10 m corresponding to the transition zone (TDS between 10 and 30 g/l in model). The low EC (below 50 mS/m in geophysics inversed model and below 3 g/l in hydrogeological model) were found in superficial layer from about 3 m into X30 and deeper than 10 m into X35.



**Figure 60.** Comparison between the 2D geoelectrical inverse model (EM profile) along the Arles to Fos canal and corresponding 3D saltwater intrusion model

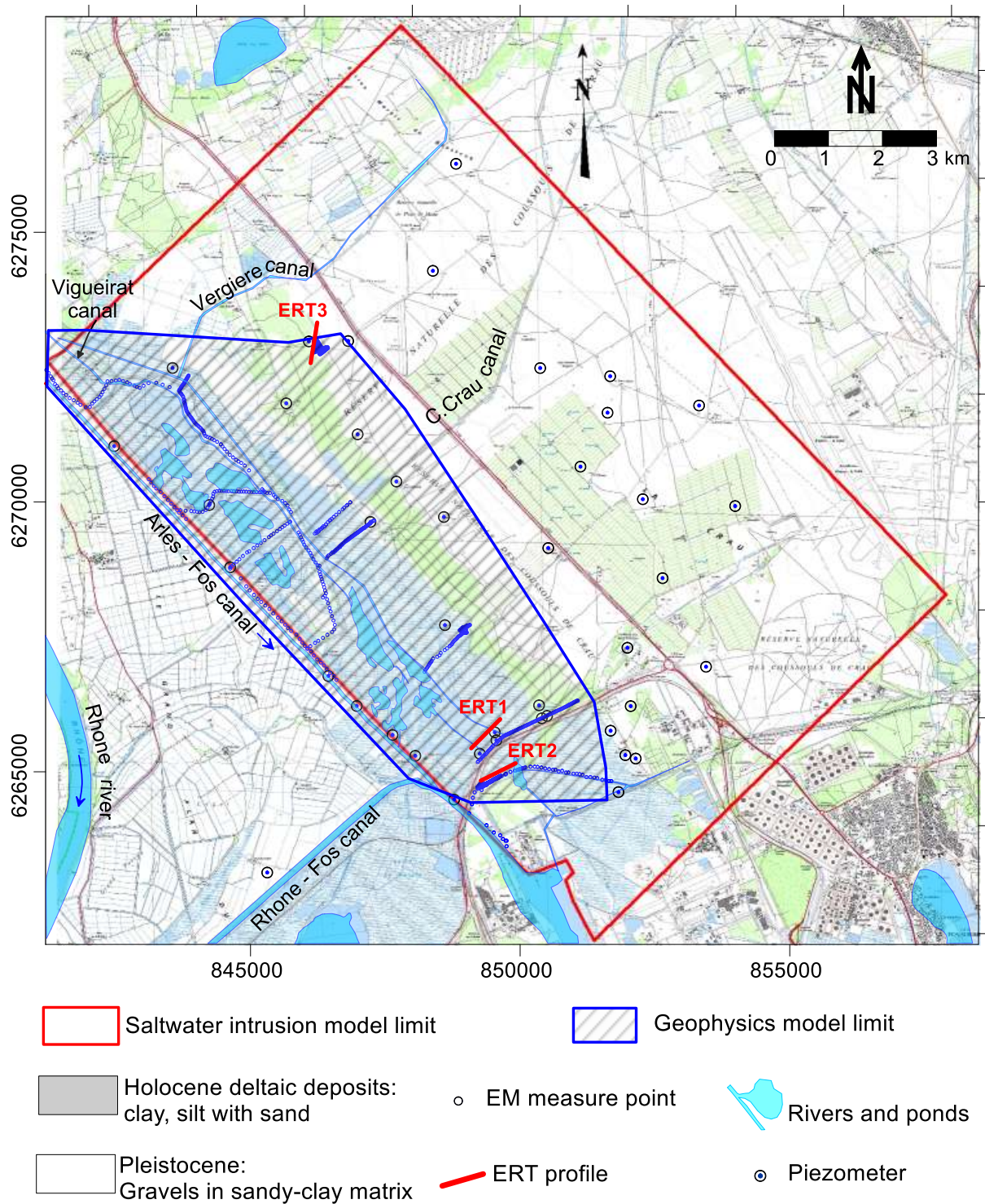
Similar to cross-section along the Arles - Fos canal (Figure 61), the saltwater pattern is an arc-shape from SE to NW. A conductive/saline zone is found below 13 m depth into L1 and below 22 m into X17 with an EC higher than 200 mS/m in geophysics model and a concentration higher than 10 g/l in groundwater model. An upper zone with EC between 80 and 200 mS/m in geophysics model and 3-10 g/l in groundwater model represents a resistive/brackish zone with a thickness of 5-7 m. The superficial layer with thickness of about 5 m at L1 and about 15-17 m at X17 and X19 represent the freshwater zone found on both models.



**Figure 61.** Comparison between the 2D geoelectrical inverse model (EM profile) in Pissarotte area and corresponding three3D saltwater intrusion model

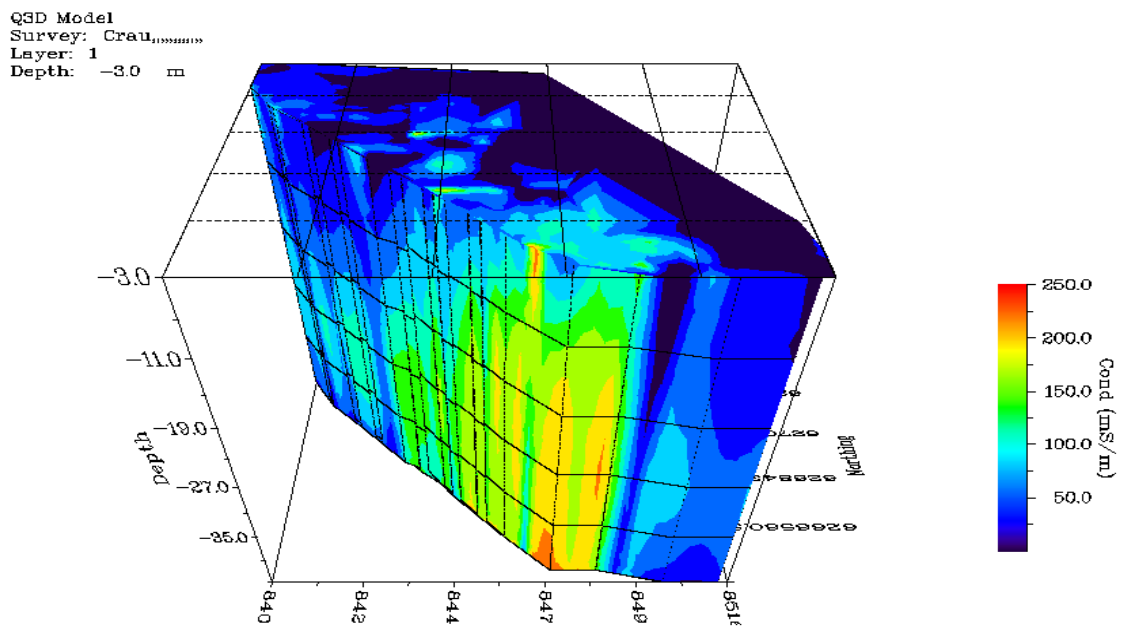
EM data can be inverted in quasi-3D (Santos et al., 2011) using a 1D spatially constrained technique. Quasi-3D spatial distribution of estimated EC has been done with EM4Soil to validate and calibrate the salt intrusion model. With EM4Soil (EM-TOMO, 2014), the forward modeling uses the cumulative function (McNeill, 1980) and the inversion algorithm the Occam regularization method (Sasaki, 1989, de Groot-Hedlin and Constable, 1990). The distribution of EM34 measurement points and limit for this model is shown in Figure 62 and results from the model shown in Figure 63 and Figure 65.

Figure 65 shows the spatial pattern of estimated EC from EM34 data at different depths. All spatial distributions show that a high conductivity zone SW the study area. These conductive zones can potentially present saltwater intrusion. Using Figure 43, Figure 44 and Figure 45, and with respect to geological material and EC, the limit of clay layer and the interface of saltwater-freshwater have been defined from 3D groundwater model.



**Figure 62.** Location of EM measurements and limits of interpolated geophysical model

From both 3D models from geophysics and groundwater model, the distribution of EC and TDS are qualitatively comparable.



**Figure 63.** 3D distribution of estimated EC ( $\sigma$  - ms/m) from a joint inversion of EM34-10, EM34-20 and EM34-40 data using a 1-D laterally constrained algorithm for quasi-3D EC imaging

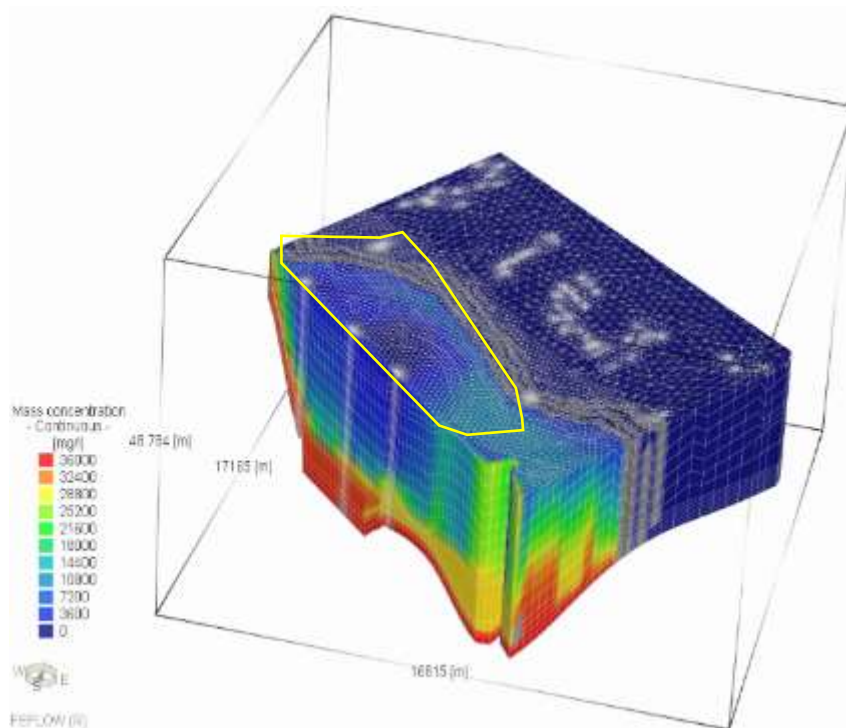
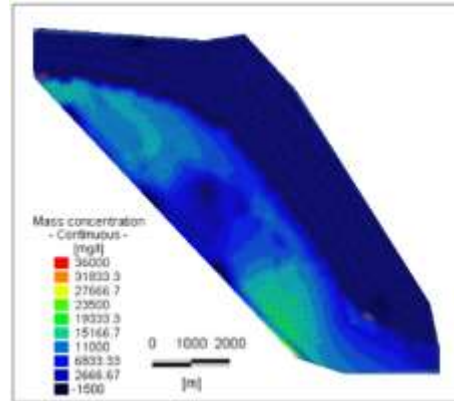
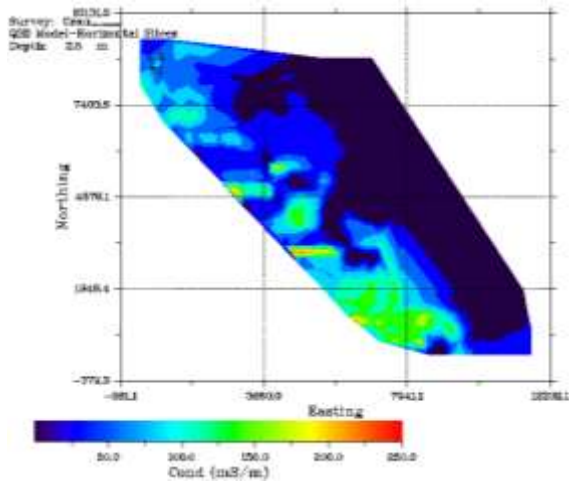
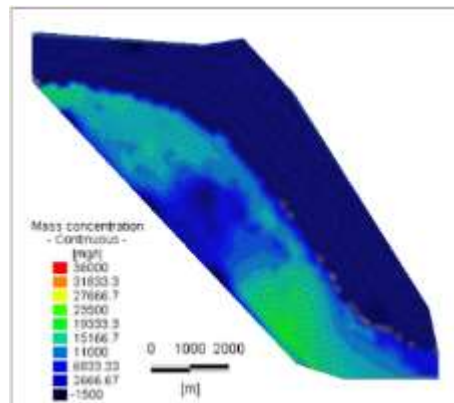
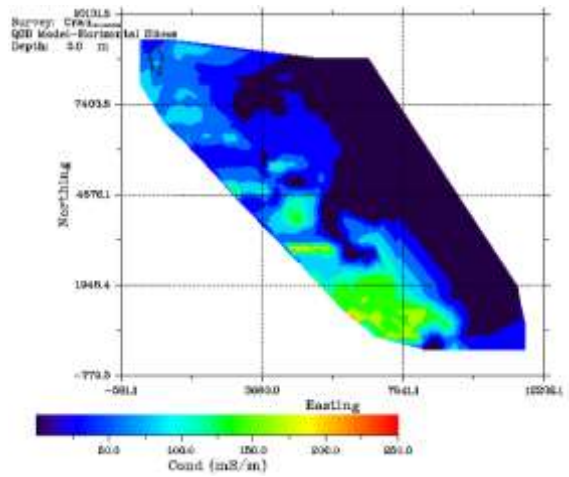


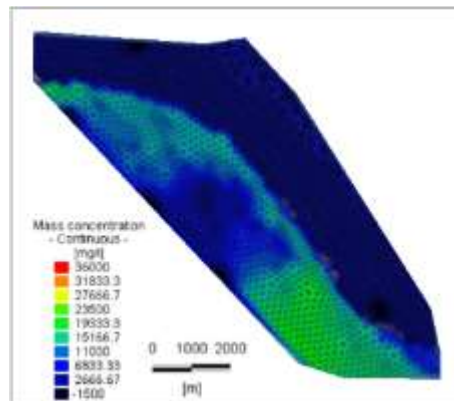
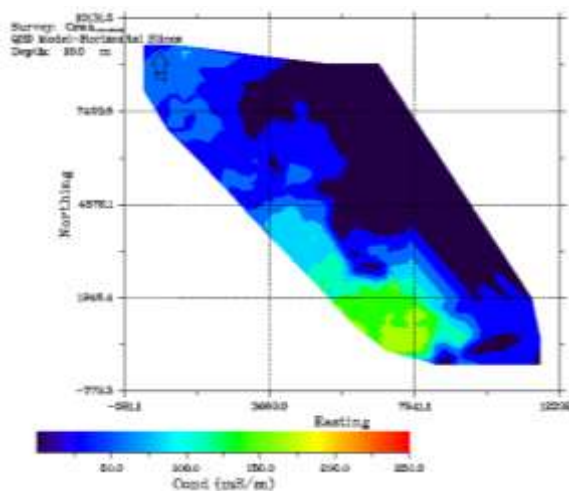
**Figure 64.** 3D distribution of TDS concentration (mg/l) from 3D groundwater model (clip at -3m from the soil surface)



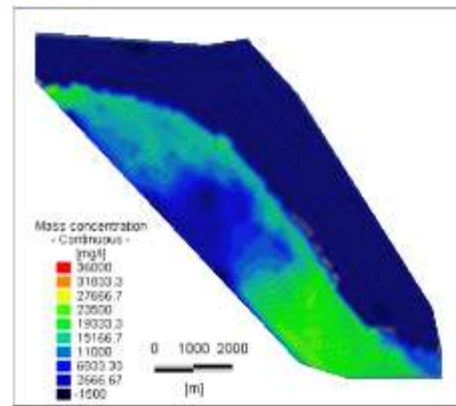
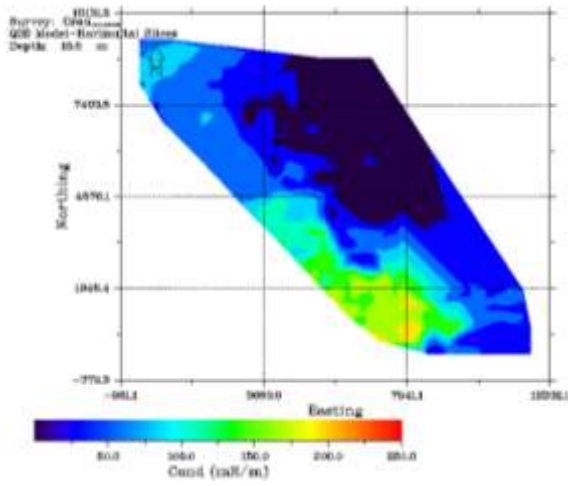
a. 2.5m



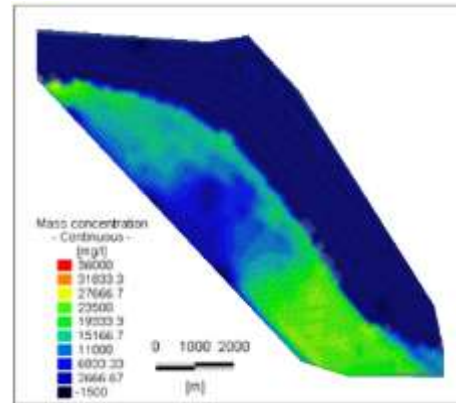
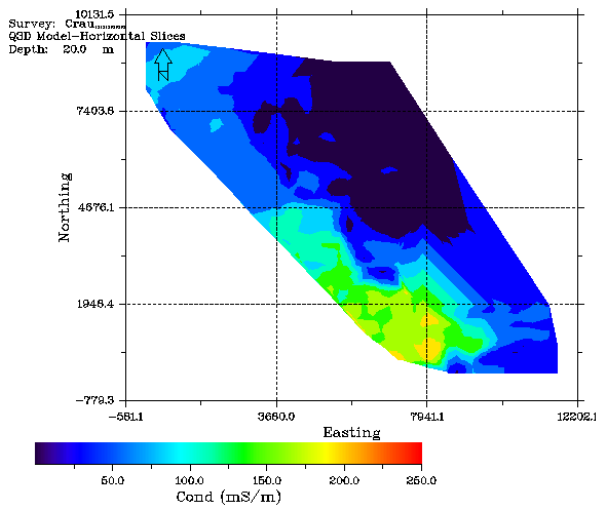
b. 5m



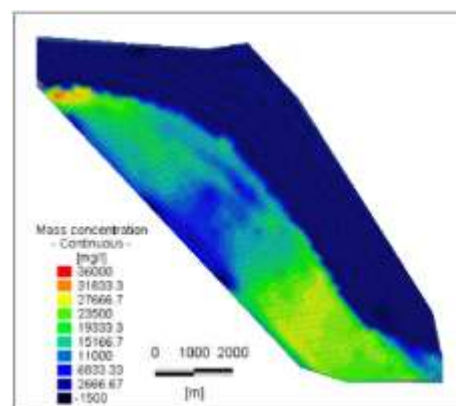
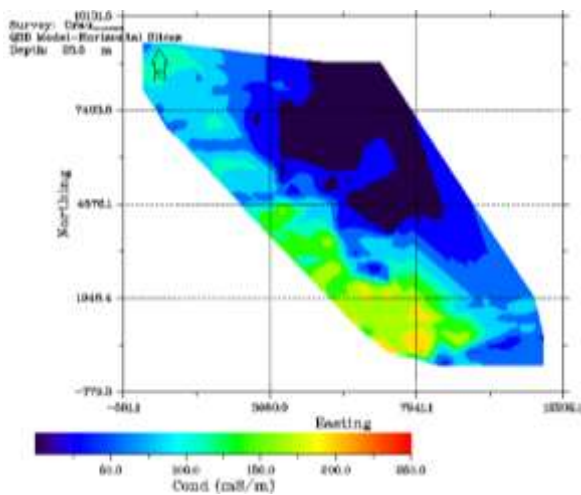
c. 10m



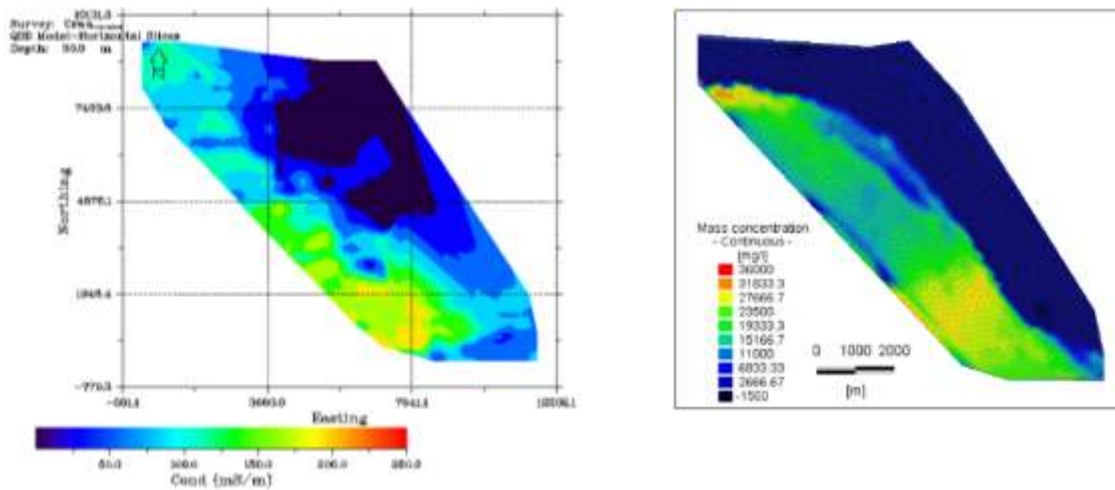
d.15m



e.20m



f.25m



*g.30m*

**Figure 65.** Comparison simulated EC from geophysics and numerical models at depth of a. 2.5m, b. 5m, c. 10m, d. 15m, e. 20m, f. 25m, g. 30m. Left) Spatial distribution of estimated EC ( ms/m) from a joint inversion of EM34-10, EM34-20 and EM34-40 data using a 1-D laterally constrained algorithm for quasi-3D conductivity imaging; right) Mass concentration distribution from numerical model

The mass concentration and fluid budget obtained from validated model is presented on [Figure 66](#). Mean recharge in marsh area occurring from ponds and canals is 12,843m<sup>3</sup>/day and groundwater discharge to surface water varies from 32,340 m<sup>3</sup>/day to 333,000m<sup>3</sup>/day and in average of 92,528 m<sup>3</sup>/day. This flux to surface water is higher than the one calculated with radon ([Table 9](#)) because it includes groundwater drained by the network of streams at the northern rim of the pond's area (Colmatage, Vergière, Centre Crau canals). These streams are characterized by elevated radon activity that confirms that these water are essentially groundwater drained locally.

We can see from [Figure 66](#) that the sum of all input and output fluxes does not equilibrate in this system. A reason for this disequilibrium could be the changes of pond's surfaces and groundwater and surface water levels, implying that this system is not necessarily in steady state condition in terms of water mass balance.

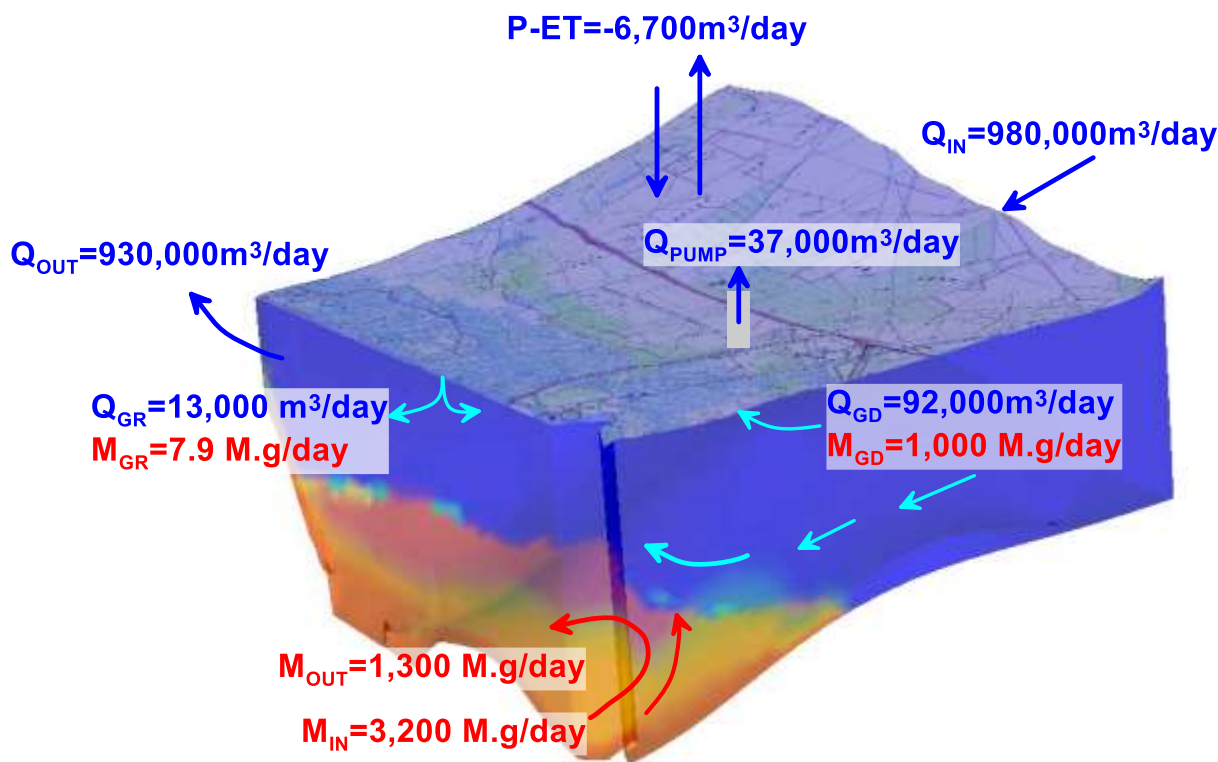


**Figure 66.** Fluid and mass budget (average of simulated results for 2014) based on the results of numerical modeling.  $Q_{GD}$  is the volume of groundwater discharge to surface waters. Inversly,  $Q_{RD}$  is the volume of groundwater recharged from surface waters (ponds and canals).

#### 4.5 Effect of recharge and pumping on saltwater intrusion

The model was used to assess the possible control of saltwater intrusion through the reduction of groundwater extraction by pumping wells or by the increase of the recharge from surface water. Various scenarios have been done to simulate the saltwater intrusion in 2014 with the following conditions:

- all pumping wells stop in this study area;
- pumping rates double with respect to current rates;
- no recharge occurs.

Simulated water heads of scenarios 1 and 2 are compared against heads obtained with the current pumping rates (Figure 67). Change on water heads varies between 0.2 and 1 m depending of the location of the observation borehole. For boreholes close the pumping wells, change is higher.

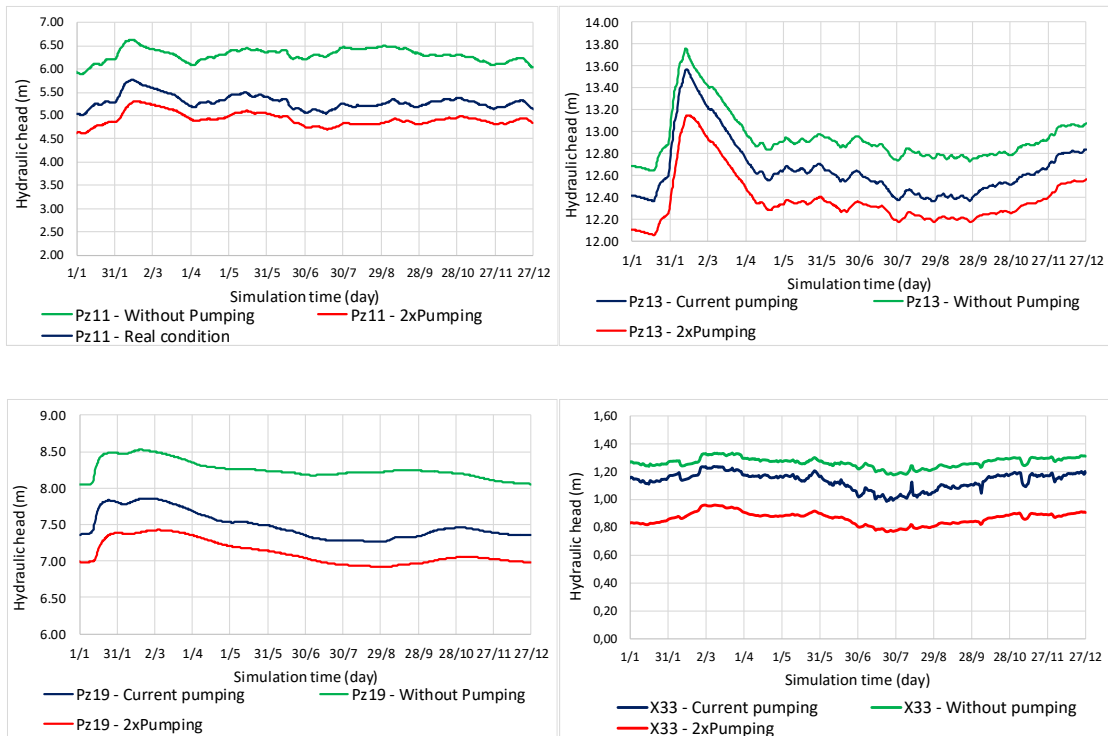


Figure 67. Comparison of hydrographs of observations wells for scenario 1 and 2

For scenario 3 without recharge, water heads are significantly higher than those of current condition (Figure 68). This is clear that the recharge in this area play an important role to groundwater. However, maximum changes are 0.5 m, i.e. less than the changes induced by the modification done on pumping rates.

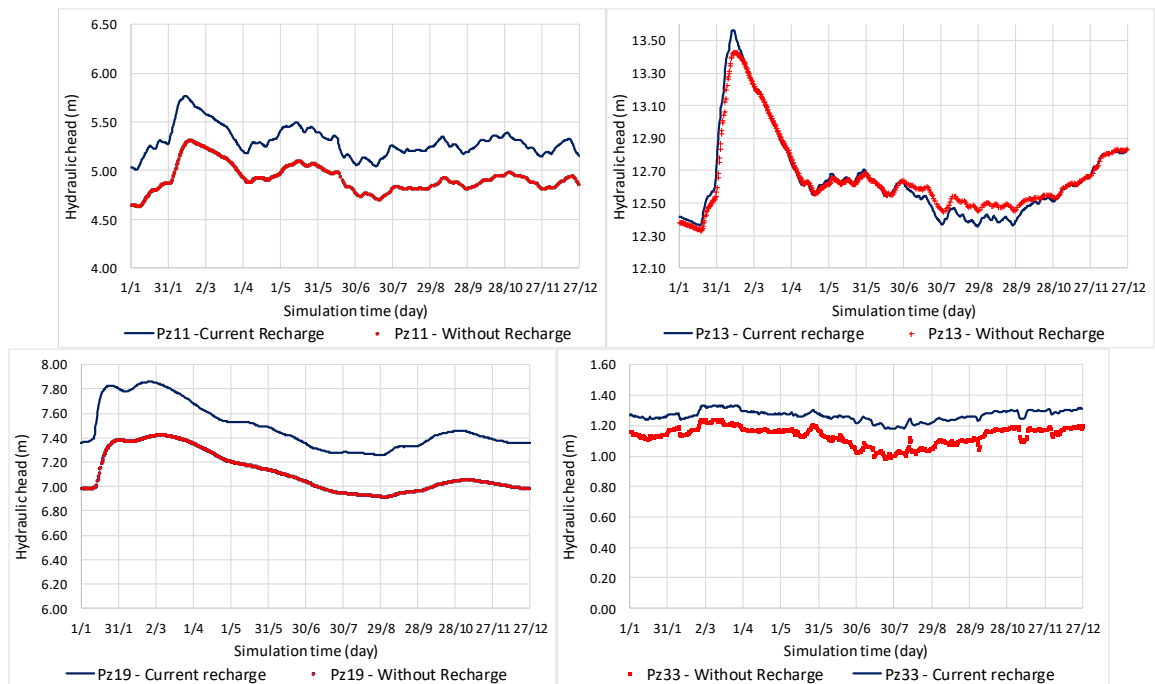


Figure 68. Comparison of hydrographs of observations wells for scenario without recharge

The water head changes therefore affect the saltwater intrusion. The limit of TDS concentration of 10,000 mg/l in the various scenarios clearly shows the effect of changes on pumping and recharge on saltwater intrusion, mainly in the SE area. The simulated equi-concentration contour 10,000 mg/l slightly move upstream with about 50 to 100 m without recharge and about 50 to 100 m for doubled pumping rates. In SW Pissarotte area, saltwater front enter up to 500 m, indicating the important role of the water extraction on the position of saltwater front. On the contrary, if pumping wells stop, the saltwater intrusion will move downstream of about 50 m (Figure 69).

Table 10 presents the results of sensitivity analysis for different scenarios. It indicates the maximum salinity simulated in piezometer XD at SW boundary and the distance from the boundary beyond which the salinity is equal 10g/l in the sector along the road N286. Based on simulated model, if all pumping wells in study area stop exploit, saltwater front of 10g/l would displaced downward of about 130m/year, conversely, doubling the pumping rate induced a landward displacement of saltwater front up to 50m in one year (near Pissarotte pumping station). The simulated mass transport model indicated also significant change in saltwater intrusion due to activities of irrigation on the surface. In case of no recharge from the surface, saltwater front displaced landward of about 20m/year and if doubling the recharge in this area could help mitigate the seawater intrusion with saline front displaced downward of about 50m every year.

Table 10. Results of sensitivity analysis

S.No.	Scenario test	Maximum Salinity	Distance from the
		in XD	model limit with
		mg/l	Salinity 10g/l
			m
1	Original calibrated parameters	33,422	1,677
2	No pumping	30,780	1,547
3	2xPumping	34,362	1,724
4	No recharge	33, 654	1,694
5	2xRecharge	31,026	1,629

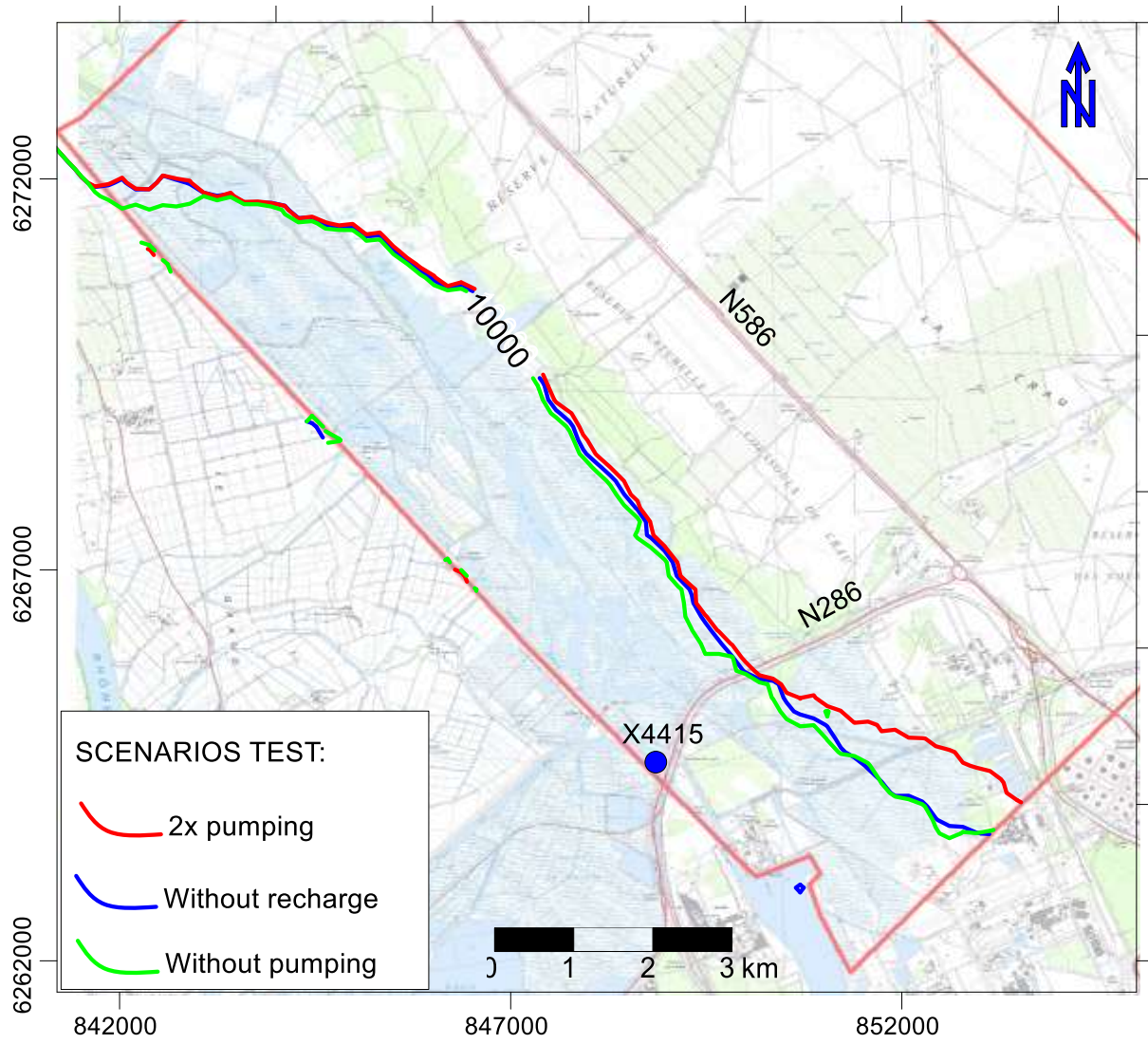


Figure 69. Displacement of the saltwater front (10g/l) after 1 year of change



# **GENERAL CONCLUSION**



The use of groundwater models is prevalent in the field of environmental science to investigate a wide variety of hydrogeological conditions. More recently, groundwater models are being applied to predict the transport of contaminants or saltwater intrusion for risk evaluation. The applicability or usefulness of a model depends on how closely the mathematical equations approximate the physical system that is being modeled. In order to evaluate the applicability or usefulness of a model, it is necessary to have a thorough understanding of the physical system and the assumptions embedded in the derivation of the mathematical equations.

To simulate the variable-density flow system in heterogeneity hydrogeological conditions is complicated and sensitive due to the non-linear coupling between the flow and transport equations. Thus, observed data of salinity from wells and boreholes are normally not enough to validate a saltwater intrusion model. The aim of this study was to propose an approach to control and reduce the effects of uncertainties and heterogeneities of variable-density groundwater modeling into coastal aquifers. Combination of different methods from geophysics and isotope can help to better parameterize and validate the saltwater intrusion modeling.

First, radon has been used to assess groundwater velocities in the study aquifer, to highlight pattern of groundwater discharges and to constraint water-mass balance. A monitoring of  $^{222}\text{Rn}$  in boreholes and wells have been done in the Crau aquifer. It is likely that the radon activity in groundwater is controlled by salinity and grain size of sediments in the aquifer where the wells are located. The radon activity measurements in boreholes have been used to estimate the groundwater (Darcy) flow velocity applying the approach of Schubert and Hamada. In our study, the decay of Radon was measured at different depths in boreholes to achieve information on hydraulic conductivity and heterogeneity of aquifer. The groundwater velocities evaluated with radon activity vary from few cm/day to more than 1 m/day. Based on salinity and radon activity observed in boreholes, the origin of saltwater in the aquifer seems to be related to ancient seawater and not current seawater intrusion, this is in agreement with previous studies from [Vella et al. 2005](#) and [De Montety. 2008](#). Our approach is useful to areas where it is difficult to operate pumping tests (lack of groundwater wells; due to the limited diameter of wells it may not be possible to install measuring devices) or tracing tests (in areas where the tracers can change the natural hydro-geochemical conditions).

Radon activity in groundwater and surface water has been used to estimate the exchange between groundwater and surface water. Using continuous measurements of  $^{222}\text{Rn}$  and the balance box model of Burnett et al., the water mass-balance of groundwater and surface water was calculated. Radon surveys in surface waters suggest no significant discharges of groundwater to surface water ( $55 \text{ l/m}^2/\text{day}$ ). This method is useful for large areas of surface water and/or too deep to install a seepage meter.

Geophysical methods are very useful techniques to inform on the hydrogeological characteristics and calibrate models. Inversed 2D and 3D geophysical models provide high resolution datasets of subsurface structure at a low cost and in a short time. However, this technique still faces difficulty while different resistivity models may produce the same apparent geophysical effect. Therefore, to reduce the errors and uncertainties in geoelectrical models, it is necessary to compare these models with geological and hydrogeological data.

In the study area, the saltwater front is located around the marsh area where it is distributed in a dense network of ponds, canals and the bulls grazing fields of the bull husbandry industry. Because space for geophysical measurements is very constrained, electromagnetic methods appear useful and need little measurement space. An electromagnetic method using a EM34 device have been applied for mapping the saltwater intrusion with a total investigation length of more than 30km. This method is very simple and rapidly operated at a low cost and on a restrained surface. In order to reduce the errors and uncertainties and to validate results of EM method, a combination of difference geophysics techniques is strongly recommended. Electrical Resistivity Tomography (ERT) was the second choice and developed within this study in three profiles. The advantage of the ERT method is the quality of the electrical resistivity data obtained with relatively high spatial resolution. Both the EM and ERT can be coupled to obtain a continuous coverage of the underground in 2D and 3D spaces. The EM34 data have been interpreted using the software EM4Soil and ERT resistivity interpretation have been done with RES2DINV.

Based on the apparent resistivity/conductivity values obtained from ERT and EM investigations, 3D saltwater distribution was characterized. The low resistivity area is located in the southwest of the study area. Low resistivities were found from 4-5 m.asl close the southwest boundary to more than 20 m.asl near X34, X35 (about 1.7km from the boundary). Observations of water in wells and boreholes also indicate brackish water. In marsh area, low resistivity was found near the surface confirming the presence of a top clay layer and the salinity of surface water caused by evaporation. Outside this area no indication of saltwater or saltwater intrusion has been found.

Based on ERT results, porosity of the aquifer was estimated using the Archie's law for each layers of the aquifer. Data provide detailed information on geometry of the aquifer that can be further interpreted using the lithological descriptions from boreholes.

A 3D finite element model was built with FEFLOW software to simulate groundwater flow and the transition between saltwater and freshwater. All mechanisms which affect saltwater intrusion in the aquifer are considered in this model, including advection, dispersion, adsorption, diffusion and chemical reactions. Our model has combined existing data from different sources to estimate the groundwater flow, the mass balance and the effects of recharge

and pumping rates in difference management scenarios. With knowledge obtained from geophysics and isotope measurements, hydrogeological parameters such as hydraulic conductivity, porosity and lithology have been achieved to reduce the errors and the uncertainties of modeling.

Coupling geophysics and groundwater modeling may help to describe the spatial characteristics of the subsurface. Geometric constraints were used to delineate geological units (elevation and thickness of layers) and distribution of heterogeneous properties. The variation of electrical conductivity is also responding to the variation of the lithology. ERT and EM methods are thus applied since the electrical conductivity is sensitive to both clay content and groundwater salinity. With comparison to geological information provided from boreholes, a detailed geological unit distribution has been done. Based on this coupling approach, the simulated numerical model is validated and flux and mass budgets are results of this study.

Flow modeling was calibrated by fitting the simulated and observed hydraulic head in observation points and validated using isotope results and geophysics. A good match was achieved between observed and simulated groundwater heads and concentrations for both models in the steady state and in the transient state. The simulated results from groundwater modeling have detailed the recharge/discharge between groundwater and surface water in marsh area. Results of the numerical model show a significant intrusion of the saltwater front in the southwestern part of the study area.

The developed model was applied to simulate displacement of saltwater intrusion resulting from different scenarios of recharge and pumping rates. The first scenario considers no pumping while the second scenario considers doubling the current pumping rate. The third and fourth scenarios test a non-recharge and double recharge condition respectively over the study area. Simulated results clearly show the effects of pumping and recharge on water table and on saltwater intrusion. Compared to the current situation, water head would drawdown approximately 0.3-0.5 m if pumping rate double. Conversely, if all pumping wells were to stop then the water head would increase by 0.2-1.0 m. Water heads simulated for non-recharge over this area show a global decrease of about 0.2-0.5 m. The simulated mass transport model also indicated a significant change in saltwater intrusion due to activities such as irrigation and abstraction. Doubling the pumping rate induced a landward displacement of saltwater front up to 50 m in one year in SE area (near Pissarotte pumping station). On the other hand, reducing the pumping rate in this area will help mitigate the seawater intrusion. In case of no pumping wells, the saltwater front displaced downward of approximate 130 m/year.

The coupling geophysics and isotope techniques appears to be a very useful tool to help saltwater intrusion modeling in coastal aquifers. Such methods can be widely applied to other sectors or others scales because of their ease of application. This approach could be applied to

study of the effects of climate change, sea level rise and over pumping leading to saltwater intrusion in coastal aquifers.

Future works may increase the potential and the reliability of the proposed approaches as follows:

- More applications should be carried out to achieve more information on hydrogeological parameters (porosity, hydraulic conductivity and storativity) to better constraint the effect of errors and uncertainties on the models, such as pumping tests or slug tests in boreholes.

- A complicated relationship between groundwater and surface water in this area could be clarified by using seepage meters in the field to quantify fluxes at the surface water.

- Extend the boundaries of the current model to the Mediterranean Sea in the southern area and to Rhone River in the western area to test the possible effect of such extended boundary conditions and simulate the effect of sea level rise due to climate change.

- Others geophysical and isotopic (Radon and Radium) investigations can be carried out in the same profiles during rainy season to consider the impact of recharge to groundwater flow pattern and the saltwater distribution.

- To clarify the hydrogeological information (porosity, lithology) in a vertical distribution, a borehole logging method in this area is recommended to clarify the heterogeneity of the aquifer.

- Scenarios develop for long periods.

- Apply this method to other areas.

## Bibliography

- Abd-Elhamid, H. F. & Javadi, A. A. 2011. A density-dependant finite element model for analysis of saltwater intrusion in coastal aquifers. *Journal of Hydrology*, 401, 259-271.
- Abdalla, O. E., Ali, M., Al-Higgi, K., Al-Zidi, H., El-Hussain, I. & Al-Hinai, S. 2010. Rate of seawater intrusion estimated by geophysical methods in an arid area: Al Khabourah, Oman. *Hydrogeology Journal*, 18, 1437-1445.
- Ackerer, P. & Younes, A. 2008. Efficient approximations for the simulation of density driven flow in porous media. *Advances in Water Resources*, 31, 15-27.
- Acworth, R. I. 2007. Measurement of vertical environmental-head profiles in unconfined sand aquifers using a multi-channel manometer board. *Hydrogeology Journal*, 15, 1279-1289.
- Acworth, R. I. & Dasey, G. R. 2001. Electrical imaging of the saline intrusion pattern beneath a tidal creek in a sand aquifer. *New Approaches Characterizing Groundwater Flow, Vols 1 and 2*, 691-696.
- Albinet M., Bonnet M., Dellery B., Durozoy G., Gouvernet Cl. & J., M. 1969. Carte Hydrogéologique Istres – Eyguières 1/50000 Feuille XX – 43 – 44. *Feuille XX – 43 – 44*.
- Allow, K. A. 2011. Seawater intrusion in Syrian coastal aquifers, past, present and future, case study. *Arabian Journal of Geosciences*, 4, 645-653.
- Amezketta, E. 2006. An integrated methodology for assessing soil salinization, a pre-condition for land desertification. *Journal of Arid Environments*, 67, 594-606.
- Anderson, M. P. & Woessner, W. W. 2002. Applied Groundwater Modeling: Simulation of Flow and Advective Transport. In: Woessner, M. P. A. W. (ed.) *Applied Groundwater Modeling*. San Diego: Academic Press.
- Archie, G. E. 1942. The Electrical Resistivity Log as an Aid in Determining Some Reservoir Characteristics.

- Bagnouls, F. & Gaussen, H. 1953. Saison sèche et indice xérothémique. *Bull. Soc. Hist. Nat de Toulouse*, 193-240.
- Barazzuoli, P., Nocchi, M., Rigati, R. & Salleolini, M. 2008. A conceptual and numerical model for groundwater management: a case study on a coastal aquifer in southern Tuscany, Italy. *Hydrogeology Journal*, 16, 1557-1576.
- Batayneh, A. T. 2006. Use of electrical resistivity methods for detecting subsurface fresh and saline water and delineating their interfacial configuration: a case study of the eastern Dead Sea coastal aquifers, Jordan. *Hydrogeology Journal*, 14, 1277-1283.
- Batayneh, A. T., Elawadi, E. A. & Al-Arifi, N. S. 2010. Use of Geoelectrical Technique for Detecting Subsurface Fresh and Saline Water: A Case Study of the Eastern Gulf of Aqaba Coastal Aquifer, Jordan. *Journal of Coastal Research*, 26, 1079-1084.
- Bauer, P., Supper, R., Zimmermann, S. & Kinzelbach, W. 2006. Geoelectrical imaging of groundwater salinization in the Okavango Delta, Botswana. *Journal of Applied Geophysics*, 60, 126-141.
- Bear, J. 1988. *Dynamics of Fluids in Porous Media*, Dover.
- Bear, J. 1999. *Seawater Intrusion in Coastal Aquifers Concepts, Methods and Practices*, Springer.
- Bear, J. 2004. Management of a coastal aquifer. *Ground Water*, 42, 317-317.
- Bear, J. & Verruijt, A. 1987. *Modeling Groundwater Flow and Pollution*, Springer Netherlands.
- Besson, A., Cousin, I., Samouelian, A., Boizard, H. & Richard, G. 2004. Structural heterogeneity of the soil tilled layer as characterized by 2D electrical resistivity surveying. *Soil & Tillage Research*, 79, 239-249.
- Borne, V. 1990. La méthode électromagnétique EM 34-3 pour la prospection de sub-surface. *Bulletin of the International Association of Engineering Geology - Bulletin de l'Association Internationale de Géologie de l'Ingénieur*, 42, 11-20.
- Bouzouf, B., Ouazar, D., Himi, M., Casas, A., Elmahi, I. & Benkhaldoun, F. 2001. Integrating Hydrogeochemical and Geophysical Data for Testing a Finite Volume Based Numerical Model for Saltwater Intrusion. *Transport in Porous Media*, 43, 179-194.

- Boyer, J., Duvail, U., Le Strat, P., Gensous, B. & Tesson, M. 2005. High resolution stratigraphy and evolution of the Rhone delta plain during Postglacial time, from subsurface drilling data bank. *Marine Geology*, 222, 267-298.
- BRGM 1995. MARTCRAU: Actualisation du modèle de la nappe de la Crau. 94-D-211, 73.
- Brisson N., L. M., Mary B., Beaudoin N 2009. Conceptual basis, formalisations and parameterization of the STICS crop model. *Editions QUAE*, 297 pages.
- Buchanan, S. & Triantafilis, J. 2009. Mapping water table depth using geophysical and environmental variables. *Ground Water*, 47, 80-96.
- Burnett, W. C. & Dulaiova, H. 2003. Estimating the dynamics of groundwater input into the coastal zone via continuous radon-222 measurements. *J Environ Radioact*, 69, 21-35.
- Burnett, W. C., Kim, G. & Lane-Smith, D. 2001. A continuous monitor for assessment of Rn-222 in the coastal ocean. *Journal of Radioanalytical and Nuclear Chemistry*, 249, 167-172.
- Cable, J. E., Burnett, W. C., Chanton, J. P. & Weatherly, G. L. 1996. Estimating groundwater discharge into the northeastern Gulf of Mexico using radon-222. *Earth and Planetary Science Letters*, 144, 591-604.
- Calvache, M. L. & Pulido-Bosch, A. 1997. Effects of geology and human activity on the dynamics of salt-water intrusion in three coastal aquifers in southern Spain. *Environmental Geology*, 30, 215-223.
- Capizzi, P., Cellura, D., Cosentino, P., Fiandaca, G., Martirana, R., Messina, P., Schiavone, S. & Valenza, M. 2010. Integrated hydrogeochemical and geophysical surveys for a study of sea-water intrusion. *Bollettino di Geofisica Teorica ed Applicata*; Vol. 51, p285.
- Carrera, J., Hidalgo, J. J., Slooten, L. J. & Vazquez-Sune, E. 2010. Computational and conceptual issues in the calibration of seawater intrusion models. *Hydrogeology Journal*, 18, 131-145.
- Cheng, A. H. D. & Ouazar, D. 2004. *Coastal aquifer management : monitoring, modeling, and case studies*, Boca Raton, FL, Lewis Publishers.

- Cheng, J. M. & Chen, C. X. 2001. Three-dimensional modeling of density-dependent salt water intrusion in multilayered coastal aquifers in Jahe River Basin, Shandong Province, China. *Ground Water*, 39, 137-143.
- Comte, J. C. 2008. Apport de la tomographie électrique à la modélisation des écoulements densitaires dans les aquifères côtiers. *Université d'Avignon et des Pays de Vaucluse, France*.
- Comte, J. C. & Banton, O. 2007. Cross-validation of geo-electrical and hydrogeological models to evaluate seawater intrusion in coastal aquifers. *Geophysical Research Letters*, 34.
- Comte, J. C., Banton, O., Join, J. L. & Cabioch, G. 2010. Evaluation of effective groundwater recharge of freshwater lens in small islands by the combined modeling of geoelectrical data and water heads. *Water Resources Research*, 46.
- Cook, P. G., Love, A. J. & Dighton, J. C. 1999. Inferring ground water flow in fractured rock from dissolved radon. *Ground Water*, 37, 606-610.
- Cooper, H. H. 1959. A hypothesis concerning the dynamic balance of fresh water and salt water in a coastal aquifer. *Journal of Geophysical Research*, 64, 461-467.
- Cronin, A. A., Elliot, T. & Kalin, R. M. 2000. Geochemical modeling and isotope studies in the Sherwood Sandstone aquifer, Lagan Valley, Northern Ireland. *Tracers and Modeling in Hydrogeology*, 425-431.
- Custodio, E. 2005. Coastal aquifers as important natural hydrogeological structures. *In Taylor and Francis (Ed) Groundwater and Human Development*, Chapter 3, 15-38.
- Dagan, G. 1989. *Flow and transport in porous formations*, Springer-Verlag.
- Dahlhaus, P., Evans, T., Nathan, E., Cox, J. & Simmons, C. 2010. Groundwater-level response to land-use change and the implications for salinity management in the West Moorabool River catchment, Victoria, Australia. *Hydrogeology Journal*, 18, 1611-1623.
- de Franco, R., Biella, G., Tosi, L., Teatini, P., Lozej, A., Chiozzotto, B., Giada, M., Rizzetto, F., Claude, C., Mayer, A., Bassan, V. & Gasparetto-Stori, G. 2009. Monitoring the saltwater intrusion by time lapse electrical resistivity tomography: The Chioggia test site (Venice Lagoon, Italy). *Journal of Applied Geophysics*, 69, 117-130.

- de Groot-Hedlin, C. D. & Constable, S. C. 1990. Occam's inversion to generate smooth, two-dimensional models from magnetotelluric data. *Geophysics*, 55, 1613-1624.
- de Montety, V., Radakovitch, O., Vallet-Coulomb, C., Blavoux, B., Hermitte, D. & Valles, V. 2008. Origin of groundwater salinity and hydrogeochemical processes in a confined coastal aquifer: Case of the Rhône delta (Southern France). *Applied Geochemistry*, 23, 2337-2349.
- Diersch, H. J. 1988. Finite element modeling of recirculating density-driven saltwater intrusion processes in groundwater. *Advances in Water Resources*, 11, 25-43.
- Diersch, H. J. 2014. FEFLOW Finite Element Modeling of Flow, Mass and Heat Transport in Porous and Fractured Media. *Springer*, 29, 741-753.
- Diersch, H. J. G., Bauer, D., Heidemann, W., Ruhaak, W. & Schatzl, P. 2011a. Finite element modeling of borehole heat exchanger systems Part 1. Fundamentals. *Computers & Geosciences*, 37, 1122-1135.
- Diersch, H. J. G., Bauer, D., Heidemann, W., Ruhaak, W. & Schatzl, P. 2011b. Finite element modeling of borehole heat exchanger systems Part 2. Numerical simulation. *Computers & Geosciences*, 37, 1136-1147.
- Diersch, H. J. G. & Kolditz, O. 2002. Variable-density flow and transport in porous media: approaches and challenges. *Advances in Water Resources*, 25, 899-944.
- Dimova, N. T. & Burnett, W. C. 2011. Evaluation of groundwater discharge into small lakes based on the temporal distribution of radon-222. *Limnology and Oceanography*, 56, 486-494.
- Dimova, N. T., Burnett, W. C., Chanton, J. P. & Corbett, J. E. 2013. Application of radon-222 to investigate groundwater discharge into small shallow lakes. *Journal of Hydrology*, 486, 112-122.
- Drost, W., Klotz, D., Koch, A., Moser, H., Neumaier, F. & Rauert, W. 1968. Point dilution methods of investigating ground water flow by means of radioisotopes. *Water Resources Research*, 4, 125-146.

- Dulaiova, H., Peterson, R., Burnett, W. C. & Lane-Smith, D. 2005. A multi-detector continuous monitor for assessment of Rn-222 in the coastal ocean. *Journal of Radioanalytical and Nuclear Chemistry*, 263, 361-365.
- Duque, C., Calvache, M. L., Pedrera, A., Martin-Rosales, W. & Lopez-Chicano, M. 2008. Combined time domain electromagnetic soundings and gravimetry to determine marine intrusion in a detrital coastal aquifer (Southern Spain). *Journal of Hydrology*, 349, 536-547.
- E. Colomb & Roux, R. M. 1986. La Crau, histoire Plio-Pléistocène. *Méditerranée* 58, 31-42.
- El Yaouti, F., El Mandour, A., Khattach, D., Benavente, J. & Kaufmann, O. 2009. Salinization processes in the unconfined aquifer of Bou-Areg (NE Morocco): A geostatistical, geochemical, and tomographic study. *Applied Geochemistry*, 24, 16-31.
- EM-TOMO 2014. EM4Soil A program for 1-D laterally constrained inversion of EM data Quasi-3D Module.
- EMTOMO 2015. EM4Soil-v2.03 – a program for 1D Laterally Constrained Inversion. *In: EMTOMO* (ed.).
- Essaid, H. I. 1992. *Simulation of freshwater and saltwater flow in the coastal aquifer system of the Purisima Formation in the Soquel-Aptos basin, Santa Cruz County, California*, Menlo Park, Calif., U.S. Geological Survey ;.
- Essink, G. H. P. O. 2001. Salt water intrusion in a three-dimensional groundwater system in the Netherlands: A numerical study. *Transport in Porous Media*, 43, 137-158.
- FAO 1997. *Seawater Intrusion in Coastal Aquifers: Guidelines for Study, Monitoring and Control*, Food and Agriculture Organization of the United Nations.
- Faye, S., Diop, I. N., Faye, S. C., Evans, D. G., Pfister, M., Maloszewski, P. & Seiler, K. P. 2001. Seawater intrusion in the Dakar (Senegal) confined aquifer: calibration and testing of a 3D finite element model. *New Approaches Characterizing Groundwater Flow, Vols 1 and 2*, 1183-1186.
- Fetter, C. W. 2001. *Applied Hydrogeology*. Fourth Edition, 598.
- Fitterman, D. V. & Deszcz-Pan, M. 2004. Characterization of saltwater intrusion in South Florida using electromagnetic geophysical methods. 18 SWIM. Cartagena 2004, Spain.

- Frohlich, R. K., Urish, D. W., Fuller, J. & O'Reilly, M. 1994. Use of geoelectrical methods in groundwater pollution surveys in a coastal environment. *Journal of Applied Geophysics*, 32, 139-154.
- Frolkovič, P. & De Schepper, H. 2000. Numerical modeling of convection dominated transport coupled with density driven flow in porous media. *Advances in Water Resources*, 24, 63-72.
- Gambolati, G., Teatini, P., Tomasi, L. & Gonella, M. 1999. Coastline regression of the Romagna region, Italy, due to natural and anthropogenic land subsidence and sea level rise. *Water Resources Research*, 35, 163-184.
- Ghassemi, E., Jakeman, A. & HA, N. 1995. Salinization of land and Water resources. *University of New South Wales Press, Sydney*.
- Gimenez, E. & Morell, I. 1997. Hydrogeochemical analysis of salinization processes in the coastal aquifer of Oropesa (Castellon, Spain). *Environmental Geology*, 29, 118-131.
- Goldman, M., Gilad, D., Ronen, A. & Melloul, A. 1991. Mapping of Seawater Intrusion into the Coastal Aquifer of Israel by the Time Domain Electromagnetic Method. *Geoexploration*, 28, 153-174.
- Graf, T. & Therrien, R. 2007. Variable-density groundwater flow and solute transport in irregular 2D fracture networks. *Advances in Water Resources*, 30, 455-468.
- Griffiths, D. H. & Barker, R. D. 1993. Two-dimensional resistivity imaging and modeling in areas of complex geology. *Journal of Applied Geophysics*, 29, 211-226.
- Guérin, R. 2005. Borehole and surface-based hydrogeophysics. *Hydrogeology Journal*, 13, 251-254.
- Gunduz, O., Aral, M. M. & Laboratory, G. I. o. T. M. E. S. 2004. *Surface and Subsurface Flow and Contaminant Transport Modeling in Lower Altamaha Watershed*, Multimedia Environmental Simulations Laboratory, School of Civil and Environmental Engineering, Georgia Institute of Technology.
- Günther, T., Dlugosch, R., M.-Müller-Petke & Costabel, S. 2014. Contribution of Nuclear Magnetic Resonance for supporting hydraulic model generation. *SWIM 2014 Conference*, 150-153.

- Guo, W., Langevin, C. D. & Survey, G. 2002. *User's Guide to SEAWAT: A Computer Program for Simulation of Three-dimensional Variable-density Ground-water Flow*, U.S. Department of the Interior, U.S. Geological Survey.
- Hamada, H. 2000. Estimation of groundwater flow rate using the decay of Rn-222 in a well. *Journal of Environmental Radioactivity*, 47, 1-13.
- Hassan, A. E. 2004. A methodology for validating numerical ground water models. *Ground Water*, 42, 347-362.
- Herckenrath, D., Fiandaca, G., Auken, E. & Bauer-Gottwein, P. 2013a. Sequential and joint hydrogeophysical inversion using a field-scale groundwater model with ERT and TDEM data. *Hydrol. Earth Syst. Sci.*, 17, 4043-4060.
- Herckenrath, D., Odlum, N., Nenna, V., Knight, R., Auken, E. & Bauer-Gottwein, P. 2013b. Calibrating a salt water intrusion model with time-domain electromagnetic data. *Ground Water*, 51, 385-97.
- Holzbecher, E. O. 1998a. Modeling Density-Driven Flow in Porous Media. 286.
- Holzbecher, E. O. 1998b. *Modeling Density-Driven Flow in Porous Media Principles, Numerics, Software* [Online]. Berlin, Heidelberg: Springer Berlin Heidelberg. Available: <http://dx.doi.org/10.1007/978-3-642-58767-2>.
- Hu, L. T. & Jiao, J. J. 2010. Modeling the influences of land reclamation on groundwater systems: A case study in Shekou peninsula, Shenzhen, China. *Engineering Geology*, 114, 144-153.
- INRA 2013. Sustainable use of irrigation water in the Mediterranean Region. Report D5.3: Report on hydrological and water quality data at the target watersheds. *SIRRIMED*, 2013.
- Jacob, N., Shivanna, K. & Suresh Babu, D. S. 2009. Radon as an indicator of submarine groundwater discharge in coastal regions. . *Current Science (Bangalore)*, 97(9), 1313-1320.
- Jin, S., Fallgren, P., Cooper, J., Morris, J. & Urynowicz, M. 2008. Assessment of diesel contamination in groundwater using electromagnetic induction geophysical techniques. *J Environ Sci Health A Tox Hazard Subst Environ Eng*, 43, 584-8.

- Kafri, U. & Goldman, M. 2005. The use of the time domain electromagnetic method to delineate saline groundwater in granular and carbonate aquifers and to evaluate their porosity. *Journal of Applied Geophysics*, 57, 167-178.
- Khaska, M., Le Gal La Salle, C., Lancelot, J., team, A., Mohamad, A., Verdoux, P., Noret, A. & Simler, R. 2013. Origin of groundwater salinity (current seawater vs. saline deep water) in a coastal karst aquifer based on Sr and Cl isotopes. Case study of the La Clape massif (southern France). *Applied Geochemistry*, 37, 212-227.
- Koch, M. & Zhang, G. 1998. Numerical modeling and management of saltwater seepage from coastal brackish canals in southeast Florida. *Environmental Coastal Regions*, 395-404.
- Koefoed, O. & Dirks, F. J. H. 1979. DETERMINATION OF RESISTIVITY SOUNDING FILTERS BY THE WIENER-HOPF LEAST-SQUARES METHOD\*. *Geophysical Prospecting*, 27, 245-250.
- Kolditz, O., Ratke, R., Diersch, H.-J. G. & Zielke, W. 1998. Coupled groundwater flow and transport: 1. Verification of variable density flow and transport models. *Advances in Water Resources*, 21, 27-46.
- L'Homer, A., Bazile, A., Thommeret, J. & Thommeret, Y. 1981. Principales e'tapes de l'e'dification du delta du Rhône de 7,000BP a` nos jours. variations du niveau marin. *Oceanis* 7, (4), 389 – 408.
- Lambert, M. J. & Burnett, W. C. 2003. Submarine groundwater discharge estimates at a Florida coastal site based on continuous radon measurements. *Biogeochemistry*, 66, 55-73.
- Land, L. A., Lautier, J. C., Wilson, N. C., Chianese, G. & Webb, S. 2004. Geophysical monitoring and evaluation of coastal plain aquifers. *Ground Water*, 42, 59-67.
- Leendertse, J. J. 1981. Discussion-contribution in: Fischer (ed.), Transport models for inland and coastal waters. *New York*.
- Lin, J., Snodsmith, J. B., Zheng, C. M. & Wu, J. F. 2009. A modeling study of seawater intrusion in Alabama Gulf Coast, USA. *Environmental Geology*, 57, 119-130.
- Lloyd, J. W. 1992. J. Bear & Y. Bachmat 1990. Introduction to Modeling of Transport Phenomena in Porous Media. xxiv+553 pp. Dordrecht, Boston, London: Kluwer. Price

- Dfl. 340, US \$198, £124 (hard covers). ISBN 0 7923 0557 4. *Geological Magazine*, 129, 373-374.
- Loke, M. H. & Barker, R. D. 1996. Rapid least-squares inversion of apparent resistivity pseudosections by a quasi-Newton method1. *Geophysical Prospecting*, 44, 131-152.
- Luszczynski, N. J. 1961. Head and flow of ground water of variable density. *Journal of Geophysical Research*, 66, 4247-4256.
- Massmann, G., Simmons, C., Love, A., Ward, J. & James-Smith, J. 2006. On variable density surface water–groundwater interaction: A theoretical analysis of mixed convection in a stably-stratified fresh surface water – saline groundwater discharge zone. *Journal of Hydrology*, 329, 390-402.
- Mckibbin, R. & O'Sullivan, M. J. 1980. Onset of convection in a layered porous medium heated from below. *Journal of Fluid Mechanics*, 96, 375-393.
- McNeill, J. D. 1980. Electromagnetic terrain conductivity measurement at low conduction numbers. *Geonics*.
- Melloul, A. J. & Goldenberg, L. C. 1997. Monitoring of Seawater Intrusion in Coastal Aquifers: Basics and Local Concerns. *Journal of Environmental Management*, 51, 73-86.
- Millham, N. P. & Howes, B. L. 1995. A Comparison of Methods to Determine K in a Shallow Coastal Aquifer. *Ground Water*, 33, 49-57.
- Mongelli, G., Monni, S., Oggiano, G., Paternoster, M. & Sinisi, R. 2013. Tracing groundwater salinization processes in coastal aquifers: a hydrogeochemical and isotopic approach in the Na-Cl brackish waters of northwestern Sardinia, Italy. *Hydrol. Earth Syst. Sci.*, 17, 2917-2928.
- Moore, W. S. 2000. Determining coastal mixing rates using radium isotopes. *Continental Shelf Research*, 20, 1993-2007.
- Neuman, S. P., Winter, C. L. & Newman, C. M. 1987. Stochastic theory of field-scale fickian dispersion in anisotropic porous media. *Water Resources Research*, 23, 453-466.
- Nguyen, F., Kemna, A., Antonsson, A., Engesgaard, P., Kuras, O., Ogilvy, R., Gisbert, J., Jorreto, S. & Pulido-Bosch, A. 2009. Characterization of seawater intrusion using 2D electrical imaging. *Near Surface Geophysics*, 7, 377-390.

- Oliosio, A., Lecerf, R., Baillieux, A., Chanzy, A., Ruget, F., Banton, O., Lecharpentier, P., Trolard, F. & Cognard-Plancq, A.-L. 2013. Modeling of Drainage and Hay Production over the Crau Aquifer for Analysing Impact of Global Change on Aquifer Recharge. *Procedia Environmental Sciences*, 19, 691-700.
- Oliveira, J., Elisio, A. C. R., Teixeira, W. E., Peres, A. C., Burnett, W. C., Povinec, P. P., Somayajulu, B. L. K., Braga, E. S. & Furtado, V. V. 2006. Isotope techniques for assessment of submarine groundwater discharge and coastal dynamics in Ubatuba coastal areas, Brazil. *Journal of Coastal Research*, 1084-1086.
- Padilla, F., Mendez, A., Fernandez, R. & Vellando, P. R. 2008. Numerical modeling of surfacewater/groundwater flows for freshwater/saltwater hydrology: the case of the alluvial coastal aquifer of the Low Guadalhorce River, Malaga, Spain. *Environmental Geology*, 55, 215-226.
- Pool, M. & Carrera, J. 2011. A correction factor to account for mixing in Ghyben-Herzberg and critical pumping rate approximations of seawater intrusion in coastal aquifers. *Water Resources Research*, 47, n/a-n/a.
- Post, V., Kooi, H. & Simmons, C. 2007. Using hydraulic head measurements in variable-density ground water flow analyses. *Ground Water*, 45, 664-671.
- Post, V. E. A. 2012. Electrical Conductivity as a Proxy for Groundwater Density in Coastal Aquifers. *Ground Water*, 50, 785-792.
- Post, V. E. A. & von Asmuth, J. R. 2013. Review: Hydraulic head measurements-new technologies, classic pitfalls. *Hydrogeology Journal*, 21, 737-750.
- Pulido-Leboeuf, P., Pulido-Bosch, A., Calvache, M. L., Vallejos, Á. & Andreu, J. M. 2003. Strontium, SO<sub>4</sub><sup>2-</sup>/Cl<sup>-</sup> and Mg<sup>2+</sup>/Ca<sup>2+</sup> ratios as tracers for the evolution of seawater into coastal aquifers: the example of Castell de Ferro aquifer (SE Spain). *Comptes Rendus Geoscience*, 335, 1039-1048.
- Qahman, K. & Larabi, A. 2006. Evaluation and numerical modeling of seawater intrusion in the Gaza aquifer (Palestine). *Hydrogeology Journal*, 14, 713-728.
- Ramalho, E. C., Dill, A. C. & Rocha, R. 2013. Assessment of the leachate movement in a sealed landfill using geophysical methods. *Environmental Earth Sciences*, 68, 343-354.

- Roure S, Duvail C & P, L. S. 2004. Geodynamique des Systèmes Plio-quadernaires des Nappes Alluviales de la Plaine de la Crau. *BRGM Report*, RP-53088-FR.
- SAFEGE 2004. Surveillance du biseau salé de la nappe de la Crau en 2004. Dossier N7209e, 28.
- SAFEGE 2006. Evolution de la salinité dans le secteur de la Pissarotte. *Report 7/2006*.
- Santos, F. A. M. 2004. 1-D laterally constrained inversion of EM34 profiling data. *Journal of Applied Geophysics*, 56, 123-134.
- Santos, F. A. M., Almeida, E. P., Castro, R., Nolasco, R. & Mendes-Victor, L. 2002. A hydrogeological investigation using EM34 and SP surveys. *Earth Planets and Space*, 54, 655-662.
- Santos, F. A. M., Triantafilis, J. & Bruzgulis, K. 2011. A spatially constrained 1D inversion algorithm for quasi-3D conductivity imaging: Application to DUALEM-421 data collected in a riverine plain. *Geophysics*, 76, B43-B53.
- Santos, F. A. M., Triantafilis, J., Taylor, R. S., Holladay, S. & Bruzgulis, K. E. 2010. Inversion of Conductivity Profiles from EM Using Full Solution and a 1-D Laterally Constrained Algorithm. *Journal of Environmental and Engineering Geophysics*, 15, 163-174.
- Saos JL, Belaud G, Charron F & P, L. 2006. Quantification des flux d'eau en irrigation gravitaire cas de la plaine de la Crau. *Rapport d'étude*, p.183 (+ annexes et rapports d'avancement n°1,2, 3, 4 and 5).
- Sasaki, Y. 1989. Two - dimensional joint inversion of magnetotelluric and dipole - dipole resistivity data. *GEOPHYSICS*, 54, 254-262.
- Sasaki, Y. 2001. Full 3-D inversion of electromagnetic data on PC. *Journal of Applied Geophysics*, 46, 45-54.
- Scheidleger A, Grath J & H., L. 2004. The European environment agency indicator-based reporting about 'Saltwater intrusion due to groundwater over-exploitation'. 609-616.
- Schincariol, R. A., Schwartz, F. W. & Mendoza, C. A. 1997. Instabilities in variable density flows: Stability and sensitivity analyses for homogeneous and heterogeneous media. *Water Resources Research*, 33, 31-41.

- Schubert, M., Brueggemann, L., Knoeller, K. & Schirmer, M. 2011. Using radon as an environmental tracer for estimating groundwater flow velocities in single-well tests. *Water Resources Research*, 47.
- Seeton, C. 2006. Viscosity–temperature correlation for liquids. *Tribology Letters*, 22, 67-78.
- Seger, M., Cousin, I., Frison, A., Boizard, H. & Richard, G. 2009. Characterisation of the structural heterogeneity of the soil tilled layer by using in situ 2D and 3D electrical resistivity measurements. *Soil & Tillage Research*, 103, 387-398.
- Shikaze, S. G., Sudicky, E. A. & Schwartz, F. W. 1998. Density-dependent solute transport in discretely-fractured geologic media: is prediction possible? *Journal of Contaminant Hydrology*, 34, 273-291.
- Shoemaker, W. B. 2004. Important observations and parameters for a salt water intrusion model. *Ground Water*, 42, 829-840.
- Simmarano, J. B. 2012. Rôle de l'irrigation sur la recharge de la nappe de la Crau : traçage isotopique (d18O) et modélisation. *CEREGE*, Master thesis.
- Simmons, C. T., Fenstermaker, T. R. & Sharp Jr, J. M. 2001. Variable-density groundwater flow and solute transport in heterogeneous porous media: approaches, resolutions and future challenges. *Journal of Contaminant Hydrology*, 52, 245-275.
- Sirhan, A. & Hamidi, M. O. 2012. Characterization by electrical and electromagnetic geophysical methods of the shallow hydrogeological system at Hebron (West Bank, Palestine) in a semi-arid zone. *Comptes Rendus Geoscience*, 344, 449-460.
- Stewart, M. & Gay, M. C. 1986. Evaluation of Transient Electromagnetic Soundings for Deep Detection of Conductive Fluids. *Ground Water*, 24, 351-356.
- Stewart, M. T. 1982. Evaluation of Electromagnetic Methods for Rapid Mapping of Salt-Water Interfaces in Coastal Aquifers. *Ground Water*, 20, 538-545.
- Strack, O. D. L. 1976. A single-potential solution for regional interface problems in coastal aquifers. *Water Resources Research*, 12, 1165-1174.
- Stuyfzand, P. J. 1989. An accurate, relatively simple calculation of the saturation index of calcite for fresh to salt water. *Journal of Hydrology*, 105, 95-107.

- Tellam, J. H., Lloyd, J. W. & Walters, M. 1986. The morphology of a saline groundwater body: Its investigation, description and possible explanation. *Journal of Hydrology*, 83, 1-21.
- Tompson, A. F. B. & Gelhar, L. W. 1990. Numerical simulation of solute transport in three-dimensional, randomly heterogeneous porous media. *Water Resources Research*, 26, 2541-2562.
- Triantafylis, J. & Lesch, S. M. 2005. Mapping clay content variation using electromagnetic induction techniques. *Computers and Electronics in Agriculture*, 46, 203-237.
- Triantafylis, J. & Monteiro Santos, F. A. 2013. Electromagnetic conductivity imaging (EMCI) of soil using a DUALEM-421 and inversion modeling software (EM4Soil). *Geoderma*, 211-212, 28-38.
- Triantafylis, J., Odeh, I. O. A., Minasny, B. & McBratney, A. B. 2003. Elucidation of physiographic and hydrogeological features of the lower Namoi valley using fuzzy k-means classification of EM34 data. *Environmental Modeling & Software*, 18, 667-680.
- Triantafylis, J., Terhune, C. H. & Santos, F. A. M. 2013. An inversion approach to generate electromagnetic conductivity images from signal data. *Environmental Modeling & Software*, 43, 88-95.
- Unesco., Joint Panel on Oceanographic Tables and Standards., Centre interuniversitaire d'etudes europeennes., International Council of Scientific Unions. Scientific Committee on Oceanic Research. & International Association for the Physical Sciences of the Ocean. 1981. *Background papers and supporting data on the International equation of state of seawater 1980*, Paris, Unesco.
- Vaidote Jakimavičiūtė - Maseliene, J. M. R. P. 2006. Modeling of coupled groundwater flow and radionuclide transport in crystalline basement using FEFLOW 5.0. *Journal of Environmental Engineering and Landscape Management*, Volume 14, Issue 2, 2006, 12.
- Vandenbohede, A., Van Houtte, E. & Lebbe, L. 2009. Sustainable groundwater extraction in coastal areas: a Belgian example. *Environmental Geology*, 57, 735-747.
- Vella, C., Fleury, T.-J., Raccasi, G., Provansal, M., Sabatier, F. & Bourcier, M. 2005. Evolution of the Rhône delta plain in the Holocene. *Marine Geology*, 222-223, 235-265.

- Vengosh, A., Spivack, A. J., Artzi, Y. & Ayalon, A. 1999. Geochemical and boron, strontium, and oxygen isotopic constraints on the origin of the salinity in groundwater from the Mediterranean Coast of Israel. *Water Resources Research*, 35, 1877-1894.
- Voss, C. I. & Souza, W. R. 1987. Variable density flow and solute transport simulation of regional aquifers containing a narrow freshwater-saltwater transition zone. *Water Resources Research*, 23, 1851-1866.
- Wang, Y. & Jiao, J. J. 2012. Origin of groundwater salinity and hydrogeochemical processes in the confined Quaternary aquifer of the Pearl River Delta, China. *Journal of Hydrology*, 438–439, 112-124.
- Webb, M. D. & Howard, K. W. F. 2011. Modeling the Transient Response of Saline Intrusion to Rising Sea-Levels. *Ground Water*, 49, 560-569.
- Winsauer, W. O., Shearin, H. M., Masson, P. H. & Williams, M. 1952. *Resistivity of brine - saturated sands in relation to pore geometry*.
- Xu, Y. S., Shen, S. L., Du, Y. J., Chai, J. C. & Horpibulsuk, S. 2013. Modeling the cutoff behavior of underground structure in multi-aquifer-aquitard groundwater system. *Natural Hazards*, 66, 731-748.
- Zarroca, M., Bach, J., Linares, R. & Pellicer, X. M. 2011. Electrical methods (VES and ERT) for identifying, mapping and monitoring different saline domains in a coastal plain region (Alt Emporda, Northern Spain). *Journal of Hydrology*, 409, 407-422.
- Zhang, Y., Swift, D. J. P., Yu, Z. Y. & Jin, L. 1998. Modeling of coastal profile evolution on the abandoned delta of the Huanghe River. *Marine Geology*, 145, 133-148.



## List of figures

<b>Figure 1.</b> Saltwater intrusion due to groundwater overexploitation in Europe (EEA, 2005).....	13
<b>Figure 2.</b> Interface between fresh water and salt water in a coastal aquifer in which the salt water intrusion is static (according to the Ghyben-Herzberg relation).....	20
<b>Figure 3.</b> Circulation of salt water from the sea to the zone of diffusion and back to the sea in homogeneous coastal aquifer (Cooper, 1959).....	20
<b>Figure 4.</b> Schematic representation of a piezometer in a groundwater system with a constant density (edited from Musczynski,1961 and Post, 2013).....	22
<b>Figure 5.</b> Schematic representation of head definitions in variable-density groundwater systems (modified from Musczynski 1961). Lightest shading corresponds to fresh water and darker shading represents increasing salinity. ....	24
<b>Figure 6.</b> Location of Crau coastal plain and the study area. Limit of the Crau aquifer and lower/upper Pleistocene (Albinet M. et al., 1969).....	29
<b>Figure 7.</b> Location of geological formations and cross sections .....	31
<b>Figure 8.</b> Geological cross section A-A' (Figure 14) (BRGM, edited) .....	32
<b>Figure 9.</b> Hydrogeological cross section B-B' (BRGM, edited) .....	32
<b>Figure 10.</b> Schematic hydrogeological cross section C-C' (BRGM, edited).....	33
<b>Figure 11.</b> Available hydraulic conductivity in Crau aquifer (yellow point measured by BRGM and red point calculated from lithological data by Simmarano, 2012) .....	34
<b>Figure 12.</b> Hydraulic conductivity distribution from INRA, 2013 .....	34
<b>Figure 13.</b> Water level distribution from 1990 to 2014. Data in 1990 and 2001 from SAFEGE (2004) .....	35
<b>Figure 14.</b> Topography of study area .....	36

<b>Figure 15.</b> Monthly rainfall (bars) and monthly temperature (dots) from Istres station. The grey filled parts shown the dry periods using the ombrothermic diagram from Bagnouls, 1953 (data from INRA).....	37
<b>Figure 16.</b> Groundwater exploitation activities in study area (sources from Safege, Symcrau and INRA).....	38
<b>Figure 17.</b> Comparison of the delta lobes progradation (Vella et al., 2005) and the Pleistocene gravel isobaths (Roure S et al., 2004). ....	39
<b>Figure 18.</b> Schematic cross-section of the investigation in studies of De Montety (2008) .....	40
<b>Figure 19.</b> Salinity evolution from 1990 to 2014. Observation data of 1990 and 2001 from SAFEGE. Data of 2014 were measured on 24/10/2014 at 10m below groundwater surface. ....	41
<b>Figure 20.</b> Methodology flowchart of the study .....	46
<b>Figure 21.</b> Location of groundwater and surface water observation points in study area .....	47
<b>Figure 22.</b> Electrical conductivity distribution in wells and piezometers at 10m below groundwater surface (data on 24/10/2013).....	48
<b>Figure 23.</b> Electrical conductivity distribution along the road N286 (a) and along Arles-Fos canal (c). Water level measurement in piezometers (blue) and hydraulic head with the correction of density (red) along the road N286 (b) and along the Arles-Fos canal (d) .....	49
<b>Figure 24.</b> Location of observation points and water level map (raw data of 24/10/2013) .....	51
<b>Figure 25.</b> Hydraulic head map with density correction (data on 24/10/2013).....	52
<b>Figure 26.</b> Geonics Electromagnetic EM34-3 instrument applied in study area.....	54
<b>Figure 27.</b> Relative response versus depth for.....	54
<b>Figure 28.</b> Comparison of relative responses for vertical and horizontal dipole modes. Note x axis = depth/intercoil spacing. (reproduced from McNeill, 1986).....	55

<b>Figure 29.</b> Principle of electrical resistivity tomography (ERT) measurement. Note : Band I indicates an electrical current (A) and V indicates the potential difference (V) which is measured by this method.....	58
<b>Figure 30.</b> Principle of EM34 profile with regard to interface between fresh and salt water. This cross section along the Pissarote secteur. ....	61
<b>Figure 31.</b> EM34 measurement in study area .....	62
<b>Figure 32.</b> Position of electrical resistivity tomography (ERT) sectors and electromagnetic (EM34) measurement points.....	62
<b>Figure 33.</b> (left) Schematic sketch of a subarea (modified after Schubert [2011] and Hamada [2000]), (right) schematic horizontal cross section of a screen borehole with filter pack (Schubert [2011]) .....	64
<b>Figure 34.</b> Radon monitoring locations, including Radon sampling in continue pumping wells, in piezometers and in surface water. ....	66
<b>Figure 35.</b> Diagrammatic view of experimental setup for single RAD-7 exchanger continuous radon-in-water monitor. (Burnett et al., 2001, Dulaiova et al., 2005) .....	70
<b>Figure 36.</b> A simplified sketch of an equilibrium radon measurement system. Lines shown represent the water pumped through the exchanger by a submersible pump (dashed) and a closed air loop (solid) that flow through a parallel monitor system of RAD-7 (Dulaiova et al., 2005).....	71
<b>Figure 37.</b> Schematic of the radon mass balance box model (edited from Natasha [2013]) .....	71
<b>Figure 38.</b> Operational configuration of the continuous $^{222}\text{Rn}$ monitoring system (left) and field campaign in study area (right).....	74
<b>Figure 39.</b> Track map of surface water radon measurements (left) and tracer distribution of $^{222}\text{Rn}$ (right) in Arles-Fos canal (blue circles) and Landre pond (orange circles) in April, 2014.....	74
<b>Figure 40.</b> Protocol of building a groundwater modeling (Anderson and Woessner, 2002) .....	77

<b>Figure 41.</b> Spatial distribution of appaeent electrical conductivity $\sigma_a$ (mS/m) with EM34-20m HDM (upper) and electrical conductivity $EC_e$ ( $\mu\text{S}/\text{cm}$ )in groundwater at -10m depth from groundwater level in piezometers (lower), red and blue colors represent the conductive and resistive layers, respectively.....	88
<b>Figure 42.</b> EM34 data statistic of all measurements .....	89
<b>Figure 43.</b> Spatial distribution of a. electrical conductivity water in piezometers ( $EC_e - \mu\text{S}/\text{cm}$ ) and b. estimated electrical condutivity from EM34 apparent electrical conductivity ( $\sigma_a - \text{mS}/\text{m}$ ) in sector EM9 (Pissarote) .....	90
<b>Figure 44.</b> Spatial distribution of a. electrical conductivity water in piezometers ( $EC_e - \mu\text{S}/\text{cm}$ ) and b. estimated electrical condutivity from EM34 apparent electrical conductivity ( $\sigma_a - \text{mS}/\text{m}$ ) in sector EM12 along the canal from Arles-Fos.....	91
<b>Figure 45:</b> Plot of 2-D cross section of estimated electrical conductivity ( $\sigma - \text{mS}/\text{m}$ ) from a joint inversion of EM34 apparent electrical conductivity ( $\sigma_a - \text{mS}/\text{m}$ ) data using a 1-D laterally constrained algorithm for quasi-3-D conductivity imaging along 10 sectors (sectors 1-12, locations of sectors shown in Figure 32).....	95
<b>Figure 46.</b> 2-D electrical resitivity tomography on section 1 (Figure 32).....	97
<b>Figure 47.</b> 2-D electrical resitivity tomography (ERT) (upper) and electromagnetic (EM34) (lower) in the sector Tonkin.....	97
<b>Figure 48.</b> 2-D electrical resitivity tomography (ERT) (upper) and electromagnetic (EM34) (below) of sector 3 in center research area. ....	98
<b>Figure 49.</b> (left) ERT profile (with location of XD boroheole) and (right) vertical distribution of electrical conductivity in pore water of XD .....	99
<b>Figure 50.</b> Conceptual model based on geological and hydrodynamic data. ....	117
<b>Figure 51.</b> a) Pumping wells location in modeling b) total daily pumping rate (data in 2014).....	119
<b>Figure 52.</b> Boundary conditions .....	121
<b>Figure 53.</b> Locations of K value estimated from previous and current studies. ....	124

- Figure 54.** Comparison of measured groundwater EC and calculated EC using equation of Archie (1942) ..... 125
- Figure 55.** Comparison between observed and simulated water heads for the validation period from 3/2013 to 3/2014. Each value was extracted from the results according to daily frequency of sampling [m] ..... 127
- Figure 56.** Comparison between observed and simulated of salt concentrations for the validation from 3/2013 to 2014[g/l]. ..... 127
- Figure 57.** Comparison of hydraulic head between a) observation measurement in piezometer (black arrows are groundwater flow directions) and b) flow model results after calibration (hydraulic head contours in m) on 23/10/2013 ..... 128
- Figure 58.** Comparison of spatial distribution of a) electrical conductivity of groundwater and b) calculated concentration at -10m asl (on 23/10/2013)..... 129
- Figure 59.** Evolution of the simulated and observed hydraulic heads during the 2004-2014 period..... 130
- Figure 60.** Comparison between the 2D geoelectrical inverse model (EM profile) along the Arles to Fos canal and corresponding 3D saltwater intrusion model ..... 131
- Figure 61.** Comparison between the 2D geoelectrical inverse model (EM profile) in Pissarotte area and corresponding three3D saltwater intrusion model ..... 132
- Figure 62.** Location of EM measurements and limits of interpolated geophysical model ..... 133
- Figure 63.** 3D distribution of estimated EC ( $\sigma$  - ms/m) from a joint inversion of EM34-10, EM34-20 and EM34-40 data using a 1-D laterally constrained algorithm for quasi-3D EC imaging..... 134
- Figure 64.** 3D distribution of TDS concentration (mg/l) from 3D groundwater model (clip at -3m from the soil surface)..... 134
- Figure 65.** Comparison simulated EC from geophysics and numerical models at depth of a. 2.5m, b. 5m, c. 10m, d. 15m, e. 20m, f. 25m, g. 30m. Left) Spatial distribution of estimated EC ( ms/m) from a joint inversion of EM34-10, EM34-20 and EM34-40 data using a 1-D

laterally constrained algorithm for quasi-3D conductivity imaging; right) Mass concentration distribution from numerical model..... 137

**Figure 66.** Fluid and mass budget (average of simulated results for 2014) based on the results of numerical modeling.  $Q_{GD}$  is the volume of groundwater discharge to surface waters. Inversely,  $Q_{RD}$  is the volume of groundwater recharged from surface waters (ponds and canals). ..... 138

**Figure 67.** Comparison of hydrographs of observations wells for scenario 1 and 2 139

**Figure 68.** Comparison of hydrographs of observations wells for scenario without recharge ..... 139

**Figure 69.** Displacement of the saltwater front after 1 year of change..... 141

## List of tables

<b>Table 1.</b> Water density in piezometers and water level with density correction (freshwater head).....	50
<b>Table 2.</b> EM34 profiles .....	61
<b>Table 3.</b> Summary of results of regular measurements of $^{222}\text{Rn}$ from groundwater samples in selected piezometers for estimation of groundwater flow (detailed information of piezometers is shown in Annex 1).....	67
<b>Table 4.</b> Summary of results of $^{222}\text{Rn}$ analysis from groundwater in continue pumping wells .....	68
<b>Table 5.</b> Radon activities in surface water in the Crau area. X and Y are coordinates according to Lambert 93 projection. <b>st.</b> , radon measurement points with the boat maintained in a stable location. <b>av.</b> , average radon activities during continuous radon measurement done on a boat transect. Coordinates are centroids of several consecutive points during navigation. ....	75
<b>Table 6.</b> EM-34 survey measurement statistics.....	88
<b>Table 7.</b> Porosity values estimated by Archie's law with $a=0.81$ and $m=2$ . Example for piezometer XD. ....	100
<b>Table 8.</b> Input parameters and boundary conditions applied to the model .....	122
<b>Table 9.</b> Groundwater discharge to surface water estimated from $^{222}\text{Rn}$ measurements. ....	130
<b>Table 10.</b> Results of sensitivity analysis .....	140



## **Annexes**

Annex 1. Information of selected observation points

Annex 2. Observation data (from 2013-2014)

Annex 3. Electrical conductivity profile data

Annex 4. Pumping well information

Annex 5. Lithology description and well construction of radon sampling piezometers

**Annex 1. Information of selected observation points**

No	Name	Type*	Coordinate (Lambert 93)		Total depth <i>m</i>	Benchma rk elevation <i>m.asl</i>	Height of benchma rk <i>m</i>	Surface elevatio n <i>m.asl</i>
			<i>X</i>	<i>Y</i>				
1	XAbis	P	843554.75	6272483.8	30.1	1.19	0.34	0.85
2	XCbis	P	845663.07	6271828.5	15	2.26	0.32	1.94
3	X17	P	842470.91	6271034.9	22.4	2.34	1	1.34
4	XBbis	P	844233.98	6269942.8	19.2	1.04	0.28	0.76
5	X19	P	844622.97	6268789.4	31.41	2.27	1.02	1.25
6	P21	W	846082.42	6272976.1	4.3	4.4	0.99	3.41
7	Pz21	P	846086.14	6272936	18.47	4.3	1.1	3.2
8	Pz1901	P	846810.81	6272982.9	9.45	7.33	0.93	6.4
9	Pz2171	P	846986.62	6271253.8	4.97	5.17	0.89	4.28
10	P16bis	W	847704.76	6270379.3	3.8	4	0.9	3.1
11	X20bis	P	847224.21	6269630.4	29.7	1.39	0.26	1.13
12	P20	W	848585.52	6269721.7	4.88	5.01	0.85	4.16
13	P9	W	850521.39	6269146.7	8.5	8.83	0.75	8.08
14	X26bis	P	848605.33	6267717.6	30.12	1.23	0.27	0.96
15	P13	W	853447.29	6266946	5.95	7.69	0.72	6.97
16	P72	W	852641.49	6268588.5	11.18	9.5	0.69	8.81
17	P70	W	852274.64	6270051.8	11.25	13.1	0.86	12.24
18	P33	W	851669.46	6272331.2	12.7	16.2	0.78	15.42
19	P33bis	W	851620.66	6271655.2	11.44	14.55	0.66	13.89
20	P27bis	W	850371.92	6272482.4	13.38	16.79	0.81	15.98
21	P26ter	W	848381.76	6274284.3	9.77	12.09	0.83	11.26
22	X36	P	850350.68	6266231.5	20.58	2.17	1.05	1.12
23	XDbis	P	849529.72	6265731.1	29.7	1.12	0.26	0.86
24	X4415	P	848776.5	6264484.8	24.1	2.24	0.28	1.96
25	L1	P	846443.54	6266773.5	21.2	2.18	0.28	1.9
26	L2	P	846968.87	6266218.5	28.7	1.96	0.37	1.59
27	L3	P	848055.88	6265296.3	24.2	2.69	0.26	2.43

No	Name	Type*	Coordinate (Lambert 93)		Total depth	Benchma rk elevation	Height of benchma rk	Surface elevatio n
			<i>X</i>	<i>Y</i>				
28	E1	S	847633.4	6265681.5	-	0	-	-
29	X13	P	849251.76	6265333.8	29.6	2.44	0.9	1.54
30	X30	P	849559.69	6265583.8	28.2	1.96	0.9	1.06
31	X33	P	850402	6265991	23.3	2.44	1	1.44
32	X35	P	850499.37	6266035.4	18.9	2.39	0.93	1.46
33	IKEA 1	P	851678.16	6265760.5	9.46	1.351	-0.2	1.551
34	IKEA 2	P	851950.82	6265307.9	9.48	1.216	-0.17	1.386
35	IKEA 3	P	852143.27	6265244.3	10.15	1.98	0	1.98
36	IKEA 4	P	852049.98	6266216.2	5.6	2.492	0	2.492
37	X23	P	840407.6	6271969	27.88	3.41	0.98	2.43
38	X4400b	P	845310.08	6263131.7	3.3	2.06	0.8	1.26
39	C3	P	846976.43	6259957.1	31.3	2.34	0.29	2.05
40	C4	P	847416.79	6260397.2	31.7	2.54	0.29	2.25
41	P4	W	851989.04	6267297.4	3.95	4.54	0.4	4.14
42	X15	P	851823.06	6264623.3	22.66	2.9	-0.2	3.1
43	P77	W	853987.57	6269924.6	6.2	15.3	0	15.3
44	P65	W	851118.35	6270655.3	10.37	11.7	0.96	10.74
45	P34	W	853318.4	6271788.2	14.44	19.1	0.66	18.44

\*Note: Type of observation works: P – Piezometer

W – Well

S – Surface water station

**Annex 2. Observation data (from 2013-2014)****Table 2.1.** Groundwater observation (m)

No.	Name	19/12/12	27/03/13	15/04/13	16/05/13	30/05/13	18/07/13	12/09/13	24/10/13	18/12/13	28/01/14	28/02/14
1	XAbis	-	-	-	0.66	0.65	0.39	0.51	0.61	0.55	0.04	0.69
2	XCbis	-	-	-	0.91	0.89	0.68	0.78	0.89	0.86	1.78	1.18
3	X17	-	-	-	-	0.61	0.39	0.39	0.49	0.42	-	0.67
4	XBbis	-	-	-	-	0.57	0.44	0.47	0.5	0.46	-	-
5	X19	-	-	-	-	0.51	0.42	0.42	0.48	0.42	0.64	0.57
6	P21	-	-	-	1.4	1.4	1.15	1.25	1.4	1.33	1.6	2.14
7	P21 Bis	-	-	-	1.4	1.42	1.18	1.26	1.42	1.35	1.65	2.1
8	P1901	-	-	-	1.79	1.84	1.58	1.66	1.84	1.77	2	2.76
9	P2171	-	-	-	1.54	1.5	1.25	1.37	1.5	1.43	1.64	1.95
10	P16bis	-	-	-	0.61	-	0.57	0.68	0.75	0.7	0.93	1.14
11	X20bis	-	-	-	0.7	0.66	0.55	0.62	0.7	0.64	0.87	0.87
12	P20	-	-	-	-	0.94	0.7	0.76	0.89	0.85	1.04	1.38
13	P9	0.96	-	0.93	0.9	0.71	0.38	0.16	0.89	0.9	1.03	1.689
14	X26bis	-	-	-	0.58	0.56	0.43	0.56	0.6	0.57	0.8	0.78
15	P13	2.69	-	-	-	2.29	2.17	-	2.67	-	-	-
16	P72	2.03	-	1.37	1.25	1.22	0.5	0.87	1.67	1.75	1.9	2.68
17	P70	2.68	-	-	-	-	2.65	2.32	2.48	-	-	-
18	P33	4.2	-	-	4.83	4	4.26	4.3	4.24	4.16	4.07	5.6
19	P33bis	3.55	-	-	2.3	3.27	-	-	3.53	3.48	3.41	4.93
20	P27bis	-	-	-	-	5.89	-	-	3.82	-	-	-
21	P26ter	-	-	-	-	4.09	4.05	4.2	4.39	-	4.19	5.9
22	X36	0.51	-	0.51	-	0.47	0.29	0.39	0.53	0.57	-	0.67

No.	Name	19/12/12	27/03/13	15/04/13	16/05/13	30/05/13	18/07/13	12/09/13	24/10/13	18/12/13	28/01/14	28/02/14
23	XDbis	0.5	0.56	0.48	-	0.45	0.31	0.39	0.53	0.48	0.68	0.57
24	X4415	0.32	-	0.28	0.35	0.27	0.22	0.22	0.36	0.27	0.32	0.29
25	L1	0.38	-	0.34	0.48	0.57	0.28		0.4	0.34	-	0.43
26	L2	0.41	-	0.41	0.494	0.43	0.34	0.34	0.45	0.39	-	0.49
27	L3	0.33	-	0.32	0.51	0.33	0.23	0.23	0.38	0.32	0.55	0.38
28	E1	-	-	-	-0.53	-0.45	-0.44	-0.47	0.54	0.45	-	-0.45
29	X13	-	-	-	-	-	-	-	-	0.42	0.48	0.49
30	X30	0.51	0.51	0.45	0.46	0.42	0.29	0.33	0.5	0.46	0.51	0.52
31	X33	0.51	0.56	0.5	0.49		0.27	0.38	0.52	0.54	0.59	0.62
32	X35	0.51	0.58	0.5	0.49	0.46	0.28	0.42	0.55	0.57	0.65	0.66
33	IKEA 1	-	-	0.731	0.691	0.671	0.551	0.651	0.771	0.771	0.821	0.901
34	IKEA 2	-	-	0.726	0.706	0.686	0.606	0.676	0.826	0.786	0.816	0.876
35	IKEA 3	-	-	-	0.71		0.69	0.71	0.86	0.79	0.81	
36	IKEA 4	-	-	-	0.972	0.892	0.702	0.872	1.092	1.092	1.162	1.302
37	X23	-	-	-	-	-	-	-	0.74	-	-	-
38	X4400b	-	-	-	-	-	-	-	-0.58	-	-	-
39	C3	31.3	-	-	-	-	-	-	0.24	-	-	-
40	C4	31.7	-	-	-	-	-	-	0.14	-	-	-
41	X15	-	-	-	-	-	-	-	1.46	-	-	-
42	P34	-	-	-	-	-	-	-	7.97	-	-	-

**Table 2.2.** Electrical conductivity at -10m.b.g.l ( $\mu\text{S}/\text{cm}$ )

No	Name	19/12/12	16/05/13	30/05/13	18/07/13	12/09/13	24/10/2013	18/12/13	28/01/14	28/02/14
1	XAbis	-	-	863	789	740	958	928	785	-
2	XCbis	-	-	790	855	945	781	779	912	-
3	X17	-	-	3470	3070	2270	3060	3130	-	-
4	XBbis	-	-	2810	3090	3000	3500	3000	-	-
5	X19	-	-	1942	2870	2520	3200	4130	2960	-
6	P21	-	-	631	635	642	578	623	627	729
7	P21 Bis	-	-	817	717	752	768	791	805	749
8	P1901	-	-	785	775	764	760	772	-	755
9	P2171	-	-	698	692	694	625	688	697	683
10	P16bis	-	-	-	643	689	707	732	765	614
11	X20bis	-	65	654	651	650	660	644	777	643
12	P20	-	-	1188	540	553	540	551	603	620
13	P9	704	-	698	681	655	642	721	-	676
14	X26bis	-	-	829	840	813	790	1065	820	-
15	P13	-	-	654	660	-	668	-	-	-
16	P72	711	-	650	634	674	700	721	720	747
17	P70	510	-	-	508	489	475	-	-	-
18	P33	-	-	-	545	559	557	557	550	589
19	P33bis	-	-	-	-	-	549	-	552	548
20	P27bis	-	-	-	-	-	685	-	-	-
21	P26ter	-	-	947	934	928	921	-	969	937
22	X36	-	-	829	783	779	780	780	-	840
23	XDbis	990	-	972	1003	949	1064	1348	1172	-

No	Name	19/12/12	16/05/13	30/05/13	18/07/13	12/09/13	24/10/2013	18/12/13	28/01/14	28/02/14
24	X4415	3390	-	3330	3340	3290	3360	5290	3300	-
25	L1	4490	-	9960	12020	-	3180	3340	-	-
26	L2	1868	-	1884	1830	1783	1870	1798	-	-
27	L3	3650	-	3610	3400	3370	3430	2240	2860	-
28	E1	823	-	729	-	-	-	-	-	-
29	X13	-	-	-	-	-	-	1330	1295	-
30	X30	-	1288	1424	860	824	853	2460	996	-
31	X33	996	868		898	898	902	944	868	-
32	X35	860	830	831	811	829	827	854	850	-
33	IKEA 1	-	639	640	595	304	328	646	626	382
34	IKEA 2	-	663	666	660	321	600	672	671	669
35	IKEA 3	-	650		650	823	722	704	752	-
36	IKEA 4	-	645	648	640	555	642	651	659	671
37	X23	-	-	-	-	-	1550	-	-	-
38	X4400b	-	-	-	-	-	48800	-	-	-
39	C3	-	-	-	-	-	52500	-	-	-
40	C4	-	-	-	-	-	41700	-	-	-
41	X15	-	-	-	-	-	782	-	-	-
42	P34	-	-	-	-	-	477	-	-	-

**Table 2.3.** Temperature observation at -10m.bgl (°C)

No.	Piezometer	19/12/12	16/05/13	30/05/13	18/07/13	12/09/13	24/10/2013	18/12/13	28/01/14	28/02/14
1	XAbis	-	-	14.1	15.6	21.5	15.8	14.5	13.2	-
2	XCbis	-	-	14.8	14.5	20.8	16.3	15.5	14.4	-
3	X17	-	-	14.1	15	20.1	17.7	15.4	-	-
4	XBbis	-	-	14.5	15.7	20.3	15.7	15.9	-	-
5	X19	-	-	15.1	15.7	21.3	17.8	15.7	13.6	-
6	P21	-	-	14.4	18.8	20.2	19.2	12.6	11.6	11.5
7	P21 Bis	-	-	15.7	15.4	21.3	19.2	15.2	14.3	16.4
8	P1901	-	-	15.7	16.2	18.3	18.6	17.8		16.4
9	P2171	-	-	14.6	19.2	19.5	18.9	12.6	11.7	12.7
10	P16bis	-	-	-	19.4	19.3	19.5	12.1	10.5	11.3
11	X20bis	-	14.2	16.2	15.9	16.5	16.1	16.2	14.3	16.3
12	P20	-	-	14.3	17	19.1	19.2	13.3	12.1	12.4
13	P9	14.5	-	14.7	16.3	17.3	17.5	14.2		14.8
14	X26bis	-	-	15.6	15.6	20	15.2	15.3	15.2	-
15	P13	-	-	16.1	16.7	-	18.1	-	-	-
16	P72	17	-	16.5	16.3	17.3	17.2	17	16.6	16.6
17	P70	15.9	-	-	16.2	16.9	17.4	-	-	-
18	P33	-	-	-	16.7	16.7	16.7	15.8	14.7	16.1
19	P33bis	-	-	-	-	-	16.9	-	15.9	16.9
20	P27bis	-	-	-	-	-	17.6	-	-	-
21	P26ter	-	-	16.1	16.3	17.3	18.2	-	16.2	16
22	X36	-	-	13.4	15.4	17.5	16.5	14.5		12.4
23	XDbis	13.2	-	13.9	15.1	20	16.6	15.7	14.7	-

No.	Piezometer	19/12/12	16/05/13	30/05/13	18/07/13	12/09/13	24/10/2013	18/12/13	28/01/14	28/02/14
24	X4415	15	-	14.8	15.6	18.5	16.6	16.2	16	-
25	L1	14.2	-	14.3	15	-	16.4	15.2		-
26	L2	14.6	-	16.1	14.9	21.5	16.4	14.7		-
27	L3	14.1	-	13.9	14.3	16	14.5	13.4	13.2	-
28	E1	8.3	-	16.1	-	-	-	-		-
29	X13	-	-	-	-	-	-	16.2	15.7	-
30	X30	-	14.3	14.6	15.7	18.9	17.1	15.3	14.9	-
31	X33	14.5	15.8		16.2	20.5	16.2	15.7	15.4	-
32	X35	13	14.9	14.7	15.4	18.3	16.9	15.8	14.6	-
33	IKEA 1	-	14.3	13.8	15.1	18.8	17.5	16.2	15.6	13.1
34	IKEA 2	-	14.9	15	16.3	19.3	17.8	16.6	15.7	15.3
35	IKEA 3	-	15		16.5	23.9	22.1	18.1	16.3	-
36	IKEA 4	-	15.8	15.8	16.8	21.1	17.5	16.3	15.7	14.8
37	X23	-	-	-	-	-	17.1	-	-	-
38	X4400b	-	-	-	-	-	19.8	-	-	-
39	C3	-	-	-	-	-	18.5	-	-	-
40	C4	-	-	-	-	-	18.5	-	-	-
41	X15	-	-	-	-	-	15.3	-	-	-
42	P34	-	-	-	-	-	16.8	-	-	-

## Annex 3. Electrical conductivity profile data

XA Bis					XC Bis				
	18/12/2013		28/02/2014			18/12/2013		28/02/2014	
Depth	EC	T	EC	T	Depth	EC	T	EC	T
<i>m.b.s.l</i>	$\mu\text{S/cm}$	$^{\circ}\text{C}$	$\mu\text{S/cm}$	$^{\circ}\text{C}$	<i>m.b.s.l</i>	$\mu\text{S/cm}$	$^{\circ}\text{C}$	$\mu\text{S/cm}$	$^{\circ}\text{C}$
0.19	917	12.8	903	13.6	1.26	(no water)		(no water)	
-0.81	916	14.2	903	14	0.26	759	12.9	797	11.9
-1.81	920	14.9	905	14.4	-0.74	759	14.3	797	12.6
-2.81	924	15.2	907	14.6	-1.74	768	15.1	797	13.2
-3.81	924	15.2	907	14.7	-2.74	768	15.2	797	13.2
-4.81	923	14.9	908	14.7	-3.74	779	15.4	797	13.3
-5.81	924	14.8	909	14.7	-4.74	775	15.4	797	13.4
-6.81	925	14.7	909	14.7	-5.74	775	15.4	797	13.6
-7.81	926	14.6	909	14.6	-6.74	776	15.4	797	13.6
-8.81	928	14.5	911	14.5	-7.74	779	15.5	797	13.6
-9.81	941	14.5	923	14.5	-8.74	782	15.6	797	13.6
-10.81	1579	14.5	2020	14.5	-9.74	784	15.6	797	13.6
-11.81	12280	14.5	12640	14.5	-10.74	784	15.6	797	13.6
-12.81	13480	14.5	13500	14.5	-11.74	781	15.6	797	13.6
-13.81	13490	14.5	13510	14.5	-12.74	778	15.6	797	13.6
-14.81	13490	14.5	13510	14.5					
-15.81	13490	14.5	13510	14.6					
-16.81	13490	14.6	13510	14.6					
-17.81	13500	14.6	13520	14.6					
-18.81	13520	14.6	13540	14.6					
-19.81	13500	14.6	13520	14.6					
-20.81	13290	14.6	13300	14.6					
-21.81	13250	14.6	13240	14.6					

X26 Bis								
	12/18/2013		28/02/2014		03/05/2014 (before purge)		03/05/2014 (after purge)	
Depth	EC	T	EC	T	EC	T	EC	T
<i>m.b.s.l</i>	$\mu\text{S/cm}$	$^{\circ}\text{C}$	$\mu\text{S/cm}$	$^{\circ}\text{C}$	$\mu\text{S/cm}$	$^{\circ}\text{C}$	$\mu\text{S/cm}$	$^{\circ}\text{C}$
0.23	836	11	818	13.2	821	12.4	832	13.5
-0.77	840	12.3	820	14.6	820	13.7	811	14.5
-1.77	840	12.3	820	15.4	819	15	803	15.2
-2.77	840	12.3	821	15.4	828	15.4	828	15.4
-3.77	840	12.3	788	15.4	827	15.4	828	15.4
-4.77	840	12.3	825	15.4	826	15.4	815	15.4
-5.77	840	12.3	800	15.4	842	15.4	834	15.4
-6.77	840	12.3	878	15.4	878	15.4	857	15.4
-7.77	840	12.3	878	15.4	880	15.4	867	15.4
-8.77	840	12.3	878	15.4	882	15.4	866	15.4
-9.77	840	12.3	881	15.4	884	15.4	865	15.4
-10.77	840	12.3	885	15.4	884	15.4	868	15.4
-11.77	840	12.3	900	15.4	900	15.4	873	15.4
-12.77	840	12.3	955	15.4	977	15.4	886	15.4
-13.77	965	15.3	1052	15.4	1065	15.4	936	15.4
-14.77	1065	15.3	1165	15.4	1193	15.4	1010	15.4
-15.77	1150	15.3	1510	15.4	1630	15.4	1293	15.4
-16.77	2910	15.3	4000	15.4	3720	15.4	2700	15.4
-17.77	13790	15.4	13050	15.4	13040	15.4	9100	15.4
-18.77	23100	15.5	23000	15.5	23000	15.5	22500	15.5
-19.77	23100	15.5	23100	15.5	23000	15.5	23100	15.5
-20.77	23100	15.5	23100	15.5	23000	15.5	23100	15.5
-21.77	23100	15.5	23100	15.5	23000	15.6	23100	15.5

XD Bis					X20 Bis				
	12/18/2013		27/02/2014			13/11/2014			
Depth	EC	T	EC	T	Depth	EC	T	EC	T
<i>m.b.s.l</i>	$\mu\text{S/cm}$	$^{\circ}\text{C}$	$\mu\text{S/cm}$	$^{\circ}\text{C}$	<i>m.b.s.l</i>	$\mu\text{S/cm}$	$^{\circ}\text{C}$	$\mu\text{S/cm}$	$^{\circ}\text{C}$
0.12	1050	13.3	1000	12.9	0.39	674	16	-	-
-0.88	1050	14.6	1000	13.5	-0.61	659	16.2	-	-
-1.88	1053	15.7	1002	14	-1.61	651	16.4	-	-
-2.88	1057	16.6	1009	14.5	-2.61	651	16.5	-	-
-3.88	1058	16.1	1024	14.6	-3.61	651	16.5	-	-
-4.88	1060	16	1032	14.7	-4.61	652	16.5	-	-
-5.88	1080	16	1035	14.7	-5.61	651	16.5	-	-
-6.88	1112	15.9	1092	14.9	-6.61	646	16.4	-	-
-7.88	1157	15.9	1076	14.8	-7.61	646	16.4	-	-
-8.88	1348	15.7	1078	14.8	-8.61	646	16.4	-	-
-9.88	2620	15.3	2330	14.9	-9.61	647	16.4	-	-
-10.88	4450	15	4640	15.1	-10.61	652	16.4	-	-
-11.88	5020	14.9	5080	15	-11.61	657	16.4	-	-
-12.88	6010	14.8	6100	15	-12.61	660	16.4	-	-
-13.88	7180	14.8	6940	14.9	-13.61	671	16.4	-	-
-14.88	21100	14.8	20700	14.9	-14.61	689	16.4	-	-
-15.88	30600	14.8	29800	14.8	-15.61	696	16.4	-	-
-16.88	42100	14.8	40800	14.8	-16.61	697	16.4	-	-
-17.88	46400	14.8	46000	14.8	-17.61	700	16.4	-	-
-18.88	46500	14.8	46000	14.8	-18.61	722	16.4	781	16.2
-19.88	46500	14.7	46000	14.8	-19.61	737	16.4	787	16.2
-20.88	46500	14.7	46000	14.8	-20.61	785	16.5	905	16.2
-21.88	46500	14.7	46000	14.7	-21.61	1747	16.5	25900	16.3
-22.88	46500	14.7			-22.61	15980	16.4	25900	16.3

L1					L2				
	12/18/2013		27/02/2014	T		12/18/2013		27/02/2014	T
Depth	EC	T	EC	T	Depth	EC	T	EC	T
<i>m.b.s.l</i>	$\mu S/cm$	$^{\circ}C$	$\mu S/cm$	$^{\circ}C$	<i>m.b.s.l</i>	$\mu S/cm$	$^{\circ}C$	$\mu S/cm$	$^{\circ}C$
0.18	1262	15.3	2560	12	-0.04	1804	14.7	4000	13.2
-0.82	1526	15.8	3530	12.5	-1.04	1802	15.3	3190	13.9
-1.82	1662	16	4270	13	-2.04	1805	15.4	2070	14.8
-2.82	2040	16.2	5800	13.6	-3.04	1805	15.2	1824	14.8
-3.82	2900	16	7150	14.2	-4.04	1803	15	1803	14.8
-4.82	3350	15.9	7760	14.6	-5.04	1803	14.8	1803	14.8
-5.82	3380	15.7	7830	14.7	-6.04	1803	14.8	1801	14.8
-6.82	3330	15.3	7750	15	-7.04	1803	14.7	1800	14.8
-7.82	3340	15.2	7750	15	-8.04	1798	14.7	1804	14.8
-8.82	5710	15.1	7840	15	-9.04	1797	14.7	1822	14.8
-9.82	14650	15.1	13990	15.1	-10.04	1795	14.7	1858	14.8
-10.82	18210	15.1	18070	15.1	-11.04	1795	14.7	1906	14.8
-11.82	18670	15.1	18160	15.1	-12.04	1794	14.7	1931	14.8
-12.82	20600	15.1	23500	15.1	-13.04	1815	14.7	2090	14.8
-13.82	25000	15.1	28600	15.1	-14.04	2250	14.7	2460	14.8
-14.82	28100	15.1	30800	15.1	-15.04	7500	14.8	17290	14.8
-15.82	32900	15.1	35200	15.1	-16.04	24500	14.8	27300	14.8
-16.82	35800	15.1	37200	15.1	-17.04	36900	14.8	38600	14.8
-17.82	39000	15.1	39600	15.1	-18.04	40100	14.8	40200	14.8
-18.82	24900	15.1	29700	15.1	-19.04	45900	14.9	46000	14.9
					-20.04	48800	14.9	49200	14.9
					-21.04	49900	14.9	49600	14.9

L3							X4415				
	12/18/2013		27/02/2014		13/11/2014			12/18/2013		28/02/2014	
Depth	EC	T	EC	T	EC	T	Depth	EC	T	EC	T
<i>m.b.s.l</i>	$\mu\text{S/cm}$	$^{\circ}\text{C}$	$\mu\text{S/cm}$	$^{\circ}\text{C}$	$\mu\text{S/cm}$	$^{\circ}\text{C}$	<i>m.b.s.l</i>	$\mu\text{S/cm}$	$^{\circ}\text{C}$	$\mu\text{S/cm}$	$^{\circ}\text{C}$
0.69			2800	12.2			0.24	3340	15.6	3290	13.7
-0.31	1923	12.7	2470	12.4	4210	16.3	-0.76	3340	16	3280	14.8
-1.31	2060	12.8	3130	12.9	4720	16.3	-1.76	3350	16.5	3280	15.6
-2.31	2090	13.1	3180	13.1	4780	16.3	-2.76	3350	16.5	3290	16.1
-3.31	2110	13.1	3190	13.6	4800	16.2	-3.76	3350	16.5	3300	16.2
-4.31	2150	13.2	3270	13.9	4810	16.2	-4.76	3350	16.4	3300	16.4
-5.31	2180	13.3	3330	14.1	4680	16.1	-5.76	3420	16.4	3360	16.4
-6.31	2210	13.4	3330	14.3	4730	15.9	-6.76	4400	16.3	4230	16.4
-7.31	2240	13.4	3340	14.3	4750	15.8	-7.76	5290	16.2	5320	16.3
-8.31	2210	13.5	3340	14.3	4810	15.8	-8.76	10860	16.2	13500	16.3
-9.31	2350	13.7	3340	14.3	4840	15.6	-9.76	36200	16.1	38100	16.2
-10.31	5530	14.2	3410	14.3	6600	14.6	-10.76	40000	16.1	41900	16.1
-11.31	9860	14.2	9410	14.3	11540	14.2	-11.76	41500	16.1	43200	16.1
-12.31	12330	14.3	16500	14.4	15300	14.2	-12.76	43000	16	44200	16.1
-13.31	17400	14.3	17950	14.4	17210	14.3	-13.76	44200	16	45400	16
-14.31	23200	14.4	23600	14.4	22800	14.3	-14.76	45600	16	47300	16
-15.31	37500	14.4	39200	14.5	38000	14.3	-15.76	46900	16	50400	16
-16.31	46500	14.5	46800	14.5	46900	14.4	-16.76	48600	16	51700	16
-17.31	48300	14.5	48500	14.5	48700	14.4	-17.76	51700	16	52800	16
-18.31	48700	14.5	48700	14.5	48900	14.5	-18.76	53000	16	53400	15.9
-19.31	49000	14.5	48900	14.5	49100	14.5	-19.76	53400	15.9	53600	15.9
							-20.76	53500	15.9	53800	15.9

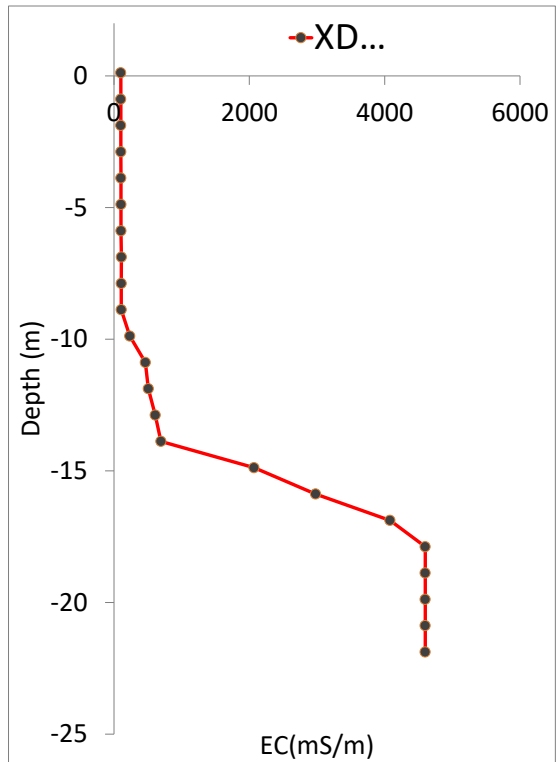
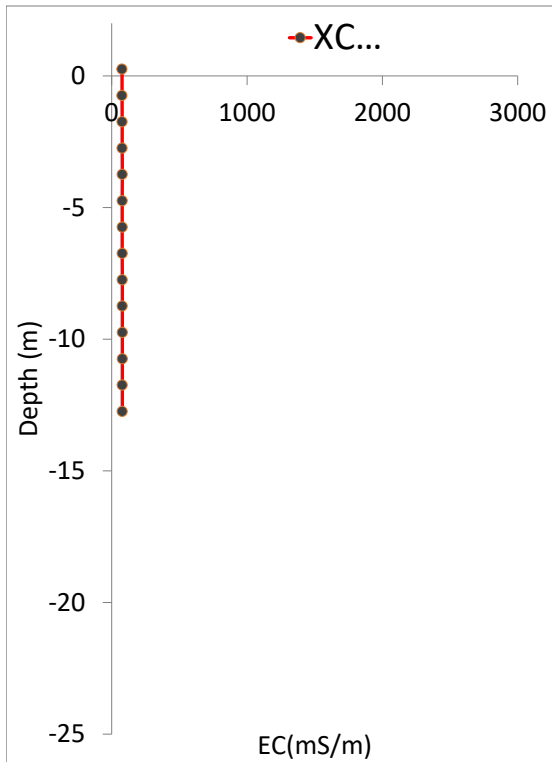
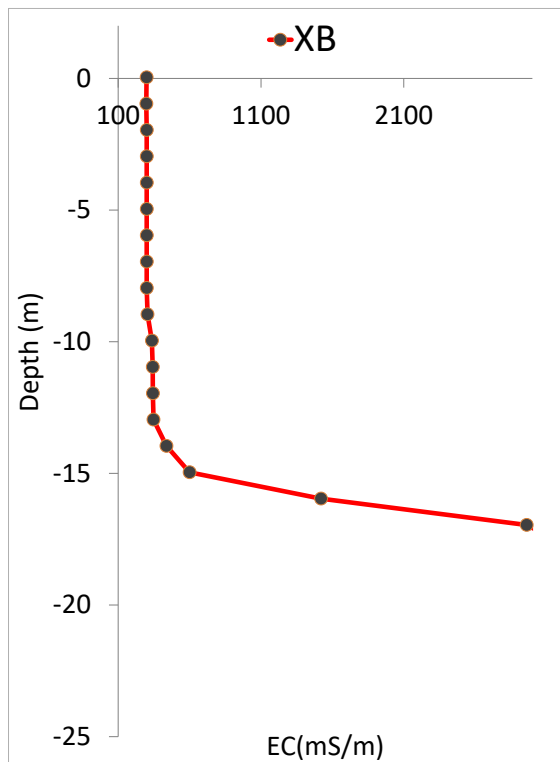
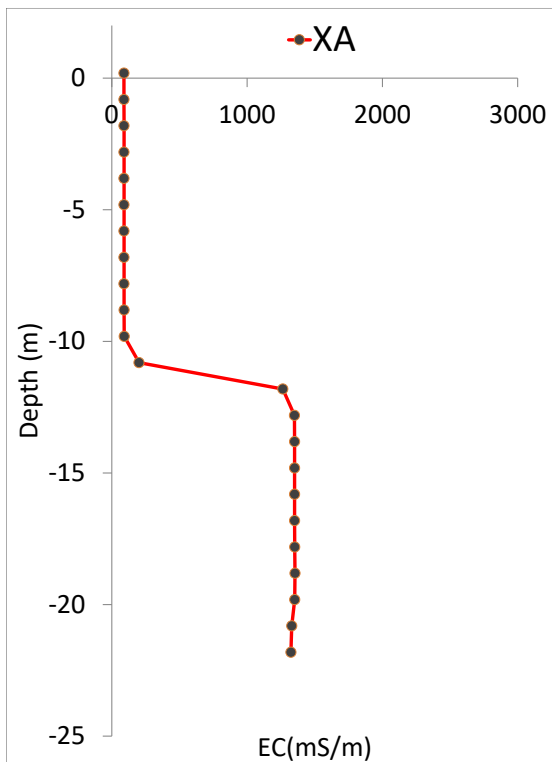
X13					X30				
	12/18/2013		28/02/2014			12/18/2013		28/02/2014	
Depth	EC	T	EC	T	Depth	EC	T	EC	T
<i>m.b.s.l</i>	$\mu\text{S/cm}$	$^{\circ}\text{C}$	$\mu\text{S/cm}$	$^{\circ}\text{C}$	<i>m.b.s.l</i>	$\mu\text{S/cm}$	$^{\circ}\text{C}$	$\mu\text{S/cm}$	$^{\circ}\text{C}$
0.44	1291	16.2	1281	15.7	-0.04	888	14.2	1180	14.1
-0.56	1293	16.2	1282	15.7	-1.04	875	15.2	1190	14.4
-1.56	1293	16.2	1282	15.8	-2.04	883	15.8	1400	14.9
-2.56	1294	16.2	1282	15.8	-3.04	1280	15.9	2380	15.3
-3.56	1293	16.2	1283	15.8	-4.04	2400	15.4	2560	15.4
-4.56	1290	16.2	1282	15.8	-5.04	2490	15.4	2540	15.4
-5.56	1292	16.2	1282	15.9	-6.04	2490	15.3	2530	15.4
-6.56	1302	16.2	1286	15.9	-7.04	2480	15.3	2500	15.4
-7.56	1330	16.2	1300	15.9	-8.04	2460	15.3	2477	15.4
-8.56	1380	16.2	1314	15.9	-9.04	2440	15.3	2560	15.4
-9.56	1660	16.1	1394	15.9	-10.04	2400	15.3	2590	15.4
-10.56	2760	15.9	2490	15.9	-11.04	2660	15.3	2760	15.3
-11.56	6250	15.8	5520	15.8	-12.04	2740	15.3	2770	15.3
-12.56	13600	15.7	12490	15.7	-13.04	3480	15.3	3100	15.3
-13.56	32100	15.6	28500	15.6	-14.04	12060	15.3	9600	15.3
-14.56	40100	15.6	39400	15.5	-15.04	26400	15.2	27000	15.2
-15.56	44800	15.5	44700	15.5	-16.04	39400	15.2	38100	15.2
-16.56	47500	15.5	47300	15.5	-17.04	42500	15.2	41800	15.2
-17.56	48100	15.4	49100	15.4	-18.04	44700	15.2	43700	15.1
-18.56	51000	15.4	51100	15.4	-19.04	46900	15.1	46700	15.1
-19.56	51800	15.4	51800	15.3	-20.04	48600	15.2	48500	15.1
-20.56	52400	15.4	52700	15.3	-21.04	49600	15.2	49500	15.1

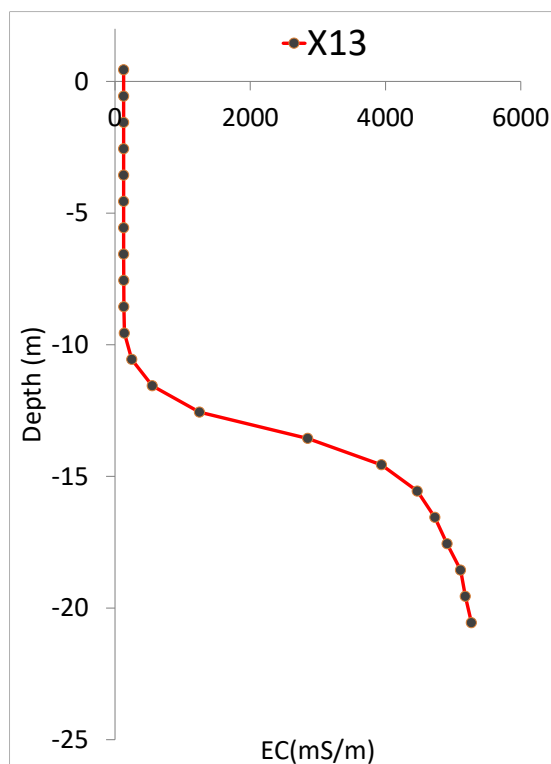
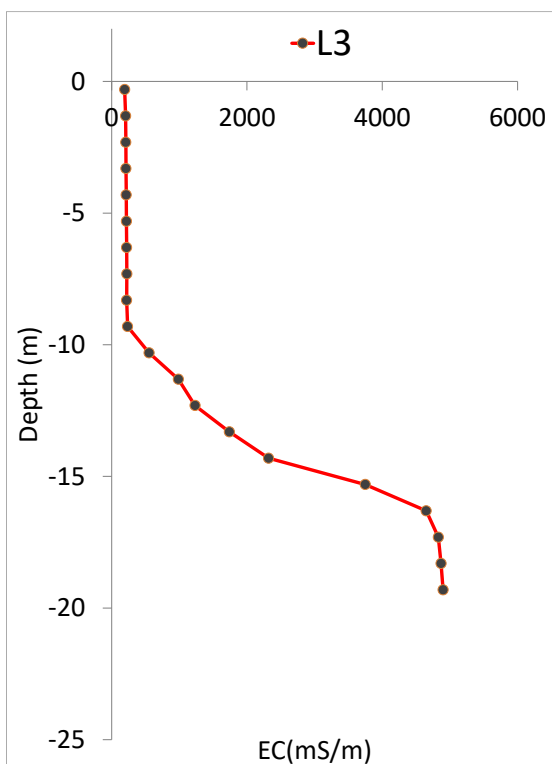
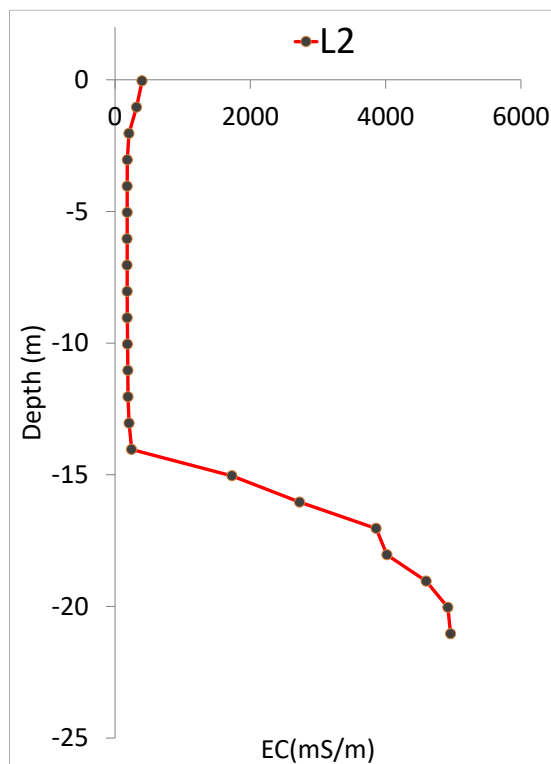
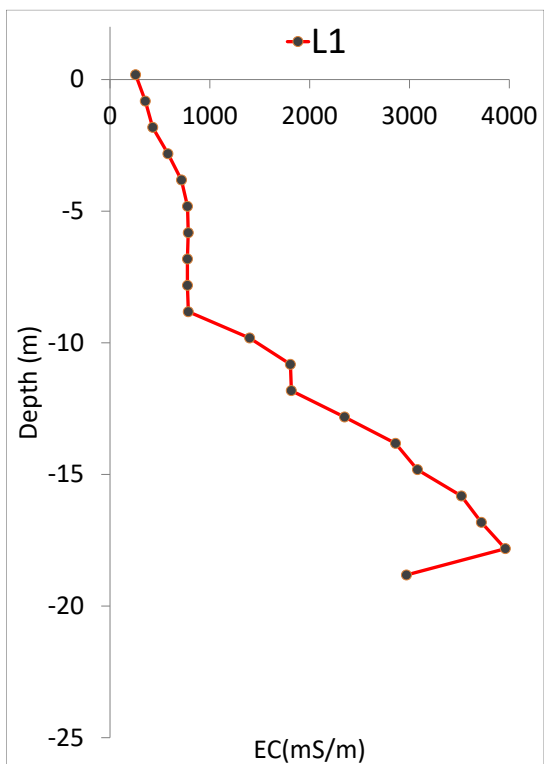
X31			XB Bis			X33				
	28/02/2014		12/18/2013				12/18/2013		28/02/2014	
Depth	EC	T	Depth	EC	T	Depth	EC	T	EC	T
<i>m.b.s.l</i>	$\mu\text{S/cm}$	$^{\circ}\text{C}$	<i>m.b.s.l</i>	$\mu\text{S/cm}$	$^{\circ}\text{C}$	<i>m.b.s.l</i>	$\mu\text{S/cm}$	$^{\circ}\text{C}$	$\mu\text{S/cm}$	$^{\circ}\text{C}$
-0.16	861	15.1	0.04	2990	13.6	0.44	932	15.3	832	15.1
-1.16	861	15.1	-0.96	2970	14.8	-0.56	929	15.3	838	15.1
-2.16	854	15.3	-1.96	3000	15.5	-1.56	925	15.6	830	15.3
-3.16	852	15.4	-2.96	3000	15.9	-2.56	933	15.7	828	15.4
-4.16	858	15.4	-3.96	3000	15.9	-3.56	936	15.7	829	15.4
-5.16	869	15.5	-4.96	3000	15.9	-4.56	938	15.7	830	15.5
-6.16	885	5.5	-5.96	3000	15.7	-5.56	938	15.7	829	5.5
-7.16	924	15.5	-6.96	3000	15.7	-6.56	943	15.7	827	15.5
-8.16	948	15.4	-7.96	3000	15.7	-7.56	944	15.7	829	15.4
-9.16	952	15.4	-8.96	3050	15.7	-8.56	948	15.7	831	15.4
-10.16	953	15.4	-9.96	3360	15.7	-9.56	948	15.7	832	15.4
-11.16	954	15.4	-10.96	3420	15.7	-10.56	956	15.7	840	15.4
-12.16	954	15.4	-11.96	3430	15.7	-11.56	988	15.7	853	15.4
-13.16	955	15.4	-12.96	3470	15.7	-12.56	1068	15.6	910	15.4
-14.16	1010	15.4	-13.96	4380	15.7	-13.56	1265	15.6	1028	15.4
-15.16	5720	15.4	-14.96	6000	15.7	-14.56	1785	15.6	1185	15.4
-16.16	8580	15.4	-15.96	15200	15.8	-15.56	3000	15.5	1728	15.4
			-16.96	29600	15.8	-16.56	17790	15.5	17790	15.5
			-17.96	33200	15.8	-17.56	18600	15.5	18610	15.5
						-18.56	18630	15.5	18650	15.4
						-19.56	18650	15.5	18680	15.4
						-20.56	20300	15.4	20300	15.4

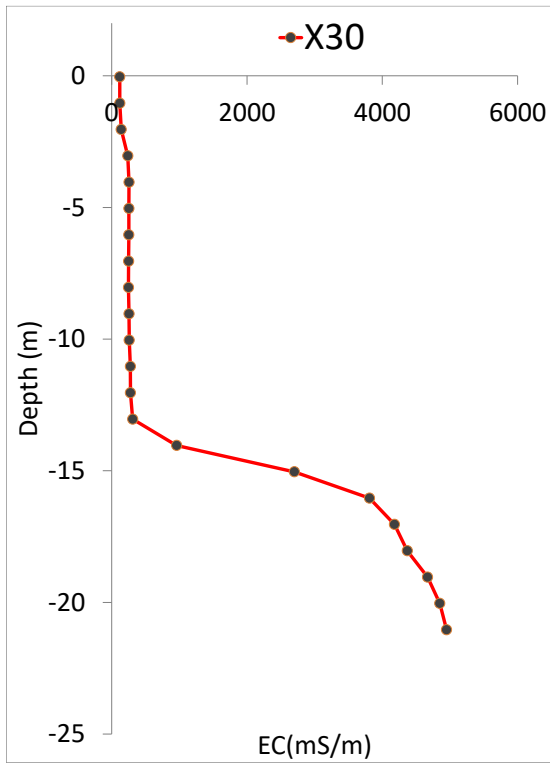
X34					X35				
	12/18/2013		28/02/2014			12/18/2013		28/02/2014	
Depth	EC	T	EC	T	Depth	EC	T	EC	T
<i>m.b.s.l</i>	$\mu S/cm$	$^{\circ}C$	$\mu S/cm$	$^{\circ}C$	<i>m.b.s.l</i>	$\mu S/cm$	$^{\circ}C$	$\mu S/cm$	$^{\circ}C$
0.25	790	12.1	816	12	0.39	854	15.8	817	12.7
-0.75	787	13	811	12.9	-0.61	854	15.8	811	13.1
-1.75	784	14.6	811	14.5	-1.61	854	15.8	811	13.9
-2.75	817	14.9	813	14.8	-2.61	854	15.8	813	14.7
-3.75	816	15.5	815	15.5	-3.61	854	15.8	813	14.7
-4.75	815	15.9	818	15.9	-4.61	854	15.8	813	14.8
-5.75	813	15.9	819	15.9	-5.61	854	15.8	816	14.9
-6.75	806	15.9	819	15.9	-6.61	854	15.8	815	15
-7.75	812	15.9	822	15.9	-7.61	854	15.8	814	15.2
-8.75	812	15.9	822	15.9	-8.61	854	15.8	812	15.4
-9.75	812	15.8	823	15.8	-9.61	854	15.8	810	15.4
-10.75	814	15.8	823	15.8	-10.61	854	15.8	812	15.4
-11.75	814	15.8	829	15.8	-11.61	854	15.8	812	15.4
-12.75	815	15.7	846	15.7	-12.61	854	15.8	811	15.4
-13.75	815	15.7	871	15.7	-13.61	854	15.8	811	15.3
-14.75	815	15.6	964	15.6	-14.61	854	15.8	811	15.3
-15.75	817	15.5	8400	15.5	-15.61	854	15.8	852	15.5
-16.75	8600	15.4	23400	15.4	-16.61	4300	15.6	4250	15.5
-17.75	23400	15.4	23500	15.4	-17.61	25400	15.5	25300	15.5
-18.75	23400	15.4	23600	15.4	-18.61				
-19.75			24200	15.4	-19.61				
-20.75			24500	15.4	-20.61				

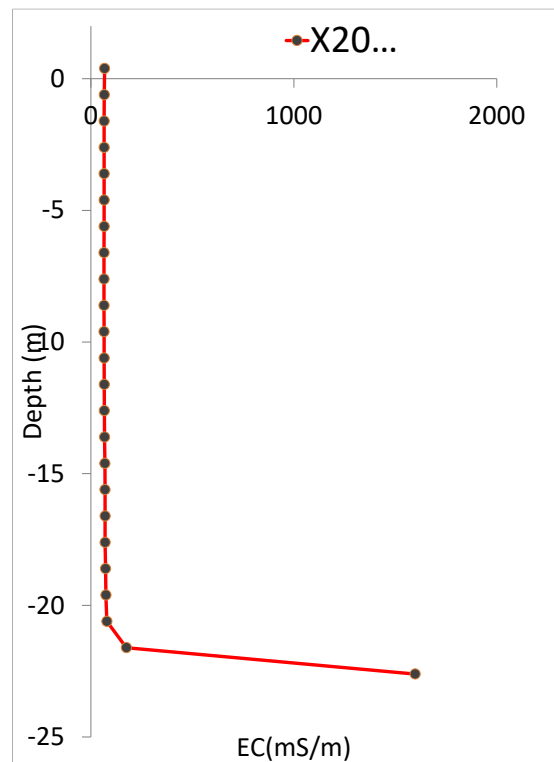
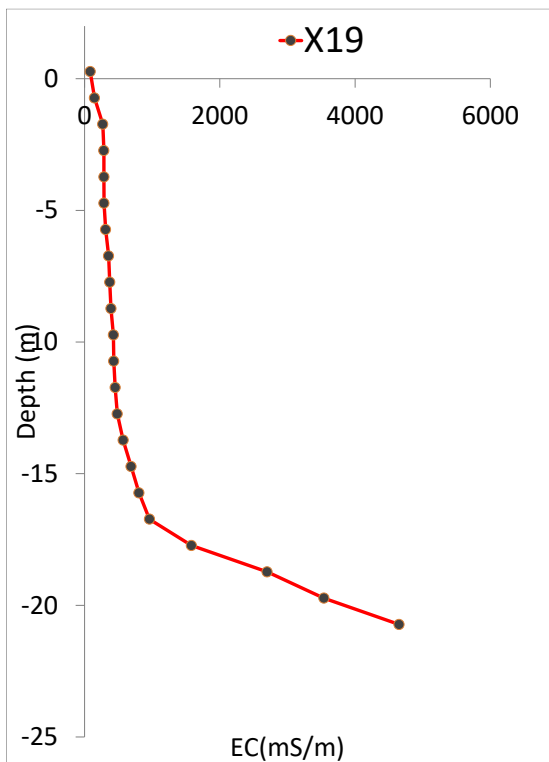
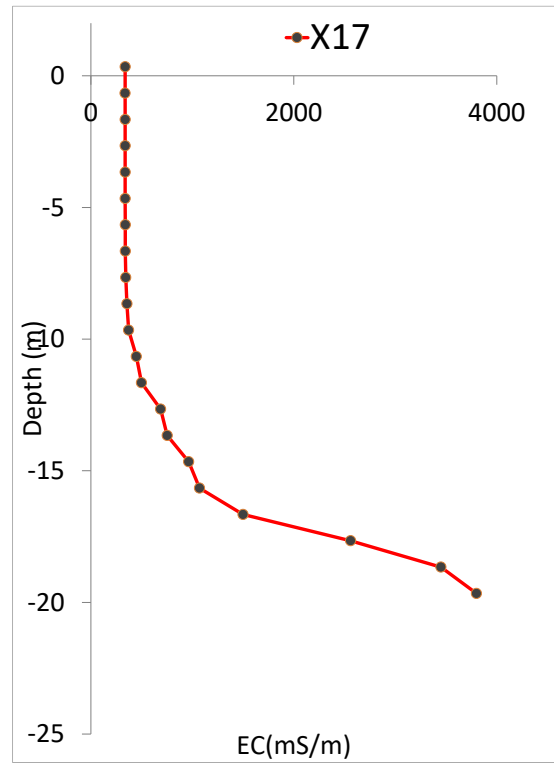
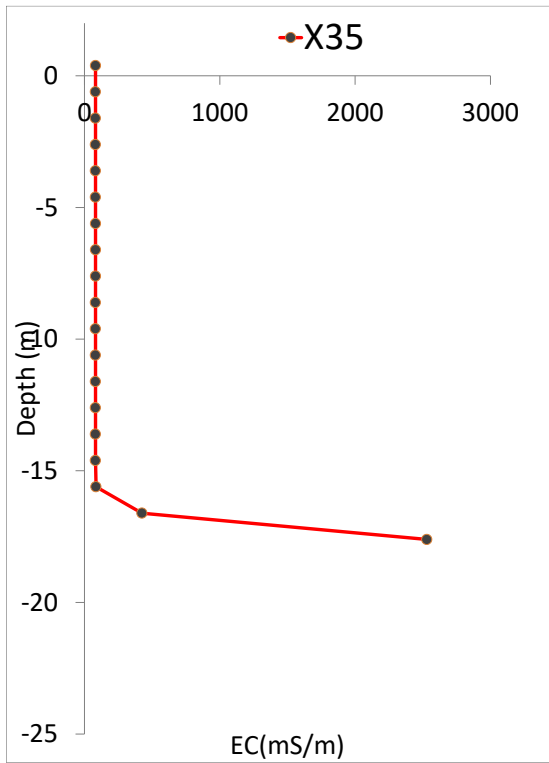
X19					X17				
	12/18/2013		28/02/2014			12/18/2013		28/02/2014	
Depth	EC	T	EC	T	Depth	EC	T	EC	T
<i>m.b.s.l</i>	$\mu\text{S/cm}$	$^{\circ}\text{C}$	$\mu\text{S/cm}$	$^{\circ}\text{C}$	<i>m.b.s.l</i>	$\mu\text{S/cm}$	$^{\circ}\text{C}$	$\mu\text{S/cm}$	$^{\circ}\text{C}$
0.27	2880	15	844	14.6	0.34	2940	15.4	3380	12.4
-0.73	2870	15.2	1469	14.8	-0.66	2950	15.4	3370	13.1
-1.73	2900	15.6	2700	15.1	-1.66	2950	15.4	3380	13.8
-2.73	3070	15.8	2860	15.4	-2.66	2960	15.7	3380	14.4
-3.73	3270	15.9	2870	15.6	-3.66	2980	15.8	3380	15
-4.73	3550	15.9	2880	15.6	-4.66	3050	15.7	3380	15.3
-5.73	3760	15.8	3120	15.6	-5.66	3060	15.5	3390	15.3
-6.73	3880	15.7	3560	15.6	-6.66	3090	15.5	3390	15.3
-7.73	4130	15.7	3730	15.6	-7.66	3130	15.4	3440	15.3
-8.73	4260	15.7	3910	15.6	-8.66	3160	15.4	3550	15.3
-9.73	4400	15.7	4270	15.6	-9.66	3440	15.4	3720	15.3
-10.73	4640	15.7	4320	15.6	-10.66	9720	15.4	4480	15.3
-11.73	5140	15.7	4530	15.6	-11.66	10120	15.5	4990	15.3
-12.73	6200	15.7	4840	15.6	-12.66	10210	15.5	6870	15.3
-13.73	7570	15.7	5710	15.6	-13.66	10210	15.5	7520	15.3
-14.73	8660	15.7	6890	15.6	-14.66	10320	15.5	9640	15.3
-15.73	11500	15.7	8050	15.6	-15.66	11540	15.5	10710	15.3
-16.73	21400	15.7	9600	15.6	-16.66	15090	15.5	14990	15.3
-17.73	31800	15.8	15810	15.7	-17.66	27700	15.5	25600	15.3
-18.73	37000	15.8	27000	15.7	-18.66	36900	15.5	34500	15.3
-19.73	42500	15.8	35400	15.7	-19.66	36900	15.6	38000	15.3

Figure 3.1. Electrical conductivity profiles in piezometers (observed on 17-18/12/2013)









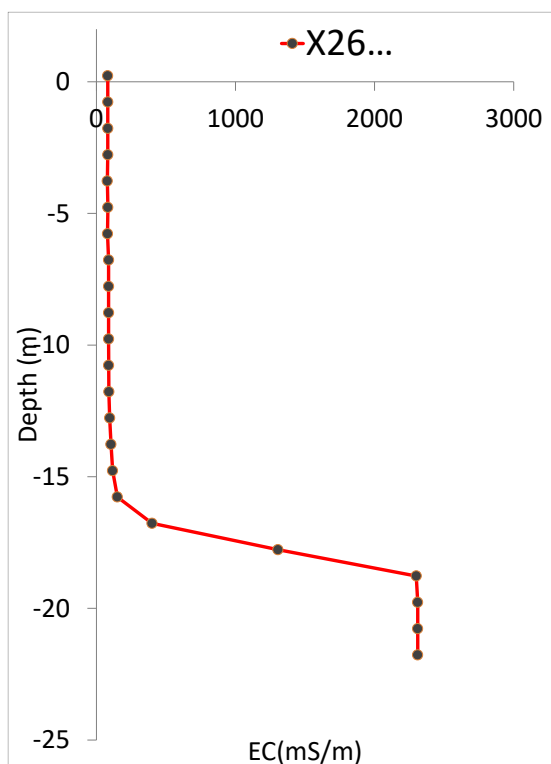
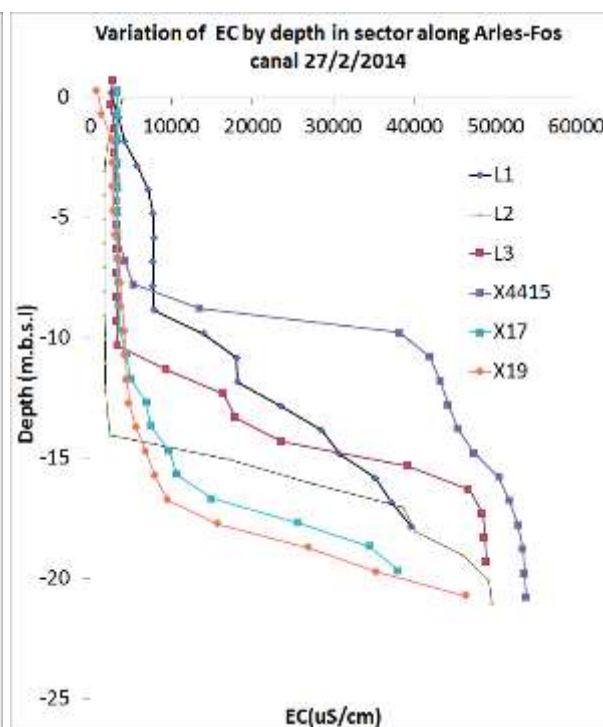
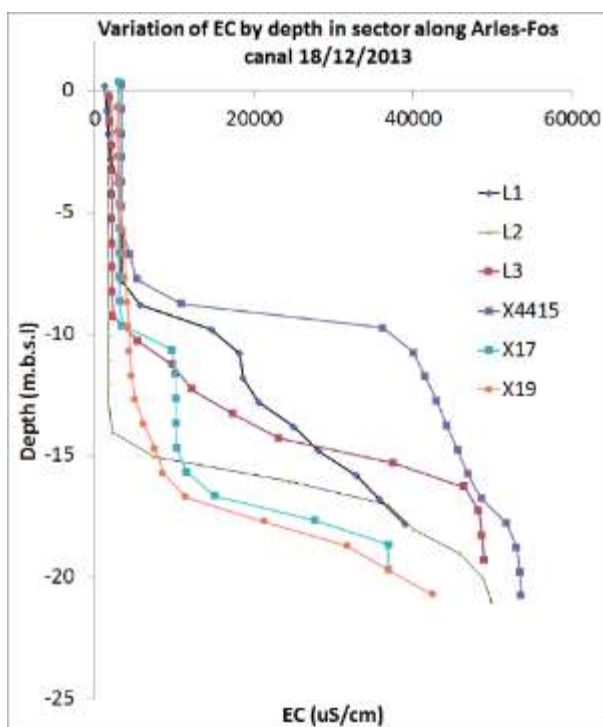
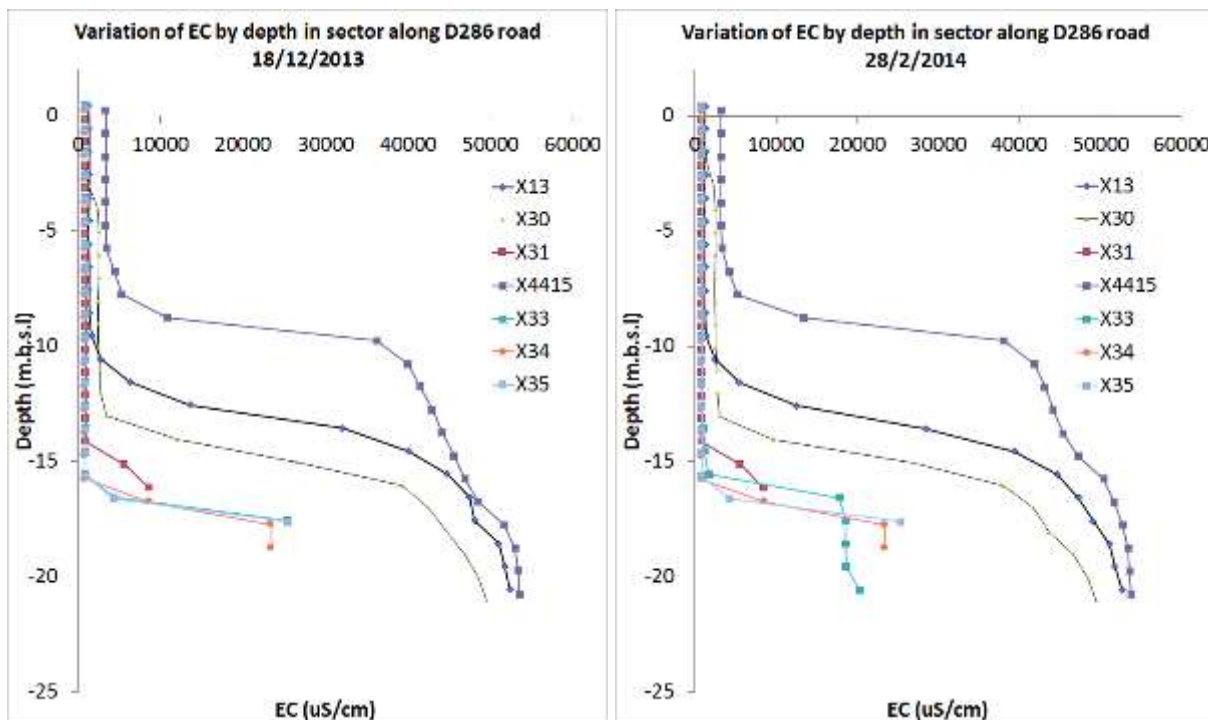


**Figure 3.2.** Variation of electrical conductivity in wells in two campaigns

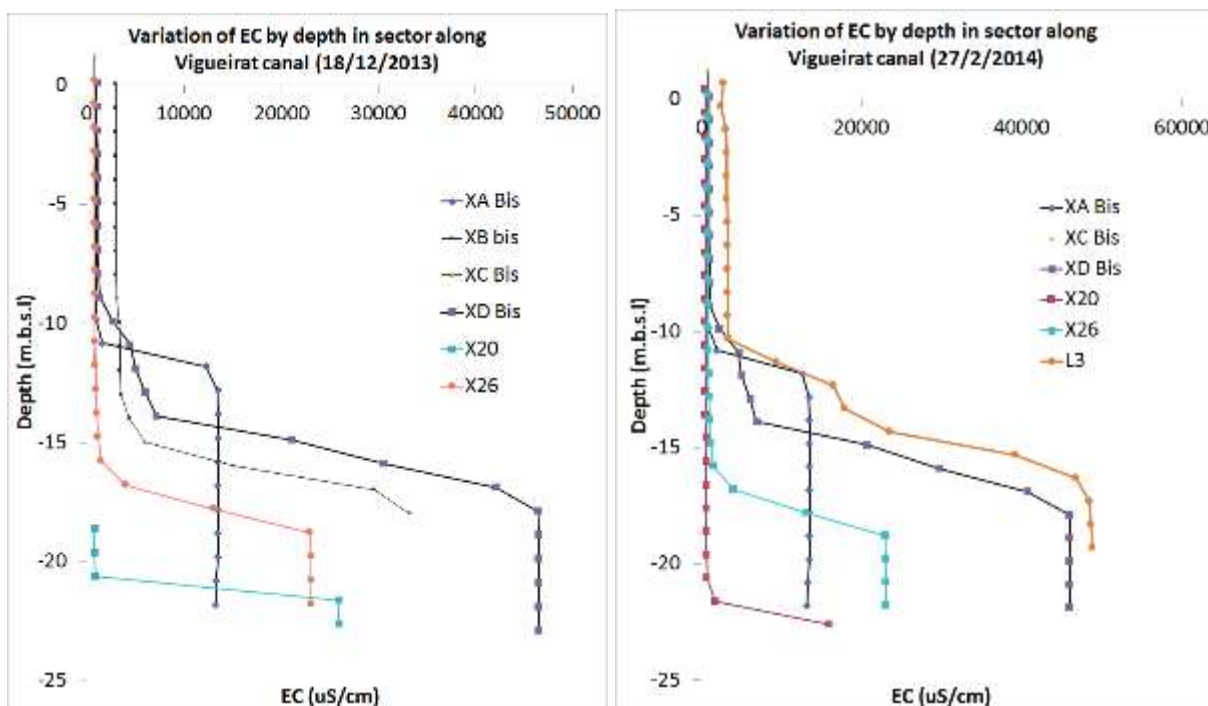
- a) Sector along the road D286
- b) Sector along the canal from Arles to Bouc
- c) Sector in center of marsh, along Vigueirat canal



a)

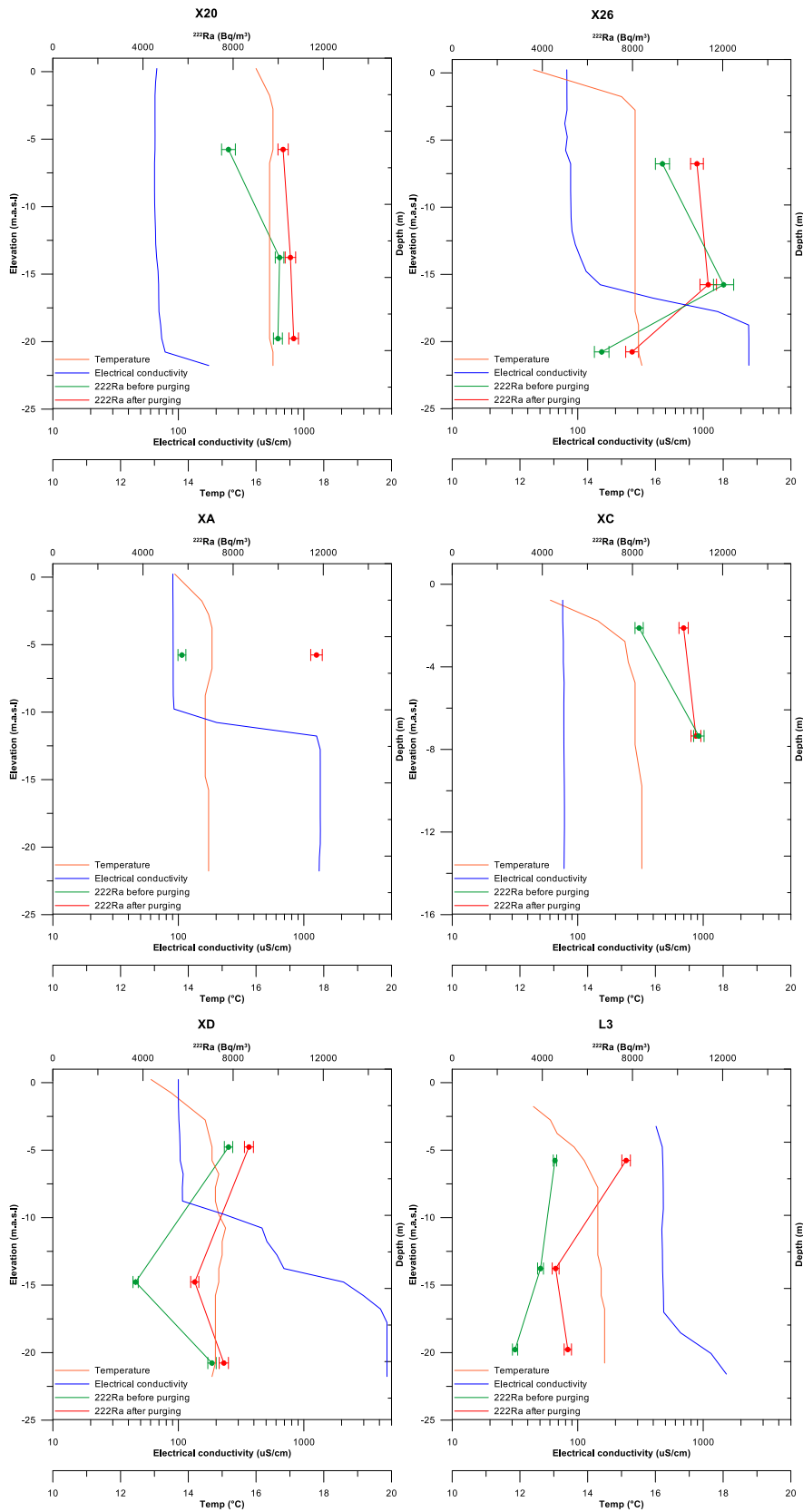


b)



c)

Figure 3.3.  $^{222}\text{Rn}$  in wells with variation of electrical conductivity and temperature



**Annex 4. Pumping well information****Table.4.1.** Municipal stations in research area

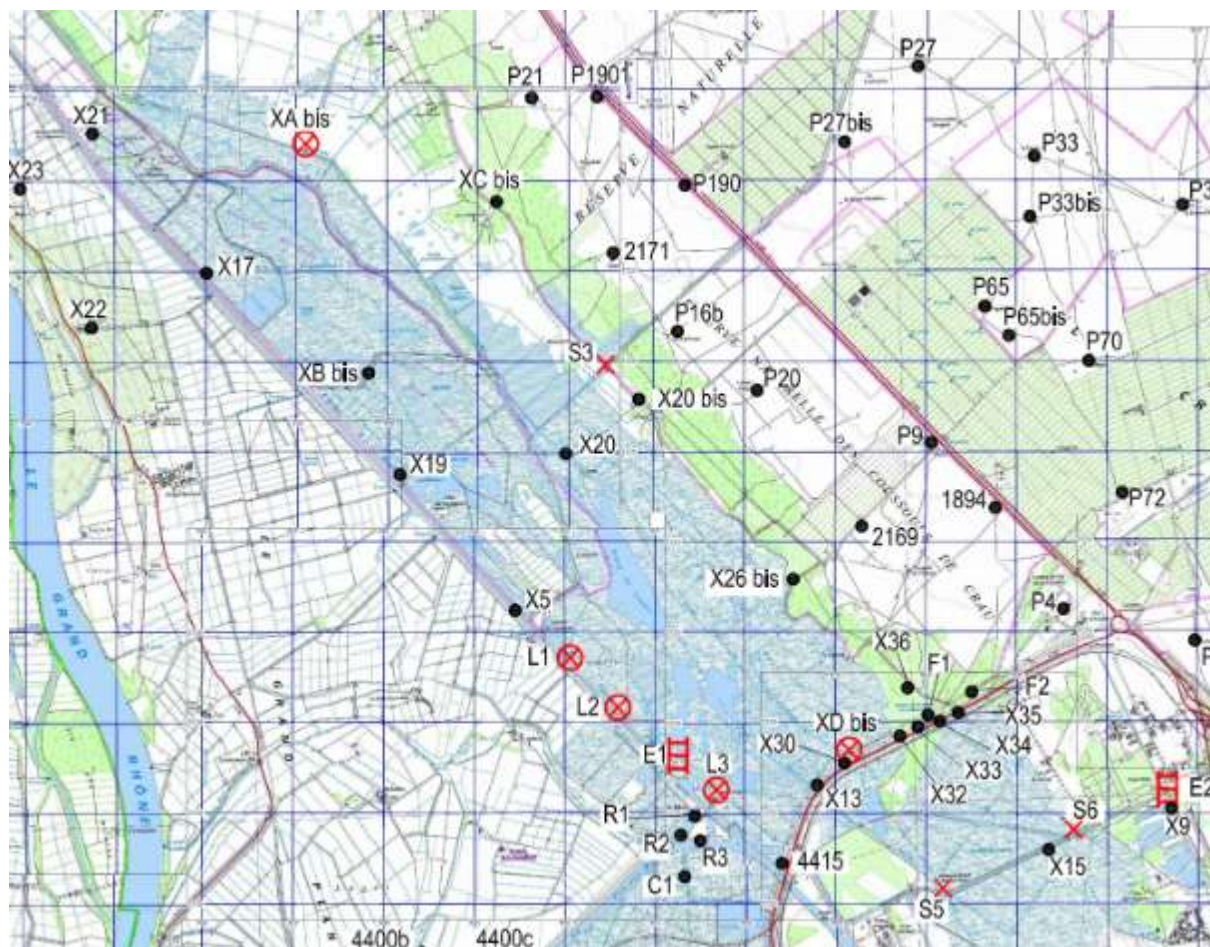
<i>No.</i>	<i>ID</i>	<i>Name</i>	<i>X</i>	<i>Y</i>	<i>Z</i>	<i>Debit</i>
			<i>Lambert 93</i>	<i>Lambert 93</i>	<i>m</i>	<i>(m<sup>3</sup>/day)</i>
1	F74	Z.I. FOS SUR MER	854490	6265526	5	72
2	P1-2	Pissarotte	850519	6266022	3	3,093
3	P3	Les Tapiés_Port de Bouc (Total)	855838	6268215	14	6,817
4	P4	Ventillon-Port autonome de Marseille	856121	6267690	14	6,773
5	P5	Fanfarigoule (Fos sur Mer)	856885	6267836	14	6,084
6	TOT	TOTAL	857635	6268346	15	9,600
7	F30	MAS VINCENT	845242	6275898	11	4,586
8	F54	PUITS COSSOUR	850187	6270843	11	3,363
<b>TOTAL</b>						<b>40,388</b>

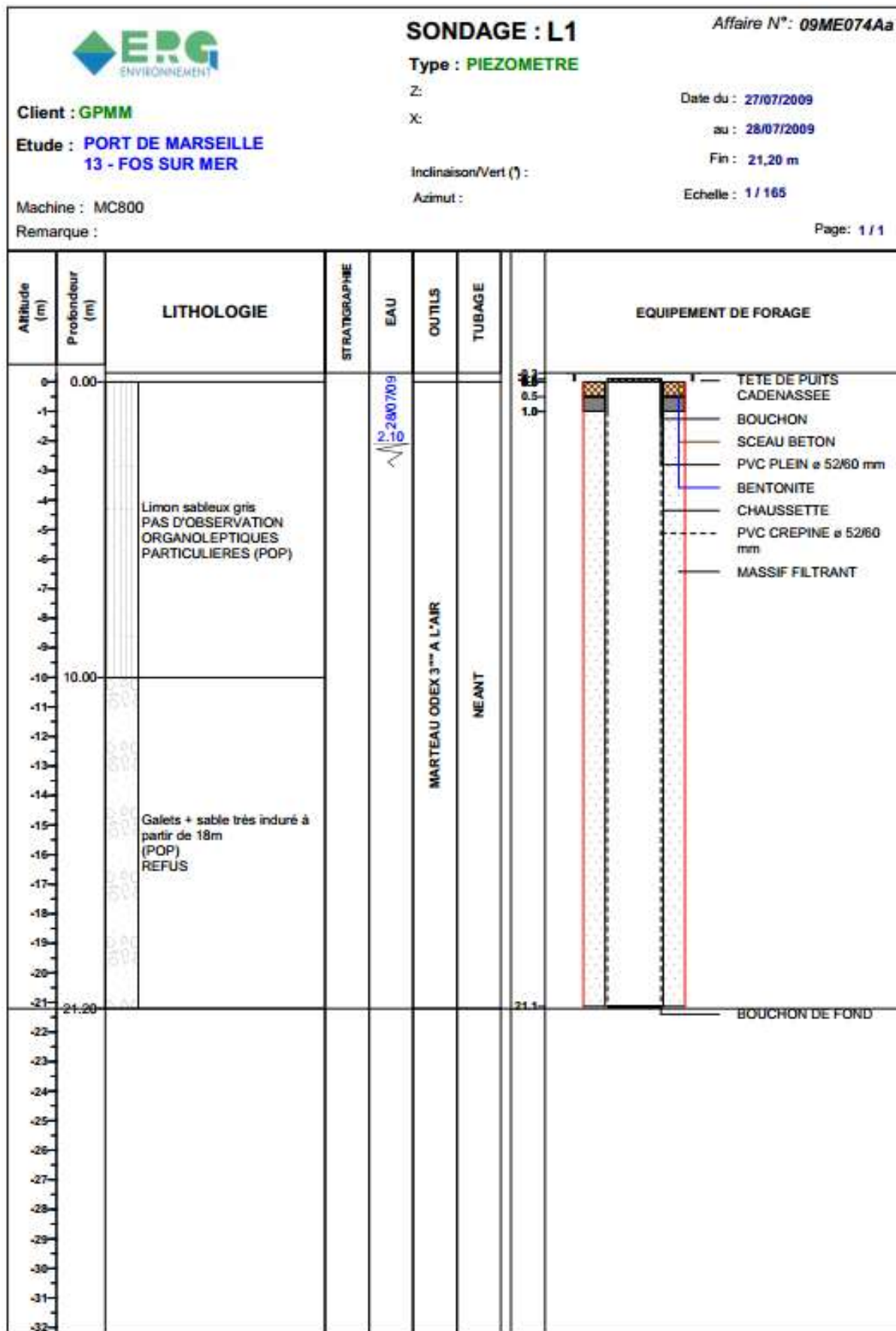
**Table.4.2.** Private pumping wells

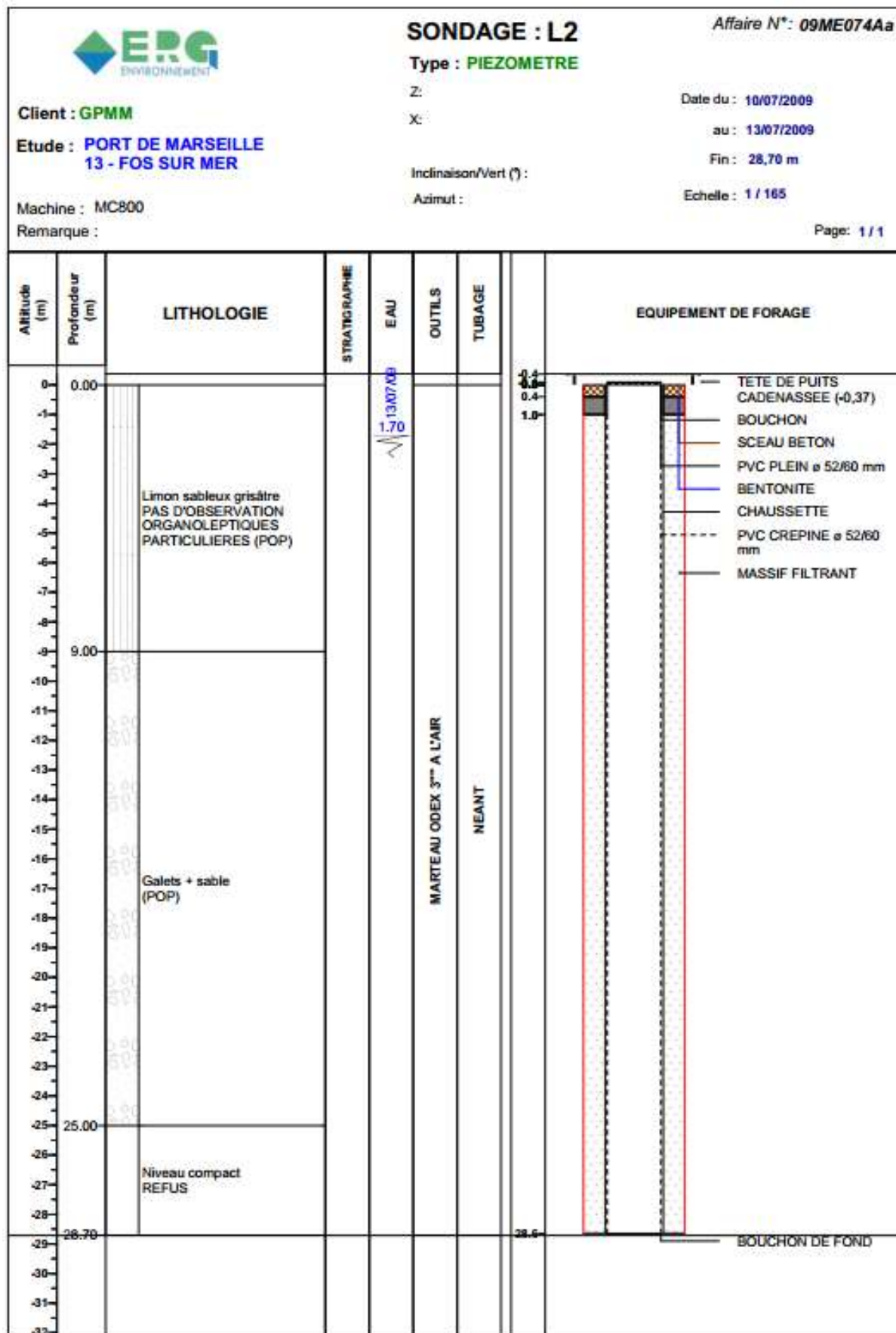
No	ID	Name	X	Y	Z	Debit
			<i>Lambert 93</i>	<i>Lambert 93</i>	<i>m</i>	<i>(m<sup>3</sup>/day)</i>
1	F1	Forages d'irrigation 1	853392	6268987	11	24
2	F10	Forages d'irrigation 10	850555	6270990	11	24
3	F11	Forages d'irrigation 11	851042	6271388	11	24
4	F12	Forages d'irrigation 12	850415	6271125	11	24
5	F13	Forages d'irrigation 13	850288	6271297	11	24
6	F14	Forages d'irrigation 14	850759	6271695	11	24
7	F15	F15	845175	6275231	11	24
8	F16	F16	844222	6272912	6	24
9	F17	F17	847915	6265052	0	24
10	F18	F18	847567	6264809	0	24
11	F19	F19	846317	6266872	0	24
12	F2	Forages d'irrigation 2	850762	6269152	11	24
13	F20	F20	845968	6267105	0	24
14	F21	F21	844933	6268249	0	24
15	F22	F22	844440	6268790	0	24
16	F23	F23	843036	6269801	0	24
17	F24	F24	842362	6270986	11	24
18	F25	F25	848234	6272319	11	24
19	F26	F26	844377	6275133	11	288
20	F27	F27	844985	6275449	11	308
21	F28	F28	845071	6275363	11	308
22	F29	F29	845136	6275841	11	256
23	F3	Forages d'irrigation 3	850810	6269780	11	24
24	F31	F31	845839	6275913	11	27
25	F32	F32	846157	6275234	11	24
26	F33	F33	846169	6277319	11	1,065
27	F34	F34	846306	6277772	11	24
28	F35	F35	846535	6276271	11	237
29	F36	F36	846680	6276805	11	24
30	F37	F37	846898	6277337	11	149
31	F38	Château de Vergières 1	847011	6276331	11	120
32	F39	F39	848194	6272121	11	24
33	F4	Forages d'irrigation 4	850687	6269935	11	24
34	F40	SCA La Grand Crau - Bayard	848233	6272319	11	16
35	F41	F41	848243	6272347	11	24
36	F42	F42	848274	6272330	11	294
37	F43	F43	848388	6271916	11	260

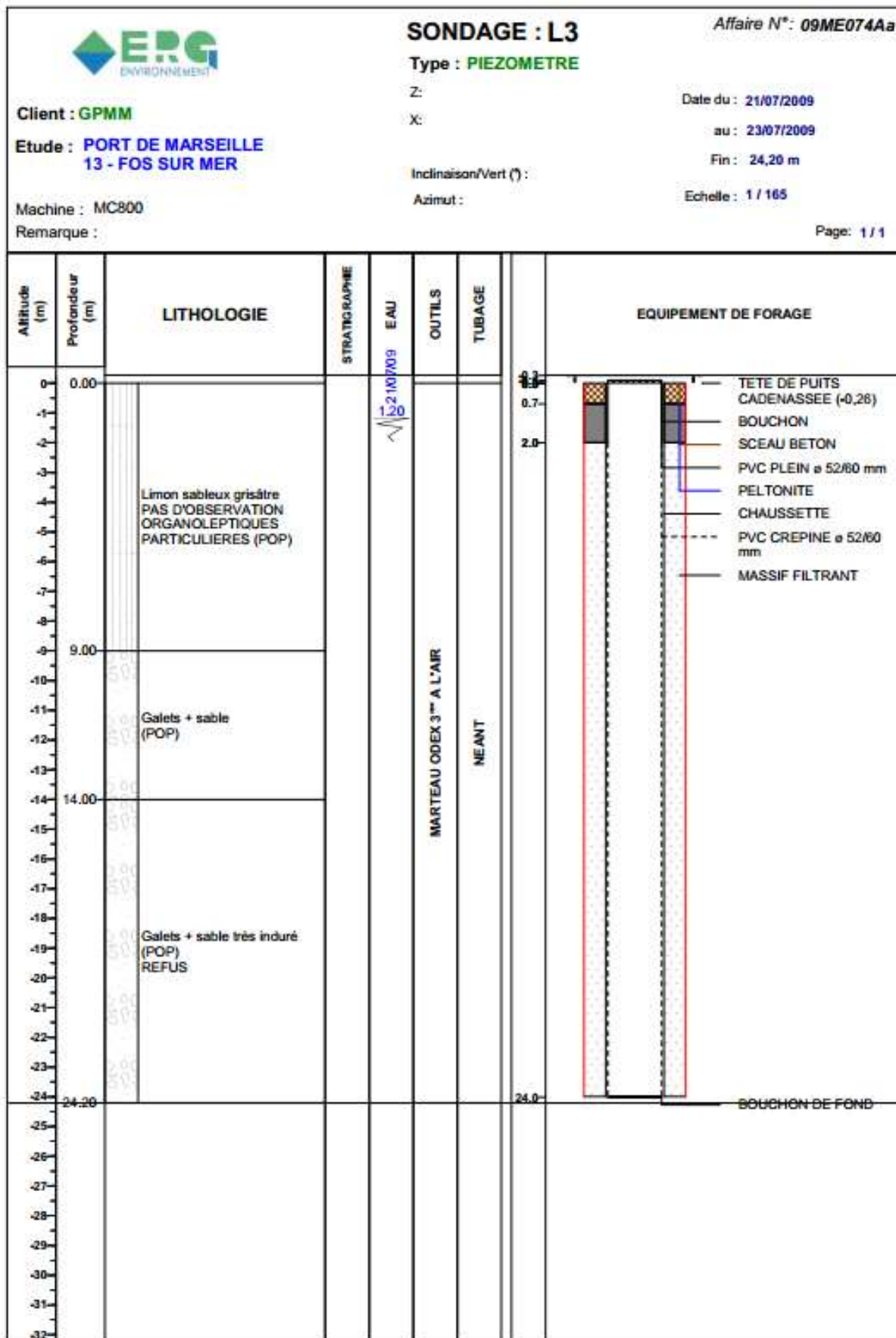
No	ID	Name	X	Y	Z	Debit
			<i>Lambert 93</i>	<i>Lambert 93</i>	<i>m</i>	<i>(m3/day)</i>
38	F44	Puits Domaine Bayard/Collongue	848484	6272458	11	2,000
39	F45	F45	848628	6272686	11	284
40	F46	F46	848640	6272698	11	24
41	F47	F47	848812	6272845	11	24
42	F48	F48	848981	6272986	11	24
43	F49	F49	848998	6272998	11	276
44	F5	Forages d'irrigation 5	850429	6269730	11	24
45	F50	F50	849273	6273712	11	24
46	F51	F51	849294	6273727	11	24
47	F52	F52	849366	6273680	11	24
48	F53	F53	849551	6273493	11	314
49	F54	Puits Cossour	850187	6270843	11	3,364
50	F55	F55	850713	6269207	11	533
51	F56	F56	850742	6269243	11	267
52	F57	F57	851245	6269172	11	311
53	F58	F58	851470	6268955	11	228
54	F59	F59	851688	6268455	11	103
55	F6	Forages d'irrigation 6	851154	6270350	11	24
56	F60	F60	851812	6268527	11	16
57	F61	F61	851896	6268565	11	474
58	F62	F62	851958	6268214	11	384
59	F63	F63	852197	6268449	11	384
60	F64	F64	852566	6267611	11	222
61	F65	F65	852778	6268900	11	384
62	F66	Puits Valinette	852901	6269502	13	1,326
63	F67	F67	853014	6268049	11	88
64	F68	F68	853170	6268951	11	121
65	F69	F69	853199	6268851	11	121
66	F7	Forages d'irrigation 7	850363	6270292	11	24
67	F71	F71	853621	6269036	11	121
68	F72	F72	853703	6269066	11	121
69	F73	Château de Vergières 2	847011	6276331	11	6
70	F8	Forages d'irrigation 8	850826	6270690	11	24
71	F9	Forages d'irrigation 9	851309	6271105	11	24
		<b>TOTAL</b>				<b>15,640</b>

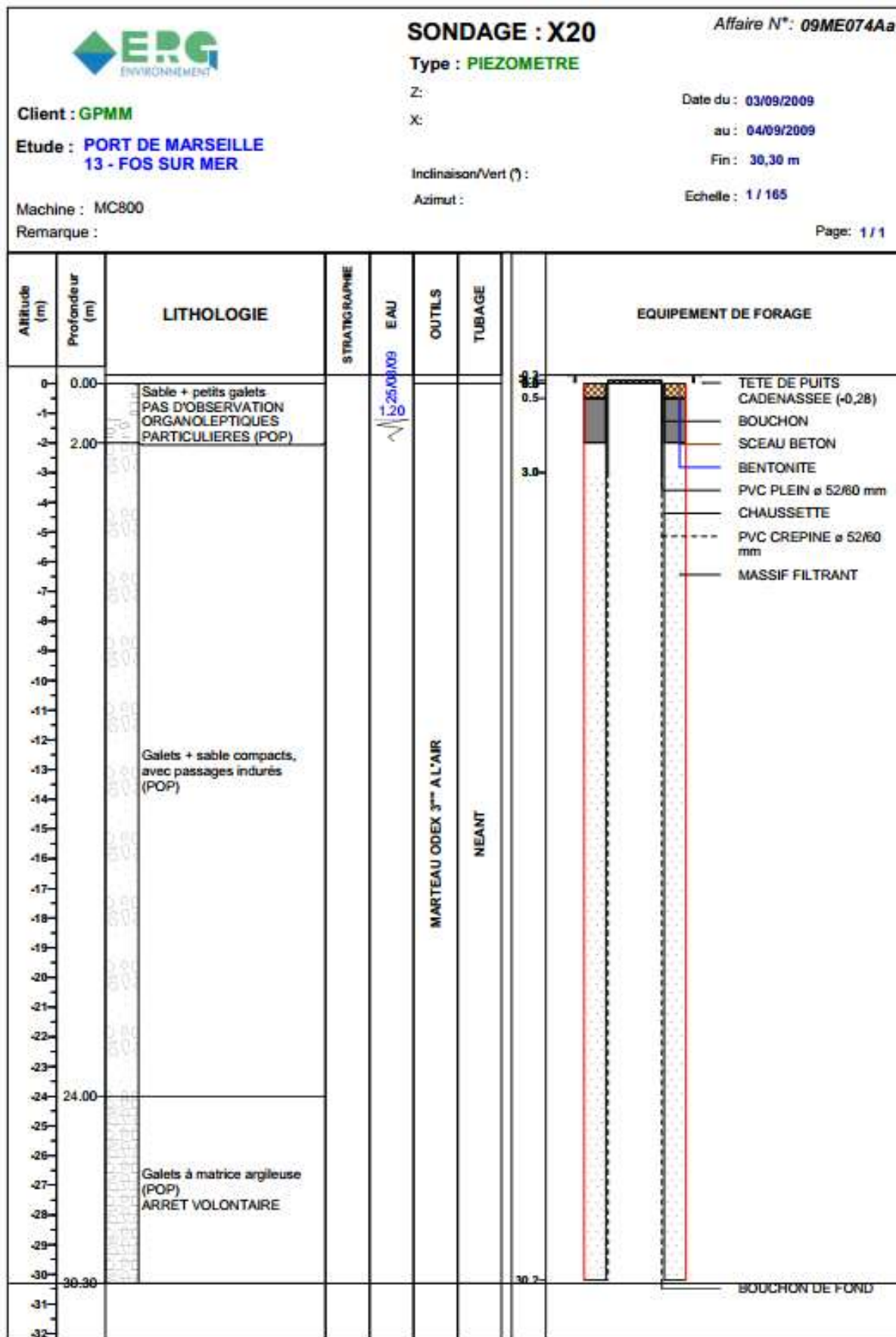
**Annex 5. Lithology description and well construction of radon sampling piezometers**

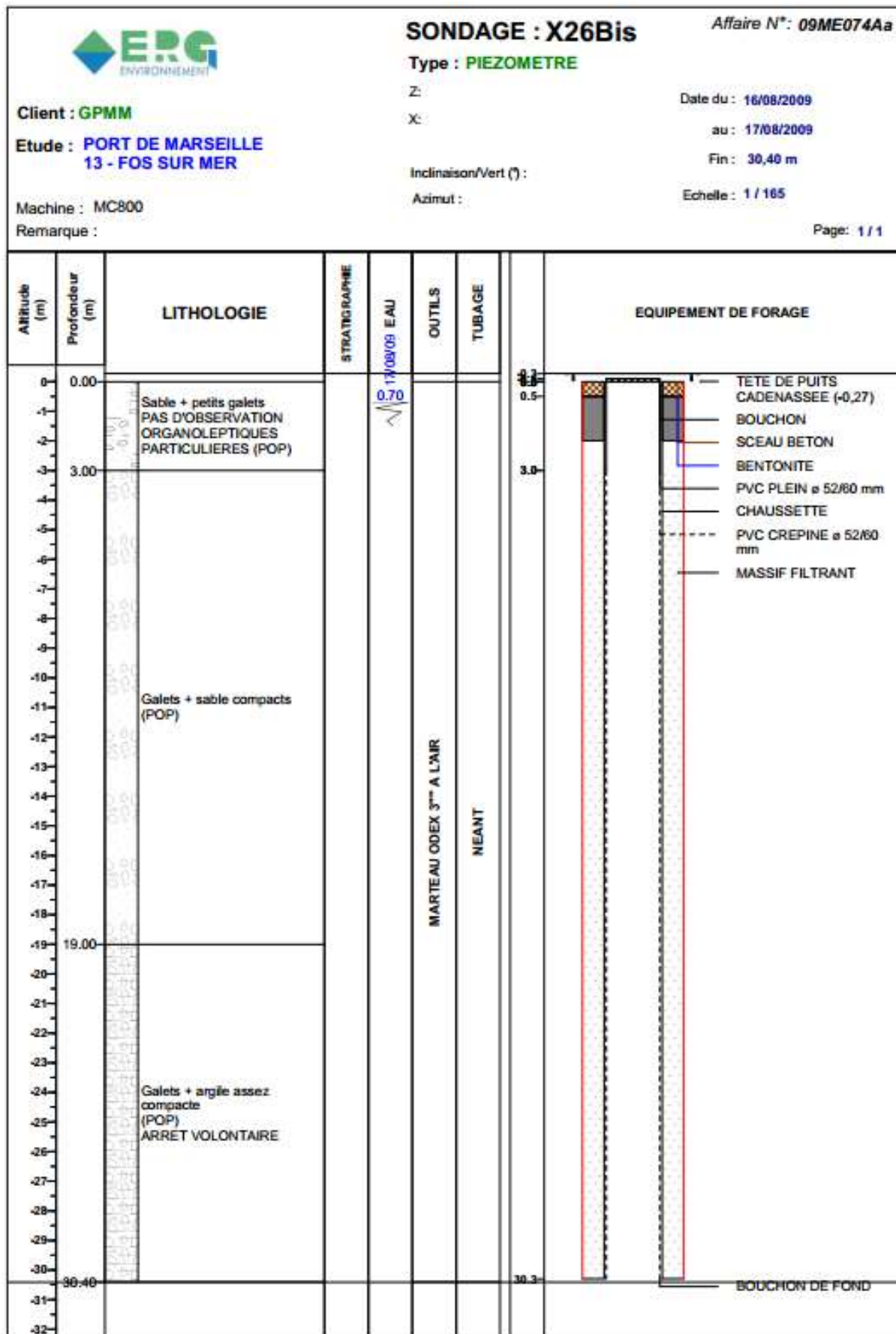


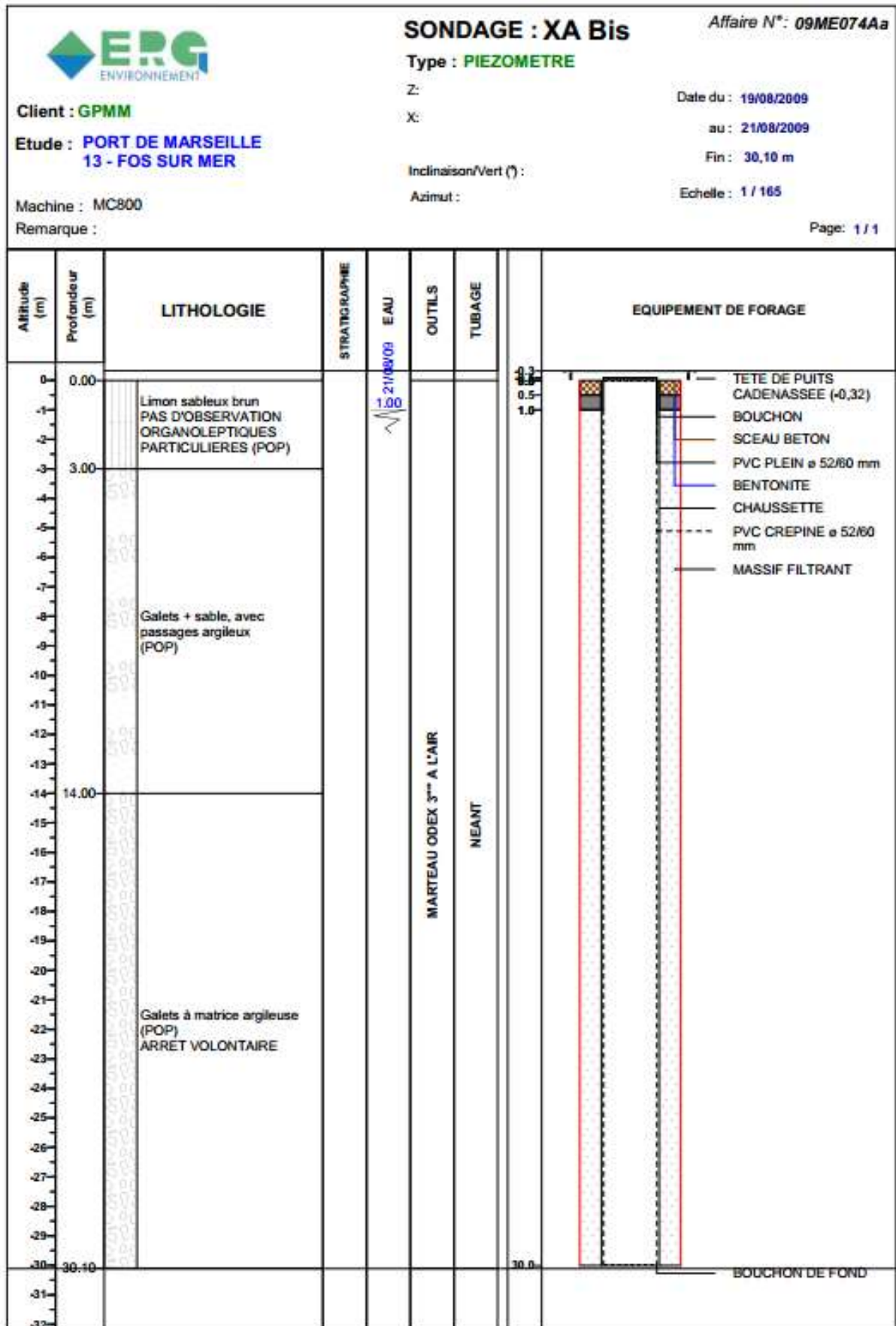


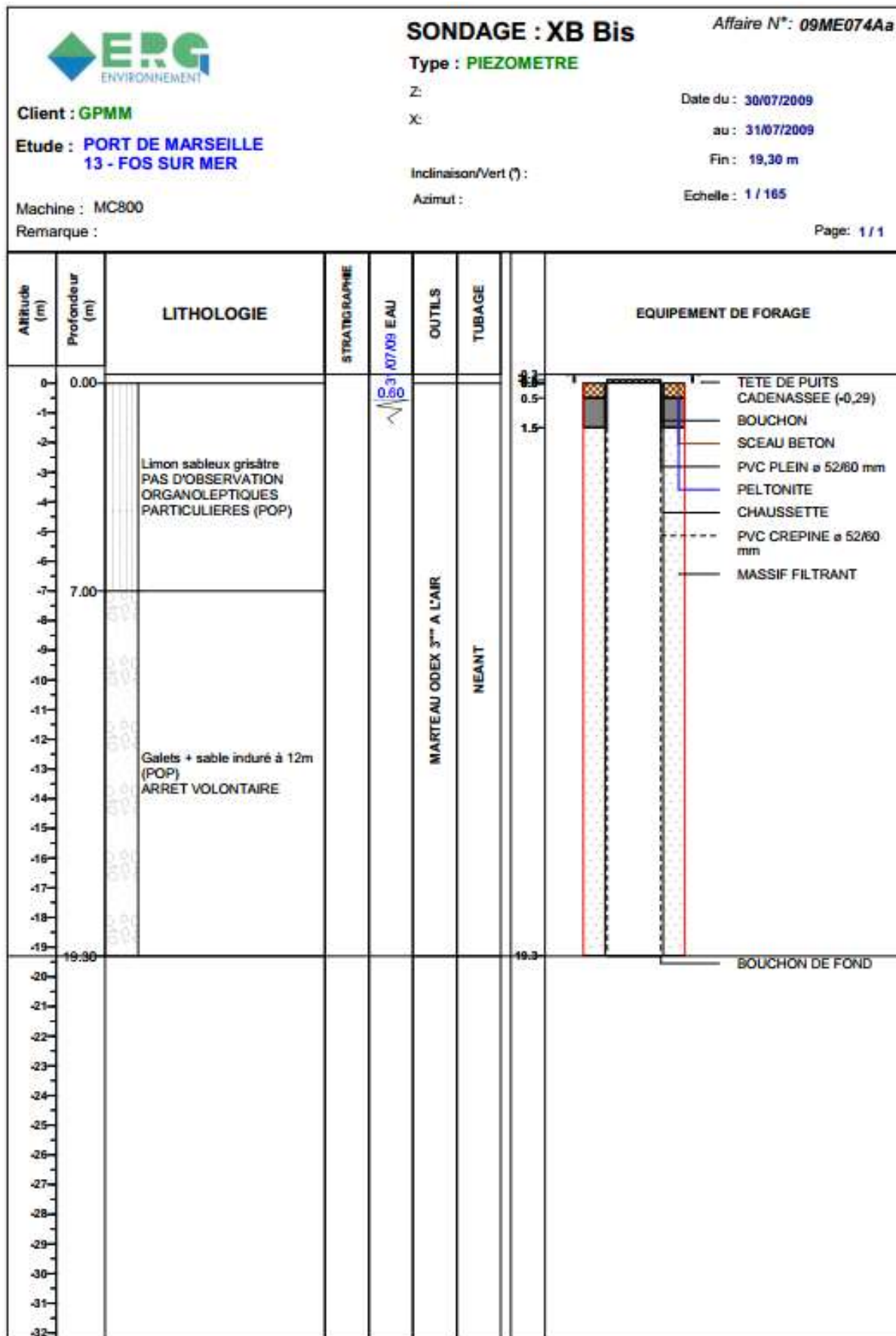


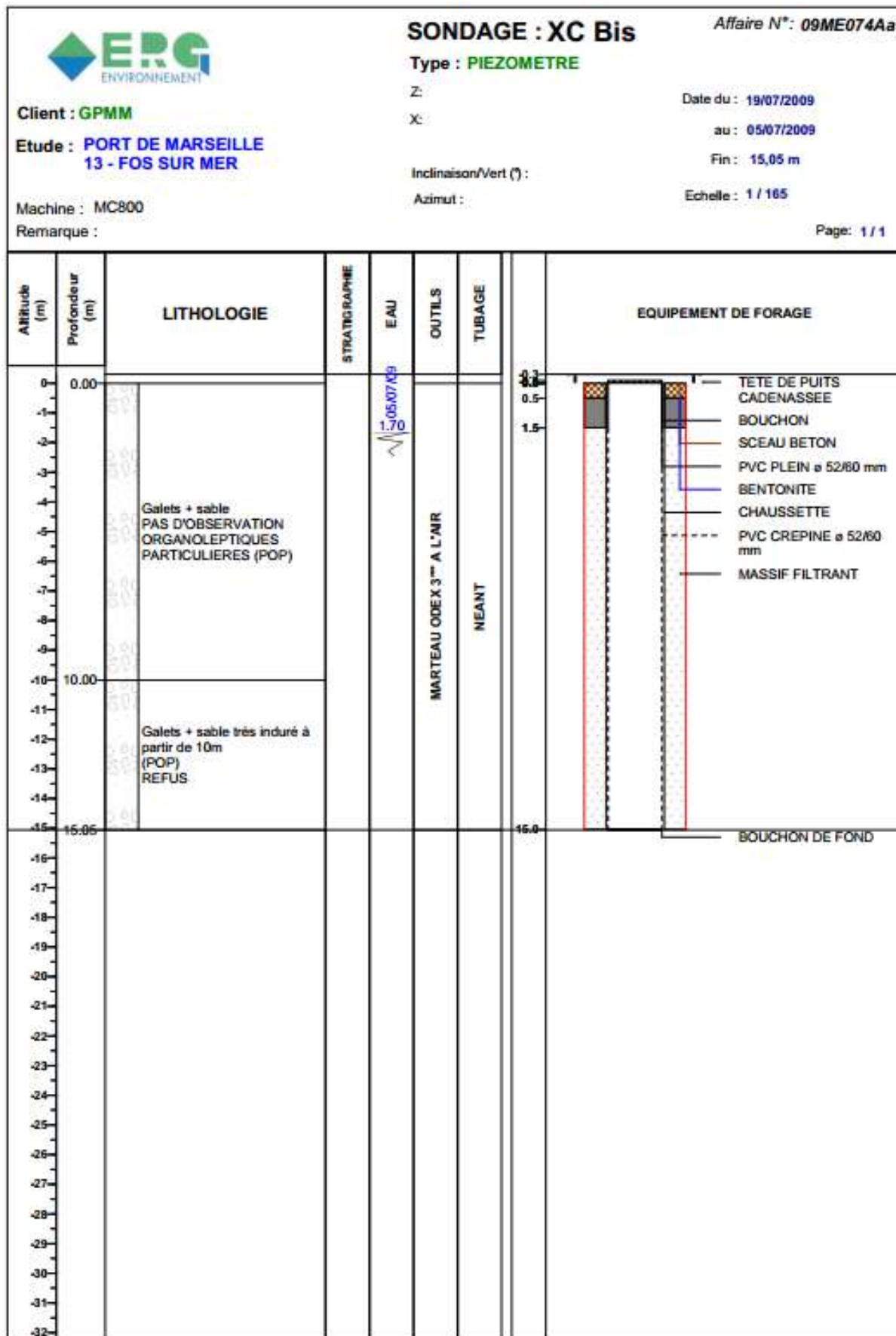


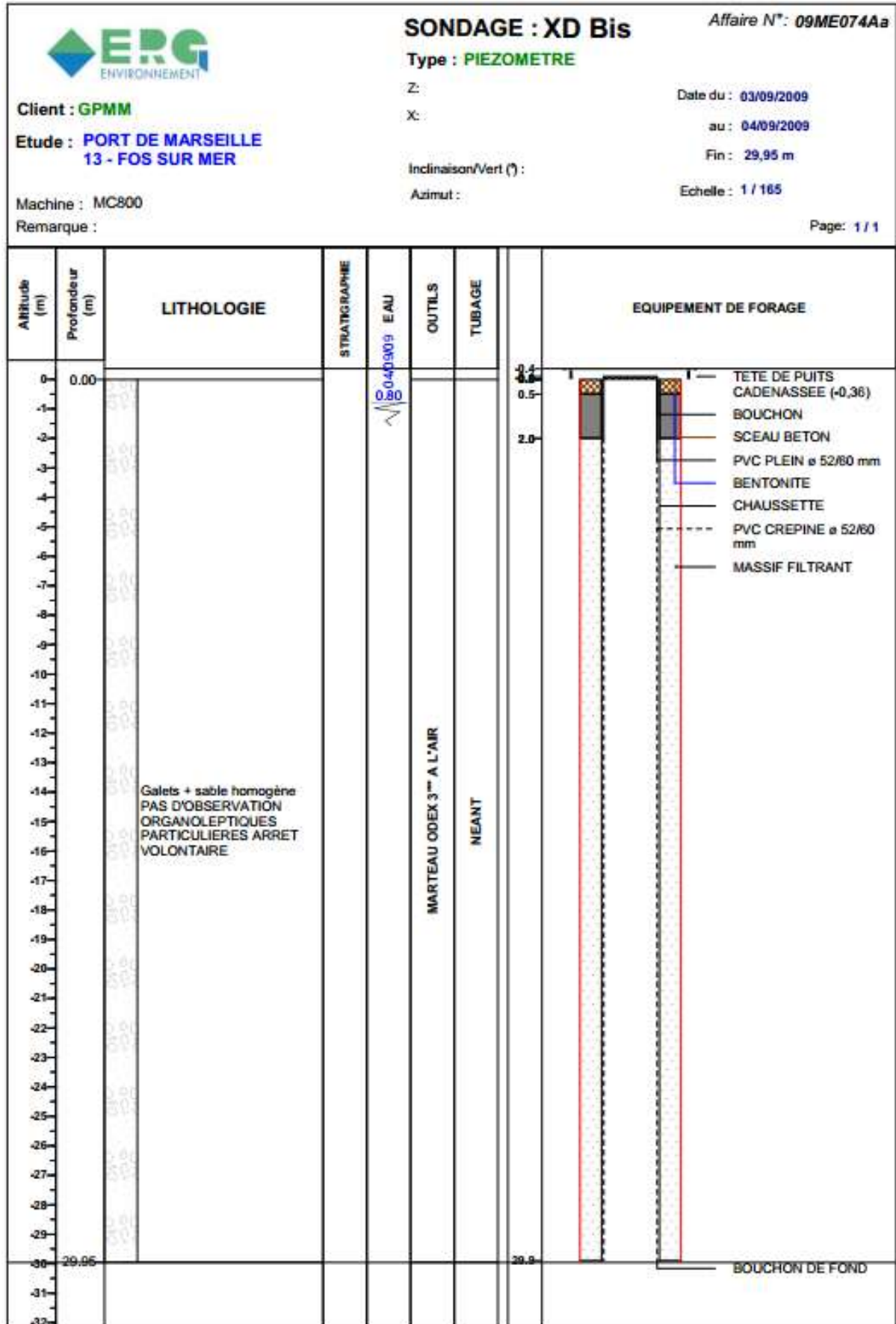












Nature	SONDAGE PZ21	Niveau d'eau mesuré par rapport au sol	0.6 m - April 27, 1972
Profondeur atteinte	19.55 m	Z Origine	3.0 - Précision : EPD
Date fin de travaux	April 26, 1972	Auteur	CAMUS

Profondeur	Formation	Lithologie	Lithologie	Stratigraphie	Altitude
0.60 1.00	Fz		Limon	Holocène	3.94 3.54
	Alluvions anciennes fluviales ou torrentielles et terrasses fluviales anciennes		Cailloutis, galets, graviers, sable	Pléistocène	
15.40			Mame ocre, graviers, calcaire sableux	Plaisancien	-10.86
19.55					-15.01



# ABSTRACT

This research has focused on the constraints related to the modeling of groundwater in coastal aquifer. In these aquifers, the concomitant presence of freshwater and saltwater alters the flow patterns typically represented by the Darcy equation. The influence of salinity on density and permeability make the mathematical resolution of flow equations more complex. Moreover, the influence of heterogeneities in the aquifer makes it more difficult and risky the parameterization model and its calibration. We propose to use strongly the results of both geophysical and isotopic investigations. Thus, we hypothesize that the description of the subsurface and the imaging of the freshwater/saltwater can help to develop and validate/calibrate the simulation of groundwater in coastal aquifers. We have also shown that geochemical measurements such as radon measurement may help to validate the simulated flow. Our approach was applied on the downstream part of the Crau aquifer. The comparison of the simulated results to observed data has shown the usefulness and applicability of our approach.

# RÉSUMÉ

La recherche a porté sur les contraintes reliées à la modélisation des écoulements des eaux souterraines en aquifère côtier. Dans ces aquifères, la présence concomitante d'eaux douces et d'eaux salées modifient les patrons d'écoulement classiquement représentés par l'équation de Darcy. L'influence de la salinité de l'eau sur ses propriétés (densité) et sur la perméabilité du milieu complexifie la représentation mathématique des équations d'écoulement et la résolution des systèmes d'équations. Par ailleurs, l'influence des hétérogénéités du milieu rend plus difficiles et hasardeux le paramétrage des modèles et leur calibration. Pour ce faire, nous avons proposé d'utiliser les résultats d'investigations géophysiques et isotopiques des eaux. Une meilleure description du milieu souterrain et l'imagerie de l'interface eau douce/eau salée peut en effet aider à un meilleur paramétrage et à une validation accrue de la simulation des écoulements des nappes côtières. Les mesures géochimiques telles celles des isotopes du radium ont aidé à la validation des flux et concentrations simulés. Notre approche a été appliquée sur la partie aval de la nappe de la Crau. La comparaison des résultats simulés par le modèle aux données de terrain résultant des suivis réalisés ont montré l'intérêt et l'applicabilité et la validation de notre approche méthodologique.

# TÓM TẮT

Nghiên cứu này tập trung vào giải quyết các hạn chế trong mô hình nước dưới đất ở các tầng chứa nước vùng ven biển. Trong các tầng chứa nước này, với sự xuất hiện đồng thời của nước nhạt và nước mặn, dòng chảy nước dưới đất thường được biểu diễn bởi phương trình của Darcy. Tuy nhiên, do ảnh hưởng của hàm lượng muối đến tỷ trọng và tính thấm của nước nên việc giải bài toán về vận động của nước dưới đất trở nên rất phức tạp. Hơn nữa, ảnh hưởng của tính bất đồng nhất trong tầng chứa nước càng làm cho việc nghiên cứu địa chất thủy văn vùng ven biển thêm khó khăn và thách thức, đặc biệt cho công tác mô phỏng và chỉnh lý các mô hình toán học. Chúng tôi đã đề xuất việc kết hợp các kết quả nghiên cứu bằng phương pháp đo địa vật lý và địa chất thủy văn đồng vị trong quá trình mô phỏng, hiệu chỉnh và kiểm chứng kết quả mô hình số. Các kết quả đo địa vật lý cho phép chính xác hóa ranh giới mặn nhạt và phân bố thành phần thạch học cũng như độ hồng của đất đá. Bên cạnh đó, ứng dụng độ phóng xạ của Radon trong nước dưới đất và nước mặt rất hiệu quả trong việc nghiên cứu về đặc tính thấm của tầng chứa nước và lượng bổ cập từ nước dưới đất. Phương pháp nghiên cứu đã được áp dụng một cách hiệu quả cho việc nghiên cứu quá trình xâm nhập mặn trong tầng chứa nước khu vực hạ lưu đồng bằng Crau, miền nam nước Pháp.

## خلاصة

ركز هذا البحث على النقاط المؤثرة على النمذجة الرياضية لأنظمة المياه الجوفية في مناطق السواحل. توضع المياه الجوفية العذبة المتلازم مع وجود المياه المالحة في هذه المناطق، يغير من نظام حركة المياه الجوفية الممثل عموماً بقانون دارسي. حيث أن تأثير ملوحة المياه على الكثافة و على خاصية النفاذية يجعل من الحل الرياضي للمعادلات الممثلة لحركة المياه أكثر تعقيداً. علاوةً على ذلك فإن تأثير عدم تجانس الخزان الجوفي يجعل من الصعوبة بمكان إيجاد المتغيرات الملائمة للنموذج الرياضي في سبيل معايرته. نقترح في هذا البحث تلازم إجراء المسوحات الجيوفيزيائية مع التحاليل النظائرية للمياه. يساعد ذلك في وصف و تحليل للخزان الجوفي و بالتالي يساهم في بناء و معايرة و التأكد من صحة النموذج الرياضي للخزان الجوفي في المناطق الساحلية. عرضنا أيضاً إمكانية استخدام التحاليل الكيميائية للمياه مثل تحليل عنصر الرادون في سبيل تأكيد صحة نموذج حركة المياه الجوفية. تم تطبيق هذه الطريقة المنهجية على الجزء الأدنى من الخزان الجوفي في منطقة لأكرو في جنوب فرنسا. مقارنة النتائج التي تم الحصول عليها من خلال النمذجة مع القياسات الحقلية تظهر أهمية البحث و إمكانية تطبيق الطريقة المنهجية المعتمدة.